AN ABSTRACT OF THE THESIS OF

Wayne Reitz for the degree of Doctor of Philosophy in Mechanical Engineering presented August 13, 1990.

Title: Influence of Laser Processing on the Corrosion and Microstructure of Zirconium Based Material.

Redacted for Privacy

Abstract Approved: _ _

James Rawers

Zirconium alloys were laser surface melted (LSM) using a continuous wave CO_2 laser at energy densities of 4, 7, and 10 kJ/cm^2. Melt widths were overlapped by 50% to achieve complete coverage. Laser melted pool depths and hardness profiles were a function of the applied laser energy densities. LSM samples examined using SEM and optical microscopy exhibited ultrafine martensitic microstructures. LSM samples were examined for alloy segregation using TEM electron diffraction, SEM-EDX, and SIMS. Corrosion performance was obtained by three techniques: 1) steam autoclave tests (400 ^{o}C, 1500 psig), 2) immersion tests in 10% $FeCl_3$ at room temperature, and 3) potentiodynamic tests in 10% $FeCl_3$ at room temperature. Potentiodynamic results were in agreement with immersion results. Coarser microstructures performed better than

fine microstructures in autoclave tests, while fine microstructures performed better than coarse microstructures in 10% $FeCl_3$ tests. LSM samples showed a 600-fold improvement in performance over wrought material when tested in 10% $FeCl_3$. Accelerated corrosion (nodular corrosion on coupons tested in autoclave and pitting corrosion on coupons tested in 10% $FeCl_3$) occurred near the laser beam overlap region. Sn and Fe alloy elements segregated near the periphery of each melt pool. Segregated regions containing increased Fe concentrations associated with each laser pass were responsible for accelerated corrosion.

Influence of Laser Processing on the Corrosion and Microstructure of Zirconium Based Material

by

Wayne Reitz

A THESIS

submitted to

Oregon State University

in partial fulfillment of
the requirements for the
degree of

Doctor of Philosophy

Completed August 13, 1990

Commencement June 1991

APPROVED:

Redacted for Privacy

Professor of Mechanical Engineering in charge of major

Redacted for Privacy

Head of Department of Mechanical Engineering

Redacted for Privacy

Dean of Graduate School

Date thesis is presented: August 13, 1990

Typed by Wayne Reitz for Wayne Reitz

ACKNOWLEDGMENTS

I appreciate the help of the thesis committee: Dr. Birkes, Dr. Hernried, Dr. Warrens, and Dr. Wolfe. Their assistance in data analysis, providing observations and suggestions and for their presence on the committee. My advisor, Dr. James Rawers, provided considerable insight and guidance to a returning graduate school student. His patience and methodology will be remembered for a long time.

I would like to thank the Babcock & Wilcox Company in Lynchburg, VA. for tuition grant and research funding. I would also like to express my appreciation to Teledyne Wah Chang, Albany, OR for assistance from metallography lab (Paul Danielson), corrosion lab, (M. Halfman and S. Aerni), chemistry lab (G. Hanson) and corrosion R&D (T. Yau). I extend my thanks to the U.S. Bureau of Mines, Albany, OR for assistance in potentiodynamic corrosion testing (S. Bullard).

However, I praise my wife, Carol Reitz, for her marvelous support during this period, even during miscarriage, pregnancy, birth, breast cancer, and chemotherapy.

TABLE OF CONTENTS

LIST OF FIGURES

LIST OF TABLES

INFLUENCE OF LASER PROCESSING ON THE CORROSION AND MICROSTRUCTURE OF ZIRCONIUM BASED MATERIAL

I. INTRODUCTION

A. OVERVIEW

This research examines the effect of laser surface melting (LSM) zirconium alloys. Corrosion performance and microstructural transformations are characterized and their relationships to LSM are established. The relationship between actual material behavior as it relates to metallurgical and compositional modifications caused by laser processing is detailed (Bonora, 1982; Follstaedt, 1987).

Results of this research have been presented at several American Society for Metals (ASM) and The Mining, Metallurgical and Metals Society (TMS) national and international conferences and are being published in those proceedings (Reitz, 1989; Reitz, 1990). A paper covering the entire research study has been reviewed by the National Association of Corrosion Engineers (NACE).

B. ZIRCONIUM

1. History and Applications

Zirconium is a relatively recent addition to the metals industry. Although the element is fairly common in the earth's crust, it is difficult to produce pure zirconium from the various zirconium silicates and oxides, due to the extreme reactivity of the metal with oxygen (Lustman, 1955). It was only in 1947, when W.J. Kroll developed the magnesium reduction process (Lustman, 1955; Rickover, 1975; Schemel, 1977), that substantial quantities of pure Zr became available. With the advent of nuclear power in the fifties, it was found that Zr possesses several properties which made it desirable for use in nuclear reactors (Fontana, 1976; Rickover, 1975; Wanklyn, 1962). These properties include: high corrosion resistance, good mechanical properties, and low thermal neutron absorption cross-section (Quach, 1984).

When Zr alloys are exposed to high temperature steam, the alloys quickly form a very hard and strongly adherent oxide film that protects the material from further rapid oxidation (Fontana, 1976; Johnson, 1969; Kass, 1964; Quach, 1984; Wanklyn, 1962; Wanklyn, 1964). Zr is highly reactive with oxygen, but rapidly forms a uniform

oxide that significantly reduces further oxidation. Since the oxide film is not easily removed, corrosion rates are measured as weight gains rather than weight losses.

Zr is resistant to corrosion in a wide range of chemical environments. Generally, it is more corrosion resistant than stainless steel. However, Zr is not resistant to fluoride, chlorine, concentrated sulfuric acid, or ferric and cupric chlorides (Cox, 1976; Maguire, 1986; Schemel, 1977; Yau, 1984; Yau, 1985). In most environments zirconium's resistance is the result of a thin self-generating oxide film on the metal that makes it appear more noble than the electromotive series indicates.

After technology permitted the extraction of hafnium from zirconium and the proper alloying elements were determined, Zr alloys became the material of choice for nuclear reactor service (Anderson, 1963; Lustman, 1955). The Zircaloys were developed after it was demonstrated that pure Zr with the impurities of O, N, C, and Si had good corrosion performance in an autoclave environment (Fontana, 1976; Kass, 1964; Rickover, 1975; Schemel, 1977; Wanklyn, 1962). It was later shown that additions of Sn, Fe, Cr, and Ni further enhanced the corrosion resistance of Zr. This new alloy was called Zircaloy-2

(Zr-2). Further tests demonstrated that Ni in Zr-2 accelerated hydrogen absorption when tested in an autoclave and resulted in Zr-2 embrittling. Zircaloy-4 (Zr-4) was developed by removing the Ni and slightly increasing the Fe concentration. There are several excellent reviews detailing the development of the Zircaloys (Douglass, 1963; Rickover, 1975).

C. LASERS

1. General

Laser is an acronym for Light Amplification by Stimulated Emission of Radiation. The two main types of lasers are: solid state, such as ruby-glass doped with neodymium or yittrium-aluminum-garnet (YAG) doped with neodymium; and gas, such as argon, helium-neon, or carbon dioxide (Arata, 1986; Bass, 1985; Winburn, 1987).

The scope of laser processing has increased from its conception (Anderson, 1988) up to the development of multikilowatt continuous wave (cw) CO_2 lasers in the 1970s. Presently, commercially available cw CO_2 lasers range from an output power of 1 watt to 15 kw (Koelsch, 1985; Winburn, 1987). Recently, neodymium

yttrium-aluminum-garnet (Nd-YAG) lasers have become commercially available with power output of up to 400 watt (Koelsch, 1985; Winburn, 1987).

Amplification of lasing action is activated in solid state lasers by a high intensity arc lamp and in gas lasers by an electric discharge. This energy places a number of atoms in higher energy levels, and, as they revert to normal levels, light photons are emitted. These photons, in turn, stimulate the emission of additional photons (Arata, 1986; White, 1987; Winburn, 1987).

The stimulating medium is enclosed in an optical cavity with mirrors, which reflect and contain the photons. One of the mirrors is partially transmissive to emit radiation for use. The resulting transmitted radiation has two important properties: spatially coherent and minimal beam divergence. These properties permit focusing of high concentrations of radiation energy (Arata, 1986; Winburn, 1987).

Laser beams are currently being used in a variety of applications - from growing crystals to quenching metal alloys into metastable states, and from depositing films to purifying surfaces (Arata, 1986; Ayers, 1979; Glaeser,

1979; Mazumder, Singe, 1987). In all of these applications a percentage of the beam energy is absorbed resulting in a change of optical energy to thermal energy (Lumsden, 1982; Picraux, 1981; Von Allmen, 1980). The absorbed energy is instantaneously transferred to the lattice. Near surface regions rapidly approach the melting temperature and a liquid/solid interface begins to move into the substrate. Upon removing the laser energy, the maximum melt depth is achieved. The liquid/solid interface velocity is temporarily zero as the bottom of the melt pool is reached, but then the interface velocity rapidly increases as it returns to the surface. Interdiffusion in the melt continues, but solidification of the metal behind the liquid/solid interface occurs so rapidly that solid state diffusion may be neglected (Clayton, C.R., 1989; Poate, 1989).

Metastable structure synthesis by laser melting and rapid quenching has opened an exciting era in physical metallurgy (Ohse, 1988). Rapid quenching provides the means for tailoring certain properties: microstructure, alloy composition, and metastable phases, previously unattainable, to meet specific material requirements (Arata, 1986; Draper, 1982; McCafferty, 1986). The improvement of surface sensitive properties such as corrosion protection, microhardness, and wear resistance

have been achieved by laser processing at high quenching rates (Arata, 1986; Davis, 1986; Draper, 1982; Steen, 1978). Laser processing allows the production of surface layers with a wide range of structures and compositions (Arata, 1986; Clayton, C.R., 1989; David, 1989; Kar, 1987; Mazumder and Kar, 1987; Ohse, 1988).

The significant laser processing parameters (Arata, 1986; Bruck, 1987; Hawkes, 1985; Kirillin, 1987; Li, 1985; Sprow, 1988) are wavelength, reflectivity, energy density, focal spot diameter, and beam speed. Important material properties are: reflectivity, thermal conductivity, diffusivity, and melting and vaporizing temperatures (Arata, 1986; Draper, 1984; Draper, 1985; Mazumder, 1982; Steen, 1978; Von Allmen, 1980).

2. Applications

During the past twenty years, both the increasing demand for advanced materials and the availability of these high power laser sources have stimulated considerable interest in applied research and development (Ferrando, 1988; Moffat, 1988). The repertoire of metallurgical applications of lasers has grown to include: cutting (Koelsch, 1985, Winburn, 1987), drilling (Koelsch, 1985; Winburn, 1987), welding (Holbert, 1987;

Mazumder, 1981; Khan, 1988; Vaccari, 1989) and heat treating (Irons, 1978; Steen, 1979) and have found their way into industrial production lines.

In addition to the use of lasers in metal working, lasers provide a method of altering the surface either by surface melting (Folkes, 1986; Giordano, 1986; Glaeser, 1979; Kaufmann, 1986; Lu, 1988) or surface alloying (Draper, p67, 1981; Draper, 1982; Folkes, 1986; Lumsden, 1982) to achieve improved surface performance. Laser surface modification permits several surface characteristics to be improved including: corrosion (Borona, 1982; Draper, 1979; Mazumder, Singe, 1987; Steen, 1978; Zaplatynsky, 1982), wear (Glaeser, 1979), and thermal barrier coatings (Miller, 1984; Zaplatynsky, 1982; Zaplatynsky, 1986).

Surface modification by rapid solidification is most readily accomplished by laser surface melting, which exploits the principle of self-substrate quenching. Using continuous wave carbon dioxide (cw-CO_2) gas lasers, melt depths can be controlled to 25 microns. Rapid solidification processing (RSP) has been successfully applied to many different alloys, including: nickel (Bruck, 1987; Mazumder, p941, 1980), iron (Mazumder, 1986), aluminum (Kear, 1988; Mazumder, 1986) and titanium (Mazumder,

p941, 1980; Peng, 1985) base alloys.

3. Laser-Metal Interaction

Inherent rapid heating and cooling rates in LSM provide an opportunity to produce novel material phases and compostions outside those dictated by equilibrium phase diagrams (Rimini, 1981; White, 1987). High cooling rates, 10^4 to 10^8 ^oK/sec, often lead to extended solubility of the solute atoms and, thus, produce novel metastable materials (Lu, 1988; Khan, 1988; Steen, 1978). This process is dependent on energy, momentum and mass transport. Energy transport determines the rate of heating and cooling, whereas, momentum and mass transport determine the extent of mixing and final composition.

a. Heat Transfer

Laser processing of metals usually involves a focused laser beam scanning over a material surface. Typically, laser power is 10 watt to 10 kw. The beam diameter is 0.5 to 3.0 mm. The scanning speeds range from 1 to 100 cm/sec. The melted surface layer, usually less than 1 mm deep (Bruck, 1987; Cieslak, 1989; David, 1989), is rapidly heated to produce locally high temperatures, melting, and possibly evaporation. Simultaneously, heat

is dissipated locally within the metal via thermal diffusion (Boettinger, 1984; Den Broeder, 1984; Kaufmann, 1986; Pang, 1987; Teramoto, 1989). Thus, the metal experiences an extremely rapid heating-cooling cycle. The steep temperature rise immediately ahead of the scanning laser beam is caused by rapid accumulation of the oncoming laser heating, whereas the temperature decline behind the scanning laser beam is dominated by the thermal diffusivity of the metal (Mazumder, p115, 1983). The cooling phase, called self-quench (Kear, 1988), controls the microstructure that, in turn, controls the physical and mechanical properties. Cooling rates of 10^4 to 10^8 ^oK/sec (Kear, 1988; Khan, 1988; Lu, 1988; McCafferty, 1982; Poate, 1989; Steen, 1978) are readily obtainable.

Direct experimental determination of the cooling rates and/or temperature distributions during laser processing is not feasible because of the small heated volume and fast temperature changes (Peng, 1985). Heat transfer phenomena can be simulated with mathematical models (Mazumder, p18, 1983; Mazumder, 1986; Tsubaki, 1977) and results verified by post-processing analysis of melt profiles (Mazumder, p941, 1980) and solidification microstructures (Kattamis, 1981).

1) laser surface melting

Laser melting is generally used in either of two applications: 1) surface melting for surface modification, or 2) melting to achieve welding. This thesis is concerned with the first application; however, whether welding or surface melting is being considered, LSM interacts with several material properties in the same manner. These include (Mazumder, p941, 1980; Mazumder, p115, 1983; Mazumder, 1986): microstructural transformation, ability to transfer heat, second phase formation, physical properties, and mechanical properties. This section discusses laser processing in the field of welding as it is applicable to surface melting.

Metallurgically, laser processed material consists of three major zones: melt zone, heat affected zone adjacent to the melt zone, and unaffected base metal. The heat affected zone (HAZ) is a function of laser processing (Chande, 1983; Giordano, 1986; Mazumder, p941, 1980; Steen, 1979). Specifically, HAZ size is directly related to laser power and specimen thickness. Additionally, HAZ size is inversely related to laser beam speed (Mazumder, 1977; Mazumder, p423, 1980).

Considerable research has been conducted over the

years to develop models to predict the effects of LSM (Hawkes, 1985; Peng, 1985; Mazumder, 1977; Mazumder, p115, 1983; Mazumder, 1986; Peng, 1985). Researchers have developed two types of models to characterize the laser processed material behavior: analytical and numerical solutions. In analytical solutions (Mazumder, p115, 1983; Peng, 1985) there are two classes of heat transfer models: two-dimensional and three-dimensional. Heat input is generally considered as a point or a line source. In laser processing, the former is normally used.

Numerical solutions remove many of the limitations that apply to analytical methods e.g., (Mazumder, 1977; Mazumder, p115, 1983): 1) flexibility of heat source, 2) automatic incorporation of geometry of workpiece, 3) ability to include temperature dependency of workpiece's physical properties, 4) truncation error from series expansion of various functions associated with analytical solutions is absent, and 5) difficulty of application of analytical solution of heat flow equation to real boundary conditions.

For laser welding, which has well defined beam characteristics, more precise mathematical modeling is possible than for the conventional welding processes

(Hawkes, 1985). However, improvement in the predictive capabilities of mathematical models requires better understanding of plasma formation (Khan, 1985) and fluid flow within the molten pool (Mazumder, p115, 1983).

2) pool temperature

Determination of molten pool temperature during laser welding is difficult since the molten pool is surrounded by hot plasma (Khan, 1985). The synergistic effect of molten pool time, degree of mixing (turbulency), incident laser energy density, and absorptivity have a major influence on the temperature attained by the molten pool (Hawkes, 1985; Kirillin, 1987).

b. Rapid Solidification

1) mass transport

Convection is the single most important factor influencing the geometry of the pool including pool shape and ripple formation (Chan, 1984; Chan, 1987; Chande, 1985; Copley, 1981; Schaefer, 1983). Convection is also primarily responsible for alloy mixing and therefore affects the elemental composition of the molten pool (Chan,

1984). For best performance, alloying should be uniform over the laser processed zone. Large local variations in composition could seriously affect performance in corrosive environments (Boettinger, 1984; Chande, 1985; Mazumder and Kar, 1987).

The inherent rapid heating and cooling rates of the LSM process often lead to an extension of solubility of solute atoms, producing novel metastable materials (Clayton, C.R., 1989; Mazumder, p18, 1983). The heat generated by the absorbed beam energy raises the temperature of the material and produces a molten pool. The surface temperature decreases radially outward from the center of the pool (Chande, 1985). The surface tension, inversely related to temperature for most metals, increases radially outward from the center of the pool (Chande, 1985; Chan, 1987; David, 1989), thus enhancing the convection within the molten pool, allowing solute transport to occur readily in the liquid phase (David, 1989; Kar, 1987).

2) alloy segregation

Free surfaces represent the interface through which materials interact with the local environment. Surface conditions often limit the performance of materials in

many practical applications. Surface composition is clearly one of the dominant characteristics affecting how a material behaves when placed in a non-equilibrium chemical or physically stressed environment (Boettinger, 1984; Draper, 1979).

Earlier work demonstrated (Chan, 1984; Chan, 1987; Chande, 1985; Mullins, 1964; Tiller, 1953) that mass transport in the laser melted pool is dominated by convection. Although liquid composition can be assumed to be almost homogeneous due to bulk mixing (Draper, p21, 1981; Schaefer, 1983), a partitioning mechanism occurring at the liquid-solid interface under rapid solidification significantly alters the composition of the solidified material (Draper, p21, 1981; Mazumder and Kar, 1987).

Solute transport is considered to occur only in the liquid phase, while energy transport is considered in both liquid and solid phases (Aziz, 1982; Kar, 1987). During solidification of the liquid, alloy elements and impurities are attracted to the liquid-gas surface if they have an affinity for higher temperature phases (Follstaedt, 1981). As the liquid-solid interface moves toward the liquid-gas surface, atoms rejected from the freezing solid enter the liquid and redistribute by diffusion and turbulent mixing (Baeri, 1979).

Studies (Baeri, 1979; Chande, 1983; Draper, 1979) have shown composition gradients exist within the molten pool from edge to center or from bottom to top, due to solidification initiating at the edge and at the bottom of the molten pool.

One study (Chande, 1983) examined the composition fluctuations from the average composition. They found that fluctuations increased as beam diameter and beam speed increased. Thus, uniformity in composition increased as diameter and speed decreased. Decreasing the speed implies that the interaction time was greater, the pool was thus molten for a longer time, and diffusion on a local scale could be expected to assist in leveling the composition gradients. A decrease in beam diameter steepens the temperature gradient in the melt pool. This produces a finer dispersion of solute-rich pockets, and local diffusion works to produce uniformly laser processed zones (Chande, 1982).

Another study (Vandenberg, 1984) has shown that most of the Fe-rich precipitates in a Cu-Al-Fe alloy, resulting from conventional melt casting, disappeared after LSM. The disappearance of the Fe-rich precipitates suggests that a major portion of the Fe is retained in

solution. X-Ray diffraction did reveal weak reflections at the proper d-spacing for Fe-rich precipitates, indicating that a small amount of Fe-rich precipitates were still present, but were of small diameter.

Research on aluminum alloys (Schaefer, 1983) showed that a microsegregation-free zone was present at the bottom of the molten pool. Diffusion distances are small and negligible during LSM and, therefore, do not contribute to homogenizing the solidified molten pool.

Microprobe results on Fe alloys (Moore, 1979) showed that Cr was uniformly distributed within shells that were concentric with the molten pool outline. The Cr content varied from one shell to the next shell.

3) zirconium experience

Early research (Woo, 1979) examining the effect of quenched Zr-4 on microstructure was based on electrical conductance heating and quenching rates of 100 to 200 ^{o}C/sec. Increasing quench rates developed various microstructures: lenticular, basketweave, and martensite. Research (Ferrando, 1988) showed that platelet width was characterized by the quench rate.

Recent research (Richard, 1987; Snow, 1979; Vifayakar, 1985; Richard, 1988; Cortie, 1982; Charquet, 1988) has examined LSM material to define the resulting microstructure and to determine the existence of second phase particles. Quench rates of approximately 10^4 ^{o}C/sec produced a martensitic type structure. Precipitates could not be detected when examined by transmission electron microscopy (TEM) at 50,000X.

c. Microstructural Transformations

Metallurgically, laser processed material consists of three major zones: melt zone, heat affected zone adjacent to the melt zone, and unaffected base metal. Characteristics of the melt zone depend on the solidification behavior of the molten pool (Schaefer, 1983). Local solidification conditions and cooling rates vary significantly within the molten pool (David, 1981; David, 1989). Previous research (Baeri, 1979; Chan, 1987; Chande, 1983; David, 1989; David, 1981; Draper, 1979) has shown that cooling rates at the edge of the pool are higher than at the bottom of the pool below the centerline. This has been confirmed by microstructural studies, showing a finer microstructure at the edge of the pool (Lewis, 1982; Teramoto, 1989).

1) quenched microstructure

Solidification of the molten pool produces a grain structure determined by the base metal grain structure and the laser processing parameters (David, 1989; Folkes, 1986; Follstaedt, 1981). The base metal acts as an ideal substrate upon which growth of the solid phase occurs (Follstaedt, 1981). Grain growth of epitaxially oriented solid is influenced by crystallographic effects (David, 1989; Folkes, 1986). Since there are preferred growth directions for solidification, a competitive process among the grains takes place in which the most favorably oriented grains grow faster and soon outgrow the less favorably oriented grains (David, 1989). The optimum grain orientation is one in which the preferred growth direction is perpendicular to the solidification front. This optimal orientation varies as the solidification front orientation changes across the molten pool (Kaufmann, 1986). Therefore, molten pool shape has an influence on the final grain structure.

Microstructure resulting from LSM is dependent on the thermal transient induced into the surface layers (Steen, 1979). Therefore, application of LSM requires knowledge of the relationships between the laser processing parameters, the induced thermal transient, and the

influence of thermal conditions during solidification on resulting microstructure (Giordano, 1986).

LSM parameters determine depth of melting (Steen, 1979), but the final microstructure and hardness profile are determined by the self-quenching rate. Therefore, thinner samples do not achieve the high hardness attainable in thicker samples (Giordano, 1986; Lewis, 1979). The depth of hardening (Steen, 1979) has been found to be linearly related to:

$$\text{hardening depth} = f\ [\ P\ (D\ V)^{0.5}\ ] \qquad (I.1)$$

where: P = laser power (watts), D = Beam diameter (mm), and V = beam speed (mm/sec).

LSM Zr has been processed without a cover gas (Barsukov, 1982; Ursu, 1986) producing zirconium nitride alloyed with oxygen. The surface possesses high hardness which decreases linearly with depth until the base metal is reached. Chemical analysis showed that no significant oxygen contamination occurred during LSM when a shielding gas is employed (Mazumder and Steen, 1982; Vandenberg, 1984).

D. CORROSION

1. Autoclave Corrosion

a. General Principles

Oxidation by gaseous oxygen is an electrochemical process (Fontana, 1967). It is not simply the chemical combination of metal and oxygen, $M + 1/2O_2 = MO$, but consists of two partial processes:

$$M = M^{+2} + 2e^{-1} \quad \text{at metal-oxide interface} \qquad (I.2)$$

$$1/2O_2 + 2e^{-1} = O^{-2} \quad \text{at oxide-gas interface} \qquad (I.3)$$

$$M + 1/2O_2 = MO \quad \text{overall} \qquad (I.4)$$

with new metal-oxide (MO) lattice sites produced either at the metal-oxide interface or at the oxide-gas interface. Metal ions are formed at the metal-oxide interface and oxygen is reduced to oxygen ions at the oxide-gas interface. Because all metal oxides conduct both ions and electrons to some extent, this electrochemical reaction occurs without the necessity of an external electronic conductor between the local anode and the local cathode.

The electrochemical nature of gaseous oxidation is comparable to aqueous galvanic corrosion (Cox, 1976; Smeltzer, 1986). This is presented schematically in Figure 1 (Cortie, 1982; Cox, 1976; Dollins, 1983). Oxide layers serve simultaneously as: 1) ionic conductors (electrolyte), 2) electronic conductors, 3) electrodes at which oxygen is reduced, and 4) diffusion barriers through which ions and electrons must migrate. Electronic conductivities of oxides are usually one or more orders of magnitude greater than their ionic conductivities. Thus, movement of either cations or oxygen ions controls the reaction rate (Fontana, 1967).

Almost without exception, cations and oxygen ions do not diffuse with comparable ease in a given oxide. Simple diffusion control would result in the growth of the oxide at either the metal-oxide or the oxide-gas interface (Moran, 1978). When controlled by lattice diffusion, the oxidation rate is most effectively retarded in practice by reducing the flux of ions diffusing through the oxide.

Refractory metals, i.e., Ta, Cb, Hf, Ti and Zr form oxides in which oxygen ion diffusion predominates over cation diffusion, so that simple diffusion control would result in oxide formation at the metal-oxide interface

(Chappell, 1978; Moran, 1978). However, after an initial period, the oxidation of these base metals is not controlled by ionic diffusion in the oxide (Cortie, 1982; Cox, 1976; Dollins, 1983). Oxide formed at the metal-oxide interface (with a large increase in volume) is porous on a microscopic scale and is cracked on a macroscopic scale. Thus, these oxides are nonprotective, and oxygen molecules can diffuse in the gas phase, filling the voids to a location very near the metal-oxide interface where the reduction reaction can occur. For refractory metals, the ideal electrochemical oxidation model with oxygen reduction at the oxide-gas interface is replaced by a mechanism offering much less resistance.

The most important parameter of metal oxidation from an engineering viewpoint is the reaction rate (Hillner, 1977; Johnson, 1974). Since the oxide reaction product is generally retained on the metal surface, the rate of oxidation is usually measured and expressed as weight gain per unit area. The various empirical rate laws sometimes observed during oxidation for various metals under various conditions are illustrated in Figure 2, in which a plot of weight gain per unit area versus time is shown.

Figure 1. Oxidation Process.

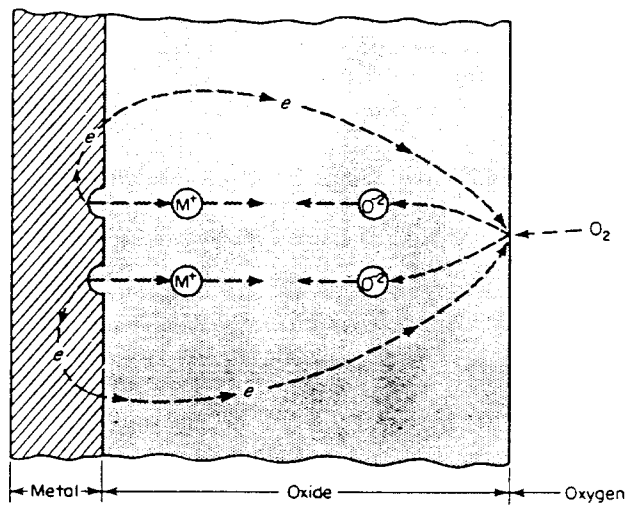

Figure 2. Theoretical Corrosion Rate Behaviors.

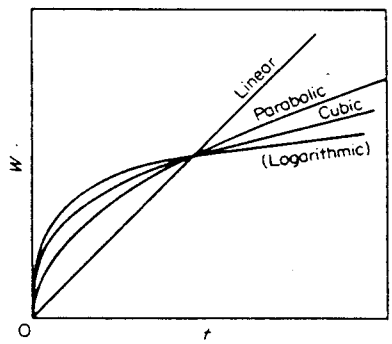

The simplest empirical relationship is the linear law (Fontana, 1967):

$$W = k_L * t \qquad (I.5)$$

where W is weight gain per unit area, t is time, and k_L is the linear rate constant. Linear oxidation is characteristic of metals forming a porous or cracked oxide so that the oxide does not represent a diffusion barrier between the two reactants. The linear rate constant represents the rate at which molecular dissociation or another reaction step at an interface is controlling the total reaction rate (Clayton, J.C., 1989; Cox, 1976; Hillner, 1977).

The ideal ionic diffusion-controlled oxidation of pure metals should follow a parabolic oxidation rate law (Fontana, 1967):

$$W^2 = (k_P * t) + C \qquad (I.6)$$

where W is weight gain per unit area, t is time, k_P is the parabolic rate constant, and C is a constant. Metals demonstrating a parabolic oxidation rate yield a straight line when the data are plotted as W^2 versus time. The form of the parabolic oxidation equation is

typical of non-steady-state diffusion-controlled reactions. This equation can be derived by assuming that the oxidation rate is controlled by diffusion through an oxide layer which is continuously increasing in thickness (Moran, 1978). The ionic diffusion flux is inversely proportional to the thickness of the diffusion barrier, and the change in oxide thickness or weight is likewise proportional to the ionic diffusion flux. In general, rate laws of a nearly parabolic nature are quite common and are usually associated with thick, coherent oxides. However, experimental data has failed to satisfy a precisely parabolic rate dependence for a thick, coherent oxide. This may indicate that morphological complications (such as voids in the oxide) are preventing the retention of ideal parabolic conditions (Scharfstein, 1971). Ionic diffusion in oxide still principally controls or limits oxidation (Fontana, 1967).

The logarithmic empirical reaction rate law (Fonatana, 1967):

$$W = k_e * \log ((C * t) + A) \qquad (I.7)$$

where k_e, C, and A are constants. Logarithmic oxidation behavior is generally observed with thin oxide layers, i.e., less than 1000 angstroms, at low temperatures

(Moran, 1978). Logarithmic oxidation results from electrical field effects within very thin oxide layers in assisting ionic transport across the oxide (Scharfstein, 1971).

Some refractory metals appear to oxidize according to a cubic law (Fontana, 1967):

$$W^3 = (k_C * t) + C \qquad (I.8)$$

where k_C and C are constants. Usually such behavior is restricted to short exposure periods (Moran, 1978; Scharfstein, 1971). For oxidation of Zr, an apparent cubic rate law has been explained as a combination of diffusion-limited oxide formation and oxygen dissolution into the metal. This type of rate law can be explained by the superposition of a morphological complication and ionic diffusion through the oxide (Clayton, J.C., 1989; Cox, 1976; Hillner, 1977).

In studying these various types of rate laws, it is apparent that a linear oxidation rate is the least desirable, since weight gain increases at a constant rate with time. Parabolic, logarithmic, and cubic oxidation rates are the more desirable for all alloys used in high-temperature oxidizing environments.

2. Electrochemical Corrosion

a. General Priniciples

Many corrosion phenomena can be explained in terms of electrochemical reactions. It follows, then, that electrochemical techniques (Barnett, 1976; Dean, 1976; EG&G, 1980; Gad-Allah, 1987; Mansfield, 1976; Peggs, 1985; Stern, 1957) can be used to study these phenomena. Measurements of current-potential relationships under carefully controlled conditions (ASTM G1-88; ASTM G5-87; ASTM G15-86; ASTM G16-71; ASTM G46-76; ASTM G62-86) yield information on corrosion rates, films, passivity, and pitting tendencies.

When a metal specimen is immersed in a corrosive medium, both reduction and oxidation processes occur on its surface (Sato, 1987). Typically, the specimen oxidizes (corrodes) and the medium (solvent) is reduced. Hydrogen ions are reduced in acidic media. Specimens function as both anode and cathode, and both anodic and cathodic currents occur in the same neighborhood on the specimen surface. Any corrosion processes that occur are usually a result of anodic currents.

Dissolution of the metal at the anode is accompanied by production of electrons - an electric current (Schultze, 1978):

$$M = M^{+n} + ne^{-} \qquad (I.9)$$

similarly, at the cathode some species in the fluid is reduced:

$$Z^{+n} + ne^{-} = Z \qquad (I.10)$$

When a specimen is in contact with a corrosive liquid e.g., concentrated or dilute acid, and the specimen is not connected to any instrumentation, the anodic and cathodic regions assume a driving force termed the corrosion potential (E_{corr}) (ASTM G15-86). A surface maintained at E_{corr} has both anodic and cathodic currents present on its surface. However, these currents are exactly equal in magnitude and no net current or corrosion is measured. The specimen is at equilibrium with the environment. E_{corr} can be defined as the potential at which the rate of oxidation is exactly equal to the rate of reduction (Peggs, 1985).

If the specimen is polarized slightly more positive

than E_{corr}, then anodic currents predominate at the expense of cathodic currents (Barnett, 1976; Dean, 1976; EG&G, 1980; Mansfield 1976; Peggs, 1985; Stern, 1957; Yau, 1982). Polarization requires the use of a voltage source to force the specimen to assume a potential other than the corrosion potential. The current measured in this case is a net current, representing the difference between anodic and cathodic currents. As the specimen potential is driven further positive, the cathodic current component becomes negligible with respect to the anodic component.

Experimentally one measures polarization characteristics by plotting the current response as a function of the applied potential (EG&G, 1980; Knittel, 1982; Maguire, 1986; Palit, 1987; Stern, 1957). Since the measured corrosion current varies over several orders of magnitude, the log current function is usually plotted versus potential on a semi-log chart. This plot is termed a potentiodynamic polarization plot. Using a semi-log display removes any indication of polarity. Potentials negative of E_{corr} give rise to cathodic current, while potentials positive of E_{corr} give rise to anodic current.

Figure 3 shows the potentiodynamic anodic polarization plot of 430 stainless steel. The logarithm of the current is plotted as a function of the applied potential. This plot can be described as follows (Pourbaix, 1973; Stern, 1957):

Region A is the active region in which the metal specimen corrodes as the applied potential is made more positive. At B further increase in the rate of corrosion ceases and the onset of passivation begins. The loss of chemical reactivity under certain environmental conditions, probably due to the formation of a film on the surface of the metal, is referred to as specimen passivation (Pickering, 1989). This point is characterized by two coordinate values, the primary passive potential (E_{PP}) and the critical current density (I_C) (EG&G, 1980; Stern, 1957; Yau, 1984). In region C the current decreases rapidly as the passivation film forms on the specimen. A small secondary peak is observed followed by region D where there is little change in current as the potential is increased. The passivation film begins to break down in region E, the transpassive region.

A potentiodynamic anodic polarization plot such as

Figure 3. Standard Potentiodynamic Anodic Polarization Plot 430 Stainless Steel.

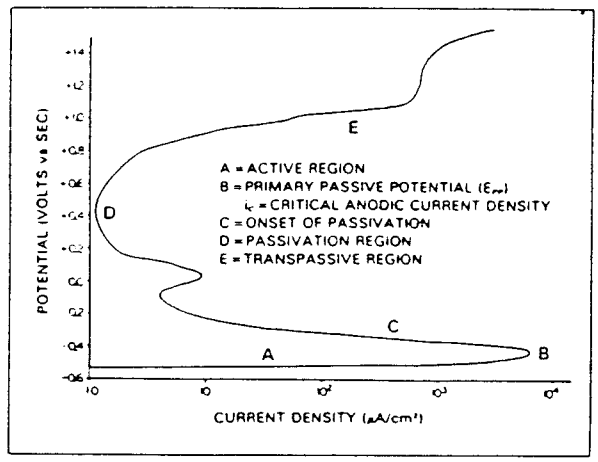

Figure 3 can yield important information such as: 1) ability of the material to spontaneously passivate in the particular medium, 2) potential region over which the specimen remains passive, and 3) corrosion rates in the active and passive regions.

Potentiodynamic polarization measurements are valuable in rapidly identifying desirable materials-environment combinations and in predicting how a material will behave when exposed to a particular environment. However, such measurments should not replace long term studies where other mechanisms may be operative.

b. Polarization Resistance

A polarization resistance measurement is performed by scanning through a potential range which is very close to the corrosion potential, E_{corr}. The potential range is generally +/- 25 mv about E_{corr}. The resulting current is plotted versus potential. The corrosion current, i_{corr} is related to the slope of the plot through the following equation (Barnett, 1976; Dean, 1976; Mansfield, 1976):

$$dE / di = (B_a * B_c) / (2.3 * i_{corr} * (B_a + B_c)) \quad (I.11)$$

where:

dE / di = slope of the Polarization Resistance plot

B_a, B_c = anodic and cathodic Tafel constants

i_{corr} = corrosion current, microamps

Rearranging provides:

$$i_{corr} = (B_a * B_c) * (di/dE) / (2.3 * (B_a + B_c)) \quad (I.12)$$

The corrosion current can be related directly to the corrosion rate through the following equation:

$$\text{Corrosion rate (mpy)} = 0.13 * I_{corr} * EW / d \quad (I.13)$$

where:

EW = equivalent weight of the corroding species, g

d = density of the corroding species, g/cm^3

I_{corr} = corrosion current density, microamps/ cm^2

3. Pitting Corrosion

Pitting is a form of extremely localized attack.

Pits are usually small in diameter and the depth is usually greater than the diameter. Corrosion pits are a unique type of anodic reaction (Isaacs 1989; Pickering, 1989). It is an autocatalytic process: self-stimulating and self-propagating. Although pits grow through self-stimulation, the process to initiate a pit is not obvious. Pitting can initiate when, for any reason, the rate of metal dissolution is momentarily high at one particular point. Anions, i.e., Cl^-, Br^-, etc., will migrate to this point. Since these ions stimulate metal dissolution, this change tends to produce conditions that are favorable to further rapid dissolution.

Since pitting is a localized form of corrosion, conventional weight-loss data cannot be used for evaluation or comparison purposes. Metal loss is small and does not indicate the depth of penetration. Pit depths need to be evaluated by objective measurements using metallography or corrosion parameters obtained by potentiodynamic tests (Fontana, 1967; Godard, 1978).

4. Corrosion Reactions in Wrought Zr Alloys

a. Autoclave Reactions

Corrosion resistance of conventionally fabricated

zirconium alloys depends upon distribution and morphology of intermetallic precipitates. The distribution of Fe in Zr-4 and its segregation to second phase precipitates during fabrication has been studied extensively (Cortie, 1982; Cox, 1976; Ferrando, 1988; Hillner, 1977; Johnson, 1969; Johnson, 1974; Kuwae, 1986; Vander Sande, 1974). Iron is not appreciably soluble in alpha-Zr (Yau, 1983) and is present as an intermetallic compound, $ZrFe_2$, distributed throughout the structure if the alloy is slow cooled. Quenching from the beta region results in a Widmanstatten type structure and the second phase particles are segregated along the grain boundaries (Cortie, 1982; Cox, 1976; Dollins, 1983; Yau, 1983). Typically, precipitates are approximately 0.5 micron in diameter and at a density of approximately 10^{10} per cubic cm (Kuwae, 1983; Kuwae, 1986).

Corrosion resistance is increased when alloying elements inhibit intergranular corrosion by reducing impurity segregation at Zr grain boundaries (Johnson, 1969). Once the solubility limit is exceeded, intermetallic compounds or second phases are formed that tend to degrade the alloy corrosion resistance when compared to pure Zr. Oxygen is considered an alloying element and is soluble in alpha-Zr up to 30%. However, oxygen content has no effect on the corrosion resistance

of Zr in chemical applications (Condon, 1981; Ferrando, 1988).

Additions of Fe and Cr lead to improved corrosion resistance. However, optimal performance is achieved when the Fe/Cr ratio is in the range of 1.5 to 5.0. Beyond this range the corrosion resistance degrades and accelerated corrosion occurs (Charquet, 1988). Iron and chromium have a low solubility (approximately 0.02% Fe and 0.005% Cr) in Zr-4 and are present principally in the form of $Zr(Cr,Fe)_2$ precipitates.

After oxidation, when the oxide is relatively thick, these precipitates do not seem to persist within the oxide. The Fe and Cr contents of the oxide almost certainly have a strong influence on the properties of the oxide film, for which the homogeneity of their distribution in the oxide may depend on the underlying surface of the alloy (Charquet, 1988).

Oxidation of Zr in an autoclave occurs in several steps: water at the water-oxide interface breaks down into H_2 and O^{-2} by combining with two electrons originating in the metal (Cortie, 1982; Dolllins, 1983; Johnson, 1974). Oxygen ions diffuse through the oxide layer to the metal-oxide interface and react there with the Zr

metal to form an oxide, thereby releasing two electrons, which migrate back to the oxide-water interface. The oxide layer is built up from the Zr-oxide interface (Sabol, 1974). To balance the inward flow of oxygen ions the electrons should diffuse outward through the Zr-oxide lattice.

The importance of any low resistance electronic pathways, i.e., intermetallic particles, is determined by the resistance of the oxide lattice to electron flow (Cortie, 1982; Dollins, 1983; Kuwae, 1983). When intermetallic particles are aligned through the oxide providing low resistivity pathways, the oxide film becomes highly conductive and possesses inferior corrosion properties (Kuwae, 1983).

Nodule formation has been noted (Kuwae, 1983; Johnson, 1977; Trowse, 1977) wherever H_2 gas diffusing through the oxide is retained at the Zr-oxide interface. Pressure of the accumulative H_2 gas gradually increases. The ZrO_2 film breaks when the H_2 gas pressure exceeds the pressure that the film can withstand. Once the protective film breaks it is difficult to repair, due to the coarse fresh surface of the underlying bulk material.

Formation of lenticular nodules begins at the film

fracture sites (Clayton, J.C., 1989; Kuwae, 1983; Trowse, 1977). Nodules growing outward push up the protective film to make a new space between the oxide and the Zr, thus promoting corrosion horizontally. Many nodules coalesce into one another and eventually cover the entire surface.

b. Immersion Reactions

Immersion tests are useful in indentifying long term corrosion resistance and are capable of simulating the actual environment encountered in service. Immersion tests are generally conducted over a long time period and reveal actual corrosion resistance, rather than accelerated conditions. An estimate of the test duration required to provide statistically significant results is obtained by the following equation (Arnold, 1988):

$$\text{Test Duration (hr)} = 200 / cr \qquad (I.14)$$

where: cr = estimated corrosion rate (mpy)

If the test is conducted for a shorter period, the corrosion process may not have reached equilibrium.

When zirconium and its alloys are immersed in 10%

$FeCl_3$ at room temperature, the samples are readily attacked (Bruce, 1989; Pruitt, 1983; Schweitzer, 1982). Zr readily dissolves in solutions containing ferric ions and some forms of chloride ions (Yau, p6. 1988; Yau and Maguire, 1988). Ferric ions are common oxidizing impurities in chloride solutions. Presence of these impurities can cause localized corrosion in the form of pitting, intergranular corrosion and stress-corrosion-cracking. The presence of an oxidizer such as ferric ions polarizes the Zr surface such that local breakdown of the passive surface occurs at preferred sites (Yau and Maguire, 1988; Yau, p231, 1988).

c. Potentiodynamic Reactions

Electrochemical techniques have been used to study the corrosion characteristics of zirconium and its alloys for over 35 years (Hackerman, 1954; Mavghini, 1954). There are several testing attributes that affect the electrochemical corrosion characteristics including: coupon surface preparation, scan rate, measuring technique, and environment. Several studies (Cragnolino, 1978; Knittel, 1982; Knittel, 1984; Palit, 1987; Roques, 1984) have been performed analyzing the affects of these testing attributes on electrochemical corrosion characteristics.

Corrosion potential (E_{corr}) of Zr is sensitive to surface preparation since E_{corr} lays within the passive region and not in or near an active region (Knittel, 1982). The corrosion potential of the 600 grit-abraded samples and the as-received electrodes approach the same value of E_{corr}; therefore, a 600 grit-abraded surface is recommended as the representative surface of as-received material (Knittel, 1982). Pickling or polishing removes most of the surface contaminations and defects. Thus, the measured E_{corr} value is more active, offering a more positive potential. Air or vacuum annealing results in the most noble E_{corr} values. Annealing causes the surfaces to react with residual gasses to form an oxide surface (Knittel, 1982).

Different scan rates may be appropriate in potentiodynamic tests. They range from slow scans of 0.6 v/hr to fast scans of 60 v/hr (Knittel, 1982; Maguire, 1986). Slow scans provide clearer definition between different regions of the polarization curve, i.e., passive to transpassive behavior. Slow scans also delay the onset of transpassive behavior due to residence time spent in the passive range. However, fast scans reduce the effects of passive film build up and allow more convenient run times. Fast scans also obscure some features

in the potentiodynamic curves (Knittel, 1984; Maguire, 1986; Palit, 1987).

Measuring techniques are varied depending on applicability to the system being studied. Potentiodynamic techniques provide rapidly obtained, but more noble values (Knittel, 1982). Potentiostep and potentiostatic techniques are useful for systems that develop a less defective film (Knittel, 1982).

Environmental changes include a multitude of attributes including: type of solution (acid, salt, mineral, etc.) (Cragnolino, 1978; Heakal, 1990; Palit, 1987; Yau, 1982; Yau, 1984) and presence of oxidizing or reducing agents (ions of Fe, Cl, etc.). Chloride and ferric ions aggressively attack Zr and its alloys (Cragnolino, 1978; Knittel, 1984; Palit, 1987; Yau, 1982; Yau, 1984; Yau, 1985).

Some solutions cause pitting, a form of localized corrosion attack resulting in metal destruction. Zr and its alloys are susceptible to pitting attack. For pitting to occur, aggressive ions must be present in solution, particularly Cl^-, Br^-, or I^- (Palit, 1987). However, cations like Fe^{+3} have no effect on pitting (Knittel, 1984). Recent work (Roques, 1984) states that

as pits initiate, further pitting is impeded, due to modification of the electrochemical potential toward the cathodic direction for non-pitted areas. This decreases the pitting probability, since the pits act as sacrificial anodes as in cathodic protection of metals.

5. Corrosion Reactions in LSM Zr Alloys

LSM can modify corrosion behavior by altering the surface composition, microstructure, or distribution of impurities and second phases. LSM causes a thin surface layer to melt, the underlying bulk provides self-quenching, with cooling rates of up to 10^8 $^oK/sec$. Melting and rapid solidification can improve corrosion resistance of alloys by eliminating or minimizing phase segregation to produce a more chemically homogeneous surface (McCafferty, 1986; Subramanian, 1989).

Research (Affolter, 1984; Dahotre, 1985; Davies, 1978; Den Broeder, 1984; Draper, 1982; Gaffet, 1986; Massalski, 1988; Moffat, 1988; Pang, 1987; Schwarz, 1988; Von Allmen, 1983; Zielinski, 1978) has indicated that some glassy alloys, produced by extremely rapid heat extraction, are more corrosion resistant than traditional corrosion resistant alloys. However, research (Turn, 1983) on Cu-Zr alloys has shown that the glassy structure

of Cu-Zr did not enhance corrosion resistance.

One concurrent study (Richard, 1988), to this research, on LSM Zr-4 examined the microstructure, chemical homogeneity, and lattice parameters. Martensitic transformation occurred without the development of any second phase. The metastable martensite, supersaturated with alloying elements, Sn, Fe, and Cr exhibited a change in lattice parameters. The "a" parameter of the HCP unit cell decreased, while the "c" parameter increased, resulting in an overall expansion of less than 0.1%.

Research in the area of LSM Zircaloys has not examined the microstructure and corrosion properties and their interrelationships. One study was conducted on Zr-4 using laser annealling to produce a beta-quench structure (Sabol, 1987). Nodular corrosion resistance in steam autoclaves was improved, but microstructural analysis was not extensive.

E. ANALYTICAL TECHNIQUES

Surface analysis methods, in combination with traditional tools for corrosion research, have proven useful for the understanding and solving of a wide variety of corrosion problems. There are a multitude of techniques

for surface and interface analysis including: Auger electron spectroscopy (AES) (Baer, 1984; Baer, 1986; Bockris, 1989), X-Ray photoelectron spectroscopy (XPS or ESCA) (Baer, 1984; Baer, 1986; Bockris, 1989; Schreifels, 1989), Rutherford backscattering spectroscopy (RBS) (Baer, 1984; Baer, 1986), nuclear reaction analysis (NRA) (Baer, 1984; Baer, 1986), laser Raman spectroscopy (Baer, 1984; Baer, 1986), Mossbauer spectroscopy (Baer, 1984), and Secondary Ion Mass Spectroscopy (SIMS) (Bockris, 1989). Each technique has advantages and limitations when considered for specific applications.

SIMS is a technique that uses a low dose of primary ions, such as Xe^+ or Ar^+, to bombard the sample under ultra-high vacuum conditions (Bockris, 1989; Evans, 1990). Secondary ions are ejected from the surface, which are indicative of the surface chemistry, and analyzed according to their mass to charge ratio in a mass spectrometer. SIMS is a surface sensitive technique yielding information from a surface region only a few atomic layers in depth (5 nanometers) (Baer, 1986), yet sensitive enough to detect surface impurities at low concentrations (ppb to ppm). Lateral spatial resolution capabilities are sensitive (2 microns). Lateral distributions of the sputtered ions is maintained through the

spectrometer so that the mass resolved image of the secondary ions can be projected onto several types of image detectors. Microfocusing of the primary beam permits analysis in ion microprobe mode.

II. EXPERIMENTAL PROCEDURE

A. SAMPLE MATERIAL

Three Zirconium alloys were supplied by Teledyne Wah Chang, Albany: pure Zr, Zr-702, and Zr-4 . The compositions and fabrication histories of these alloys are described below in Table 1. Zr-702 is formally known as "Grade R60702". Zr-702 is specified for general corrosion resistant service. The presence or absence of hafnium does not affect strength or corrosion resistance, thus the Hf specification is rather generous. Zr-4 is formally known as "Grade R60804". Zr-4 is alloyed with Sn, Fe, and Cr. Zr-4 absorbs less hydrogen generated by the corrosion reaction than Zr-2, which contains Sn, Fe, Cr, and Ni.

Zirconium alloys have an affinity for C, N, and O at normal fabrication temperatures of 760°C (Fontana, 1967; Wanklyn, 1962; Yau, 1988). Zirconium is well known for its ability to getter oxygen and the tenacity of the oxide. During typical fabrication processes an oxide layer forms as a result of hot working in the atmosphere. Therefore, it was necessary to remove the oxide film from the wrought product prior to laser processing. This was accomplished using 600 grit SiO_2 and then rinsing in tap

water and alcohol.

Table 1. Zirconium Alloy Fabrication Condition and Composition

Alloy	pure Zr		Zr-702		Zr-4		
ingot *							
	355377	355377	840835	840170	214267	226220	218208
thick(mm)							
	3.4	3.4	2.0	3.4	3.4	3.4	3.4
fabrication							
	cold	hot	cold	cold	cold	cold	cold
element(ppm)							
Sn	500	500	1900	100	14,800	15,800	14,700
Fe	600	600	850	600	2080	2100	2050
Cr	50	50	120	70	1080	1160	1100
Fe/Cr	12	12	7.1	8.5	2.0	1.9	1.9
O	800	800	1500	1000	1240	1520	1350
N	30	30	48	65	32	20	28
C	100	100	170	140	160	160	140
Hf	73	73	1000	100	77	43	42
Al	63	63	100	90	65	41	60
Si	25	25	68	42	96	100	83

* for the remaining work only the last 3 digits of the ingot will be referred to and "HR" designates Hot worked.

B. LASER PROCESSING

Laser processing was performed on an AVCO HLP-1 laser at the Materials Engineering Research Laboratory (MERL) at the University of Illinois. This is a CO_2 continuous wave laser capable of 7 kw power.

Two different sample geometries were laser processed: 4" x 20" plates, for immersion and potentiodynamic testing; and 1-1/4" x 1-3/4" coupons for autoclave testing.

The material to be laser surface melted (LSM) was placed on a computer controlled table capable of x-y-z motion. The laser beam was stationary and the table moved beneath the beam. After each pass the table was indexed one-half the beam width to provide 50% overlap and ensure complete coverage. This is shown schematically in Figure 4. The beam width is adjustable by using mirrors within the laser unit and is measured from the width of a resolidified molten line on the material

Figure 4. Schematic of Laser Processing.

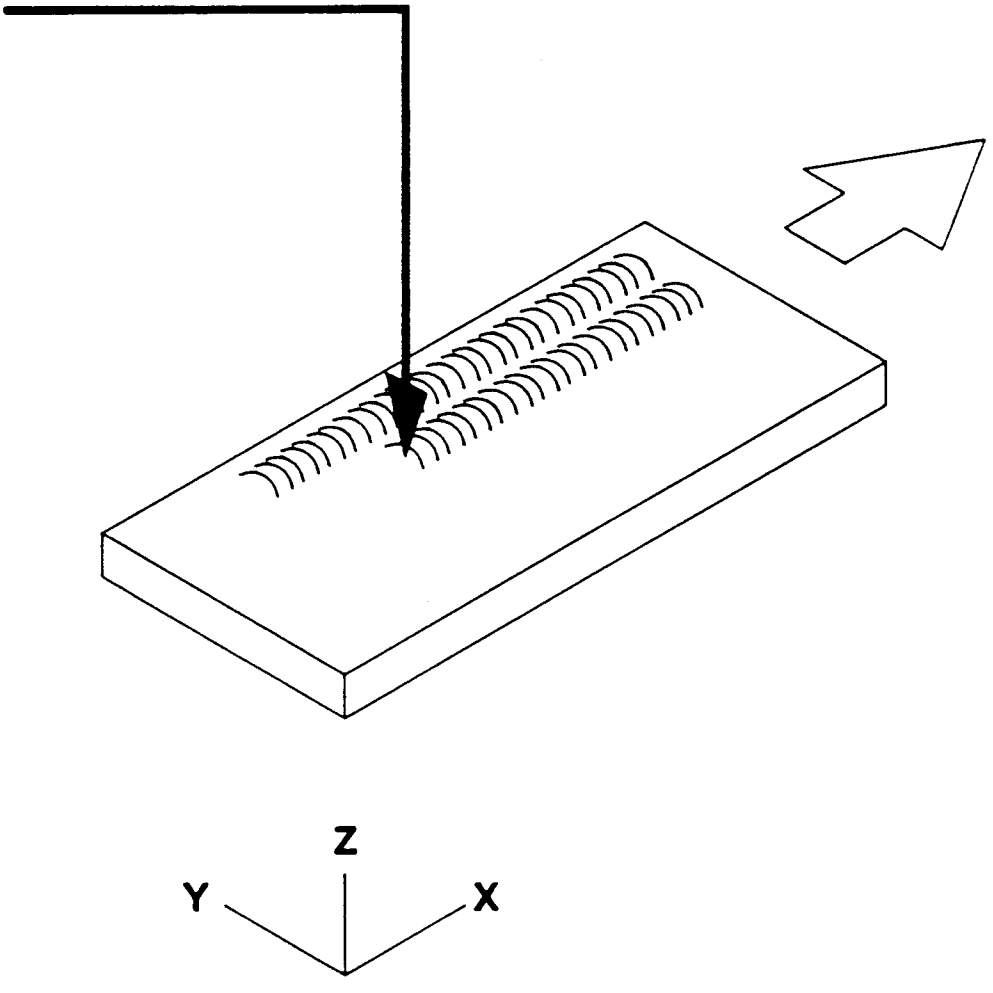

surface. After each laser pass the table was repositioned to the start line and then indexed. All laser processing was conducted in the same direction. As the laser beam proceeds over the sample surface the trailing edge of the molten pool solidifies, thus producing a regular pattern of ripples (Arata, 1986; Cieslak, 1989). The laser processing was conducted in an open atmospheric environment with a Helium cover gas over the molten area. The laser processing parameters used in this study are presented in Table 2.

Table 2. Laser Processing Parameters

Power (kw)	Feedrate (mm/sec)	Beam Dia (mm)	Energy Density (kJ/cm^2)
3	84	1	4
7	42	3	7
5	21	3	10

The Energy Density values have been used in the remainder of this work to identify the various processing parameters used.

C. CORROSION SAMPLE PREPARATION

Three basic surface conditions of control coupons (non-laser surface melted) were prepared: 1) as-rolled, 2) as-rolled and grit-blasted, and 3) as-rolled and metallographically polished. The as-rolled surface has a tenacious oxide present, the as-rolled and then grit-blasted surface was oxide-free, and the metallographic polishing removes the surface oxide.

Immersion and potentiodynamic coupons were machined from plate stock that had been LSM. These plates were LSM on only one side. The non-LSM surfaces of the immersion coupons were coated with a protective organic film (Plasti-Dip by PDI, Inc.). Two coats were applied to ensure complete protection. This organic material was chosen because it was shown to be non-reacting in the environment being tested.

Potentiodynamic coupons consisted of discs that were 2 cm^2 in diameter machined from the LSM plate. These discs were fitted into a coupon fixture that permitted only the LSM surface to be exposed to the acid solution. The fixture allowed only 1 cm^2 of surface to be exposed.

The autoclave coupons were machined, grit-blasted,

and pickled prior to LSM. (The pickle solution consisted of 3% HF, 35% HNO_3, and 63% H_2O). The nominal coupon size was t x 1.25" x 1.75". A minimum of 0.010" was machined from all major surfaces, which is the standard technique to ensure that there will be no oxide contamination in the tested material. Autoclave coupons required 100% surface processing since masking materials would not survive the autoclave environment and since possible contamination of the masking materials within the autoclave could not be tolerated. These coupons were aligned on the x-y-z table under the laser beam and clamped into place. After laser processing one major surface (1.25" x 1.75" face) the coupons were flipped over to expose the back face, which was then laser processed. The coupon sides, which include the hanger hole and 4 edges, were LSM by allowing the laser beam to run-over the edge, resulting in a melted edge.

The immersion coupons were identified by placing the ID on the back surface prior to painting on the clear protective coating. The autoclave coupons were identified by vibratooling the ID on the end of the coupon. The potentiodynamic coupons were identified on the back surface. The LSM material did not receive any special surface conditioning prior to corrosion testing, but were washed in alcohol.

D. AUTOCLAVE TESTING

Prior to testing, the coupons were weighed to 0.1 mg and dimensioned to 0.08 mm. Autoclave coupons were tested in a closed-loop autoclave for several successive time intervals. Each interval operated at 400°C +/- 5 (750°F) and 10.34 MPa +/- 0.6 (1500 psig) steam for 14 days +/- 1 hour. In the autoclave, the coupons hung on a type 300 stainless steel fixture that permitted total exposure to the steam environment. After each test interval the coupons were removed, air-dried, and visually examined at 5X to determine the condition of the oxide film. The coupons (weighing approximately 2 grams each) were weighed to determine the weight gain. After each weighing and inspection the coupons were reloaded into the autoclave for another 14-day interval. Seven 14-day runs were performed, for a total of 98 day exposure. The normal weight gain for Zr-4 has been established by industry at less than 35 mg/dm^2 for the first two-week interval.

E. IMMERSION TESTING

Research has established that zirconium and its alloys are readily attacked in certain oxidizing solutions

(Yau, 1984; Yau, 1988). One of these solutions is $FeCl_3$ mixed with water. Immersion tests were performed in a 10% $FeCl_3$ static solution, at room temperature for 34 days (800 hours). This test consisted of placing the coupons in a tray and then pouring in the solution to a depth of twice the thickness of the coupons. Two sample sets were tested. Prior to testing the coupons were dimensioned (+/-0.08 mm) and weighed (+/- 0.1 mg). After applying the protective coating the coupons were reweighed. The coupons were weighed periodically to determine weight loss (+/- 0.0001 gram). Upon removing the coupons from the acid solution, they were rinsed in two water baths and one alcohol bath and then allowed to air dry. The drying time was 1 to 2 hours. The coupons were weighed every 3 to 4 days and then placed back into a fresh batch of 10% $FeCl_3$. The tray containing the solution and coupons was covered to minimize the normal evaporation that occurs at room temperature.

F. POTENTIODYNAMIC TESTING

The potentiodynamic polarization measurements were conducted using an EG&G Princeton Applied Research Corp. (PARC) corrosion measuring system. This system consists of a Model 376 processor, a Model 173 potentiostat, a Model 175 Universal programmer, a corrosion cell and a

plotter. The corrosion cell system (modified Greene cell) consists of a glass cell, specimen assembly, counter electrodes, bridge tube and saturated colomel electrode (SCE) (ASTM G1-88, 1988; ASTM G5-87, 1987; ASTM G15-86, 1986). This system is shown schematically in Figure 5. A flat washer limits the area of the corrosion specimen to 1 cm^2, which is exposed to 1 liter of the electrolytic solution. O-rings prevented leakage which would cause crevice corrosion. The oxidizing solution was refreshed for each coupon tested.

Samples of 1.5 cm diameter were cut from the LSM plate and the edges were polished with 600 grit emery paper. Immediately after the samples were immersed in the 10% $FeCl_3$, a forward scan (anodic) was conducted starting in the cathodic region, approximately -1.0 volts with respect to the SCE, and scanning into the anodic region to approximately +1.0 volts with respect to the SCE. A reverse scan (cathodic) was then conducted returning to -1.0 volts. A rapid scan rate of 16 mv/sec was used.

After the reverse scan, the sample was allowed to remain in the solution and freely corrode, and the corrosion potential was measured as a function of time. After the corrosion potential stabilized the equilibrium corrosion potential (E_{corr}) was obtained (Fontana, 1967).

Figure 5. Schematic of Greene Cell.

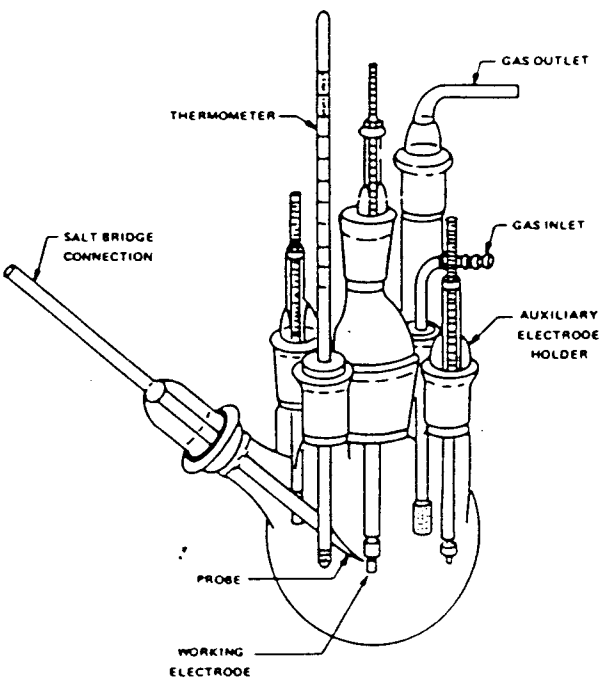

A second reverse (cathodic) scan was conducted from approximately +100 mv in the anodic region through E_{corr} and back to the initial starting potential. The corrosion current was measured as a function of the voltage. The corrosion current value (microamps) is divided by the area of the sample, which is conveniently arranged to be 1 cm^2. The corrosion current now becomes the corrosion current density (microamps per cm^2) and is plotted versus the voltage. The resulting plot defines a potentiodynamic anodic polarization plot. From this plot, I_{corr} was determined by the standard Tafel extrapolation technique (Fontana, 1967).

Potentiodynamic testing was also conducted on one sample set (835-10, 835-7, and 835-4) after metallographically polishing to various thicknesses. Each coupon was polished to remove approximately 0.04 mm from each major surface (front and back). Therefore, the resulting tested coupon thicknesses were 1.80 mm (initial thickness), 1.72 mm, 1.64 mm, and 1.56 mm. After removing equal amounts from both surfaces, the two polished surfaces were tested.

G. METALLOGRAPHIC SAMPLE PREPARATION

Samples were evaluated using several techniques:

optical microscopy, scanning electron microscopy (SEM), transmission electron microscopy (TEM), SEM microprobe, and Secondary Ion Mass Spectrometry (SIMS).

The TEM samples were metallographically polished from the back side (non-laser processed), which removed the metal substrate and allowed the LSM material to remain intact. The polishing process consisted of using finer and finer grit paper, i.e., 120 to 600 grit. By polishing at an angle from the back surface, a tapered region that consisted solely of the LSM material was produced. After pickling, the tip of the tapered region was sufficiently thin to allow the TEM investigation to be conducted.

The sample preparation for the optical, SEM, microprobe and SIMS studies consisted of mounting the sample in plastic, i.e., Bakelite. Samples were polished using successively finer grit paper beginning with 120, then 400, and then 600 grit. A final polish was then performed using a nylon cloth in combination with a chemical etchant. An alumina slurry composed of 20 gram Linde C alumina (1.0 micron) and 300 ml H_2O was applied to the polishing wheel. In addition several drops of an acid solution (3 ml HF, 22 ml HNO_3, and 250 ml H_2O) were added to the polishing wheel to aid in the removal of

flowed metal and scratches.

Metallographic preparation for optical microscopy consisted of grinding, rough polishing using 1.0 micron alumina with an acid solution of 3 ml HF, 22 ml HNO_3, and 250 ml H_2O, and final polishing on short-napped cloth using 0.05 micron alumina with an acid solution of 30 ml HNO_3, 30 ml H_2O_2, 20 drops HF, and 160 ml H_2O. After final polishing the acid solution is swabbed on the still wet sample for 5 to 10 seconds. A stain etch consisting of 2 to 3 ml HF and 97 ml methanol is immediately squirted on the sample following the swab etch until etching occurs, whereupon, the entire mount is immersed in the etch solution, swabbed for 3 to 5 seconds and left in the solution for an additional 5 to 10 seconds. After removal from the stain etch solution, the sample is squirted with the final polish acid solution, rinsed in water and dried. Samples were then observed at 500X magnification using differential interference contrast illumination.

H. MICROHARDNESS TESTING

Microhardness testing was conducted on a Tukon Microhardness Tester, model LR, manufactured by Wilson, Inc., using a diamond pyramid indenter resulting in a

diamond pyramid hardness number (DPH). The indenter consists of a diamond in the form of a square based pyramid with an included angle of 136° between opposite faces. A 0.1 kg load was applied and the diagonal of the indentation was measured in millimeters.

Prior to testing, the surface was polished as described in the preceding sections, except no etching was performed.

Three basic zones can be identified in the photomicrographs (Figures 29 through 33): melt, heat affected zone (HAZ), and substrate. The hardness of these zones were characterized by moving the hardness indenter from the melt surface down through the melt pool, through the HAZ, and finally, into the substrate. The indenter was positioned sufficiently far enough away from the previous indentation that work hardening would not influence subsequent readings.

III. DATA COLLECTION AND REDUCTION

Three basic corrosion phenomena were observed during the corrosion testing: 1) oxide formation associated with the steam autoclave testing, 2) pitting, and 3) general metal loss. The last two are associated with the 10% $FeCl_3$ acid environment used in the immersion and potentiodynamic testing. This section presents the weight gain and weight loss data used in determining the corrosion rates for the various tests employed.

A. AUTOCLAVE

1. Weight Gain

Prior to initiating the autoclave runs, the coupons' weight and dimensions were carefully measured. Coupons were weighed after each 2 week autoclave run to measure the weight gain due to oxide formation. The raw data are presented in APPENDIX A. The weights and dimensions were required to determine oxidation rates, which are characterized in terms of weight gain per exposed area (increased weight due to oxygen adsorption and formation of ZrO_2).

The weight gain due to oxidation is readily converted to a corrosion rate in milligram per square decimeter (mg/dm^2), via the following equation:

$$\text{corrosion rate} = (wt(n) - wt(0)) / A \qquad \text{(III.1)}$$

where: wt(n) is the coupon weight after the nth run (mg)
wt(0) is the initial coupon weight (mg)
A is the area of the coupon (dm^2)

Corrosion rates for the LSM Zr-4 coupons at the three energy densities are presented in APPENDIX B.

2. Nodule Formation

Oxidation was observed to begin during the first experimental 2-week period in the autoclave. The nascent areas of oxide are termed nodules, because of their physical nature; nodules are small, round, and raised. Nodules were first observed after the initial 2-week test period. They are depicted in Figure 6. These nodules are uniformly spaced over the surface of the coupon. The oxidation continues throughout the additional test periods and is exemplified by Figure 7, which depicts a six-week exposure.

Figure 6. Nodule Formation After 2 Weeks in Autoclave.

Figure 7. Nodule Formation After 14 Weeks in Autoclave.

B. IMMERSION

The data from the first immersion test run are presented in APPENDIX C. A problem was experienced during this run. Some of the samples were not sufficiently coated to form an impregnable seal adjacent to the exposed area. This permitted liquid to seep in between the protective coating and the metal. Of the four control coupons, which were covered 100% with the protective coating, one was found to contain liquid. This was discovered upon completion of the test and water was observed on the sample after the protective coating was removed. The sample was under suspicion because its weight gain as a function of time was significantly different from the other control samples that showed a weight loss due to corrosion. The remaining three control coupons did not exhibit unusual weight gains. All of the suspect coupons (coupons exhibiting weight gain rather than weight loss) were visually examined upon the completion of the corrosion testing to establish that the corrosive medium did not seep in between the coating and the coupon and thus bias the weight loss measurements. Interim data from samples that showed weight gain irregularities were not considered valid. After testing, the protective coatings were removed and the samples cleaned and

weighed. The difference in weight before and after testing were used to determine corrosion response.

The data from the second immersion test run are presented in APPENDIX D. Special care was exercised in applying the protective coating on this second set of coupons. This coating had good integrity, thereby permitting accurate intermediate weight loss measurements. These coupons were weighed every 5 to 7 days.

1. Weight Loss - Corrosion Rate

Corrosion rates can be directly determined and expressed as weight loss per unit time. However, it is conventional to report corrosion rate as depth removed per unit time. The importance of expressing the corrosion rate as depth per unit time versus weight loss per unit time is apparent in engineering applications when the life of a component is considered. Weight loss provides a rate based on the area exposed to the corrosive environment; whereas, depth of penetration provides the engineer with a tool to estimate the life of the component.

$$\text{Corrosion rate (cm/sec)} = W / (d * A * t) \qquad \text{(III.2)}$$

where: w = weight loss (g)

d = density (g/cc)

A = area (cm^2)

t = time (sec)

The standard corrosion rate is expressed in milli-inches per year (mpy), which is obtained as follows:

$$CR\ (mpy) = w\ /\ (d * A * t) * 3600\ sec/hr * 24\ hr/d * 365\ d/yr * 1/2.54\ in/cm * 1000 mil/in * 1000\ mg/g \qquad (III.3)$$

which reduces to:

$$CR\ (mpy) = w * 534\ /\ (\ d * A * t\ ) \qquad (III.4)$$

where: w = weight (mg)

d = density (g/cc)

A = area (in^2)

t = time (hr)

The 1st immersion run corrosion rate data using equation (III.4) are presented in APPENDIX E. The 2nd immersion run corrosion rate data using equation (III.4)

are presented in APPENDIX F.

2. Pit Size and Frequency Comparisons

The analysis presented in the previous section dealt with the overall weight loss which is typical of general corrosion. After the immersion test, the samples were examined under an optical microscope to evaluate the types and extent of corrosion. In addition to surface corrosion another method of metal dissolution occurs, pitting. Pitting is a form of accelerated localized corrosion (Knittel, 1984; Yau, 1982; Yau, 1988).

The pits could be evaluated and the pit depth determined by using the fine focus and estimating the depth by the change in focal point. A Zeiss microscope, model 4649161 manufactured by West Germany, was equipped with a calibrated eyepiece (0.000357 "/unit at 100X) for length measurement and a calibrated fine focus adjusting knob (0.0000395 "/unit at 200X) for depth measurement. The tolerance for error in measuring is +/- 5% of the calibration units. APPENDIX G is a tabulation of this investigation.

C. POTENTIODYNAMIC

Two different potentiodynamic tests were conducted on each sample: a) forward-reverse potentiodynamic scan in which the type of corrosion could be characterized as passive / pitting / active behavior, and b) a second forward scan used to determine the E_{corr} and I_{corr} values (Dean, 1976; EG&G, 1980; Knittel, 1982; Sato, 1989; Yau, 1985). The plots are presented in APPENDIX M.

1. Corrosion Rate

The corrosion rate for the potentiodynamic test can be derived from Faraday's Law:

$$Q = nFW / M \qquad \text{(III.5)}$$

where:
- Q = coulombs
- n = # of electrons involved in the electrochemical reaction
- F = Faraday's constant (96,487 C)
- W = weight of the electroactive species
- M = molecular weight

rearranging provides:

$$W = QM/nF \qquad \text{(III.6)}$$

Equivalent weight is defined as:

$$EQ = M/n \qquad \text{(III.7)}$$

Substituting (III.7) into (III.6) provides

$$W = Q\ (EQ)\ /F \qquad \text{(III.8)}$$

$$Q = i*t \qquad \text{(III.9)}$$

Substituting Equations (III.7), (III.8), and (III.9) into Equation (III.6) yields:

$$W = i * t\ (EQ)\ /\ F. \qquad \text{(III.10)}$$

W/t is the corrosion rate (CR) in gram/second. Corrosion rate is traditionaly expressed in milli-inches per year (mpy) (see the previous section "Weight Loss - Corrosion Rate). These units provide an indication of penetration.

Dividing Equation (III.10) by electrode area and

metal alloy density:

$$w/(d*t*A) = CR\ (cm/sec) = i\ (EQ)\ /\ (d * F * A) \qquad (III.11)$$

Convert seconds to years and centimeters to milli-inches. Convert Faraday (amp-sec / EQ) to microamps.

$$CR\ (mpy) = i\ (EQ)\ 31.6E6 * 1E3\ /\ (d * F * A * 2.5E6) \qquad (III.12)$$

Express i/A as current density and combine the constants.

$$CR(mpy) = 0.13 * Icorr * (EQ)\ /\ d \qquad (III.13)$$

where: I_{corr} = corrosion current density (microamp/cm2, (determined from the potendynamic scan)

EQ = equivalent weight of corroding species (g)

d = density of the corroding species (g/cc)

This equation allows the corrosion rate to be calculated directly from I_{corr}.

2. Electrochemical Values

Examining the potentiodynamic curves in APPENDIX M yields the summary of electrochemical values (APPENDIX H).

D. HARDNESS MEASUREMENT

Microhardness measurements were obtained from various regions of the melt pool and HAZ to characterize the alloy dispersion and quench rate. Mircohardness was measured using a diamond pyramid indentor. The filar readings (diagonal of the square impression) measured in millimeters are provided in Table 3.

Table 3. Diamond Pyramid Filar Readings (mm)*

	Zr-702**			Zr-4***		
energy density	10	7	4	10	7	4
position						
melt surface	158	162	153	157	143	140
HAZ	171	167	166	170	158	149
matrix	187	186	182	182	179	177

* average of 5 values, standard deviation = 3.78

** coupons 2.0 mm thick, low alloy content, ingot 835

*** coupons 3.4 mm thick, high alloy content, ingot 267

Microhardness measurements were obtained by taking the filar readings and converting them via a conversion chart to diamond pyramid hardness (DPH) values. The conversion of diagonal length to DPH is as follows:

$$DPH = 1.854 * P / D^2 \qquad \text{(III.14)}$$

where: P = applied load (kg)

D = diagonal length of square impression (mm)

magnification = 50X

Conversion factor = 0.1936

Table 4 summarizes the average values for the various zones within the melt, HAZ, and base material.

Table 4. Hardness Data (DPH)

Alloy/ Ingot	Zr-702 (835)			Zr-4 (267)		
Energy	4	7	10	4	7	10
Position						
melt	213	190	184	255	241	195
HAZ	195	174	164	195	195	174
matrix	146	146	146	148	148	148

E. MICROSCOPY

Materials with different laser processing conditions were examined with optical microscopy and SEM. Photomicrographs are provide in the following sections representing the surface ripples, melt pools, corrosion formation, phase formation and grain size.

1. Surface Ripples

Ripples on the laser passes are actually the back edge of the molten pool, as the laser beam proceeds across the surface. Laser ripples are only a function of the laser parameters, and not a function of the various

Zr alloy concentrations (Copley, 1981). An optical examination at low magnification (50X) provides the spacing from peak-to-peak of the frozen standing waves. The data is presented in Table 5.

Table 5. Surface Ripple Spacing (mm)

energy density (kJ/cm^2)	power (kW)	feed rate (mm/s)	spacing (mm)
10	5	50	1.5
7	7	100	3
4	3	200	6

2. Melt Pools

Melt pool depths of the laser passes were determined by polishing a transverse sample and examining the material at 50X. Three levels of energy density were used in processing five different materials. The data is presented in Table 6. (Recall the power and feedrates provided in the previous chapter.)

Table 6. Melt Pool Depths (mm)

ingot	377	377H	267	835	170
thick(mm)	3.4	3.4	3.4	2.0	3.4
fab *	cr	hr	cr	cr	cr
energy density (kJ/cm^2)					
10	1.19	1.07	1.24	1.80	1.07
7	.99	1.04	1.09	.91	1.07
4	.46	.53	.53	.51	.38

* cr = cold rolled, hr = hot rolled

3. Corrosion Performance

Three basic corrosion phenomena were observed during the corrosion testing: 1) oxide formation associated with the autoclave testing, 2) pitting, and 3) general metal loss. In subsequent sections photomicrographs will provide details concerning these environmental degradations.

4. Phase Formation

X-ray diffraction data showed the presence of only

alpha Zr and Zr oxide, as shown in Figures 8 and 9. Figure 8 is the diffraction pattern for wrought Zr-4. Notice the fuzzy diffraction spots probably indicating residual stress induced by metal working. Figure 9 shows the diffraction pattern for LSM Zr-4. Notice the minimum number of diffraction spots and the lack of fuzziness. This diffraction pattern indicates no residual stress and an absence of precipitates. In addition to X-ray analysis, no second phase or precipitates were found using SEM-EDX and SIMS.

5. Grain Size

The grain size determinations were performed per ASTM E-112. The LSM material exhibited a grain size of ASTM #12 (0.006 mm in diameter). The non-laser processed material exhibited a grain size of ASTM #4 to #8, which is typical for conventional processing.

F. CHEMISTRY

Chemical analyses were performed on LSM samples. SEM-EDX, electron microprobe, and SIMS were employed to characterize the chemical variations within the melt pool.

Figure 8. Electron Diffraction Pattern of Wrought Zr-702.

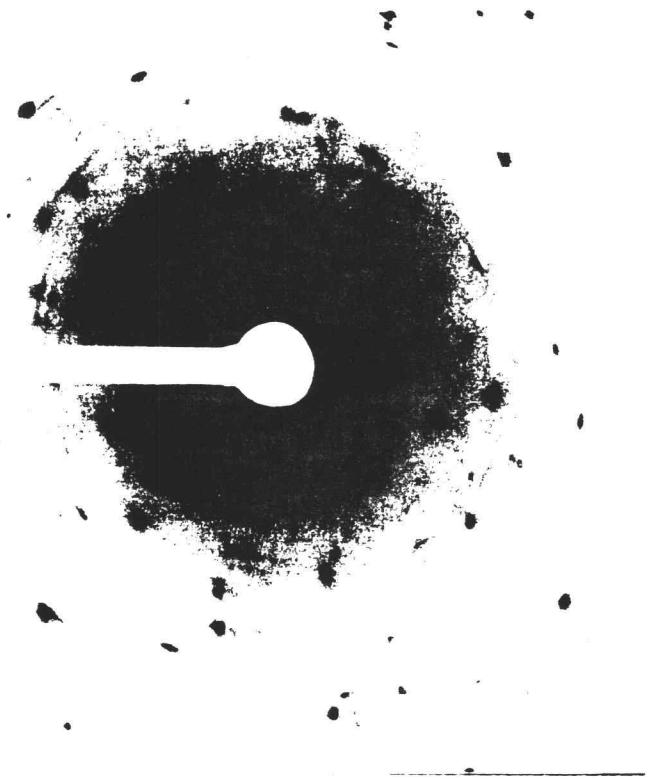

Figure 9. Electron Diffraction Pattern of LSM Zr-702.

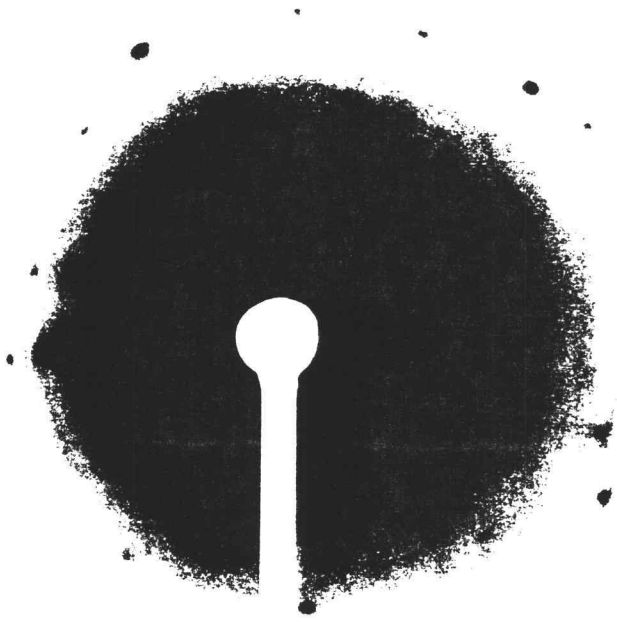

Secondary Ion Mass Spectrometry (SIMS) was employed to determine the extent of Sn and Fe segregation. The Sn is more concentrated at the melt pool wall, where it has twice the concentration of the central region of the melt pool (see Figure 10 and Table 7). The second type of elemental segregation detected was Fe-rich areas. The Fe-rich locations were in the melt pool approximately 200 microns from the melt pool wall. These Fe-rich arcs parallel to the melt pool wall were higher in Fe by a factor of 10 .

Table 7. Sn and Fe Segregation (ppm)

	pure Zr	Zr-702	Zr-4
Ingot	377	835	267
Element/Position			
Sn			
matrix	500	1900	14,800
melt pool edge	1000	3500	28,000
Fe			
matrix	600	850	2080
melt pool	5500	8000	20,000

Figure 10. Sn and Fe Segregation Within the Melt Pool.

a) Sn-rich arc,

b) Fe-rich arc parallel with Sn-rich arc, and

c) corrosion initiation site.

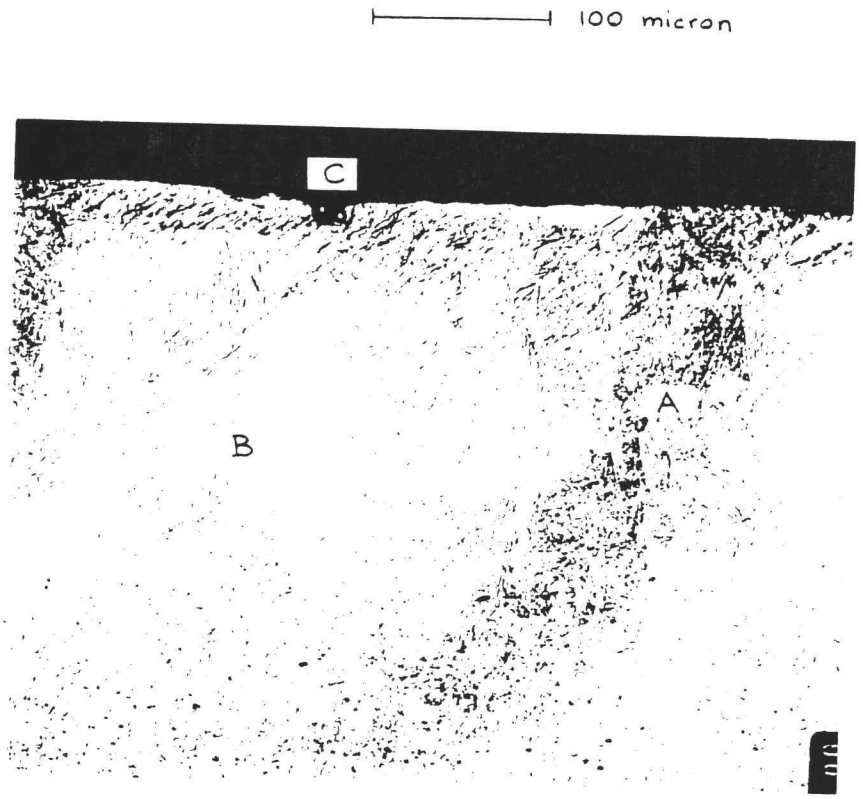

IV. RESULTS

A. Autoclave

The steam autoclave data are presented in Figure 11. The oxide formation as measured by weight gain, is plotted against time, thus, producing the corrosion rate. Each symbol is associated with the numbers listed at the top portion of the graph. The first value indicates the laser energy density (kJ/cm^2) and the second value indicates the Zr-4 ingot. For this test 2 different heats of Zr-4 were employed with different levels of laser processing on each. The control samples consisted of non-laser processed coupons from the same heats as the laser processed material, but with a machined surface.

1. Laser Effects

Figure 11 shows that LSM increases the corrosion rate. LSM with the low laser energy density (4 kJ/cm^2) produces a corrosion rate that is triple that of the wrought product. LSM with the medium laser energy density (7 kJ/cm^2) yields approximately double the corrosion rate of the control.

Figure 11. Steam Autoclave Corrosion Rates (98 Days).

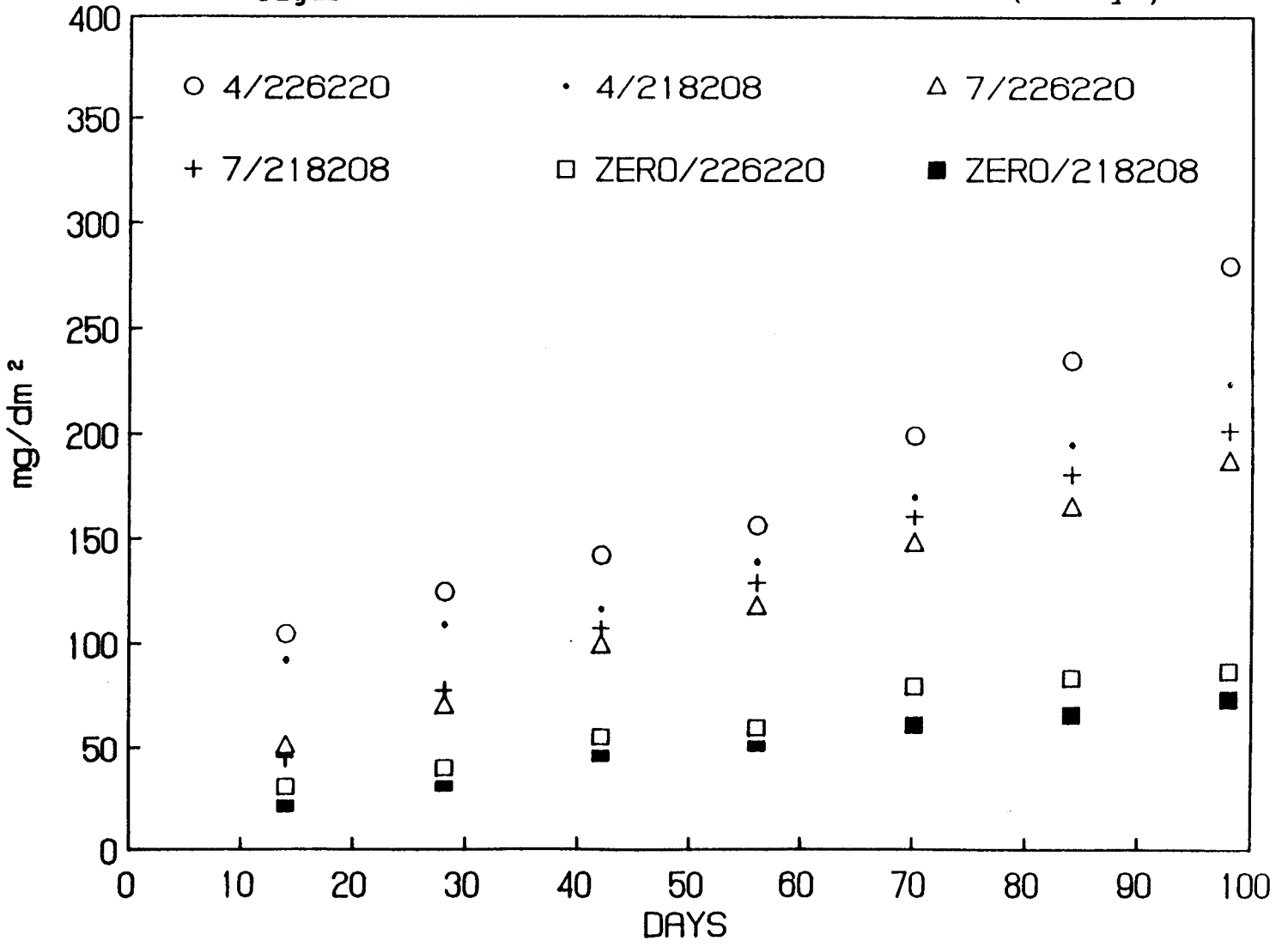

Typically, the initial corrosion rate of Zr-4 is characterized by a cubic corrosion rate resulting from the formation of a thin, black, tightly adherent, protective corrosion film (Fontana, 1967; Johnson, 1969). Further exposure changes the corrosion mechanism and results in a linear behavior. The corrosion product remains lustrous black even after the linear rate law has been established. Eventually, the corrosion film becomes uniform gray-tan after prolonged exposure.

The early stages of the corrosion of pure Zr behave similarly to Zr-4. First, a thin, black, tightly adherent, protective corrosion film develops. Then, a rapid increase in the corrosion kinetics occurs, coincident with the formation of localized white corrosion, commonly termed nodular corrosion. This is followed by the loss of corrosion product oxide through spalling and flaking.

Autoclave corrosion curves typically consist of 2 distinct regions (Hillner, 1977): 1) cubic pre-transition, and 2) linear post-transition. The controls exhibit the transition point (change from cubic to linear corrosion rate behavior) at about 35 days (40 mg/dm^2) (Yau, p231, 1988). Table 8 summarizes these characteristics.

Table 8. Transition Points* and 98 Day Corrosion Rates

Energy density (kJ/cm^2)	0**	7	4
transition point (days)	35	42	55
transition point (mg/dm^2)	40	110	150
Corrosion Rate after 98 days (mg/dm^2)	70	190	250

* obtained from Figure 12.

** 0 designates "control", non-LSM

The transition point occurs at the time that the protective corrosion film is breached (Hillner, 1977). During the initial corrosion phase while in the cubic region, the protective corrosion film is tightly adherent. When the corrosion film is no longer tightly adherent nor totally intact, the corrosion rate changes and becomes linear. Table 8 shows that as the applied laser energy density is reduced, the occurrance of the transition point is delayed. In the limiting case the "zero" laser energy density processing might be expected to possess a transition point beyond 55 days and 150 mg/dm^2. However, this is erroneous as will be discussed later.

Figure 12. Autoclave Transition Points.

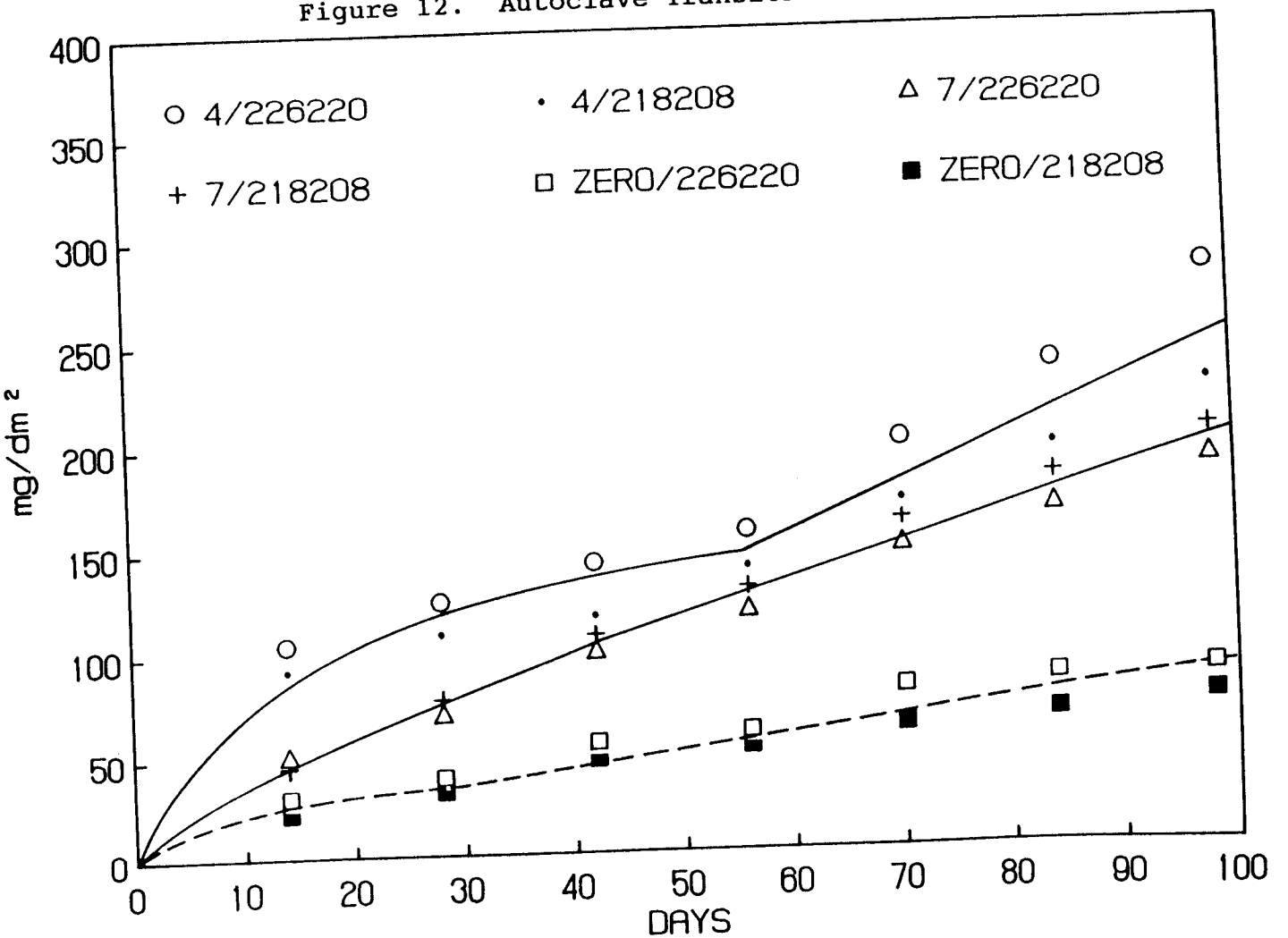

At all times the corrosion behavior of the controls are better than the LSM material.

A statistical analysis employing a Comparison of Means test was performed on ingot 218208 to determine the effect of LSM after autoclave testing for 98 days. The results are presented in Table 9 (see APPENDIX I for details).

Table 9. Comparison of Means for LSM Effect.

Factor LSM (kJ/cm^2)	$t_{calculated}$	$t_{critical}$ [t(df,alpha/2)]
4 vs 7	5.38*	t(9, 0.005) = 3.250
7 vs 0	15.49*	t(9, 0.005) = 4.032

* significantly different. Confidence Level is 99%.

These results show that LSM can adversely affect the corrosion performance.

2. Fabrication and Chemistry Effects

The chemical alloy composition of the two heats 226220 and 218208 used for the autoclave test are very

similar, with only slight concentration variations in the major alloy elements and impurities. (See Table 1). In general, heat 226220 has a very slight increase in alloy composition for all elements. The following chemical differences are observed (Table 10).

Table 10. Chemical Differences Between Two Zr-4 Ingots.

Ingot	226220	218208	Delta%
Element (ppm)			
Sn	15,800	14,700	6.9
Fe	2100	2050	2.4
Cr	1160	1100	5.2
Fe/Cr	1.9	1.8	3.4
O	1520	1350	11.2
N	20	28	(40.0)
C	160	140	12.5
Hf	43	42	2.3
Al	41	60	(46.3)
Si	100	83	17.0

The Zr-4 alloy with the higher Sn, Fe and Cr content is expected to be more corrosion resistant, which is not the case as observed here (Kass, 1963).

Since the alloy compositions were slightly different, a 2-tailed Student's T test was performed to compare

the mean autoclave corrosion rate at 98 days between the two Zr-4 ingots. The Comparison of Means test is presented in Table 11 (see APPENDIX J for details). The t-values obtained were then compared to the tabulated critical t-values. The data from the 4 kJ/cm^2 energy density and the controls showed that the two ingots were significantly different at the alpha/2 = 0.01 level (probability of accepting the hypothesis and being correct is 0.98), while the LSM coupons processed at 7 kJ/cm^2 did not exhibit a significant difference between the two ingots, even at the alpha/2 = 0.10 level. The non-LSM coupons exhibited the same level of significance as the lowest laser energy processed coupons.

Table 11. Between Ingot Comparisons

LSM	$t_{calculated}$	$t_{critical}$ [t(df,alpha/2)]
4	3.06*	t(9,0.01) = 2.82
7	-1.00	t(6,0.10) = 1.44
0	5.66*	t(3,0.01) = 4.54

* significant difference at the level of alpha/2 = 0.01

Any differences in the fabrication history should disappear after LSM processing since the volume of material examined and corrosion tested has been heated into the liquid regime; totally homogenizing the LSM region

and removing all previously formed second phase constituents. However, chemical segregation can still occur during resolidification influencing the minor chemical concentration distribution.

Previous work (Fontana, 1967; Kass, 1964; Wanklyn, 1962) has shown that adding Sn, Fe, and Cr to pure Zr improves the corrosion resistance. However, the corrosion resistance begins to decrease after a limiting concentration is reached for each of these alloy additions. Basically, a particular concentration exists that optimizes the corrosion resistance. As the alloying level departs from this concentration (increase or decrease), then the corrosion resistance is reduced. By maintaining the Sn, Fe, and Cr levels at 15,000 and 2000 and 1100 ppm, respectively, the optimum corrosion resistance can be maintained.

3. Nodular Corrosion

Previous research (Fontana, 1967; Johnson, 1969) has shown that initially, a thin, black oxide film develops to a thickness of approximately 0.5 microns. Subsequently, nodular corrosion develops and is characterized by areas of white, thick corrosion product. When the oxide thickness reaches approximately 5 microns, spalling

commences.

There is no stoichiometric difference between the thin, black oxide film and the thick, white, nodular corrosion product (Kuwae, 1983). As the thin, black oxide film increases in thickness, the translucent nature of the protective film degrades, accounting for the formation of a thick, white corrosion product. Zr oxide is known to be brittle, and as the thickness increases the brittle nature manifests itself.

Nodule formation was observed after the first 2-week autoclave corrosion run. The corrosion surface is exemplified by the photomicrograph in Figure 13. Subsequent runs did not initiate new nodules, rather the initial nodules appeared to grow and coalesce, covering more area as exposure time increased (Figures 14, 15, and 16).

The nodules were observed to initiate at the edge of the laser overlap regions. The centers of the melt regions are essentially free of nodule formation. This segregation of initiation sites is thought to result from elemental segregation or heat treating effect resulting from subsequent laser passes.

Figure 13. Nodule Formation 2 Weeks in Autoclave.

1 mm

Figure 14. Autoclave Coupon Surface After 6 Weeks.

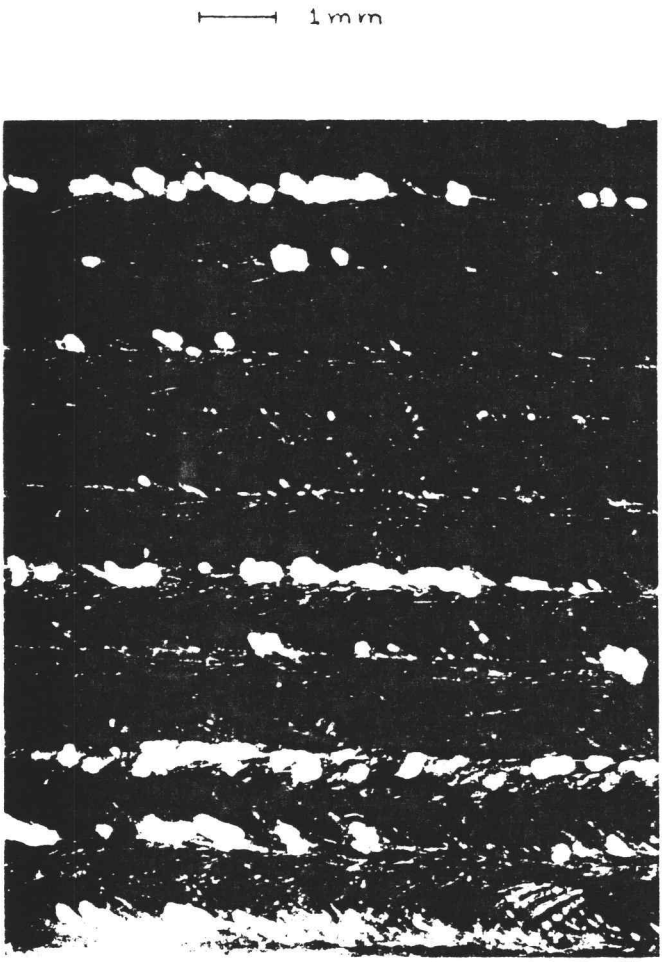

Figure 15. Autoclave Coupon Surface After 10 Weeks.

1mm

Figure 16. Autoclave Coupon Surface After 14 Weeks.

SIMS analysis showed regions of Sn and Fe segregated in the LSM zone (Figure 10). The nodule initiation sites appear in the Fe-rich areas. In these Fe-rich areas the Fe concentration can be one order of magnitude higher than the remainder of the solidified melt pool. As previously explained, an optimum alloy concentration exists; above or below that level the corrosion resistance degrades. The high Fe levels of approximately 20,000 ppm (2 w/o) result in accelerated corrosion. A detailed discussion of this alloy segregation is presented below in the section on "Microstructure and Phases".

B. Immersion

1. Weight Loss

The corrosion rates for the two immersion tests, each run for a total of 34 days, have been combined for evaluation (see APPENDICES C and D). There were five different starting Zirconium alloys each with three laser processing parameters.

Analysis of Variance (ANOVA) was performed on the weight loss data to establish the significant attributes. ANOVA is a statistical procedure for deciding whether

differences exist among two or more population means and measure their synergistic effects. The results are presented in Table 12. (See APPENDIX K for details.)

Table 12. ANOVA of Combined Immersion Runs 1 and 2.

Code	Factor	DF[1]	F-Test Ratio	F(DF,90,.99)
A	Test Run	1	31.72*	6.9
B	LSM	2	55.17*	4.9
C	Material	4	16.09*	3.5
	A x B	2	0.19	4.9
	A x C	4	1.38	3.5
	B x C	8	7.88*	2.7
	A x B x C	8	2.01	2.7
	Error	90		

(1) DF = degrees of freedom

* significant at the alpha = 0.01 level.

The information contained in Table 12 shows that there is a significant difference in the data between: 1) the two different corrosion runs, 2) various LSM parameters, and 3) different starting materials. Also, there is a significant interaction factor between the LSM parameters and the material. Since this interaction factor is significant, this data is best explained by expanding the data into a Table of Means (see Table 13).

Table 13. Immersion Corrosion Rates (mpy) Summary in Table of Means*

LSM Material	10	7	4	avg
355377	.4	.5	.2	.4
355377HR	.9	.4	.3	.5
214267	.6	.5	.4	.5
840835	.8	.4	.2	.5
840170	.4	.3	.2	.3
avg	.6	.4	.3	0.4

* each value is the average of 8 coupons, standard deviation = .13

Note: These values should be compared to corrosion rates of 20 to 300 mpy, as will be addressed in the section on "Fabrication and Chemistry Effects".

a. Laser Effect

Typically, the lowest laser energy density deposition (4 kJ/cm^2) resulted in the most improvement to corrosion resistance. As the amount of energy applied increased, the corrosion performance degraded, but still remained an order of magnitude below the polished surface

performance and were 3 orders of magnitude below the grit-blasted surface performance.

A 2-tailed Student's T-Test was performed to establish the significance levels for the three laser processing parameters. The results, which are summarized in Table 14 (see APPENDIX L for details), show that with 99% confidence the range that contais the mean for each level of LSM is unique, i.e., no overlap.

Table 14. Significance Levels Based On LSM Parameters.

LSM	Confidence Interval 99%
10	$.505 < X_{10} < .735$*
7	$.355 < X_{7} < .504$*
4	$.221 < X_{4} < .339$*

* significantly different.

The three LSM parameters produce significantly different corrosion results at the 99% confidence level.

This shows that even though LSM can result in 2 to 3 orders of magnitude improvement in corrosion resistance, the various LSM parameters also produce significantly different results when compared among themselves.

b. Fabrication and Chemistry Effects

Examining the data in the previous sections shows that significant differences exist in the way that the various LSM parameters and materials respond when corrosion tested.

Corrosion resistance is strongly influenced by the condition of the coupon's surface (Kuwae, 1986; Wanklyn, 1964). Smooth surfaces increase the corrosion resistance (Webster, 1985). A grit-blasted surface in 10% $FeCl_3$ normally yields a poor corrosion resistance of 300 mpy. The as-rolled surface exhibits a corrosion rate of 20 mpy, whereas a polished surface produces a corrosion rate of 5 mpy.

The cold-rolled, pure Zr (377) and cold-rolled, Zr-702 (170) have similar chemistries (see Table 1). These two materials are consistently more corrosion resistant than the remaining materials (see Table 13). The hot-rolled, pure Zr (377HR), cold-rolled Zr-4 (267), and cold-rolled, thin gauge Zr-702 (835) have similar corrosion properties.

Analyzing for possible chemical segregation in LSM

samples is difficult due to the inherently low alloy content within these materials. The Zr-4 material has the highest alloy content consisting of 15,000 ppm Sn, 2000 ppm Fe, and 1000 ppm Cr. Pure Zr contains 100 ppm Sn, 600 ppm Fe, and 100 ppm Cr. The segregation effects consist of enriched areas and partially depleted zones of 2 to 10 times the bulk concentration. It is difficult, if not impossible, for SEM-EDX and electron microprobe to locate the segregated areas and quantify the enriched or partially depleted zones due to the large volume of material excited by the probing beam. This will be addressed further in the section "Microstructure and Phases".

2. Pitting

The tendency towards pitting is directly related to the applied laser energy density and resulting microstructure and possible chemical segregation as shown in Figure 17.

a. Laser Effects

LSM influences the tendency for pits to form and the depth to which they develop. Material processed with the lowest laser energy density (4 kJ/cm^2) developed the fewest pits and pits with the least depth of penetration.

Comparing the information in Table 13 and Figure 17 reveals that by decreasing the laser energy density from 10 to 4 kJ/cm^2, the corrosion rate decreases from 0.6 to 0.3 mpy. At the same time, the propensity towards pitting decreases approximately by one order of magnitude. Since the pitting behavior is almost negligible when LSM with the lowest laser energy density (4 kJ/cm^2), the observed and measured corrosion is more influenced by generalized corrosion than by pitting corrosion. Table 13 includes the pitting response in the overall corrosion rate, while Figure 17 represents only the pitting response.

The two corrosion responses, general and pitting, can be separated by calculating the weight loss due to pitting compared to the weight loss due to general corrosion. The pit diameter, as determined by optical microscopy, is typically one-half of the depth. Using the depth and diameter, the volume (and the weight) of the material removed by pitting can be calculated. Table 15 lists the weight of the material removed based on the volume of the pits per the total exposed surface area.

Figure 17. Pitting Behavior.

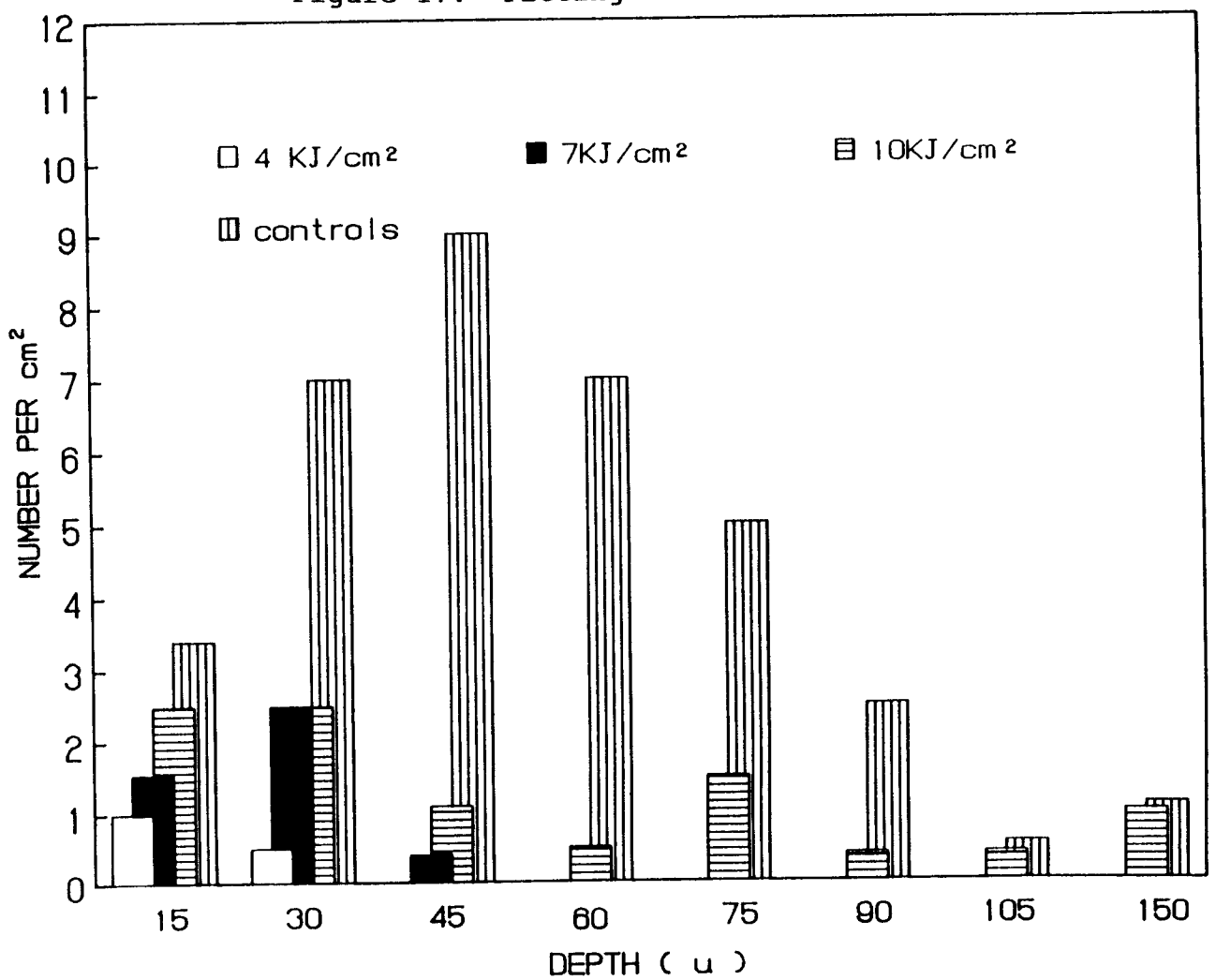

Table 15. Corrosion Rate (mpy) Based on Pit Volume and % of Total Corrosion Rate due to Pitting.

LSM Material	10	%	7	%	4	%
355377A	.3	75	.01	2	0	0
355377B	.06	7	.01	2	0	0
214267	.24	40	.01	1	0	0
840835	.30	40	.01	1	.03	2
840170	.01	2	.01	3	.01	.5
average		30%		2%		0.6%

Based on this data, the pitting is responsible for an average of 30% of the corrosion rate as a result of processing with the highest laser energy density (10 kJ/cm^2), approximately 2% of the corrosion rate for the medium laser energy density (7 kJ/cm^2), and approximately 0.6% of the corrosion rate for the lowest laser energy density (4 kJ/cm^2).

The medium laser energy density LSM (7 kJ/cm^2) yielded material with an intermediate pitting propensity and these pits penetrated to an intermediate depth when compared to the highest and lowest laser energy density LSM. Laser processing at 7 kJ/cm^2 produced material that was slightly more prone to corrosion than material LSM

with 4 kJ/cm^2 when pitting propensity is considered (see Figure 17).

Material processed with the highest LSM energy density (10 kJ/cm^2) exhibited an increased pitting frequency and an increase in the pit depth compared to the other LSM parameters. When compared to the non-LSM material, the high laser energy density LSM developed fewer pits and these pits did not penetrate as deep as the non-LSM coupons.

Therefore, the lowest laser energy density application yielded the lowest pitting factor.

C. Potentiodynamic

1. Corrosion Parameters

A detailed examination of the LSM coupons was performed to determine the effect of any surface phenomena that might exist, such as, atmospheric contamination, vaporization, etc. Several types of microstructure developed from laser processing the 2.0 mm thick Zr-702 samples. This material also showed the greatest variety in microstructure (Figure 32). The highest LSM energy density (10 kJ/cm^2) actually affected the entire

thickness via melting or in the HAZ formation. Therefore, this material was selected for extensive potentiodynamic studies.

Additionally, all the other materials in combination with the three LSM parameters were tested. See APPENDIX M for actual curves. APPENDIX M includes the plots for steady state E_{corr} and steady state I_{corr}.

a. Laser Effects

Figure 18 contains the results for the 2.0 mm thick Zr-702 material LSM at 0, 4, 7, and 10 kJ/cm^2. The "0" value represents the control, which is non-laser surface melted (wrought, as-received surface). The non-LSM sample exhibits a large anodic initial E_{corr} and active corrosion. The middle and high laser energy densities (7 and 10 kJ/cm^2) exhibit slightly lower initial E_{corr} and the occurrence of pitting. However, the shape of the potentiodynamic curves are very similar. The lowest energy density (4 kJ/cm^2) exhibits an E_{corr} that is cathodic and the occurrence of pitting is less pronounced as indicated by the absence of "steps" in the potentiodynamic curves. Thus, LSM at 4 kJ/cm^2 provides the most corrosion resistance.

The following tests were performed to identify whether surface related effects were influencing the corrosion performance; the samples were incrementally polished and tested. Approximately 75 microns were removed at 3 intervals, each resulting in exposed subsurfaces laying at 75, 150 and 225 microns below the laser processed surface. This data is presented in Figures 19 through 24, where Figures 19, 20, and 21 show the performance of all three LSM parameters after an incremental polish. Figures 22, 23, and 24 show the performance of each new subsurface for a given LSM parameter.

The first polish, 75 microns into the LSM region, as shown in Figure 19, revealed an extensive passive region for the material processed with the highest laser energy density (10 kJ/cm^2). This passiveness was less pronounced as the laser energy density was reduced. The initial E_{corr} was reduced from +0.24 to -0.11 volts. The initial E_{corr} for the lowest laser energy density did not change as a result of removing 75 microns.

After removing 150 microns the passive region became consistent for all three LSM parameters, as shown in Figure 20. The initial E_{corr} remained at approximately -0.15 volts.

Figure 18. Potentiodynamic Plots of Ingot 835 LSM at 0, 4, 7, and 10 kJ/cm^2.

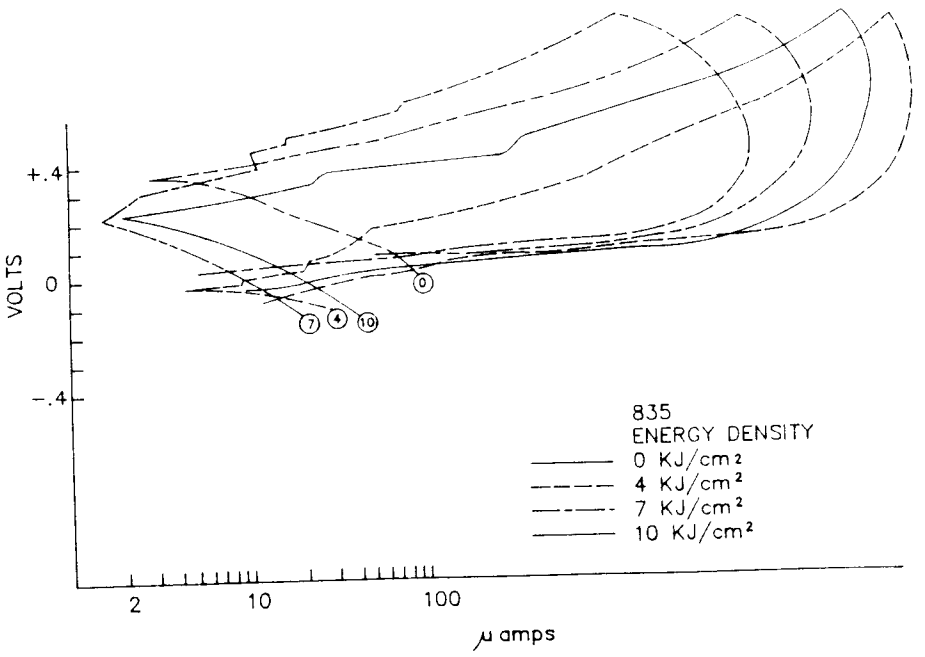

Figure 19. Potentiodynamic Plots of Ingot 835 LSM at 4, 7, and 10 kJ/cm^2 After Removal of 75 Microns.

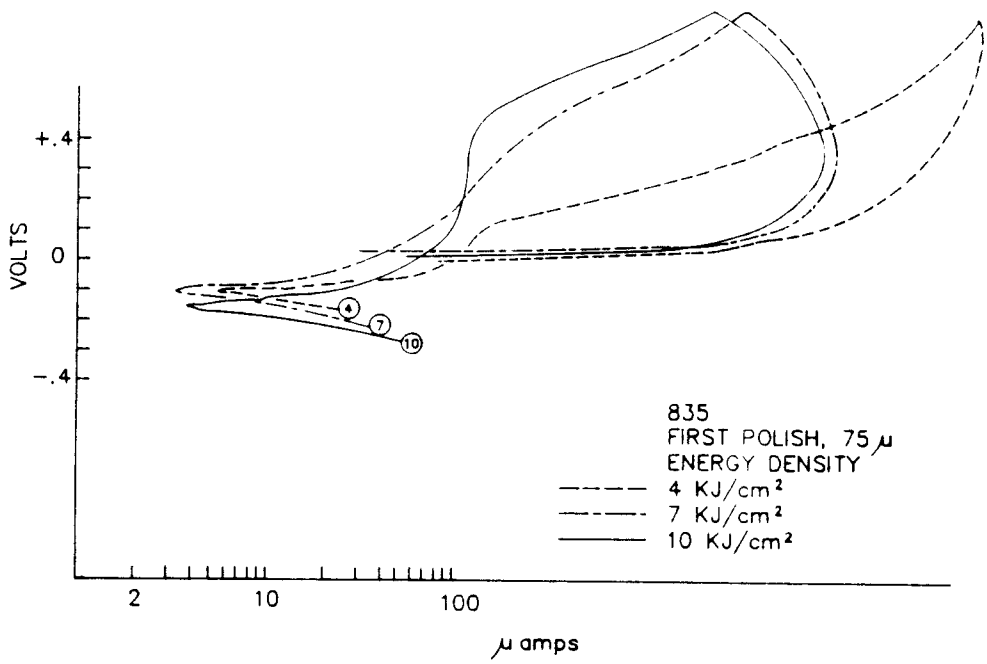

Figure 20. Potentiodynamic Plots of Ingot 835 LSM at 4, 7, and 10 kJ/cm^2 After Removal of 150 Microns.

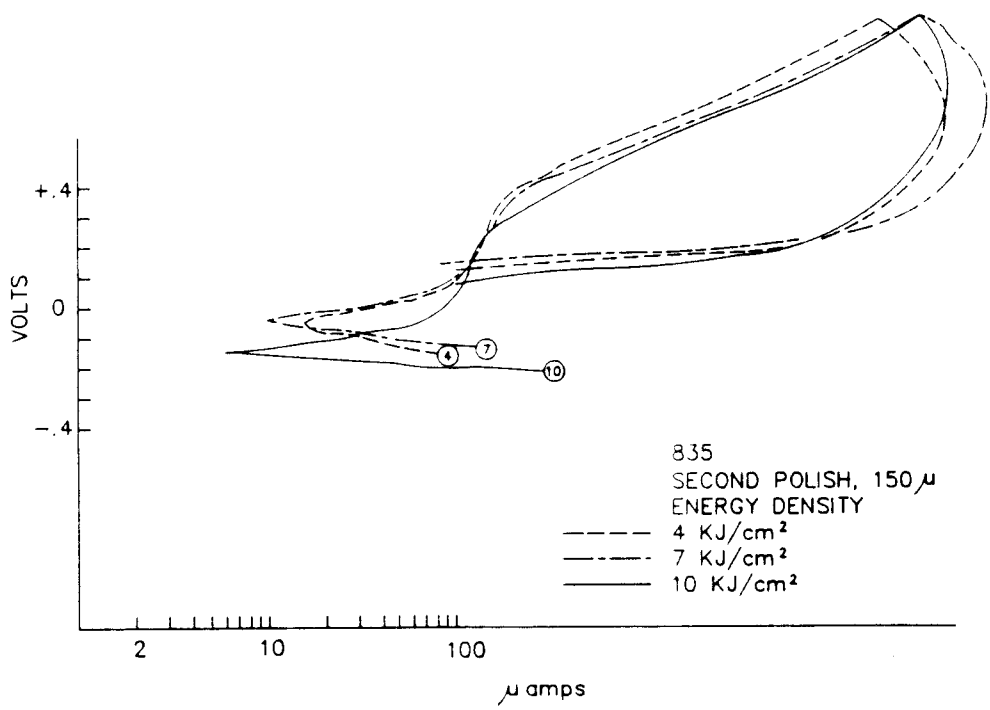

Figure 21. Potentiodynamic Plots of Ingot 835 LSM at 4, 7, and 10 kJ/cm^2 After Removal of 225 Microns.

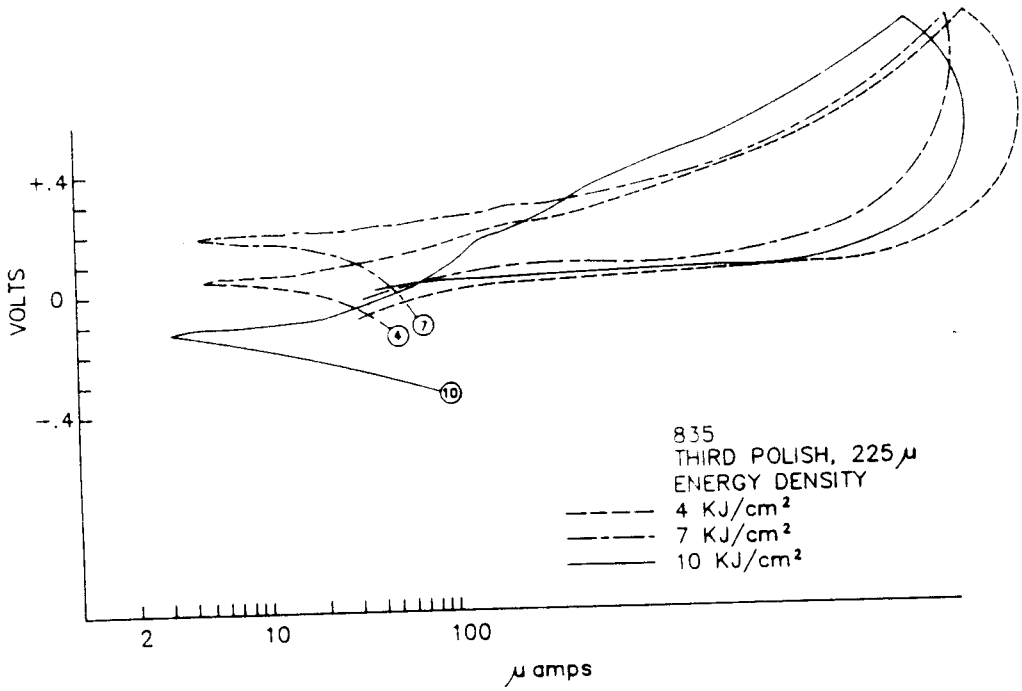

Figure 22. Potentiodynamic Plots of Ingot 835 LSM at 10 kJ/cm^2 After Removal of 0, 75, 150, and 225 Microns.

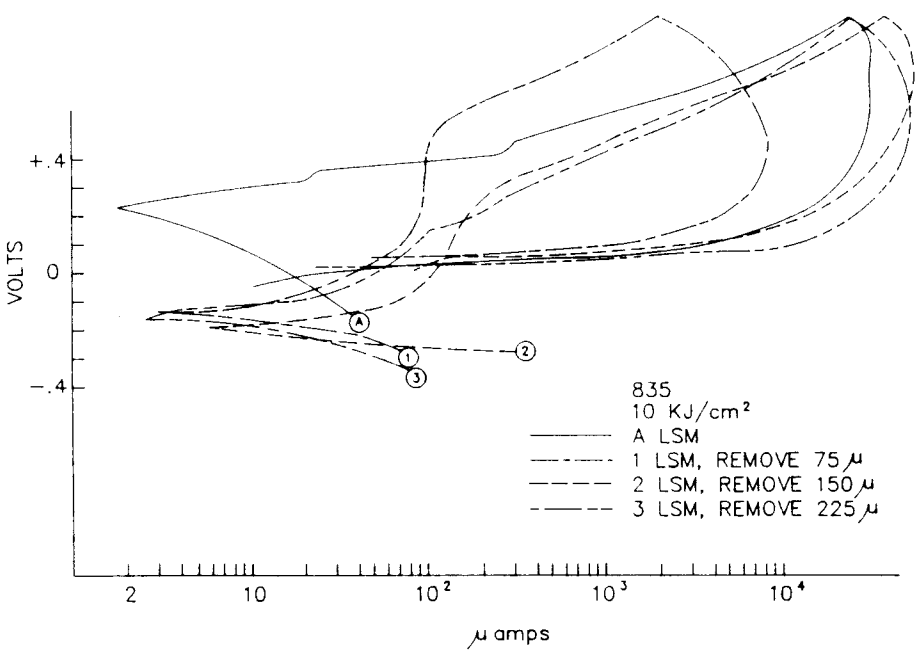

Figure 23. Potentiodynamic Plots of Ingot 835 LSM at 7 kJ/cm^2 After Removal of 0, 75, 150, and 225 Microns.

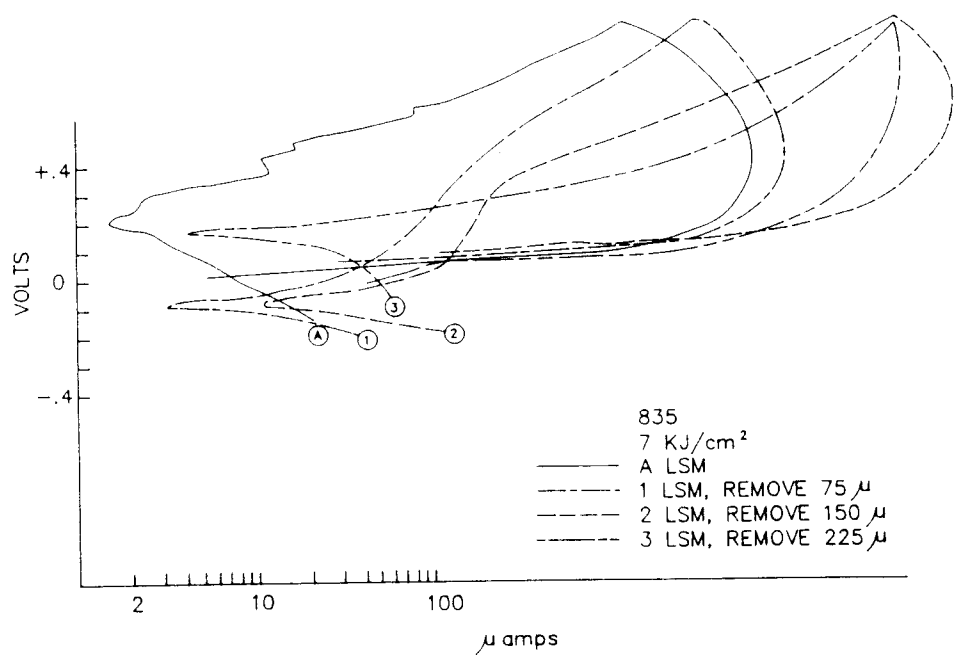

Figure 24. Potentiodynamic Plots of Ingot 835 LSM at 4 kJ/cm^2 After Removal of 0, 75, 150, and 225 Microns.

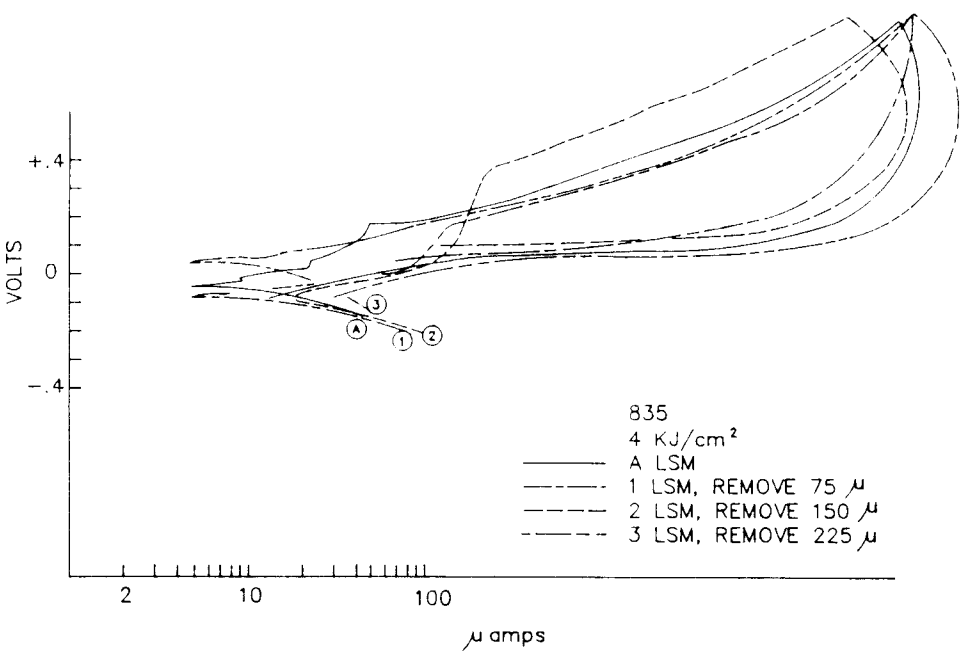

After removing 225 microns the passive region disappeared, as shown in Figure 21. However, the initial E_{corr} remained considerably lower than the E_{corr} for original laser processed surface.

Figure 22 shows the corrosion performance of the various subsurfaces from the high laser energy density (10 kJ/cm^2) samples. "A" is the laser processed surface and "1, 2, and 3" show the responses as each layer of metal is removed. There is a tremendous improvement upon removing the first layer of metal. Subsequent layers removed do not enhance the corrosion properties.

Figure 23 shows the corrosion performance of the various surfaces exposed by polishing of the medium laser energy density (7 kJ/cm^2) samples. Once again, the removal of the initial layer results in a tremendous improvement in the corrosion resistance. Removal of the second layer shows approximately the same response. Upon removal of the third layer, exposing the surface 225 microns below the laser processed surface, the corrosion resistance begins to degrade.

Figure 24 shows the corrosion performance of the various subsurfaces exposed by polishing of the lowest

laser energy density (4 kJ/cm^2) samples. Again, the removal of the initial layer increased the corrosion resistance. The removal of the second layer shows futher improvement in corrosion resistance. It is not until the removal of the third layer that the corrosion resistance begins to degrade.

For the medium and high laser energy density (7 and 10 kJ/cm^2) the 1st and 2nd subsurfaces reveal a more cathodic initial E_{corr} and indicate a region of passiveness. The 3rd subsurface behaves as the LSM surface behaves. For the low laser energy density (4 kJ/cm^2), the first and second subsurfaces indicate the onset of a passive region, which the as-processed and third subsurface do not possess.

The first subsurface of the high energy density exhibited a passive region, whereas the low and medium do not. The 2nd subsurfaces all generated a passive region. The 3rd subsurfaces revealed active corrosion for all LSM parameters.

This data from Figures 18 through 24 are summarized in Table 16. A qualitative measure of the propensity for passivation is provided in the relationship between steady-state E_{corr} and initial E_{corr} as shown below

(EG&G, 1980; Pickering, 1989):

when:

$$E_{corr(ss)} > E_{corr(initial)} \qquad (IV.1)$$

then passivation occurs.

Table 16. Potentiodynamic Characteristics of Subsurfaces.

LSM		I_{init}	E_{corr} init	E_{pit}	E_x	E_{corr} ss	I_{corr} ss	Corrosion Rate(mpy)
	surface							
10	as-is	--	.24	.36	.01	.12	5.8	2.7
	1st	110	-.11	.43	.08	.28	4.1	1.9
	2nd	140	-.16	.15	.05	.01	4.3	2.0
	3rd	--	-.14	.15	.06	--	--	
7	as-is	--	.21	--	.04	.12	2.5	1.2
	1st	105	-.07	.29	.08	.09	4.8	2.2
	2nd	170	-.06	.28	.11	--	--	
	3rd	--	.17	--	-.05	--	--	
4	as-is	--	-.03	--	-.05	.14	2.4	1.1
	1st	125	-.07	.16	.06	.11	4.5	2.1
	2nd	170	-.06	.28	.11	--	--	
	3rd	--	.03	--	-.05	--	--	

b. Fabrication and Chemistry Effects.

Potentiodynamic results for the remaining four materials are summarized in Figures 25 through 28.

Figure 25 shows the performance of cold-rolled, pure Zr at the three different LSM parameters. All of the curves are consistent, possessing the same values for initial E_{corr} of +0.20 volts.

Figure 26 depicts the performance of hot-rolled, pure Zr with practically the same results as the cold-rolled, pure Zr. The initial E_{corr} remained at approximately +0.20 volts.

Results for the high alloy content material, Zr-4, is presented in Figure 27. Typically, Zr-4 material performs better (higher corrosion resistance) than the Zr-702 material in the non-LSM condition. All of the LSM Zr-4 samples possess the same initial E_{corr} of +0.10 volts and no indication of pitting.

Figure 25. Potentiodynamic Plots of Ingot 377 LSM at 4, 7, and 10 kJ/cm^2.

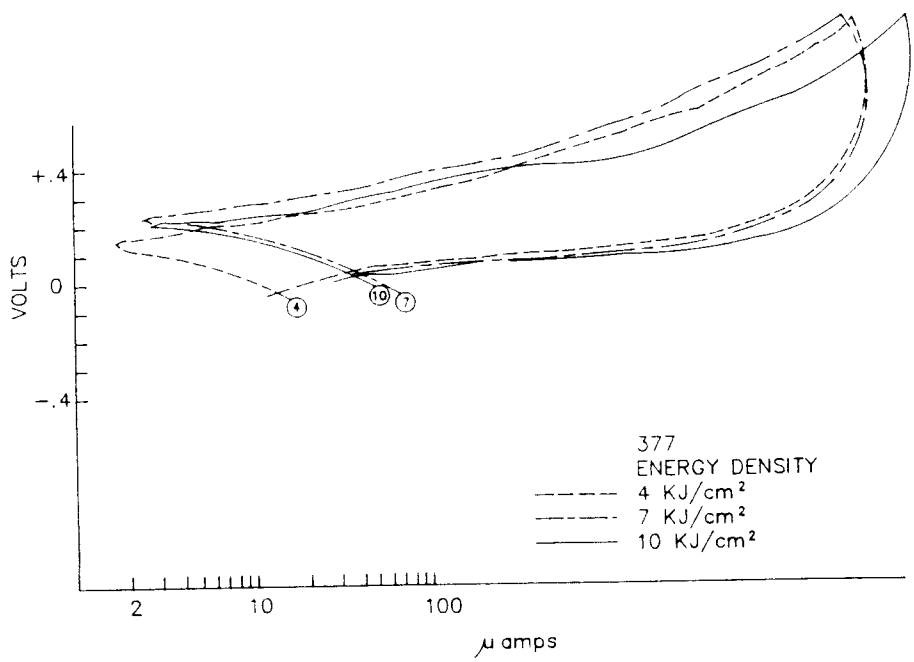

Figure 26. Potentiodynamic Plots of Ingot 377HR LSM at 4, 7, and 10 kJ/cm^2.

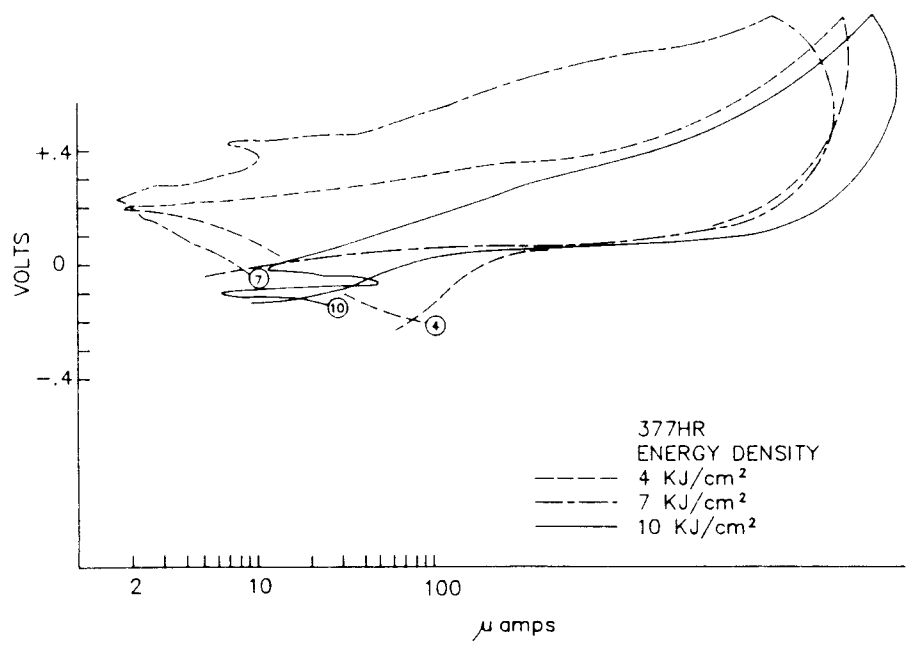

Figure 27. Potentiodynamic Plots of Ingot 267 LSM at 4, 7, and 10 kJ/cm^2.

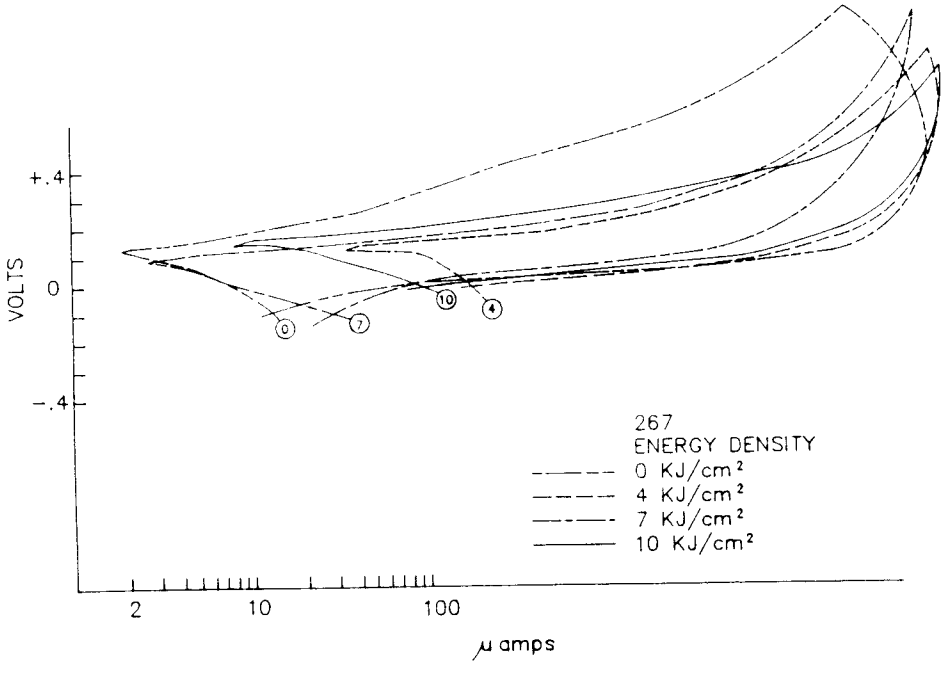

Figure 28. Potentiodynamic Plots of Ingot 170 LSM at 4, 7, and 10 kJ/cm^2.

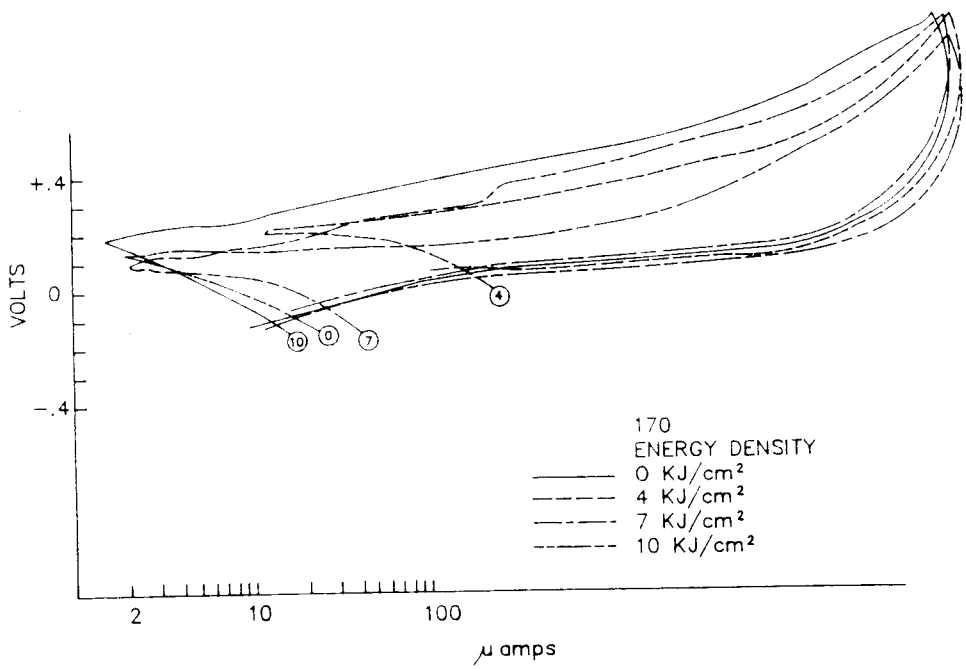

To confirm that LSM does not adversely affect the opposite (non-LSM) surface, the back side of the low laser energy density (4 kJ/cm^2) Zr-4 sample was also tested. Its corrosion properties are comparable to the non-LSM coupon of the thin Zr-702 presented in Figure 18.

The Zr-702 material behaves similarly to the Zr-4, both were 3.4 mm thick (see Figure 28). An initial E_{corr} of +0.15 volts was observed for this material. The as-rolled surface was consistent with the LSM surfaces.

No differences were observed for E_{corr}, E_{pit}, or E_x for the laser processed coupons from the various materials.

2. Pit Formation

a. Laser Effects

In a cyclic potentiodynamic test, the area of the hysteresis loop is directly proportional to the probability of pitting (Peggs, 1985). It is easily discerned that the lowest laser energy density (4 kJ/cm^2) produces the hysteresis loop with the smallest area, whereas the control and the medium and high laser energy densities (7 and 10 kJ/cm^2) produce approximately the same area within

the loops.

Another measure for the propensity to pit is in the comparison of steady-state E_{corr} and the potential that is reached when the return scan crosses over the forward scan, E_x (EG&G, 1980; Peggs, 1985). Figure 27 shows that LSM Zr-4 can greatly reduce the propensity for pitting, as shown by the relationship below:

when:

$$E_{corr(ss)} > E_x \qquad \text{(IV.2)}$$

then pitting occurs.

All the steady-state curves produced essentially the same E_{corr} and I_{corr} (see Table 17). The resulting similar corrosion rates calculated using I_{corr} show that general corrosion is not the influencing factor for corrosion performance, but that the pitting effect predominates.

Table 17. Steady-State Potentiodynamic Data.

LSM	Surface	E_{corr}	I_{corr}	Corrosion Rate (mpy)
10	as-is	.12	5.8	2.7
	1st	.28	4.1	1.9
	2nd	.01	4.3	2.0
7	as-is	.12	2.5	1.2
	1st	.09	4.8	2.2
	2nd	--	--	
4	as-is	.14	2.4	1.1
	1st	.12	4.5	2.1
	2nd	--	--	

b. Fabrication and Chemistry Effects

When Figures 18 and 25 through 28 are compared, it becomes apparent that the Zr-4 material has a slight advantage over the other materials in regard to reducing pitting. The area of the hysteresis loop is smaller for the Zr-4 material at all three levels of LSM. This occurs by design, as the various alloys have been developed over the years. Improved corrosion resistance was one of the criteria for developing Zr-702 and then Zr-4.

D. HARDNESS

1. Melt Pool Geometry and Chemistry Effects

A review of Table 4, Diamond Pyramid Hardness (DPH) Data, demonstrates the consistency of wrought, cold-rolled product hardness between Zr-4, Zr-702, and pure Zr. All are nominally 147 DPH. The HAZ ranged from 164 to 195 DPH, with the highest energy density (10 kJ/cm^2) producing the softer HAZ. The melted volume was 184 to 255 DPH depending on the laser parameter and ingot alloy. As the laser energy density decreases, the hardness values increase.

The alloy concentration increases from pure Zr to Zr-702 to Zr-4. As a result of rapidly quenching the melt zone and the inherent turbulent mixing associated with laser melting (Kar, 1982; Mazumder, p18, 1987), the second phase particles are eliminated yielding a super-saturated solid-solution. At any laser energy density, the solidified melt pool hardness increases as the alloy content of the base material increases.

Since Zr vaporizes at 3580°C (6440°F), the temperature of the molten pool is assumed to be cooler than

the vaporizing temperature. Otherwise, significant amounts of material would be ablated. The three major alloying elements, Sn, Fe, and Cr have vaporizing temperatures of 2340, 2800 and 2840°C, respectively (4210, 5040, and 5110°F). Since Sn and Fe are readily detectable using SIMS, SEM-EDX, and electron microprobe, a further refinement estimating the maximum laser processing temperature, is that the molten pool temperature is below 2300°C (4200°F). Table 18 lists the commonly occurring precipitates and the temperature required to dissolve a second phase constituent of any composition.

Table 18. Second Phase Melt Temperature (Shubet, 1973).

Prec.	T_M(°C)	T_M(°F)
Zr(Sn)	2000	3600
Zr(Fe)	1650	3000
Zr(Cr)	1650	3000
Zr(Sn,Fe)	930	1670

Based on the melting and vaporizing temperatures and the alloy distribution characteristics, the molten pool is between 2000 and 2340°C. This accounts for the dissolution and homogenizing of all precipitates.

E. MICROSTRUCTURE AND PHASES

1. Laser Effects

Optical microscopy of laser processed samples revealed a variety of microstructures. Figures 29 through 33 show the transverse microstructure of the five different starting materials and the three different laser processing conditions. Energy densities of 10, 7 and 4 kJ/cm^2 are shown in the "a, b, and c" portions of each figure. Melt pool depth is directly related to applied energy density.

Close examination of Figures 29 through 33 reveals that the resulting microstructure is strongly dependent upon the laser energy deposited in the material. Low energy densities generate a martensitic type structure that is characterized by an extremely fine lenticular formation. The martensitic structure typically results from extremely fast quenching from the melt temperature through the beta-phase. The shallow melt pool depth provides an excellent heat sink via the remaining substrate. Heat transfer occurs in the through-thickness direction as well as laterally.

Figure 29. Microstructure of Ingot 377 LSM at a) 10 kJ/cm^2, b) 7 kJ/cm^2, and c) 4 kJ/cm^2.

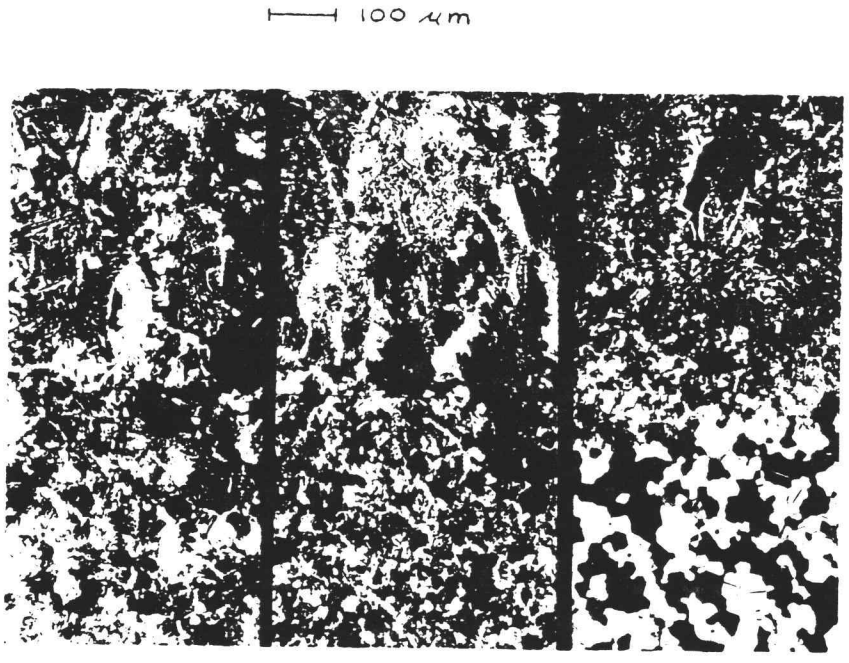

a) b) c)

Figure 30. Microstructure of Ingot 377HR LSM at a) 10 kJ/cm^2, b) 7 kJ/cm^2, and c) 4 kJ/cm^2.

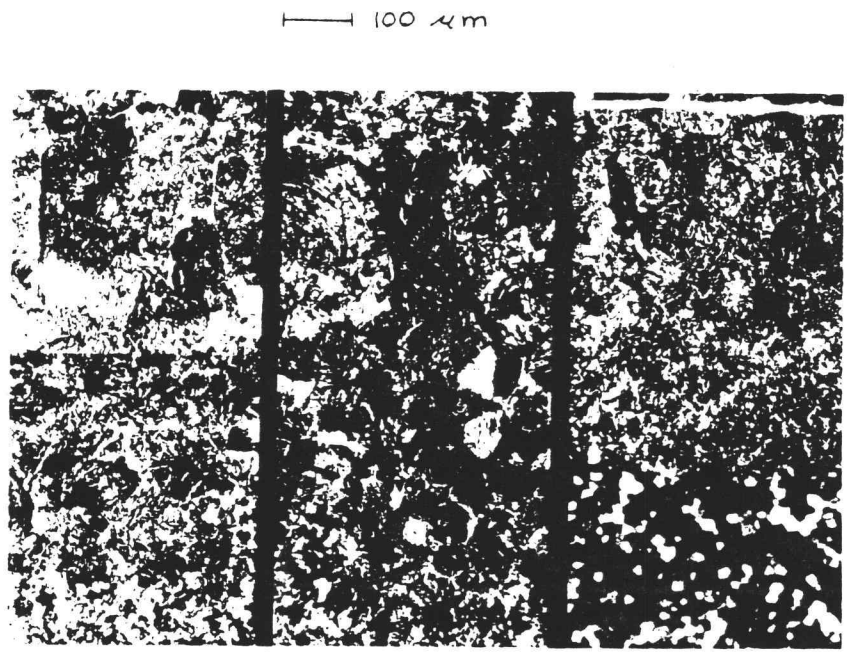

a) b) c)

Figure 31. Microstructure of Ingot 267 LSM at a) 10 kJ/cm^2, b) 7 kJ/cm^2, and c) 4 kJ/cm^2.

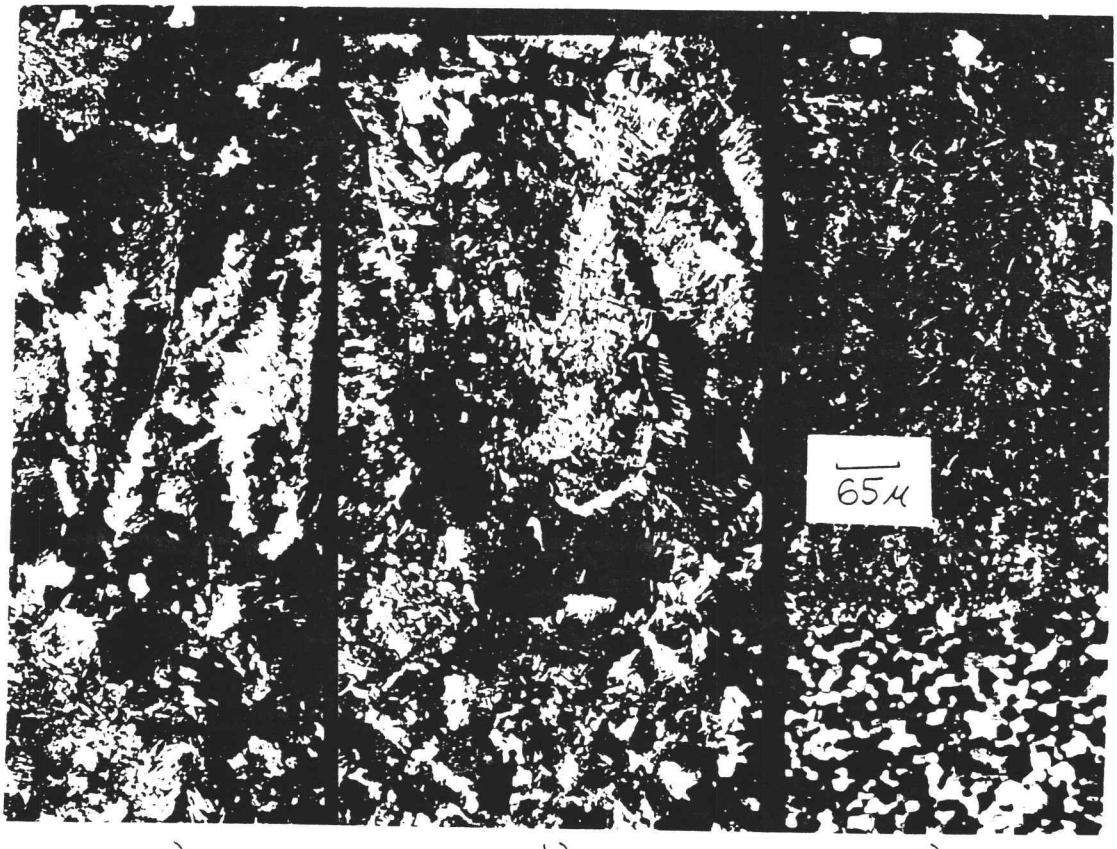

a) b) c)

Figure 32. Microstructure of Ingot 835 LSM at a) 10 kJ/cm^2, b) 7 kJ/cm^2, and c) 4 kJ/cm^2.

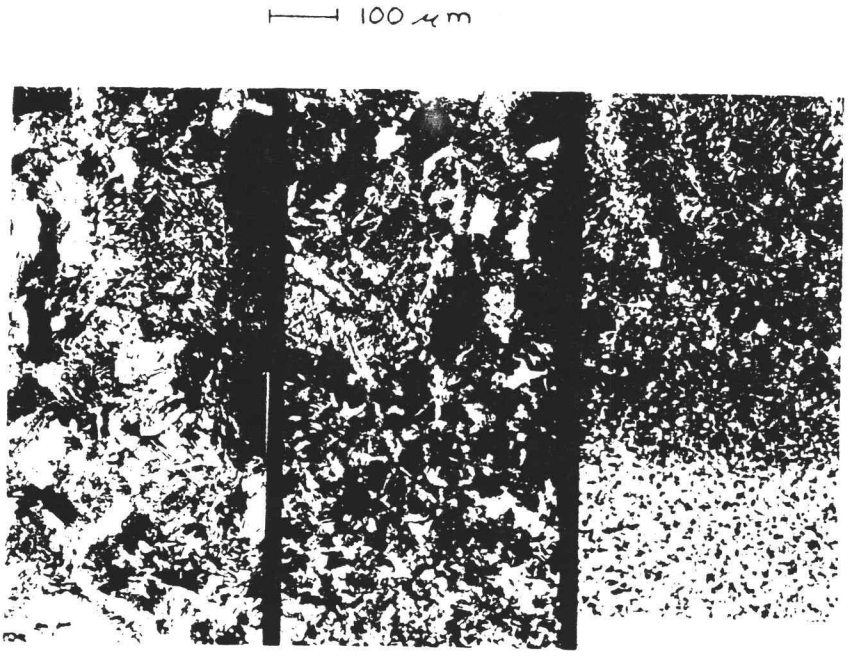

a) b) c)

Figure 33. Microstructure of Ingot 170 LSM at a) 10 kJ/cm^2, b) 7 kJ/cm^2, and c) 4 kJ/cm^2.

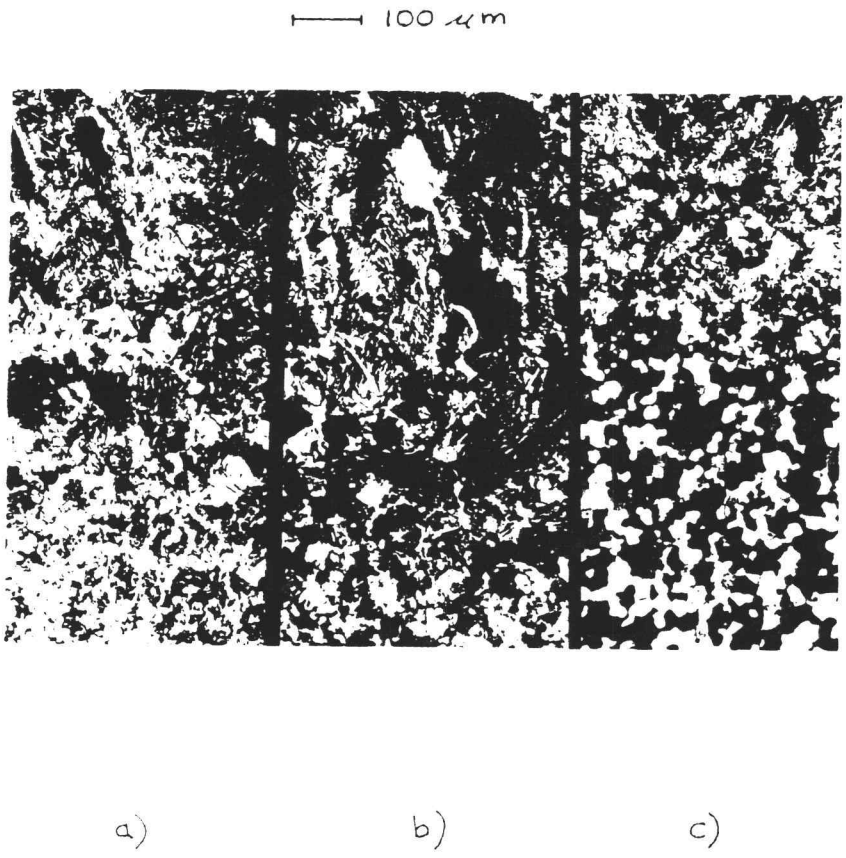

The highest energy density (10 kJ/cm^2) generated the coarsest microstructure. When examining the topmost surface layer, wider spacing of the parallel platelets within each colony is discernable. Larger colony sizes are associated with the topmost layer than with the melt pool periphery. Both of these attributes are characteristic of slower quench rates.

The medium energy density (7 kJ/cm^2) shows medium refinement of microstructure when compared to the lowest and highest energy densities. The medium energy density produced material with the greatest amount of Widmanstatten (basketweave) structure and colonies of medium size with parallel platelet spacing of medium dimensions.

The lowest laser energy density (4 kJ/cm^2) consistently produced the shallowest melt pool, whereas the 7 and 10 kJ/cm^2 laser energy densities produced about the same melt pool depths. Table 19 lists the melt pool depths for each processed group.

Table 19. Melt Pool Depths (mm)

energy (kJ/cm^2)	pureZr cr	pureZr hr	Zr-4 267	Zr702 835*	Zr702 170	avg n=4
4	.46	.53	.53	.51	.38	.47
7	.99	1.04	1.09	.91	1.07	1.05
10	1.19	1.07	1.24	1.90	1.10	1.15

* sample thickness 2.0 mm, all other samples were 3.4 mm these values were excluded from averages

The lowest laser energy density (4 kJ/cm^2) consistently generated an average melt pool depth of 0.5 mm, while the energy densities of 7 and 10 kJ/cm^2 generated an average melt pool depth of 1.05 and 1.15 mm. The melt pool depths do not correlate very well with the laser energy densities. However, a comparison of average melt pool depth to laser power densities is remarkably high (R = -.999) as seen in Table 20.

Table 20. Melt Pool Depths vs Energy and Power Densities

				R
melt pool depth (mm)	.47	1.05	1.15	
power density (kw/cm^2)	382	99	71	-.999
energy density (kJ/cm^2)	4	7	10	+.926

Recall the following relationships for power and energy density:

$$\text{Power Density } (kw/cm^2) = \text{Energy Density } (kw * sec/cm^2) * \text{beam vel } (cm/sec) \text{ / beam dia } (cm) \quad (IV.3)$$

Power density is a measure of the incident laser beam power divided by the area of the beam impinging on the surface. The laser energy density is a measure of the power density divided by the beam velocity times the beam diameter. Laser energy density includes a dwell time for any discrete location. As the dwell time increases and the incident power density increases, the energy density increases, and correspondingly, the depth of the melt pool increases. Much of the literature discusses LSM characteristics in terms of power density, which does not reflect the true laser processing input on the material surface.

Optical microscopy is capable of distinguishing the melt pool periphery using the special Sn-etch metallographic preparation, as described in the "Experimental" Chapter. The melt pool periphery is highlighted and resembles an arc initiating at the surface, extending to the bottom of the melt pool and intersecting the subse-

quent melt pool.

Alloy segregation was undetectable using SEM-EDX and electron microprobe. Since the resolution level is about 5000 angstroms, any local elemental concentrations must be finer than the minimum detection limits.

SIMS, with a resolution level of approximately 2 microns, was employed to study microsegregation by analyzing a 2 micron diameter by 10 atom layers deep volume (Evans, 1990). Tin and iron were found to be segregated. Sn is more concentrated at the melt pool wall, where it is twice as high as the central region of the melt pool (see Figure 10). The Sn-rich arcs extend from the surface, down to the bottom of the pool and then intersect the adjacent melt pool periphery (overlapping of laser beam passes).

Fe-rich areas were located in the melt pool approximately 200 microns from the melt pool wall. These Fe-rich arcs are parallel to the Sn-rich arcs, but are higher in Fe than the melt pool by a factor of 10, and coincide with the nodule genesis location. The Sn-rich arcs are Fe-poor, whereas the Fe-rich arcs have a concentration level of Sn similar to the melt pool.

2. Fabrication and Chemistry Effects

The higher alloy material, Zr-4, possesses a large fraction of second phase particles. The cold-rolled microstructure is finer than the hot-rolled microstructure. However, these effects do not influence the resulting LSM microstructure.

Any differences in the fabrication history should disappear after LSM processing since the volume of material examined and corrosion tested has been heated into the liquid regime; totally homogenizing the LSM region and removing all previously formed second phase constituents. However, chemical segregation can still occur during resolidification influencing the minor chemical concentration distribution.

V. DISCUSSION

This section will discuss the relationships and interactions of data and results with respect to two perspectives: corrosion rate and microstructure (quench rate).

The microstructure is refined by LSM. The wrought product (non-LSM) exhibited an equiaxed, coarse grain structure when compared to the microstructure of the LSM samples. The lowest laser energy density (4 kJ/cm^2) produces the fastest quench, while the wrought product manufacturing process (hot forging and water quench) produces the slowest quench. At the limit, as the quench rate slows, the wrought product microstructure is achieved. The finest microstructure is associated with the lowest laser energy density (4 kJ/cm^2). The extremely fast quench results from the small melt pool and the large heat reservoir. By comparison the highest laser energy density (10 kJ/cm^2) produced a slower quench rate and a correspondingly slightly coarser microstructure, which was still finer than the wrought product microstructure.

The melt pool depth is also a measure of the extent to which the microstructure becomes more refined. The shallow melt pool is associated with the fastest quench and the finest microstructure, while the deepest melt pool is associated with the slower quench.

This variation in microstructure affected the corrosion performance during the three different corrosion tests. The potentiodynamic and immersion tests, both of which were conducted in a 10% $FeCl_3$ environment, showed that the fastest LSM quench generated the finest microstructure with outstanding corrosion results. Up to a 600-fold increase in corrosion resistance was achieved and the propensity for pitting was significantly reduced. The slower quench, from the highest laser energy density (10 kJ/cm^2), yielded a corrosion resistance less than the fastest quench, but still an order of magnitude better than that of the wrought product (the slowest quench rate).

The fastest quench material is also characterized by the highest diamond pyramid hardness (DPH) values. The fastest quench produces a martensitic type structure, which is well known by its high hardness values. The slower quench results in slightly lower hardness, but still substantially higher than the matrix region.

Corrosion performance of the LSM coupons tested in the steam autoclave was disappointingly poor. Laser processing greatly reduces the corrosion resistance. Nodular corrosion is accelerated in the laser pass overlap region. The location of the nodular corrosion product on the laser passes coincides with the location of the Fe-rich areas within the melt zone. These localized Fe-rich areas are responsible for the accelerated corrosion as discussed in the "Results" chapter under the subheading "Microstructure and Phases".

The pitting that occurs from the $FeCl_3$ solution presents itself in a periodic fashion, similar to the appearance of the nodular corrosion. When the pits occur, they, also, appear predominately in the laser pass overlap region.

Typically, the martensitic type microstructure provides the best corrosion resistance in an acid environment, while the coarser, wrought product, microstructure performs the best in a steam autoclave environment. This is due to the different type of corrosion that occurs in each environment.

In the steam environment, the Zr behaves anodically, combining with the available oxygen, producing an oxide film (Yau, 1988). The second phase particles behave cathodically, completing the required electron circuitry. As long as the electrical circuit is maintained, a tightly adherent, slow growing, protective oxide film is generated (Sato, 1987). When the oxide film exceeds several microns in thickness and the second phase particles can no longer provide a complete electrical circuit, the oxide film loses its protective behavior and degrades, permitting accelerated oxidation. Therefore, abundant second phase particles enhance the corrosion resistance in a steam autoclave environment.

In an acid environment, the reverse is true: the Zr atoms behave cathodically and the alloying elements, Fe in particular, behave anodically (Chappell, 1978). As in the autoclave environment, both the Fe and Zr elements are necessary for corrosion to occur. In the acid environment, the chemical reaction results in the Zr ionizing, disassociating from the matrix, and migrating into the acid solution. Since the Fe-rich areas are localized in the laser pass overlap region, the pitting occurs preferentially in these areas (Smith, 1990). The Fe-rich areas promote the dissolution of Zr ions from the matrix, resulting in the formation of a pit. The lower

Fe concentration everywhere else in the LSM surface provides a pit resistant surface and reduces the general corrosion rate.

VI. CONCLUSIONS

Laser surface melting (LSM) offers several unique opportunities for metal processing. Previously unattainable microstructures can be generated and their physical properties should be investigated. Previous research, as identified in the "Introduction" chapter, has dealt with laser processing of materials, testing for a particular attribute, and then adjusting the laser processing parameters to obtain maximum improvement for the particular attribute of interest. This project investigated the corrosion properties of LSM Zirconium base alloys and examined the processed material to determine the mechanism responsible for corrosion. The data indicate that microstructure and chemical microsegregation are the controlling factors for corrosion performance of LSM material.

The corrosion tests simulated the typical environments, to which zirconium base alloys are subjected. The nuclear industry is concerned with oxide film formation, while the chemical processing industry is concerned with metal dissolution. A useful material lifetime should be established for the novel microstructures introduced by LSM.

A. MICROSTRUCTURE

As the laser energy density decreases, the quench rate increases. As the laser energy density decreases, the microstructure becomes increasingly refined as shown by the interlamellar spacing within each grain. The melt pool depth is directly related to the laser energy density. As the laser energy density decreases, the melt pool depth decreases.

Laser processing causes Sn and Fe segregation. The Sn-rich areas result from solidification kinetics in the zirconium base alloys. The Sn segregates to the portion of the melt that solidifies first, since Sn prefers the lower temperature phase of zirconium (alpha). The Fe remains in solution for a longer period of time since it prefers the high temperature phase of zirconium (beta).

B. AUTOCLAVE

Nodular corrosion initiates at the laser pass overlap regions due to Fe segregation. Fe segregation causes accelerated oxidation due to increased ion concentration in localized areas. As the laser energy density and beam width decrease, the number of laser pass overlap regions increase, and the corrosion resistance decreases.

This is directly related to the increased surface area that contains the Fe-rich segregation.

As the quench rate increases due to LSM, the transition point (time to transition and corrosion rate at transition) increases.

C. IMMERSION

LSM increases the corrosion resistance due to the second phase particles dissolving and remaining in the melt as a supersaturated solid solution.

Laser processing reduces the propensity for pitting.

D. POTENTIODYNAMIC

LSM increases the corrosion resistance due to the second phase particles dissolving and remaining in the melt as a supersaturated solid solution. This confirms the results obtained from the immersion tests.

Passive subsurfaces exist at a certain depth, continued metal removal restores the active behavior.

As the quench rate increases, the area of the hysteresis loop decreases. This confirms the results obtained from the immersion tests.

VII BIBLIOGRAPHY

Affolter, K., and Von Allmen, M., ''Glass-Forming Ability in Laser Quenched Transition-Metal Alloys,'' Appl. Phys. A, 33, 1984, pp. 93-96.

Anderson, K.J., ''Being Coherent: Three Decades of Laser Development,''MRS Bulletin, Dec. 1988, pp. 24-25.

Anderson, W.K., Corrosion of Zr Alloys, W.K. Anderson and W. Cashin, (eds.), ASTM Symp. Proc., ASTM, Phila., 1963.

Arata, Y., Plasma, Electron and Laser Beam Technology, ASM, Metals Park, OH, 1986.

Arnold, C.G., and Schweitzer, P.A.,''Corrosion Testing Techniques,'' Corrosion and Corrosion Protection Handbook, P.A. Schweitzer, (ed.), Marcel Dekker, N.Y., 1988, pp. 587-616.

ASTM G15-86,''Standard Definitions of Terms Relating to Corrosion and Corrosion Testing,'' ASTM G15-86, Phila., 1986, pp. 104-107.

ASTM G16-71, ''Standard Practice for Applying Statistics to Analysis of Corrosion Data,'' ASTM G16-71, Phila., 1984, pp. 108-122.

ASTM G1-88,''Standard Practice for Preparing, Cleaning, and Evaluating Corrosion Test Specimens,'' ASTM G1-88, Phila., 1988, pp. 61-67.

ASTM G46-76,''Standard Practice for Examination and Evaluation of Pitting Corrosion,'' ASTM G46-76, Phila., 1986, pp. 197-202.

ASTM G5-87,''Standard Reference Test Method for Making Potentiostatic and Potentiodynamic Anodic Polarization Measurements,'' ASTM G5-87, Phila., 1987, pp. 97-101.

ASTM G61-86,''Standard Test Method for Conducting Cyclic Potentiodynamic Polarization Measurements for Localized Corrosion Susceptibility of Iron-, Nickel-, or Cobalt-Based Alloys,''ASTM G61-86, Phila., 1986, pp. 254-257.

Ayers, J.D., and Schaefer, R.J., ''Consolidation of Plasma-Sprayed Coatings by Laser Remelting,'' Laser Applications in Materials Processing, SPIE, vol. 198, 1979, pp. 57-64.

Aziz, M.J., ''Model for Solute Redistribution During Rapid Solidification,'' J. Appl. Phy., 53, (2), Feb. 1982, pp.

1158-1168.

Baeri, P., Campisano, S.U., Grimaldi, M.G., and Rimini, E., ''Surface Accumulation of Impurities After Laser-Induced Melting,'' Laser and Electron Beam Processing of Materials, MRS Symp., C.W. White and P.S. Peercy, (eds.), Academic Press, N.Y., 1979, pp. 130-136.

Baer, D.R., and Dake, L.S., ''AES, XPS, RBS, NRA, and Laser Raman Studies of High Temperature Corrosion,'' Oxidation of Metals and Assoc. Mass Transport, TMS Conf. Proc., M.A. Dayanda, S.J. Rothman, and W.E. King, (eds.), TMS, Phila., 1986, pp. 185-216.

Baer, D.R., ''Solving Corrosion Problems with Surface Analysis,''Appl. of Surface Sci., 20, 1984, pp. 382-396.

Barnett, S.,''Electrochemical Nature of Corrosion,'' Electrochemical Tech. for Corrosion, NACE Symp., R. Baboian, (ed.), NACE, Houston, TX, 1976, pp. 1-10.

Barsukov, A.D., and Khorina, G.Y., ''Effect of Laser Radiation on the Surface Structure of Zr,'' Sov. Non-Ferrous Met. Res., 10, (5), 1982, pp. 408-410.

Bass, M., ''Lasers and Electron Beams,'' Surface Alloying by Ion, Electron and Laser Beams, ASM Mat'l Sci. Sem., L.E. Rehn, S.T. Picraux and H. Wiedersich, (eds.), ASM, Metals Park, OH, 1985, pp. 357-372.

Bockris, J.O., ''Spectroscopic Observations on the Nature of Passivity,'' Corrosion, 24, (2,3), 1989, pp. 291-312.

Boettinger, W.J., and Perepezko, J.H., ''Fundamentals of Rapid Solidification,'' Rapidly Solidified Crystalline Alloys, TMS, Phila., PA, May 1985, pp. 21-58.

Boettinger, W.J., Coriell, S.R., and Sekerka, R.F., ''Mechanisms of Microsegregation-Free Solidification,'' Mat'l. Sci. and Eng., 65, 1984, pp. 27-36.

Bonora, P.L., Bassoli, M., Cerisola, G., De Anna, P.L., Tosello, G., Tosto, S., Mazzoldi, P., and Della Mea, G.,''Electrochemical and Corrosion Behavior of Ion Implanted and Laser Irradiated Metals'', Corrosion of Metals Processed by Directed Energy Beams, C.R. Clayton and C.M. Preece, (eds.), TMS, N.Y., 1982, pp. 101-118.

Bruce, C., ''Ferric Chloride,'' Handbook of Corrosion Data, C.Bruce, (ed.), ASM, Metals Park, OH, 1989, pp. 261-267.

Bruck, G.J., ''High-Power Laser Beam Cladding,'' J. Metals,

Feb. 1987, pp. 10-13.

Chande, T., and Mazumder, J., ''Composition Control in Laser Surface Alloying,'' Met. Trans. B, 14B, June 1983, pp. 181-190.

Chande, T., and Mazumder, J., ''Mass Transport in Laser Surface Alloying: Iron-Nickel System,'' Appl. Phys. Lett., 41, (1), July 1982, pp. 42-43.

Chande, T., and Mazumder, J., ''Two-Dimensional, Transient Model for Mass Transport in Laser Surface Alloying,'' J. Appl. Phys., 57, (6), March 1985, pp. 2226-2232.

Chan, C.L., Mazumder, J., and Chen, C.C., ''Three-Dimensional Axisymmetric Model for Convection in Laser-Melted Pools,'' Mat. Sci. and Tech., 3, (4), 1987, pp. 306-311.

Chan, C.L., Mazumder, J., and Chen, C.C., ''A Two-Dimensional Transient Model for Convection in Laser Melted Pool,'' Met. Trans. A, 15A, Dec. 1984, pp. 2175-2184.

Chappell, M.J., and Leach, J.S.,''Passivity and Breakdown of Passivity of Valve Metals,'' Passivity of Metals, R.P. Frankenthal, and J. Kruger, (eds.), Electro. Soc., Princeton, N.J., 1978, pp. 1003-1034.

Charquet, D., ''Improvement of the Uniform Corrosion Resistance of Zr-4 in the Absence of Irradiation,'' J. Nucl. Mat'l., 160, 1988, pp. 186-195.

Cieslak, M.J., and Jellison, J.L., ''A Perspective on Welding Science,'' MRS Bulletin, 14, (2), Feb. 1989, pp. 32-38.

Clayton, C.R., ''Application of Directed Energy Beams in Fundamental and Applied Studies of the Aqueous Corrosion of Metals,'' Environmental Degradation of Ion and Laser Beam Treated Surfaces, G.S. Was and K.S. Grabowski, (eds.), TMS, Phila., PA, 1989, pp. 33-55.

Clayton, J.C., ''Cladding Corrosion and Hydriding in Irradiated Defected Zircaloy Fuel Rods,'' Corrosion, 45, (12), Dec. 1989, pp. 996-1002.

Condon, J.B., ''Calculations of Oxidation Rates of Zr,'' Corrosion, 37, (12), Dec. 1981, pp. 721-723.

Copley, S.M., Beck, D.G., Esquivel, O., and Bass, M., ''Solidfication of Continuous Laser-Melted Trails,'' Lasers in Metallurgy, TMS Symp Proc., K. Mukherjee and J. Mazumder,

(eds.), TMS, Phila., PA, 1981, pp. 11-20.

Cortie, M.B., ''The Effects of Second-Phase Particles on the Corrosion and Structure of Zr-4,'' Masters Thesis, Univ. of Petoria, Oct. 1982, Pretoria, South Africa, pp. 1-59.

Cox, B., ''Oxidation of Zirconium and Its Alloys,'' Advances in Corrosion Science and Technology, vol. 5, M.G. Fontana and R.W. Staehle, (eds.), Plenum, N.Y., 1976, pp. 251-321.

Cragnolino, G., and Galvele, J.R.,''Anodic Behavior and Pitting of Zr and Zr-4 in Aqueous Solutions of NaCl,'' Passivity of Metals, R.P. Frankenthal, J. Kruger, (eds.), Electrochemical Society, Princeton, N.J., 1978, pp. 1053-1058.

Dahotre, N.B., Wakade, C., and Mukherjee, K., ''Laser Melting and Microstructure of A Metallic Glass,'' Laser Proc. of Mat'l, K. Mukherjee and J. Mazumder, (eds.), TMS, Phila., 1985, 101-115.

David, S.A., and Vitek, J.M., ''Soldification Behavior and Microstructural Analysis of Austenitic SS Laser Welds,'' Lasers in Metallurgy, TMS Conf. Proc., K. Mukherjee and J. Mazumder, (eds.), TMS, N.Y., 1981, pp. 247-254.

David, S.A., and Vitek, J.M.,''Correlation Between Solidification Parameters and Weld Microstructures,'' Int. Metal Rev., 34, (5), 1989, pp. 213-245.

Davies, H.A., ''Rapid Quenching Techniques and Formation of Metallic Glasses,'' Rapidly Quenched Metals III, RQM Conf., B. Cantor, (ed.), The Metals Soc., London, July 1978, pp. 1-21.

Davis, J.W., Haasz, A.A., and Stangeby, P.C.,''Laser Induced Release of Gases From First Wall Coatings for Fusion Applications,'' J. Nucl. Mat., 138, 1986, pp. 227-234.

Dean, S.W., Jr., ''Electrochemical Methods of Corrosion Testing,'' Electrochemical Tech. for Corrosion, NACE Symp., R. Baboian, (ed.), NACE, Houston, TX, 1976, pp. 56-60.

Den Broeder, F.J., Vandenberg, J.M., and Draper, C.W., ''Microstructures of Cu-Zr Phases Formed by Laser Surface Treatment,'' Thin Solid Films, 111, 1984, pp. 43-51.

Dollins, C.C., and Jursich, M., ''A Model for the Oxidation of Zr-Based Alloys,'' J. Nucl. Mat'l., 113, 1983, pp.

19-24.

Douglass, D.L., ''The Physical Metallurgy of Zr,'' Atomic Energy Review, 1, (4), 1963, pp. 71-237.

Draper, C.W., and Ewing, C.A., ''Review: Laser Surface Alloying: A Bibliography,'' J. Mat'l. Sci., 19, 1984, pp. 3815-3825.

Draper, C.W., and Poate, J.M., ''Laser Surface Alloying,''Int. Metal Review, 30, 2, 1985, pp. 85-108.

Draper, C.W., Den Broeder, F.J., Jacobson, D.C., Kaufmann, E.N., McDonald, M.L., and Vandenberg, J.M., ''Studies of Laser-Alloyed Zr-Containing Surface Layers,'' Laser and Electron-Beam Interactions with Solids, B.R. Appleton and G.K. Celler, (eds.), Elsevier Sci., 1982, pp. 419-424.

Draper, C.W., ''Laser Alloying of Deposited Metal Films on Nickel,''Laser and Electron Beam Processing of Materials, MRS Symp., C.W. White and P.S. Peercy, (eds.), Academic Press, N.Y., 1979, pp. 721-727.

Draper, C.W., ''Laser Surface Alloying: The State of the Art,'' Lasers in Metallurgy, K. Mukherjee and J. Mazumder, (eds.), TMS, N.Y., 1981, pp. 67-92.

Draper, C.W., ''The Effects of Laser Surface Melting,'' Lasers in Metallurgy, K. Mukherjee and J. Mazumder, (eds.), Proc. of TMS Symp., TMS, Phila., PA, 1981, pp. 21-32.

EG&G,''Basics of Corrosion Measurements,'' EG&G Princeton Appl. Research, Analytical Instrument Division, Princeton, N.J., 1980, pp. 1-12.

Evans, C., Jr., and Blattner, R., ''Static Secondary Ion Mass Spectrometry,'' Charles Evans and Assoc., Newsletter, 5, (2), March 1990, pp. 10-11.

Ferrando, W.A.,''Processing and Use of Zr-based Materials,'' Adv. Mater. Manuf. Process, 3, (2), 1988, pp. 195-231.

Folkes, J., West, D.R., and Steen, W.M., ''Laser Surface Melting and Alloying of Titanium,''Laser Surface Treatment of Metals, Conf. Proc., C.W. Draper and P. Mazzoldi, (eds.), Martinus Nijhoff, Boston, 1986, pp. 451-459.

Follstaedt, D.M., and Picraux, S.T.,''Microstructures of Surface-Melted Alloys,'' ASM Materials Sci. Sem., L.E. Rehn, S.T. Picraux, and H. Wiedersich, (eds.), ASM, Metals Park, OH, 1987, pp. 175-222.

Follstaedt, D.M., ''Metallurgy and Microstructure of Pulsed Melted Alloys,'' Laser and Electron-Beam Interactions with Solids, Proc. MRS Mtg., B.R. Appleton and G.K. Celler, (eds.), North-Holland, N.Y., 1981, pp. 377-387.

Fontana, M.G., Advances in Corrosion Science and Technology, vol. 5, M.G. Fontana and R.W. Staehle, (eds.), Plenum, N.Y., 1976, pp. 227-245.

Fontana, M.G., and Greene, N.D., Corrosion Engineering, McGraw-Hill, N.Y., 1967.

Gad-Allah, A.G., Abd El-Ranman, H.A., ''Kinetics of Open-Circuit Barrier Layer Formation on Metallic Surfaces in Aqueous Solutions,'' Corrosion, 43, (11), Nov. 1987, pp. 698-702.

Gaffet, E., and Martin, G., ''A Simple Model for the Crystal-to-Amorphous Phase Transition Under Laser Annealing Conditions,'' Mat'l. Sci. and Eng., 82, 1986, pp. L13-L17.

Giordano, L.G., and Ramous, E., ''Rapid Solidification of Surface Layers by CW Laser,'' Laser Surface Treatment of Metals, Conf. Proc., C.W. Draper and P. Mazzoldi, (eds.), Martinus Nijhoff, Boston, 1986, pp. 483-495.

Glaeser, W.A., and Fairand, B.P., ''Laser Surface Melting for Abrasion Resistance,'' Wear of Materials, ASME Conf. Proc., W. Glaeser and S. Rhee, (eds.), ASME, N.Y., April 1979, pp. 304-312.

Godard, H.P., ''Localized Corrosion,'' NACE Basic Corrosion Handbook, NACE, Houston, TX, 1978, pp. 8/1-8/15.

Hackerman, N., and Cecil, O.B., ''The Electrochemical Polarization of Zr in Neutral Salt Solutions,'' J. Electro. Soc., 101, (8), Aug. 1954, pp. 419-425.

Hawkes, I., Walker, A., Steen, W.M., and West, D.R., ''The Application of Laser Surface Melting and Alloying to Alloys Based on the Fe-C System,'' Laser Proc. of Mat'l, K. Mukherjee and J. Mazumder, (eds.), TMS, Phila, PA, 1985, pp. 169-182.

Heakal, F.E., Mogoda, A.S., Mazhar, A.A., and Ghoneim, A.A., ''Effect of Fluoride Media on the Stability of Anodic ZrO_2 Films,'' Corrosion, 46, (3), March 1990, pp. 247-253.

Hillner, E., ''Corrosion of Zirconium-Based Alloys - An Overview,'' Zirconium in the Nuclear Industry, ASTM STP 633, A.L. Lowe, Jr. and G.W. Parry, (eds.), ASTM, 1977, pp.

211-235.

Holbert, R.K., Mustaleski, T.M., and Frye, L.D., ''Laser Beam Welding of Stainless Steel Sheet,'' Welding J., August 1987, pp. 21-25.

Irons, G.C., ''Laser Fusing of Flame Sprayed Coatings,'' Welding J., Dec. 1978, pp. 29-32.

Isaacs, H.S., ''The Localized Breakdown and Repair of Passive Surfaces During Pitting,'' Corr. Sci., 29, (2,3), 1989, pp. 313-323.

Johnson, A.B., Jr., and Horton, R.M.,''Nodular Corrosion of the Zircaloys,'' Zirconium in the Nuclear Industry, ASTM STP 633, A.L. Lowe, Jr. and G.W. Parry, (eds.), ASTM, 1977, pp. 295-311.

Johnson, A.B., Jr., LeSurf, J.E., and Proebstle, R.A., ''Study of Zirconium Alloy Corrosion Parameters in the Advanced Test Reactor,'' Zirconium in Nuclear Applications, ASTM STP 551, J.H. Schemel and H.S. Rosenbaum, (eds.), ASTM, 1974, pp. 495-513.

Johnson, A.B., Jr., ''Corrosion and Failure Characteristics of Zr Alloys in High-Pressure Steam in Temperature Range 400 to 500 C,''Appl.-Related Phen. for Zr and Its Alloys, ASTM STP 458, W.R. Thomas, S.S. Christopher, and P.L. Rittenhouse, (eds.), ASTM, 1969, pp. 271-285.

Kar, A., and Mazumder, J., ''One-Dimension Diffusion Model for Extended Solid Solution in Laser Cladding,'' J. Appl. Phys., 61, (7), April 1987, pp. 2645-2655.

Kass, S.,''The Development of the Zircaloys,'' ASTM STP 368, Phila., PA, 1964, pp. 3-27.

Kattamis, T.Z., ''Solidification Microstructure of Laser Processed Alloys,'' Lasers in Metallurgy, Proc. of TMS Symposium, K. Mukherjee and J. Mazumder, (eds.), TMS, Phila., PA, 1981, pp. 1-10.

Kaufmann, E.N., and Wallace, R.J., ''Crystallization and Nucleation Phenomena in CW Melted Alloys,'' Laser Surface Treatment of Metals, Conf. Proc., C.W. Draper and P. Mazzoldi, (eds.), Martinus Nijhoff, Boston, 1986, pp. 93-110.

Kear, B., ''Rapid Solidification Technology,'' J. Mat'ls. Educ., 9, (6), 1988, pp. 87-118.

Khan, P.A., and DebRoy, T., ''Determination of Weld Pool

Temperature During Laser Welding of AISI 202 Stainless Steel,'' Laser Proc. of Mat'l, K. Mukherjee and J. Mazumder, (eds.), TMS, Phila., PA, 1985, pp. 71-81.

Khan, P.A., DebRoy, T., and David, S.A.,''Laser Beam Welding of High-Manganese Stainless Steels - Examination of Alloying Element Loss and Microstructural Changes,'' Welding Research, Jan. 1988, pp. 1s-5s.

Kirillin, A.V., Kostanovskii, A.V., and Vinogradov, V.L., ''Measurement of the Melting Point of Refractory Materials by Laser Surface Heating,'' High Temperatures-High Pressures, 19, 1987, pp. 473-476.

Knittel, D.R., and Bronson, A.,''Pitting Corrosion on Zirconium - A Review,'' Corrosion, 40, (1), Jan. 1984, pp. 9-14.

Knittel, D.R., Maguire, M.A., Bronson, A., and Chen, J., ''The Effect of Surface Treatment and Electrochemical Methods on the Pitting Potentials of Zr in Chloride Solutions,'' Corrosion, 38, (5), May 1982, pp. 265-273.

Koelsch, J.R., ''Industrial Lasers - Putting Light to Work,'' Production Engineering, Sept. 1985, pp. 50-54.

Kuwae, R., Sato, K., Higashinakagawa, E., Kawashime, J., and Nakamara, S.,''Mechanism of Zircaloy Nodular Corrosion,'' J. Nucl. Mat'l., 119, 1983, pp. 229-239.

Kuwae, R., Sato, K., Kawashima, J., and Higashinakagawa, E.,''Influence of Some Factors on Nodular Corrosion Behavior of Zr-2,'' J. Nucl. Sci. and Tech., 23, (7), July 1986, pp. 661-663.

Lewis, B.G., and Strutt, P.R.,''Practical Implications of EB Surface Melting,'' Corrosion of Metals Processed by Directed Energy Beams, TMS Conf. Proc., C.R. Clayton and C.M. Preece, (eds.), TMS, N.Y., 1982, pp. 119-128.

Lewis, B.G., Gilbert, D.A., and Strutt, P.R., ''Laser and Electron Beam Melting of Materials,'' Proc. of MRS Symp., C.W. White and P.S. Peercy, (eds.), 1979, pp. 747-753.

Li, L.J., and Mazumder, J., ''A Study of the Mechanism of Laser Cladding Processes,'' Laser Processing of Materials, K. Mukherjee and J. Mazumder, (eds.), TMS, Phila., 1985, pp. 35-50.

Lumsden, J.B., Gnanamuthu, D.S., and Moores, R.J., ''Corrosion Resistance of AISI 4140 Steel Laser Surface Alloyed with Cr and Ni,'' Corrosion of Metals Processed by

Directed Energy Beams, C.R. Clayton and C.M. Preece, (eds.), TMS, N.Y., 1982, pp. 129-134.

Lustman, B., and Kerze, F., Metallurgy of Zirconium, McGraw-Hill, N.Y., 1955.

Lu, Y.C., Jin, C., Lin, T.L., Chen, L.Y., and Su, B.R., ''Microstructure and Properties of Epitaxial Layers by Laser Glazing,'' Mat'l. Lett., 6, (7), April 1988, pp. 229-232.

Maguire, M.A., and Yau, T.L., ''Corrosion-Electrochemical Properties of Zr in Mineral Acids,'' NACE Conf., Paper No. 265, Houston, TX, 1986, pp. 1-20.

Mansfield, F., ''Polarization Resistance Measurements - Experimental Procedure and Evaluation of Test Data,'' Electrochemical Tech. for Corrosion, NACE Symp., R. Baboian, (ed.), NACE, Houston, TX, 1976, pp. 18-26.

Massalski, T.B., Woychik, C.G., and Dutkiewicz, J., ''Solidification Structures in Rapidly Quenched Cu-Ti-Zr Alloys,'' Met. Trans. A, 19A, July 1988, pp. 1853-1860.

Mavaghini, M., Adams, G.B., Jr., and Rysselberghe, P.V., ''Studies on the Anodic Polarization of Zr and Zr Alloys,'' J. Electro. Soc., 101, (8), Aug. 1954, pp. 400-409.

Mazumder, J., and Kar, A., ''Solid Solubility in Laser Cladding,'' J. Metals, Feb. 1987, pp. 18-23.

Mazumder, J., and Steen, W.M., ''Welding of Ti-6Al-4V by a Continuous Wave CO_2 Laser,'' Metal Construction, 12, 1980, pp. 423-427.

Mazumder, J., and Steen, W.M., ''Heat Transfer Model for CW Laser Material Processing,'' J. Appl. Phys., 51, (2), Feb. 1980, pp. 941-947.

Mazumder, J., and Steen, W.M., ''Laser Welding of Ti-6Al-4V,'' Laser 77 Opto-Electron Conf. Proc., W. Weidelich, (ed.), 1977, pp. 304-315.

Mazumder, J., and Steen, W.M., ''Microstructures and Mechanical Properties of Lasers Welded Ti-6Al-4V,'' Met. Trans. A, 13A, 1982, pp. 865-871.

Mazumder, J., ''Laser Welding,'' Laser in Materials Processing, M. Bass, (ed.), Ch. 3, North-Holland, N.Y., 1983, pp. 115-200.

Mazumder, J., Singe, J., and Raja, S., ''Laser Cladding of

Mg and Nb Alloys for Improved Environmental Resistance,''AFOSR Report 86-0034, Jan. 1987, pp. 1-36.

Mazumder, J., ''Laser Heat Treatment: The State of the Art,'' J. Metals, 5, 1983, pp. 18-26.

Mazumder, J., ''Laser Welding: State of the Art Review,'' J. Metals, 34, 1982, pp. 16-24.

Mazumder, J., ''Laser Welding: State of the Art Review,'' Lasers in Metallurgy, K. Mukherjee and J. Mazumder, (eds.), TMS, N.Y., 1981, pp. 221-246.

Mazumder, J., ''Mathematical Modeling of Laser Surface Treatments,'' NATO ASI Series, Series E, vol. 115, Laser Surface Treat. Met., 1986, pp. 297-307.

McCafferty, E., and Moore, P.G., ''Electrochemical Behavior of Laser - Processed Metals Surfaces,'' Laser Surface Treatment of Metals, Conf. Proc., C.W. Draper and P. Mazzoldi ,(eds.), Martinus Nijhoff, Boston, 1986, pp. 263-295.

McCafferty, E., Moore, P.G., Ayers, J.D., and Hubler, G.K., ''Effect of Laser Processing and Ion Implantation on Aqueous Corrosion Behavior,'' Corrosion of Metals Processed by Directed Energy Beams, C.R. Clayton and C.M. Preece, (eds.), TMS, Phila., PA, 1982, pp. 1-22.

Miller, R.A., and Berndt, C.C., ''Performance of Thermal Barrier Coatings in High Heat Flux Environments,'' Thin Solid Films, 119, 1984, pp. 195-202.

Moffat, T.P., and Lichter, B.D.,''Environmental Effects on Advanced Materials,'' J. Metals, Dec. 1988, pp. 18-30.

Moore, P.G., and Weinman, L.S., ''Surface Alloying Using High-Power Continuous Lasers,'' SPIE, vol. 198, Laser Appl. in Mat'l. Proc., 1979, pp. 120-125.

Moran, J.J., ''Corrosion at High Temperatures,'' NACE Basic Corrosion Guide, NACE, Houston, TX, 1978, pp. 12/1-12/20.

Mullins, W.W., and Sederka, R.F., ''Stability of a Planar Interface During Solidification of a Dilute Binary Alloy,'' J. Appl. Phy., 35, (2), Feb. 1964, pp. 444-451.

Ohse, R.W., ''Laser Application in High Temperature Material,'' Pure Appl. Chem., 60, (3), March 1988, pp. 309-322.

Palit, G.C., and Gadiyar, H.S., ''Pitting Corrosion of Zr

in Chloride Solution,'' Corrosion, 43, (3), March 1987, pp. 140-148.

Pang, D., Wang, J., Ding, B., Song, Q., and Yang, Z.,''Relationships Between Quenching Rates and Properties in Amorphous Alloys,'' Mat'ls. Lett., 5, (11,12), Oct. 1987, pp. 439-441.

Peggs, I.D., and Skrastins, D.P.,''The Metallography of Electrochemical Corrosion Testing,'' Corrosion, Microstructure, and Metallography, Proc. of Intern. Metall. Soc., D.O. Northwood, W.E. White and G.F. Vander Voot, (eds.), Vol. 12, ASM, Metals Park, OH, 1985, pp. 25-35.

Peng, T.C., and Mazumder, J., ''Comparison of Heat-Transfer Modeling for Laser Melting of Ti-Alloys,'' Laser Proc. of Mat'l., K. Mukherjee and J. Mazumder, (eds.), TMS, Phila., PA, 1985, pp. 51-59.

Pickering, H.W., ''The Significance of the Local Electrode Potential within Pits, Crevices, and Cracks,'' Corr. Sci., 29, (2,3), 1989, pp. 325-341.

Picraux, S.T., and Follstaedt, D.M., ''Surface Modification and Alloying: Aluminum,'' Surface Modification and Alloying, J.M. Poate, G. Foti, and D.C. Jackson, (eds.), Plenum Press, N.Y., 1981, pp 287-322.

Poate, J.M., ''Laser-Solid Interactions: Phase Formation and Segregation Phenomena,'' Environmental Degradation of Ion and Laser Beam Treated Surfaces, G.S. Was and K.S. Grabowski, (eds.), TMS, Phila., PA, 1989, pp. 23-30.

Pourbaix, M., Lectures on Electrochemical Corrosion, Plenum Press, N.Y., 1973.

Pruett, K.M., ''Ferric Chloride,'' Compass Corrosion Guide II, K.M. Pruett, (ed.), Compass, La Mesa, CA, 1983, pp. A38-A41.

Quach, V., and Northwood, D.O., ''Control of Microstructure in Brazed Zone of Zr-4 Nuclear Fuel Sheathing by Optimization of (C+P+Si) Contents and Cooling Schedules,'' Optimizing Materials for Nuclear Application, 1984, pp. 51-62.

Reitz, W., and Rawers, J., ''Immersion Corrosion Studies of Laser Processed Zr,'' J. Mat'l. Sci. Ltr., 9, (3), March 1990, pp. 355-357.

Reitz, W., and Rawers, J., ''Microstructure and Corrosion of Laser Melted Zr Alloys,'' Surface Modification

Technologies III, TMS Conf. Proc., T.S. Sudarshan and D.G. Bhat, (eds.), TMS, Phila., 1989, pp. 445-459.

Richard, A., Charissoux, C., Calvet, J., Contre, M., and Mardon, J.,''Laser Surface Quenching of Zr Alloys,'' LAMP '87 Proc., May 1987, pp. 425-430.

Richard, A., ''Surface Quenching Treatment of Zircaloy by Laser,'' French Annals of Chemistry, 13, (4,5), 1988, pp. 285-302.

Rickover, H.G., Gieger, L.D., and Lustman, B.,''History of the Development of Zr Alloys for use in Nuclear Reactors,'' NR:D:1975, USERDA, 3/75, pp. 1-81.

Rimini, E., ''Energy Deposition and Heat Flow for Pulsed Laser, Electron and Ion Beam Irradiation,'' Surface Modification and Alloying, J.M. Poate, G. Foti, and D.C. Jackson, (eds.), Plenum Press, N.Y., 1981, pp. 15-50.

Roques, Y., Mankowski, G., Chatainier, G., and Dabosi, F.,''Pitting of Zr-4 in Chloride-Containing Aqueous Methanolic Solutions,'' Corrosion, 40, (10), Oct. 1984, pp. 561-567.

Sabol, G.P., McDonald, S.G., and Airey, G.P., ''Microstructure of the Oxide Films Formed on Zirconium-Based Alloys,'' Zirconium in Nuclear Applications, ASTM STP 533, J.H. Schemel and H.S. Rosenbaum, (eds.), ASTM, 1974, pp. 435-448.

Sabol, G.P., McDonald, S.G., Nurminen, J.I., and Jacobsen, W.A., ''Laser Beam Beta Heat Treatment of Zircaloy,'' Zr in the Nucl. Ind., 7th Intern. Symp., ASTM STP 939, R. Adamson and L. Van Swan, (eds.), ASTM, Phila, PA, 1987, pp. 168-186.

Sato, N., ''Some Concepts of Corrosion Fundamentals,''Corr. Sci., 27, (3), 1987, pp. 421-433.

Sato, N., ''Toward a More Fundamental Understanding of Corrosion Processes,'' Corrosion, 45, (5), May 1989, pp. 354-368.

Schaefer, R.J., and Mehrabian, R., ''Processing / Microstructure Relationships in Surface Melting,'' Mat'l. Res. Soc. Symp. Proc., Elsevier Sci., 13, 1983, pp. 733-744.

Scharfstein, L.R., and Henthorne, M.,''Testing at High Temperature,'' Handbook on Corrosion Testing and Evaluation, W.H. Ailor, (ed.), Electrochemical Soc., Princeton, N.J., 1971, pp. 291-366.

Schemel, J.H.,''ASTM Manual on Zr and Hf'', ASTM STP 639, Phila., PA, 1977, pp. 1-93.

Schreifels, J., Labine, P., Gailey, R., Goewert, S., O'Brien, M., and Jost, S., ''An Auger Depth Profile Study of Corrosion-Inhibiting Films Formed Under Cooling Water Conditions,'' Corrosion, 45, (5), May 1989, pp. 420-428.

Schultze, J.W., ''Electron Transfer Reactions on Passive Film,'' Passivity of Metals, R.P. Frankenthal and J. Kruger, (eds.), Electro. Soc., Princeton, N.J., 1978, pp. 82-101.

Schwabe, K., Hermann, S., and Oelssner, W., ''Influence of Water on Anodic Dissolution and Passivation Metals,'' Passivity of Metals, R.P. Frankenthal and J. Kruger, (eds.), Electro. Soc., Princeton, N.J., 1978, pp. 413-435.

Schwarz, R.B., ''Formation of Amorphous Metallic Alloys by Solid-State Reactions,'' MRS Bulletin, XI, (3), May/June 1986, pp. 55-58.

Schweitzer, P.A., ''Ferric Chloride,'' Corrosion Resistance Tables, P.A. Schweitzer, (ed.), Marcel Dekker, N.Y., 1982, pp. 448-450.

Shubet, G.J., Metallography, Structures, and Phase Diagrams, Metals Handbook, vol. 8, T. Lyman, (ed.), ASM, Metals Park, OH., 1973.

Smeltzer, W.W., ''Oxidation Mechanisms of Metals and Alloys,'' Oxidation of Metals and Assoc. Mass Transport, TMS Conf. Proc., M.A. Dayanda, S.J. Rothman, and W.E. King, (eds.), TMS, Phila., 1986, pp. 109-134.

Smith, S., ''Sn and Fe Segregation Investigation,'' Charles Evans & Assoc. Report, May 13, 1990, pp. 1-16.

Snow, D.B., and Breinan, E.M., ''Microstructural Transformation by the Laserglaze (TM) Process in Zr-4 Sheet,'' Appl. of Lasers in Mat'l Processing, ASM Conf. Proc., Metals Park, OH, 1979, pp. 229-243.

Sprow, E.E., ''The Laser-Welding Spectrum: What it has to Offer You,'' Tool Prod., 54, (3), June 1988, pp. 56-59.

Steen, W.M., and Courtney, C.G., ''Surface Heat Treatment of En8 Steel Using a 2kW Continuous-Wave CO_2 Laser,'' Metals Techn., 6, (12), Dec. 1979, pp. 456-462.

Steen, W.M., ''Surface Coating Using a Laser,'' Int. Conf.

on Advances in Surface Coating Technology, The Welding Institute, Abington Hall, Cambridge, 1978, pp. 175-187.

Stern, M. and Geary, A.L.,''Electrochemical Polarization. A Theoretical Analysis of the Shape of Polarization Curves,'' J. Electro. Soc., 104, (1), Jan. 1957, pp. 56-63.

Subramanian, R., Sircar, S., and Mazumder, J.,''Laser Cladding of Zr on Mg for Improved Corrosion Properties,'' Environmental Degradation of Ion and Laser Beam Treated Surfaces, TMS Conf. Proc., G.S. Was and K.S. Grabowski, (eds.), TMS, Phila., 1989, pp. 59-70.

Teramoto, T., Takeuchi, S., Akai, M., and Nariai, H., ''Irradiation Test of Stainless Steel by High Power CO_2 Laser,'' J. Nucl. Sci. and Tech., 26, (6), 1989, pp. 625-635.

Tiller, W.A., Jackson, R.A., Rutter, J.W., and Chalmers, B.,''The Redistribution of Solute Atoms During the Solidification of Metals,''ACTA Met., 1, July 1953, pp. 428-437.

Trowse, F.W., Sumerling, R., and Garlick, A.,''Nodular Corrosion of Zircaloy-2 and Some Other Zirconium Alloys in Steam Generating Heavy Water Reactors and Related Environments,'' Zirconium in the Nuclear Industry, ASTM STP 633, A.L. Lowe, Jr. and G.W. Parry, (eds.), ASTM, 1977, pp. 236-257.

Tsubaki, T., and Boley, B.A., ''One-Dimensional Solidification of Binary Mixtures,'' Mech. Res. Comm., 4, (2), 1977, pp. 115-122.

Turn, J.C., Jr., and Latanision, R.M., ''The Influence of Structure on the Corrosion of Glassy Cu-Zr Alloys,'' Corrosion, 39, (7), July 1983, pp. 271-279.

Ursu, I., Mihailescu, I.N., Nistor, L.C., Popescu, M., Teodorescu, V.S., Prokhorov, A.M., Ralchenko, V.G., and Konov, V.I., ''Mechanism of Surface Compound Formation by CW CO_2 Laser Irradiation of Zr Samples in Air,''J. Appl. Phys., 59, (2), Jan. 1986, pp. 668-670.

Vaccari, J.A., ''Welding Thick Stainless Steel,'' American Machinist, 133, Jan. 1989, pp. 62-63.

Vandenberg, J.M., and Draper, C.W., ''An X-Ray Diffraction Study on the Microstructure of Laser Surface Melted Cu-Al-Fe Alloys,'' Mat'ls. Lett., 2, (5A), June 1984, pp. 386-392.

Vander Sande, J.B., and Bement, A.L., ''An Investigation of Second Phase Particles in Zr-4 Alloys,'' J. Nucl. Mat'l., 52, 1974, pp. 115-118.

Vijayakar, S.J., Banerjee, S., and Goswami, G.L., ''A Comparsion of Microstructures of Gas Tungsten Arc and Laser Welds in Zr-2,'' Symp. of Recent Developments in Welding Met. Proc., 1985, pp. II/6/1-II/6/18.

Von Allmen, M., ''Coupling of Beam Energy to Solids,'' Laser and Electron Beam Processing of Materials, Conf. Proc., C.W. White and P.S. Peercy, (eds.), Academic Press, N.Y., 1980, pp. 6-19.

Von Allmen, M., ''Laser-Generated Glassy Phases,''Mat. Res. Soc. Symp. Proc., Elsevier Sci., 13, 1983, pp. 691-702.

Wanklyn, J.N.,''Recent Studies of the Growth and Breakdown of Oxide Films on Zr and Its Alloys,'' ASTM STP 368, Phila., PA, 1964, pp. 58-75.

Wanklyn, J.N. and Jones, P.J.,''The Aqueous Corrosion of Reactor Materials,'' J. Nucl. Mat., 6, (3), 1962, pp. 291-329.

Webster, R.T., and Yau, T.L., ''Zr in Sulphuric Acid Applications,'' NACE Conf. Proc., T.F. Degnan, (ed.), NACE, Houston, TX, 1985, pp. 69-74.

White, C.W., and Aziz, H.J., ''Energy Deposition, Heat Flow, and Rapid Solidification During Pulsed-Laser- and Electron-Beam Irradiation,''ASM Materials Sci. Sem., L.E. Rehn, S.T. Picraux, and H. Wiedersich, (eds.), ASM, Metals Park, OH, 1987, pp. 19-50.

Winburn, D.C., What Every Engineer Should Know About Lasers, Marcel Dekker, N.Y., 1987, pp. 98-108.

Woo, O.T., and Tangri, K., ''Transformation Characteristics of Rapidly Heated and Quenched Zr-4 - Oxygen Alloys,'' J. Nucl. Mat'l., 79, 1979, pp. 82-94.

Yau, T.L., and Maguire, M.A., ''Electrochemical Protection of Zr Against SCC by Oxidizing HCl Solutions,'' Corrosion, 41, (7), July 1985, pp. 397-405.

Yau, T.L., and Maguire, M.A., ''Electrochemical Protection of Zr in Oxidizing HCl Acid Solutions,'' Corrosion, 40, (6), June 1984, pp. 289-296.

Yau, T.L., and Maguire, M., ''Control of Localized Corrosion of Zr in Oxidizing Chloride Media,'' Outlook, 9,

(2), Teledyne Wah Chang, Albany, OR, 1988, pp. 3-5.

Yau, T.L., and Webster, R.T., ''The Effects of Iron on the Corrosion Resistance of Zr,''Corrosion, 39, (6), June 1983, pp. 218-226.

Yau, T.L., ''The Performance of Zr Alloys in Sulfide Solutions,''Corrosion, 38, (12), Dec. 1982, pp. 615-620.

Yau, T.L., ''Zircadyne 702: One of the Few Metals that Resists Attack in Formic Acid,'' Outlook, 9, (3), Teledyne Wah Chang, Albany, 1988, pp. 6-8.

Yau, T.L., ''Zirconium,'' Corrosion and Corrosion Protection Handbook, P.A. Schweitzer, (ed.), Marcel Dekker, N.Y., 1988, pp. 231-278.

Zaplatynsky, I., ''Performance of Laser-Glazed Zirconia Thermal Barrier Coatings in Cyclic Oxidation and Corrosion Burner Rig Tests,'' Thin Solid Films, 95, 1982, pp. 275-284.

Zaplatynsky, I., ''The Effect of Laser Glazing on Life of ZrO_2 TBC's in Cyclic Burner Rig Tests,'' NASA Tech. Mem., Rpt. E-3026, August 1986, pp. 1-10.

Zielinski, P.G., Ostatek, J., Kijek, M., and Matyja, H., ''Formation and Stability of Metallic Glasses Containing Zirconium,'' Rapidly Quenched Metals III, 3rd Intern. Conf. on Rapidly Quenched Metals, B. Cantor, (ed.), Brighton, England, July 1978, pp. 337-346.

VIII. APPENDICES

APPENDIX A.
Weight Gains for Autoclave Tests (2-week periods).

coupon*	wt0	wt1	wt2	wt3	wt4	wt5	wt6	wt7	t	w	l	area (dm2)
3-3-1	20.4446	20.4685	20.4723	20.4762	20.4794	20.4858	20.4906	20.4963	3.4200	25.7900	35.4300	0.2246
3-3-3	20.4821	20.5065	20.5104	20.5143	20.5171	20.5250	20.5326	20.5413	3.4200	25.8100	35.4200	0.2247
3-3-4	20.0985	20.1202	20.1240	20.1282	20.1309	20.1422	20.1544	20.1685	3.4200	25.8500	35.4600	0.2253
3-3-6	20.4091	20.4319	20.4370	20.4408	20.4439	20.4549	20.4671	20.4807	3.4200	25.4300	35.4900	0.2222
3-3-7	20.1903	20.2135	20.2188	20.2228	20.2266	20.2358	20.2448	20.2553	3.4200	25.7000	35.4700	0.2242
3-3-8	20.3934	20.4141	20.4183	20.4218	20.4251	20.4358	20.4468	20.4574	3.4200	25.6200	35.4900	0.2237
3-3-9	20.4625	20.4862	20.4912	20.4950	20.4979	20.5047	20.5115	20.5191	3.4200	26.0300	35.4100	0.2264
3-3-10	20.2149	20.2409	20.2472	20.2519	20.2553	20.2664			3.4200	25.9800	35.3700	0.2257
3-7-1	20.8260	20.8384	20.8424	20.8484	20.8521	20.8589	20.8635	20.8687	3.7000	25.3500	36.4500	0.2305
3-7-2	20.7757	20.7868	20.7906	20.7973	20.8016	20.8090	20.8131	20.8188	3.7000	25.3900	36.4200	0.2307
3-7-3	20.8716	20.8832	20.8885	20.8961	20.9019	20.9091	20.9131	20.9174	3.7000	25.3900	36.3000	0.2300
3-7-4	20.7350	20.7463	20.7501	20.7566	20.7609	20.7669	20.7702	20.7747	3.7000	25.3700	36.3200	0.2299
3-c-2	22.6065	22.6135	22.6157	22.6197	22.6206	22.6258	22.6267	22.6277	3.5400	25.9400	38.5800	0.2458
3-c-4	22.5994	22.6067	22.6093	22.6128	22.6140	22.6191	22.6200	22.6211	3.5400	25.8600	38.6600	0.2456
3-c-5	22.3472	22.3548	22.3568	22.3608	22.3620	22.3665	22.3674	22.3686	3.5400	25.9100	38.6400	0.2459
1-3-1	11.1910	11.2118	11.2160	11.2092	11.2221	11.2305	11.2366	11.2436	1.9000	25.8200	36.5000	0.2122
1-3-2	11.2280	11.2486	11.2518	11.2549	11.2574	11.2632	11.2673	11.2732	1.9000	25.8000	36.4000	0.2115
1-3-3	11.2181	11.2378	11.2422	11.2453	11.2480	11.2539	11.2580	11.2631	1.9000	25.9700	36.3800	0.2127
1-3-4	11.2056	11.2235	11.2252	11.2304	11.2328	11.2397	11.2450	11.2518	1.9000	25.8500	36.3800	0.2117
1-3-5	11.2344	11.2533	11.2567	11.2597	11.2626	11.2689			1.9000	25.8400	36.3500	0.2115
1-7-1	10.8832	10.8934	10.8985	10.9142	10.9104	10.9191	10.9248	10.9306	1.9300	25.6000	34.2100	0.1982
1-7-2	10.8492	10.8593	10.8647	10.8703	10.8760	10.8819	10.8855	10.8890	1.9300	25.5900	34.5300	0.1999
1-7-3	10.7793	10.7880	10.7919	10.7966	10.8021	10.8073	10.8104	10.8137	1.9300	25.6000	34.4700	0.1997
1-7-4	10.8220	10.8315	10.8366	10.8422	10.8477	10.8536	10.8569	10.8607	1.9300	25.6000	34.5200	0.1999
1-c-1	11.8594	11.8640	11.8655	11.8692	11.8705	11.8728	11.8738	11.8755	1.8800	25.8000	38.5900	0.2233
1-c-2	11.9393	11.9449	11.9474	11.9504	11.9513	11.9533	11.9544	11.9562	1.8800	25.8100	38.6000	0.2235

* The coupons were coded such that the first character of the coupon ID signified the ingot of Zr-4, the second character designated the laser power (kw) applied ("C" indicates control, non-LSM). The third character is the individual coupon number. Thus, the ID "1-3-2" signifies ingot 218208, 3 kw power setting (energy density of 4 kJ/cm2), and coupon number 2 .

1-X-Y = ingot 218208
3-a-b = ingot 226220

APPENDIX B.
Corrosion Rates for Autoclave Tests (2-week periods).

COUPON	mg/dm2 wt1-wt0		mg/dm2 wt2-wt0		mg/dm2 wt3-wt0		mg/dm2 wt4-wt0		mg/dm2 wt5-wt0		mg/dm2 wt6-wt0		mg/dm2 wt7-wt0	
3-3-1	106.4008	AVERAGE	123.3181		140.6805		154.9267		183.4189		204.7881		230.1640	
3-3-3	108.5799	STD.DEV.	125.9349		143.2898		155.7498		190.9048		224.7247		263.4397	
3-3-4	96.3313		113.2004		131.8452		143.8311		193.9944		248.1530		310.7462	
3-3-6	102.6235		125.5787		142.6826		156.6358		206.1471		261.0597		322.2737	
3-3-7	103.4993		127.1436		144.9883		161.9407		202.9836		243.1342		289.9765	
3-3-8	92.5553		111.3347		126.9841		141.7393		189.5819		238.7659		286.1614	
3-3-9	104.6961	103.7325	126.7839	124.5469	143.5706	142.2428	156.3815	158.2709	186.4209	197.6980	216.4603	233.8694	250.0338	278.9708
3-3-10	115.1737	7.0045	143.0812	9.7327	163.9011	10.8434	178.9823	11.4342	228.1326	14.5523		19.5174		32.9604
3-7-1	53.7883		71.1393		97.1659		113.2156		142.7124		162.6662		185.2225	
3-7-2	48.1186		64.5916		93.6361		112.2767		144.3557		162.1292		186.8388	
3-7-3	50.4387	50.3723	73.4840	68.7212	106.5301	97.8176	131.7494	117.4702	163.0562	147.2143	180.4489	164.5822	199.1460	185.9656
3-7-4	49.1436	2.4673	65.6898	4.2777	93.9383	6.0240	112.6389	9.5274	138.7329	10.8219	153.0846	11.4548	172.6550	10.8353
3-c-2	28.4746		37.4237		53.6949		57.3560		78.5085		82.1695		86.2373	
3-c-4	29.7195	29.6989	40.3046	38.9211	54.5537	54.5160	59.4391	58.9913	80.2020	79.0623	83.8661	82.7238	88.3444	87.1990
3-c-5	30.9026	1.2141	39.0349	1.4438	55.2994	0.8029	60.1788	1.4637	78.4764	0.9872	82.1359	0.9894	87.0153	1.0655
1-3-1	98.0357		117.8314		85.7812		146.5822		186.1736		214.9244		247.9172	
1-3-2	97.4180		112.5508		127.2108		139.0334		166.4617		185.8508		213.7520	
1-3-3	92.6402		113.3314		127.9093		140.6062		168.3512		187.6316		211.6146	
1-3-4	84.5408	92.4002	92.5699	108.3453	117.1292	115.5317	128.4643	137.6053	161.0527	169.0336	186.0843	193.6228	218.2004	222.8711
1-3-5	89.3664	5.6562	105.4428	9.8720	119.6280	17.2774	133.3403	6.9530	163.1291	9.9927		14.2231		16.9213
1-7-1	51.4523		77.1785		156.3746		137.2061		181.0919		209.8447		239.1019	
1-7-2	50.5175		77.5268		105.5365		134.0463		183.5565		181.5628		199.0688	
1-7-3	43.5711	48.2633	63.1030	72.7068	86.6415	112.3948	114.1865	128.4930	140.2290	160.7295	155.7543	180.4268	172.2813	201.0004
1-7-4	47.5122	3.5511	73.0187	6.7220	101.0259	30.4070	128.5330	10.1888	158.0405	16.8337	174.5448	22.4353	193.5496	27.9031
1-c-1	20.5969	22.8280	27.3132	31.7797	43.8803	46.7755	49.7011	51.6996	59.9995	61.3237	64.4771	66.0236	72.0890	73.8570
1-c-2	25.0591	3.1553	36.2463	6.3166	49.6708	4.0945	53.6982	2.8263	62.6478	1.8726	67.5702	2.1871	75.6249	2.5003

APPENDIX C. Weight Loss from 1st Immersion Run.

		WT(0)	WT(7)	WT(8)	WT(9)	WT(10)	WT(11)	MPY
	HOURS	0.0000	480.0000	484.0000	554.0000	628.0000	794.0000	
377-5-cr	A1	2.6345				2.6344		A1 0.0860
	A2	2.6490					2.6483	A2 0.4746
	A3	2.5851					2.5847	A3 0.2712
	A5	2.5987					2.5984	A5 0.2034
377-5-HR	B2	2.2158					2.2140	B2 1.2203
	B3	2.3002					2.2990	B3 0.8136
	B4	2.1643					2.1635	B4 0.5424
	B5	2.3212					2.3194	B5 1.2203
267-5	C2	2.3373					2.3367	C2 0.4068
	C3	2.3415					2.3412	C3 0.2034
	C4	2.3330					2.3323	C4 0.4746
	C5	2.2934					2.2926	C5 0.5424
835-5-.071	D1	1.3333				1.3325		D1 0.7458
	D2	1.2854					1.2841	D2 0.8814
	D4	1.3414					1.3403	D4 0.7458
	D5	1.2864					1.2855	D5 0.6102
170-5	E1	2.4065				2.4061		E1 0.3440
	E2	2.3318					2.3310	E2 0.4068
	E3	2.3926					2.3922	E3 0.2712
	E4	2.3754					2.3751	E4 0.2034
377-7-cr	F1	2.5420				2.5418		F1 0.1720
	F2	2.3845					2.3839	F2 0.4068
	F4	2.5790					2.5780	F4 0.6780
	F5	2.5227					2.5221	F5 0.4189
377-7-HR	G2	2.2624					2.2619	G2 0.3390
	G3	2.2681					2.2677	G3 0.2712
	G4	2.2957					2.2953	G4 0.2712
	G5	2.2766					2.2760	G5 0.4068
267-7	H1	2.2879				2.2870		H1 0.7739
	H3	2.2305					2.2298	H3 0.4746
	H4	2.2764					2.2757	H4 0.4746
	H5	2.2941					2.2938	H5 0.2034
835-7-.071	I2	1.3284					1.3279	I2 0.3390
	I3	1.3233					1.3228	I3 0.3390
	I4	1.3162					1.3158	I4 0.2712
	I5	1.3221					1.3217	I5 0.2712
170-7	J1	2.4141				2.4137		J1 0.3440
	J3	2.3797					2.3795	J3 0.1356
	J4	2.3868					2.3861	J4 0.4746
	J5	2.3889					2.3887	J5 0.1356
377-3-CR	K2	2.6280		2.6278				K2 0.2034
	K3	2.5665					2.5662	K3 0.2034
	K4	2.5884					2.5881	K4 0.2034
	K5	2.5739					2.5736	K5 0.2034
377-3-HR	L1	2.8026		2.6278				L1 0.2603
	L2	2.4488		2.4463				L2 0.2595
	L3	2.7202		2.7200				L3 0.2605
	L4	2.4271		2.4268				L4 0.2600
267-3	M1	2.1716				2.1712		M1 0.3440
	M3	2.1554					2.1550	M3 0.2712

APPENDIX C (continued)

	M4	2.2917			2.2910	M4 0.4746
	M5	2.1769			2.1766	M5 0.2034
835-3-.071	N1	1.3986		1.3984		N1 0.1720
	N2	1.3618			1.3611	N2 0.4746
	N3	1.3573			1.3570	N3 0.2034
	N4	1.3654			1.3653	N4 0.0678
170-3	O2	2.3976			2.3974	O2 0.1356
	O3	2.4162			2.4153	O3 0.0678
	O4	2.4023			2.4022	O4 0.0678
	O5	2.4106			2.4105	O5 0.0001
	P1	2.6359		2.6359		P1 0.0000
	P2	2.1848			2.1848	P2 0.0000
	P3	2.0493			2.0493	P3 0.0000
	P4	2.7740	2.7442			P433.1436
	Q1	1.2150	1.2100			Q1 5.5610
	Q2	1.2012			1.1996	Q2 1.0847
	Q3	1.2004			1.1977	Q3 1.8305
	Q4	1.2016			1.1998	Q4 1.2203
	Q5	1.2031			1.1970	Q5 4.1356
	R1	2.2350		2.2339		R1 0.9459
	R2	2.2435			2.2425	R2 0.6780
	R3	2.1965			2.1954	R3 0.7458
	R4	2.2328			2.2320	R4 0.5424
	R5	2.1476			2.1473	R5 0.2034
	S1	2.1110		2.1106		S1 0.3440
	S2	2.1529			2.1518	S2 0.7458
	S3	2.1375			2.1367	S3 0.5424
	S4	2.1511			2.1507	S4 0.2712
	S5	2.1515			2.1502	S5 0.8814

mpy = 534 * wtloss *1000 / 6.4* 2.54^(-2) * hours

APPENDIX D. Weight Loss from 2nd Immersion Run.

date	01/27/89	03/06/89	01/31/89	02/05/89	02/13/89	02/20/89	02/27/89	03/06/89	03/13/89
comment	W/O CT	W/O CT	wt w/ct	5.0000	13.0000	20.0000	27.0000	34.0000	41.0000
sample	gram								
A6	2.6292		2.6416	2.6415	2.6413	2.6410	2.6407	2.6406	2.6406
A7	2.6037		2.6229	2.6229	2.6228	2.6230	2.6225	2.6224	2.6226
A8			2.3563					2.3555	
A10	2.6036	2.6026	2.6206	2.6208	2.6204	2.6203	2.6200	2.6198	
B6	2.3486		2.3635	2.3631	2.3628	2.3627	2.3624	2.3622	2.3619
B7	2.3570		2.3733	2.3730	2.3724	2.3722	2.3719	2.3717	2.3714
B8	2.3614		2.3781	2.3776	2.3773	2.3770	2.3766	2.3767	2.3765
B10	2.3613	2.3599	2.3747	2.3743	2.3741	2.3741	2.3736	2.3735	
C6	2.3054		2.3212	2.3211	2.3207	2.3206	2.3201	2.3199	2.3197
C8	2.3224		2.3401	2.3399	2.3396	2.3393	2.3390	2.3388	2.3385
C9	2.3273		2.3475	2.3472	2.3470	2.3468	2.3466	2.3465	2.3462
C10	2.3395	2.3376	2.3562	2.3558	2.3554	2.3553	2.3549	2.3546	
D7	1.2865		1.3047	1.3044	1.3041	1.3041	1.3040	1.3038	1.3036
D8	1.3443		1.3602	1.3596	1.3592	1.3591	1.3588	1.3587	1.3582
D9	1.2920		1.3051	1.3047	1.3045	1.3042	1.3041	1.3040	1.3038
D10	1.3482	1.3467	1.3576	1.3572	1.3568	1.3566	1.3562	1.3561	
E6	2.3396		2.3584	2.3581	2.3582	2.3582	2.3579	2.3580	2.3580
E7	2.4477		2.4643	2.4643	2.4644	2.4639	2.4637	2.4636	2.4634
E9	2.4558		2.4751	2.4749	2.4749	2.4746	2.4742	2.4741	2.4738
E10	2.4237	2.4234	2.4412	2.4411	2.4413	2.4408	2.4407	2.4406	
F6	2.5743		2.5923	2.5922	2.5920	2.5919	2.5915	2.5913	2.5907
F7	2.5256		2.5434	2.5433	2.5431	2.5429	2.5429	2.5427	2.5423
F8	2.5849		2.6060	2.6057	2.6052	2.6051	2.6049	2.6048	2.6043
F10	2.5761	2.5751	2.5933	2.5929	2.5929	2.5929	2.5927	2.5925	
G6	2.2879		2.3088	2.3084	2.3082	2.3082	2.3081	2.3079	2.3079
G7	2.2882		2.3089	2.3085	2.3085	2.3085	2.3083	2.3083	2.3082
G8	2.2775		2.2969	2.2965	2.2966	2.2965	2.2962	2.2962	2.2962
G9	2.2850		2.3087	2.3085	2.3082	2.3081	2.3080	2.3078	2.3079
G10	2.2574	2.2566	2.2751	2.2747	2.2747	2.2747	2.2743	2.2742	
H6	2.3168		2.3354	2.3354	2.3350	2.3350	2.3348	2.3345	2.3344
H7	2.3060		2.3218	2.3215	2.3214	2.3211	2.3209	2.3207	2.3207
H8	2.3279		2.3462	2.3459	2.3456	2.3456	2.3454	2.3454	2.3452
H10	2.3414	2.3404	2.3602	2.3600	2.3596	2.3595	2.3594	2.3591	
I6	1.3120		1.3298	1.3296	1.3293	1.3294	1.3294	1.3291	1.3287
I7	1.3186		1.3383	1.3381	1.3380	1.3379	1.3376	1.3375	1.3374
I9	1.3201		1.3350	1.3349	1.3345	1.3346	1.3345	1.3343	1.3344
I10	1.3122	1.3114	1.3279	1.3276	1.3275	1.3271	1.3270	1.3269	
J7	2.4032		2.4183	2.4181	2.4182	2.4180	2.4180	2.4181	2.4178
J8	2.4144		2.4316	2.4313	2.4312	2.4311	2.4312	2.4311	2.4309
J9	2.4157		2.4314	2.4313	2.4310	2.4311	2.4312	2.4312	2.4309
J10	2.4261	2.4252	2.4371	2.4371	2.4368	2.4367	2.4365	2.4365	
K6	2.5973		2.6175	2.6172	2.6172	2.6172	2.6172	2.6171	2.6168

APPENDIX D (continued)

K7	2.5829		2.6022	2.6020	2.6020	2.6018	2.6017	2.6018	2.6016
K8	2.6104		2.6298	2.6297	2.6296	2.6296	2.6295	2.6297	2.6295
K9	2.5321		2.5478	2.5475	2.5474	2.5474	2.5473	2.5473	2.5473
K10	2.5548	2.5546	2.5680	2.5675	2.5677	2.5674	2.5674	2.5678	
L1			2.5480					2.5475	
L2			2.4315					2.4309	
L3			2.3149					2.3143	
L4			2.5433					2.5426	
M6	2.3020		2.3187	2.3182	2.3182	2.3179	2.3176	2.3177	2.3178
M7	2.2057		2.2205	2.2201	2.2202	2.2198	2.2196	2.2196	2.2197
M8	2.2993		2.3148	2.3146	2.3145	2.3141	2.3142	2.3142	2.3142
M9	2.2088		2.2255	2.2254	2.2254	2.2250	2.2248	2.2249	2.2250
N6	1.3641		1.3755	1.3755	1.3756	1.3754	1.3752	1.3753	1.3755
N7	1.3493		1.3638	1.3636	1.3635	1.3634	1.3634	1.3633	1.3632
N8	1.3430		1.3591	1.3590	1.3588	1.3591	1.3588	1.3588	1.3587
N9	1.3635		1.3755	1.3751	1.3750	1.3753	1.3751	1.3749	1.3748
O6	2.3962		2.4105	2.4104	2.4105	2.4107	2.4103	2.4101	2.4103
O8	2.3886		2.4069	2.4066	2.4066	2.4065	2.4063	2.4062	2.4061
O9	2.3849		2.4036	2.4034	2.4034	2.4035	2.4033	2.4032	2.4032
O10	2.3817	2.3812	2.3989	2.3986	2.3984	2.3987	2.3985	2.3983	
P6	2.1458		2.1595	2.1594	2.1597	2.1596	2.1594	2.1593	2.1596
P7	2.1420		2.1576	2.1573	2.1573	2.1575	2.1574	2.1572	2.1575
P8	2.1433		2.1621	2.1619	2.1620	2.1619	2.1622	2.1619	2.1621
P9	2.1380		2.1559	2.1556	2.1556	2.1556	2.1558	2.1555	2.1558
Q6	1.2030		1.2143	1.2130	1.2120	1.2116	1.2109	1.2101	1.2098
Q7	1.2034		1.2141	1.2131	1.2126	1.2125	1.2122	1.2116	1.2117
Q8	1.2060		1.2206	1.2196	1.2190	1.2086	1.2183	1.2177	1.2177
R6	2.1741		2.1887	2.1875	2.1865	2.1857	2.1852	2.1844	2.1841
R7	2.2402		2.2468	2.2445	2.2418	2.2400	2.2383	2.2366	2.2360
R8	2.2164		2.2307	2.2282	2.2259	2.2239	2.2222	2.2209	2.2204
S6	2.1471		2.1588	2.1563	2.1548	2.1542	2.1537	2.1528	2.1528
S7	2.1470		2.1603	2.1576	2.1561	2.1555	2.1549	2.1542	2.1541
S8	2.1473		2.1643	2.1612	2.1597	2.1592	2.1583	2.1576	2.1575

APPENDIX E. 1st Immersion Run Corrosion Rate.

	(mpy)
A1	0.0860
A2	0.4746
A3	0.2712
A5	0.2034
B2	1.2203
B3	0.8136
B4	0.5424
B5	1.2203
C2	0.4068
C3	0.2034
C4	0.4746
C5	0.5424
D1	0.7458
D2	0.8814
D4	0.7458
D5	0.6102
E1	0.3440
E2	0.4068
E3	0.2712
E4	0.2034
F1	0.1720
F2	0.4068
F4	0.6780
F5	0.4189
G2	0.3390
G3	0.2712
G4	0.2712
G5	0.4068
H1	0.7739
H3	0.4746
H4	0.4746
H5	0.2034
I2	0.3390
I3	0.3390
I4	0.2712
I5	0.2712
J1	0.3440
J3	0.1356
J4	0.4746
J5	0.1356
K2	0.2034
K3	0.2034
K4	0.2034
K5	0.2034
L1	0.26
L2	0.26
L3	0.261
L4	0.259
M1	0.3440
M3	0.2712
M4	0.4746
M5	0.2034
N1	0.1720
N2	0.4746
N3	0.2034
N4	0.0378
O2	0.1356
O3	0.0678
O4	0.0678
O5	0.0001
P1	0.0000
P2	0.0000
P3	0.0000
P4	33.1436
Q1	5.5610
Q2	1.0847
Q3	1.8305
Q4	1.2203
Q5	4.1356
R1	0.9459
R2	0.6780
R3	0.7458
R4	0.5424
R5	0.2034
S1	0.3440
S2	0.7458
S3	0.5424
S4	0.2712
S5	0.8814

APPENDIX F. 2nd Immersion Run Corrosion Rates (mpy).

date	5 days		13 days		20 days		27 days		34 days	
sample	MPY	avg stdev	MPY	avg stdev	MPY	avg stdev	MPY	avg stdev	MPY	avg stdev
A6	0.4486		0.5176		0.6729		0.7476		0.6597	
A7	0.0000		0.1725		-0.1121		0.3323		0.3298	
A8									0.5060	
		-0.1495		0.3451		0.2991		0.5261		0.5058
A10	-0.8972	0.6852	0.3451	0.1725	0.3364	0.3938	0.4984	0.2091	0.5278	0.1660
B6	1.7944		1.2077		0.8972		0.9138		0.8576	
B7	1.3458		1.5528		1.2336		1.1630		1.0555	
B8	2.2429		1.3803		1.2336		1.2461		0.9236	
		1.7944		1.2940		1.0093		1.0592		0.9071
B10	1.7944	0.3663	1.0352	0.2227	0.6729	0.2747	0.9138	0.1713	0.7916	0.1127
C6	0.4486		0.8627		0.6729		0.9138		0.8576	
C8	0.8972		0.8627		0.8972		0.9138		0.8576	
C9	1.3458	1.1215	0.8627	0.9921	0.7850	0.8411	0.7476	0.9138	0.6597	0.8576
C10	1.7944	0.5791	1.3803	0.2588	1.0093	0.1448	1.0799	0.1357	1.0555	0.1616
D7	1.3458		1.0352		0.6729		0.5815		0.5937	
D8	2.6915		1.7253		1.2336		1.1630		0.9895	
D9	1.7944	1.9065	1.0352	1.2940	1.0093	1.0093	0.8307	0.9346	0.7257	0.8246
D10	1.7944	0.5645	1.3803	0.3304	1.1215	0.2423	1.1630	0.2827	0.9895	0.1979
E6	1.3458		0.3451		0.2243		0.4154		0.2639	
E7	0.0000		-0.1725		0.4486		0.4984		0.4618	
E9	0.8972	0.6729	0.3451	0.0863	0.5607	0.4206	0.7476	0.5192	0.6597	0.4123
E10	0.4486	0.5791	-0.1725	0.2988	0.4486	0.1411	0.4154	0.1573	0.2639	0.1895
F6	0.4486		0.5176		0.4486		0.6646		0.6597	
F7	0.4486		0.5176		0.5607		0.4154		0.4618	
F8	1.3458		1.3803		1.0093		0.9138		0.7916	
		0.6729		0.5607		0.6168		0.6023		0.5442
F10	1.7944	0.6729	0.6901	0.4107	0.4486	0.2670	0.4984	0.2198	0.5278	0.1463
G6	1.7944		1.0352		0.6729		0.5815		0.5937	
G7	1.7944		0.6901		0.4486		0.4984		0.3958	
G8	1.7944		0.1725		0.4486		0.5815		0.4618	
G9	0.8972	1.6149	0.8627	0.6901	0.6729	0.5383	0.5815	0.5815	0.5937	0.5278
G10	1.7944	0.4012	0.6901	0.3228	0.4486	0.1229	0.6646	0.0587	0.5937	0.0933
H6	0.0000		0.6901		0.4486		0.4984		0.5937	
H7	1.3458		0.6901		0.7850		0.7476		0.7257	
H8	1.3458		1.0352		0.6729		0.6646		0.5278	
		1.1215		0.7764		0.5888		0.6438		0.6102
H10	0.8972	0.6344	1.0352	0.1992	0.7850	0.1586	0.6646	0.1045	0.7257	0.0990
I6	0.8972		0.8627		0.4486		0.3323		0.4618	
I7	0.8972		0.5176		0.4486		0.5815		0.5278	
I9	0.4486	0.8972	0.8627	0.7333	0.4486	0.5607	0.4154	0.5192	0.4618	0.5278
I10	1.3458	0.3663	0.6901	0.1652	0.8972	0.2243	0.7476	0.1842	0.6597	0.0933

APPENDIX F (continued)

J7	0.8972		0.1725		0.3364		0.2492		0.1319	
J8	1.3458		0.6901		0.5607		0.3323		0.3298	
J9	0.4486	0.6729	0.6901	0.5176	0.3364	0.4206	0.1661	0.3115	0.1319	0.2474
J10	0.0000	0.5791	0.5176	0.2440	0.4486	0.1074	0.4984	0.1419	0.3958	0.1360
K6	1.3458		0.5176		0.3364		0.2492		0.2639	
K7	0.8972		0.3451		0.4486		0.4154		0.2639	
K8	0.4486		0.3451		0.2243		0.2492		0.0660	
K9	1.3458	1.2560	0.6901	0.4831	0.4486	0.4262	0.4154	0.3655	0.3298	0.2375
K10		0.6654		0.1444		0.1663		0.1115		0.1000
L6									0.300	
L7									0.35	
L8									0.400	0.375
L9									0.45	0.064
M6	2.2429		0.8627		0.8972		0.9138		0.6597	
M7	1.7944		0.5176		0.7850		0.7476		0.5937	
M8	0.8972		0.5176		0.7850		0.4984		0.3958	
M9	0.4486	1.3458	0.1725	0.5521	0.5607	0.7626	0.5815	0.7476	0.3958	0.5409
		0.7093		0.2559		0.1229		0.2118		0.1352
N6	0.0000		-0.1725		0.1121		0.2492		0.1319	
N7	0.8972		0.5176		0.4486		0.3323		0.3298	
N8	0.4486		0.5176		0.0000		0.2492		0.1979	
N9	1.7944	0.8075	0.8627	0.4141	0.2243	0.2243	0.3323	0.2991	0.3958	0.2639
N10		0.6654		0.3780		0.1773		0.0455		0.1043
O6	0.4486		0.0000		-0.2243		0.1661		0.2639	
O7										
O8	1.3458		0.5176		0.4486		0.4984		0.4618	
O9	0.8972	0.9869	0.3451	0.4486	0.1121	0.1794	0.2492	0.3323	0.2639	0.3826
O10	1.3458	0.3753	0.8627	0.3134	0.2243	0.2582	0.3323	0.1313	0.3958	0.1180
P6	0.4486		-0.3451		-0.1121		0.0831		0.1319	
P7	1.3458		0.5176		0.1121		0.1661		0.2639	
P8	0.8972	1.0766	0.1725	0.3451	0.2243	0.1570	-0.0831	0.1163	0.1319	0.2375
P9	1.3458	0.4012	0.5176	0.4565	0.3364	0.1701	0.0831	0.1509	0.2639	0.1104
Q6	5.8317		3.9683		3.0280		2.8244		2.7707	
Q7	4.4859	3.4093	2.5880	2.0014	1.7944	3.7681	1.5784	1.2627	1.6492	1.3458
Q8	4.4859	2.1653	2.7605	1.6074	13.4577	5.5377	1.9107	1.2411	1.9131	1.1279
R6	5.3831		3.7958		3.3644		2.9075		2.8367	
R7	10.3175	7.1774	8.6267	5.2105	7.6260	6.7737	7.0611	4.1038	6.7288	3.9186
R8	11.2147	3.3117	8.2816	2.9993	7.6260	4.5427	7.0611	2.7436	6.4650	2.4862
S6	11.2147		6.9014		5.1588		4.2367		3.9581	
S7	12.1119	11.7530	7.2464	7.7985	5.3831	6.3027	4.4859	5.5658	4.0241	5.1192
S8	13.9063	1.3606	7.9366	0.7155	5.7195	1.2244	4.9843	1.3913	4.4199	1.3637

APPENDIX G.

Pit Depth Evaluation (micron) (#/cm²)

sample	10	20	30	40	50	60	70-150	> 150
377-10	5	1	1		3	2		1
377H-10	1	3		1	2			
267-10	3	2			1		1	1
835-10	2		3	2	2		1	1
170-10	1	6						
377-7				1				
377H-7	4	3	1					
267-7		2						
835-7		2						
170-7	3	5	1					
377-4	1							
377H-4	n/a							
267-4	1							
835-4	1	2						
170-4	1	1						
377-c	0							
835-0		1	5	7	5	1		1
170-0	5	16	20	13	6	5	1	1
267-0	5	5	2	1	3	1		

APPENDIX H.

Electrochemical Values (from Appendix M).

sample	Steady-State Icorr	Steady-State Ecorr	Initial Epit	Ex	Ipass	Epass
377-10	7.0	.21		.04		
377H-10	4.5	.15		-.04		
267-10	52	.04		-.02		
835-10	5.8	.12	(.36)	.01		
170-10	1.8	.14		-.09		
377-7	14.0	.16		.05		
377H-7	3.0	.14		0.0		
267-7	3.7	.02		-.10		
835-7	2.5	.12		.04		
170-7	3.5	.11		-.05		
377-4	2.5	.13		0.0		
377H-4	12.0	.15		-.14		
267-4	40	.12		0.0		
835-4	2.4	.14	(.18)	-.05		
170-4	100	.13		.08		
170-0	(2.2)	(.07)		(-.11)		
835-0	32	.12		.08		

zzz-y-x-b, zzz - ingot, y - enegry density,
x - # of polishings, b - back surface of LSM coupon

835-10-1	4.1	.28	.44	.08	100	.01
835-10-2	4.3	.01	.15	.06	100	0.0
835-10-3	(4.5)	.11	.05	.05		
835-7-1	4.8	.09	.29	.08		
835-7-2	(4.5)	?	.25	.05	100	0.0
835-7-3	(15)	.19		.05		
835-4-1	4.5	.12	.16	.06		
835-4-2	4.8	?	.25	.05	100	0.0
835-4-3	4.5	.10		-.08		
835-10-0-b	130	.12		.10		
835-10-1-b	6.9	.09	.20	.07	100	0.0
835-10-2-b	7.0	.18	.15	.07	100	0.0
835-7-0-b	13	.19				
835-7-1-b	3.2	.13	.22	.01	100	-.10
835-7-2-b	4.0	.08	.28	.11	100	-.15
835-4-0-b	4.2	.14		.03		
835-4-1-b	2.5	.18	.17	.06	100	-.05
835-4-2-b	3.5	.13	.28	.11	100	-.15

APPENDIX I. Comparison of Means for LSM Effect t-test

Hypothesis test about difference between 2 population means, small sample, 2-tailed test.

H_o: $(U_1 - U_2) = 0$
H_A: $(U_1 - U_2)$ not equal 0

LSM	4	7	0	(values from App. B last column)
U	279	186	87	
s	33.0	10.8	1.0	
n	7	4	3	

test statistic

$$t = (U_1 - U_2) - 0) / ((S_p^2 * (1/n_1 + 1/n_2))^{0.5}$$

reject region: $t < -t_{alpha/2}$ or $t > t_{alpha/2}$

	$t_{calculated}$
4 vs. 7	5.38 *
7 vs. 0	15.49 *

$t_{critical}$: $t(9,.005) = 3.25$
$t(5,.005) = 4.032$

* significantly different at alpha = 0.01 level.

APPENDIX J. Between Ingot Comparisons t-test.

H_o: $(u_1 - u_2) = 0$
H_A: $(u_1 - u_2)$ not equal 0

Ingot		(1) 226220	(2) 218208
LSM			
4	u	278	223
	n	7	4
	s	32.96	16.92
7	u	186	201
	n	4	4
	s	10.83	27.90
zero	u	87.2	73.8
	n	3	2
	s	1.065	2.500

$t = (u_1 - u_2) / (S_p^2 * (1/n_1 - 1/n_2))^{0.5}$

$S_p^2 = ((n_1 - 1) * s_1^2 + (n_2 - 1) * s_2^2) / (n_1 + n_2 - 2)$

Reject Region: $t < -t_{alpha/2}$ or $t > t_{alpha/2}$

LSM	$t_{calculated}$	D.F.
4:	3.06	9
7:	-1.00	6
0:	5.66	3

$t_{critical}$: t(9,.01) = 2.821 t(9,.005) = 3.25
t(6,.10) = 1.44
t(3,.01) = 4.54 t(3,.005) = 5.841

APPENDIX K. Immersion Test F-test.

PROG:ANOVA3 FILE:a:wt888934.mrg

FACTOR	SUM SQ	D.F.	MEAN SQ	F-TEST RATIO
BLOCK (A)	.6583519	1	.6583519	31.72637 *
LASER (B)	2.289782	2	1.144891	55.17297 *
ALLOY (C)	1.335445	4	.3338614	16.08898 *
A X B	7.88307E-03	2	3.9415E-3	.189945
A X C	.1143227	4	2.8580E-2	1.377319
B X C	1.307457	8	.1634321	7.875892 *
A X B X C	.3344593	8	4.1807E-2	2.014724
ERROR	1.867584	90	2.0759E-2	

F(1,90,.99) = 6.9
F(2,90,.99) = 4.9
F(4,90,.99) = 3.5
F(8,90,.99) = 2.7

APPENDIX L. Immersion LSM Parameters t-test.

H_o: ($u_1 = u_2 = u_3$)
H_A: at least 2 means are different

(values from App. C and D, last columns)

LSM	10	7	4
avg	.62	.43	.28
stdev	.2831	.1834	.1457
n	40	40	40

confidence level: alpha = 0.01
alpha/2 = 0.005

x +/- $t(39,0.005) * s / n^{0.5}$

99% Confidence Interval

LSM

10: $.62 +/- 2.576 * .2831/ 40^{0.5}$

7: $.43 +/- 2.576 * .1834/ 40^{0.5}$

4: $.28 +/- 2.576 * .1457/ 40^{0.5}$

$.5047 < X_{10} < .7353$ *

$.3553 < X_7 < .5037$ *

$.2207 < X_4 < .3393$ *

* all means are significantly different.

APPENDIX M. Potentiodynamic Curves

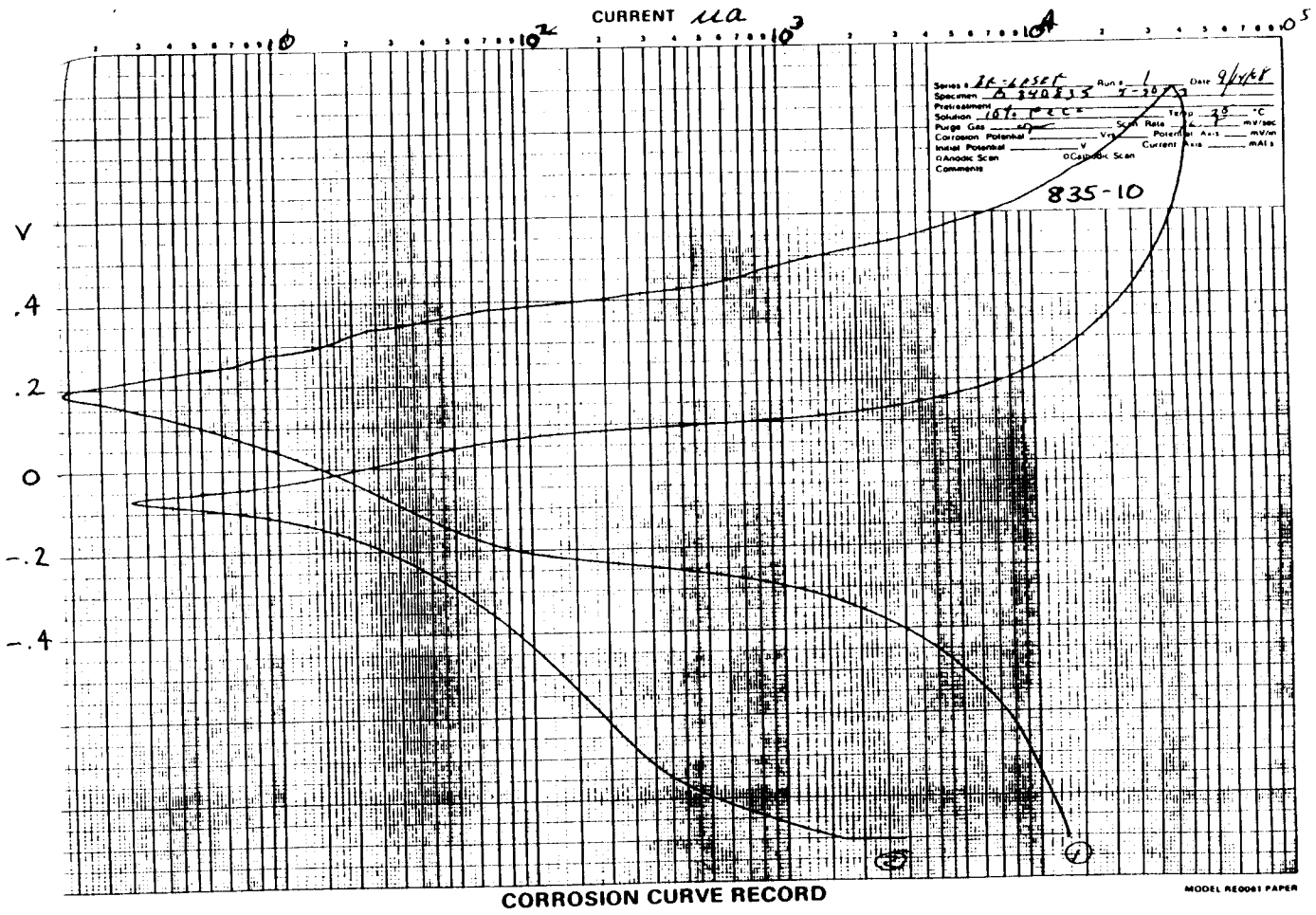

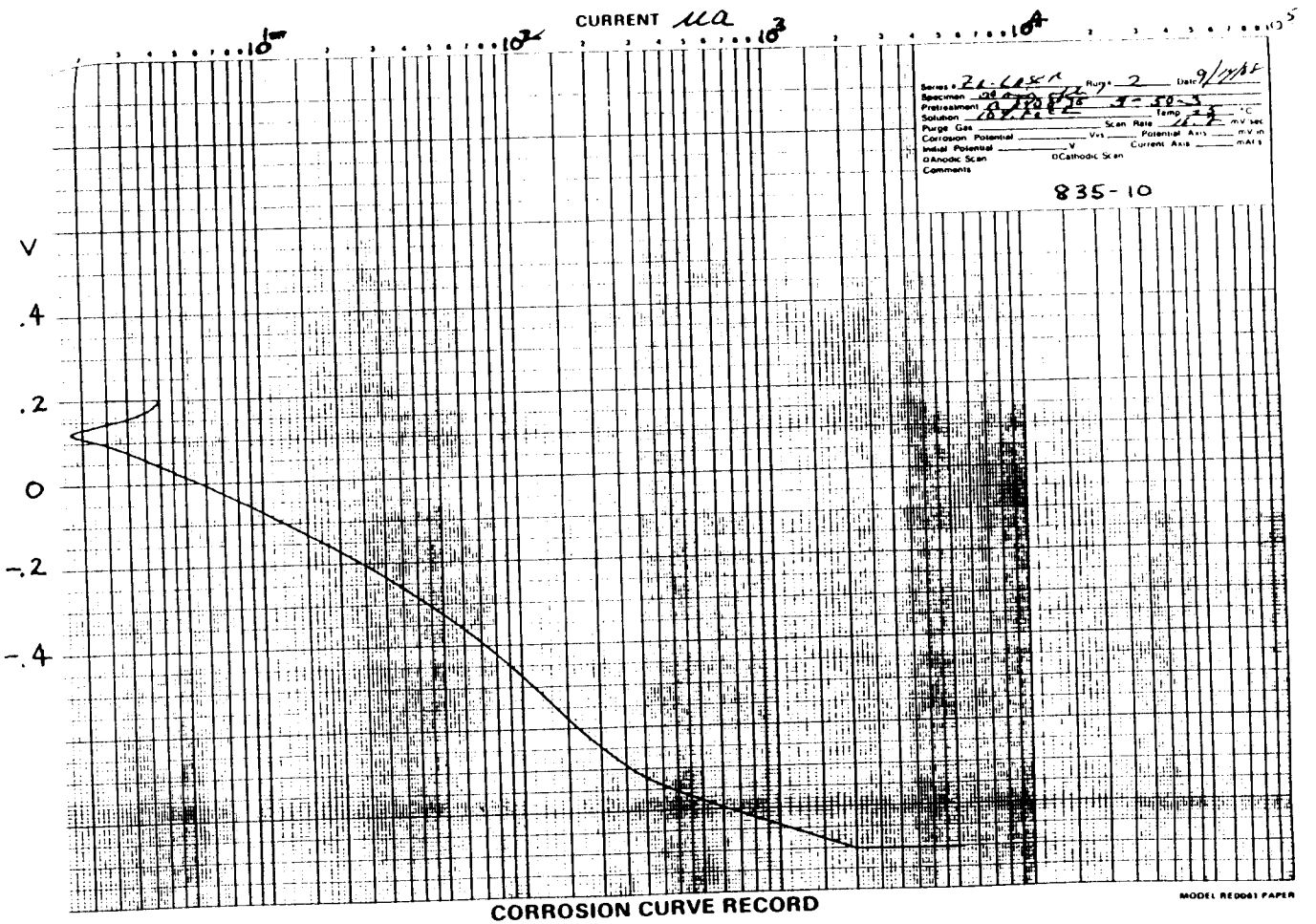

CORROSION CURVE RECORD

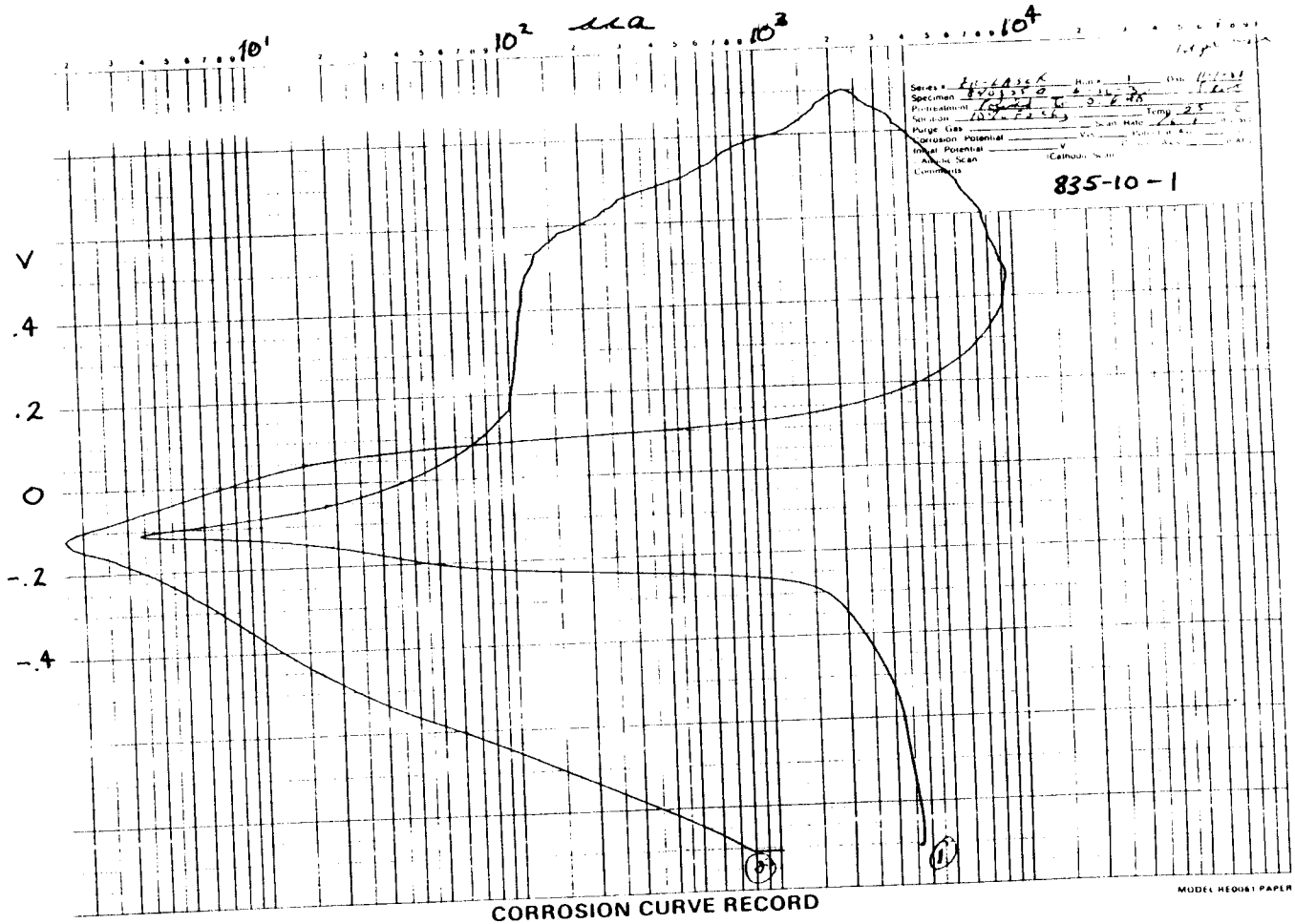

CORROSION CURVE RECORD

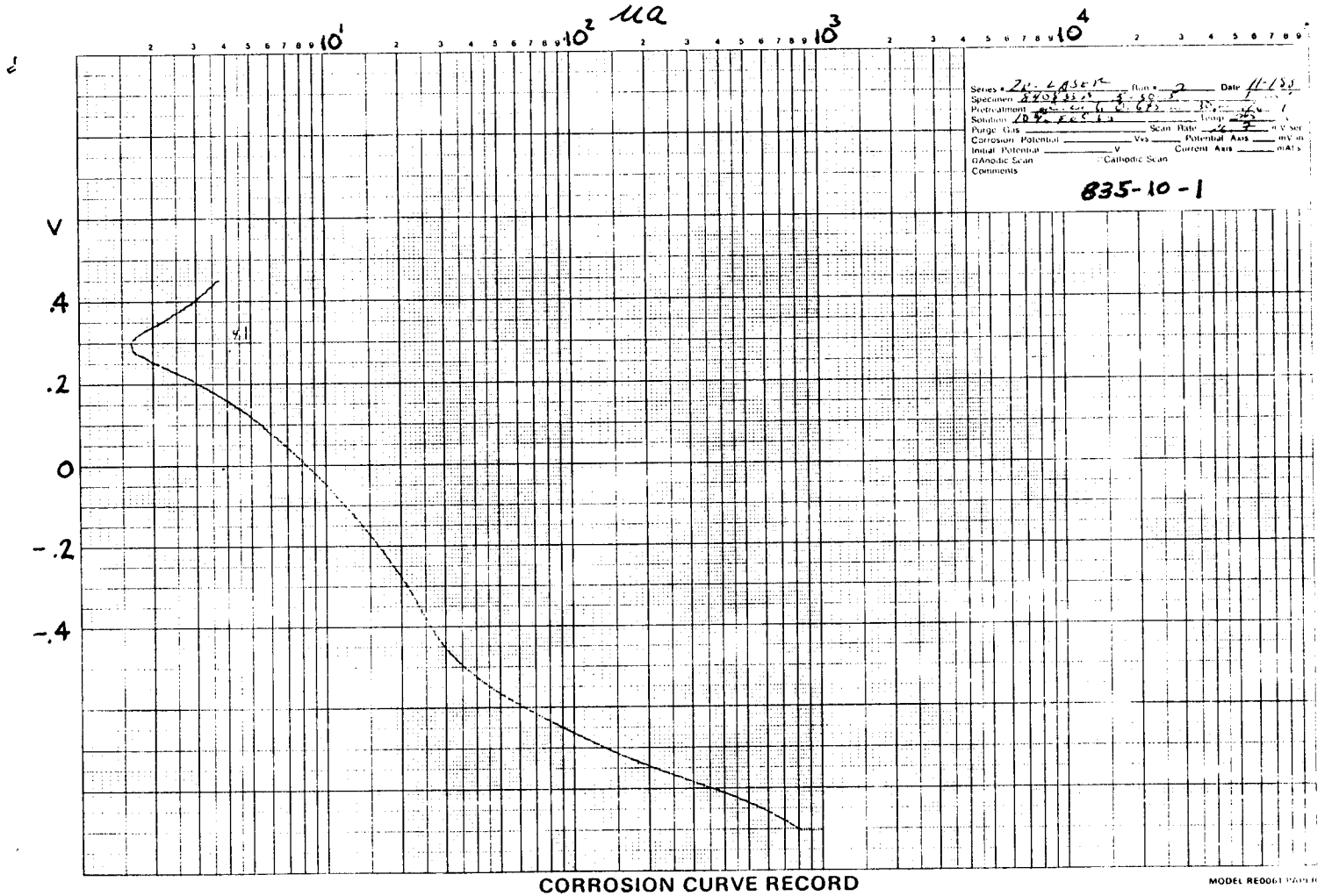

CORROSION CURVE RECORD

MODEL RE0061 PAR

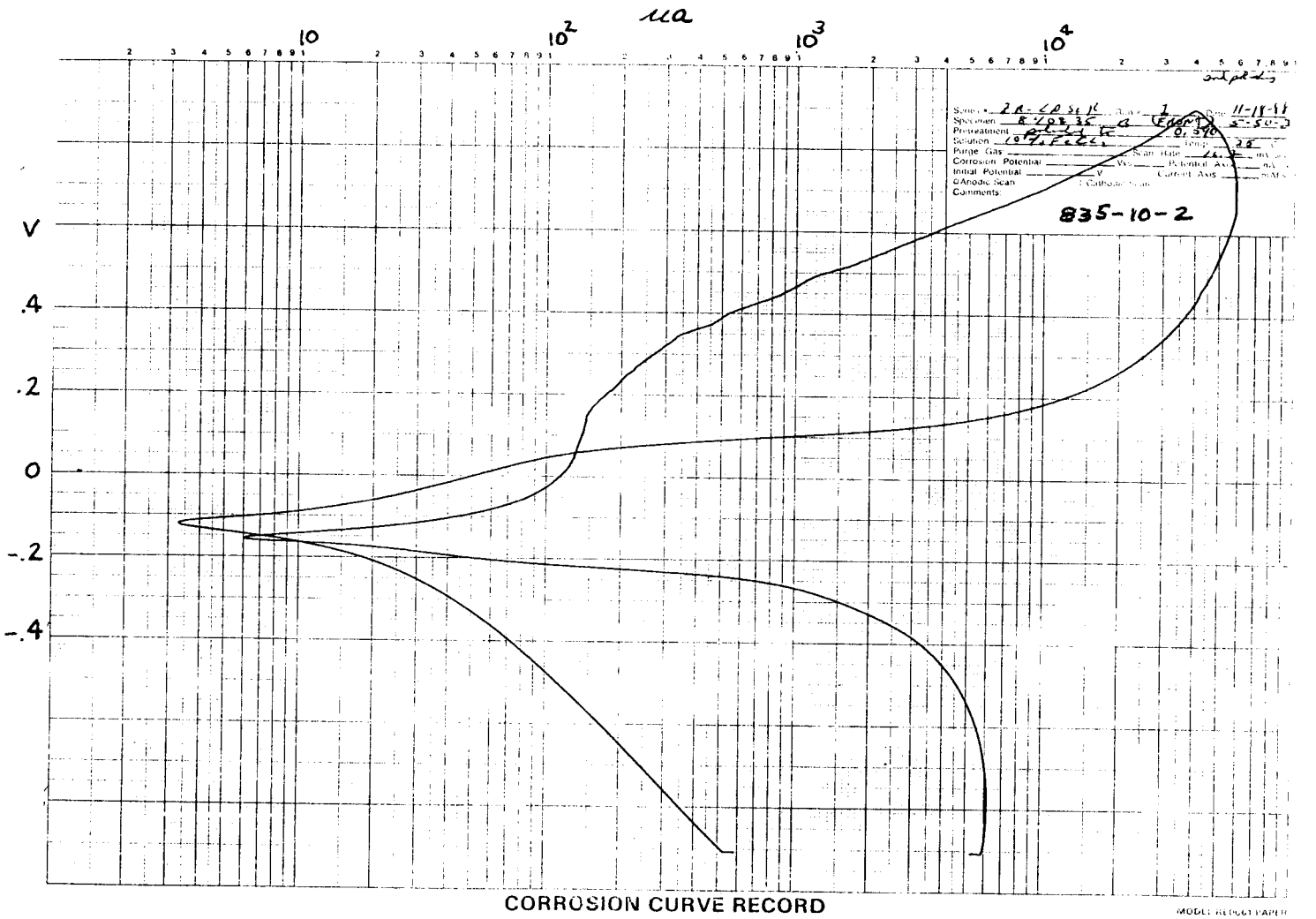

CORROSION CURVE RECORD

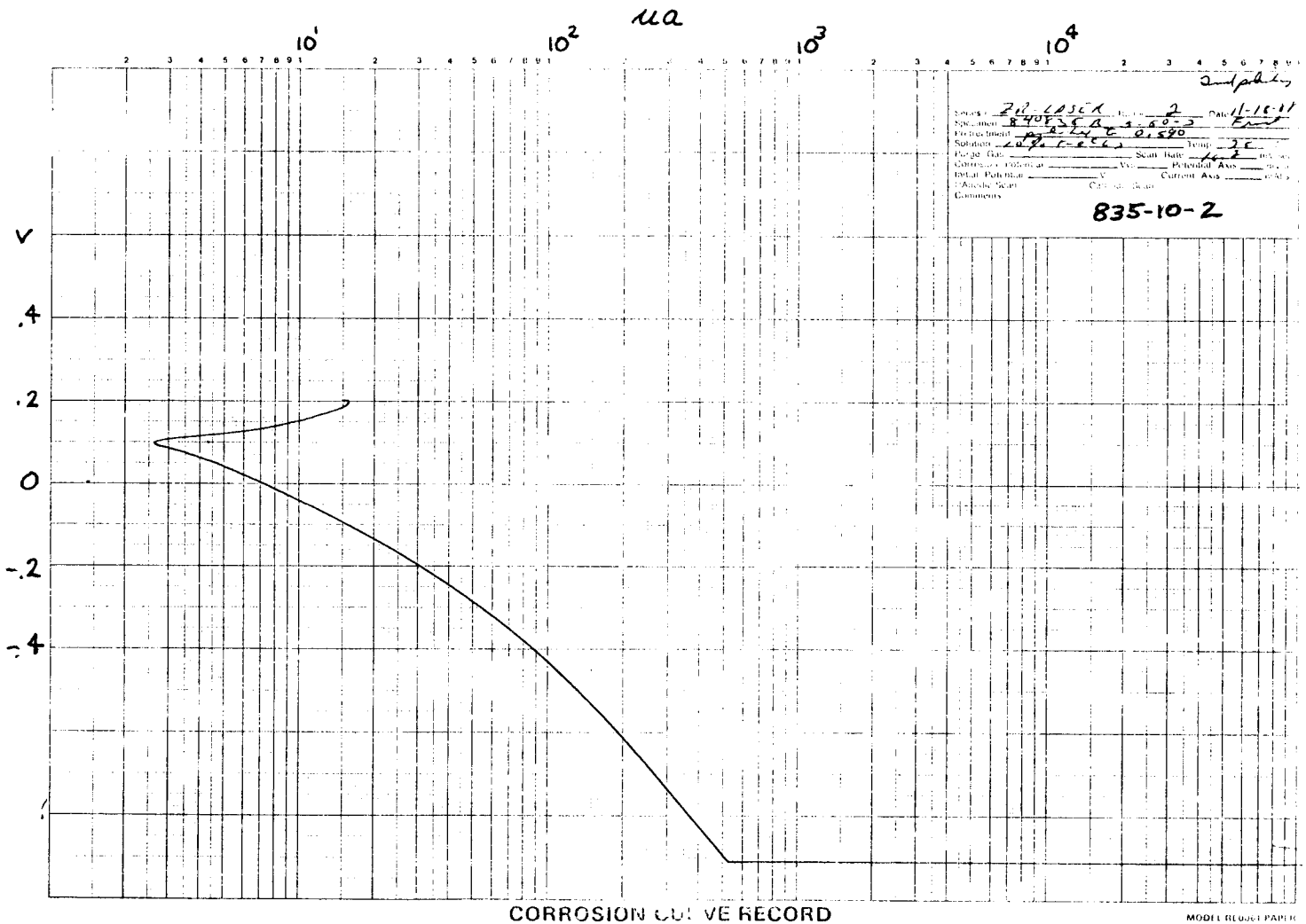
ua
10^1
10^2
10^3
10^4
V
.4
.2
0
-.2
-.4
835-10-2
CORROSION CURVE RECORD
MODEL REUSE PAPER

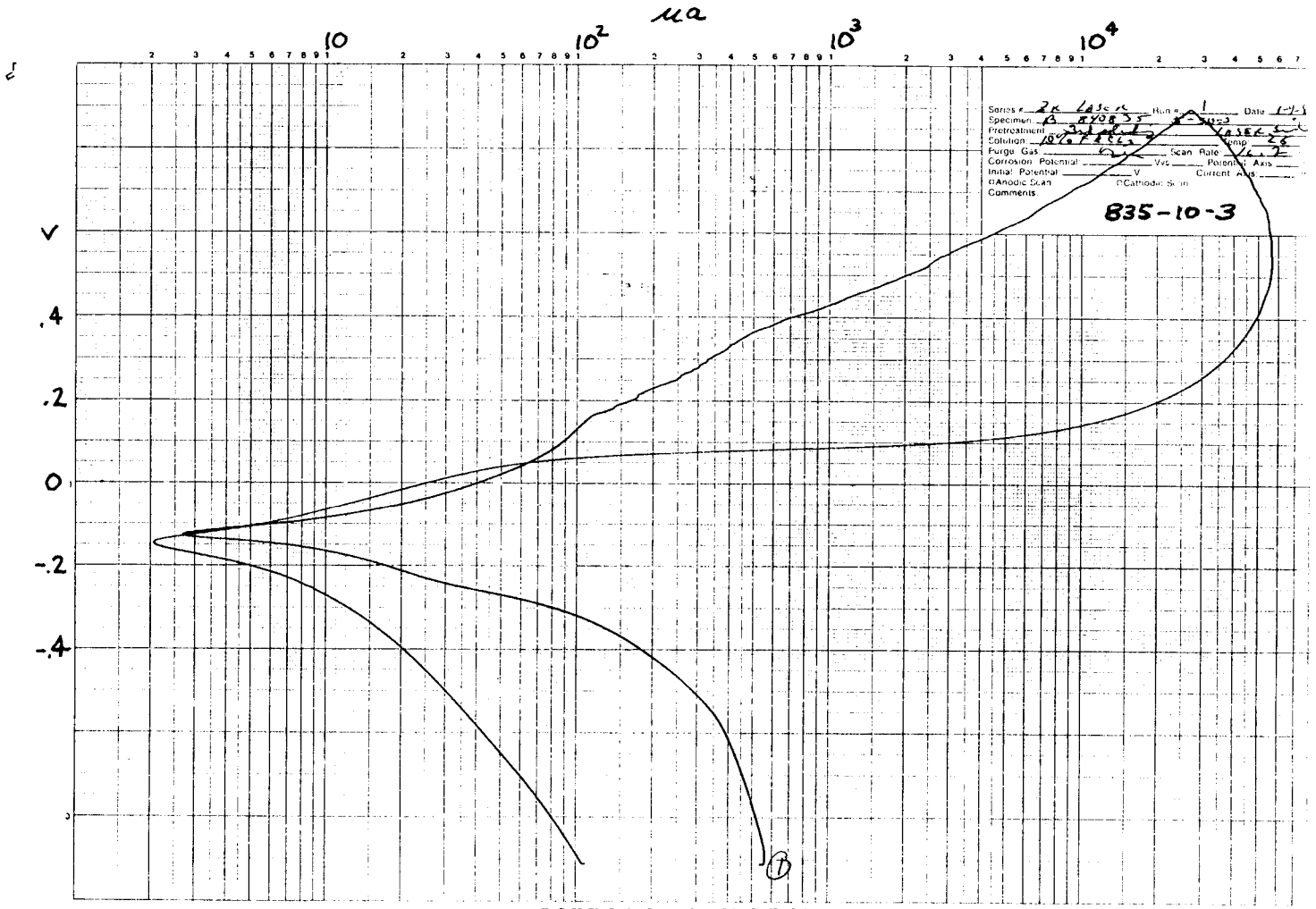

CORROSION CURVE RECORD

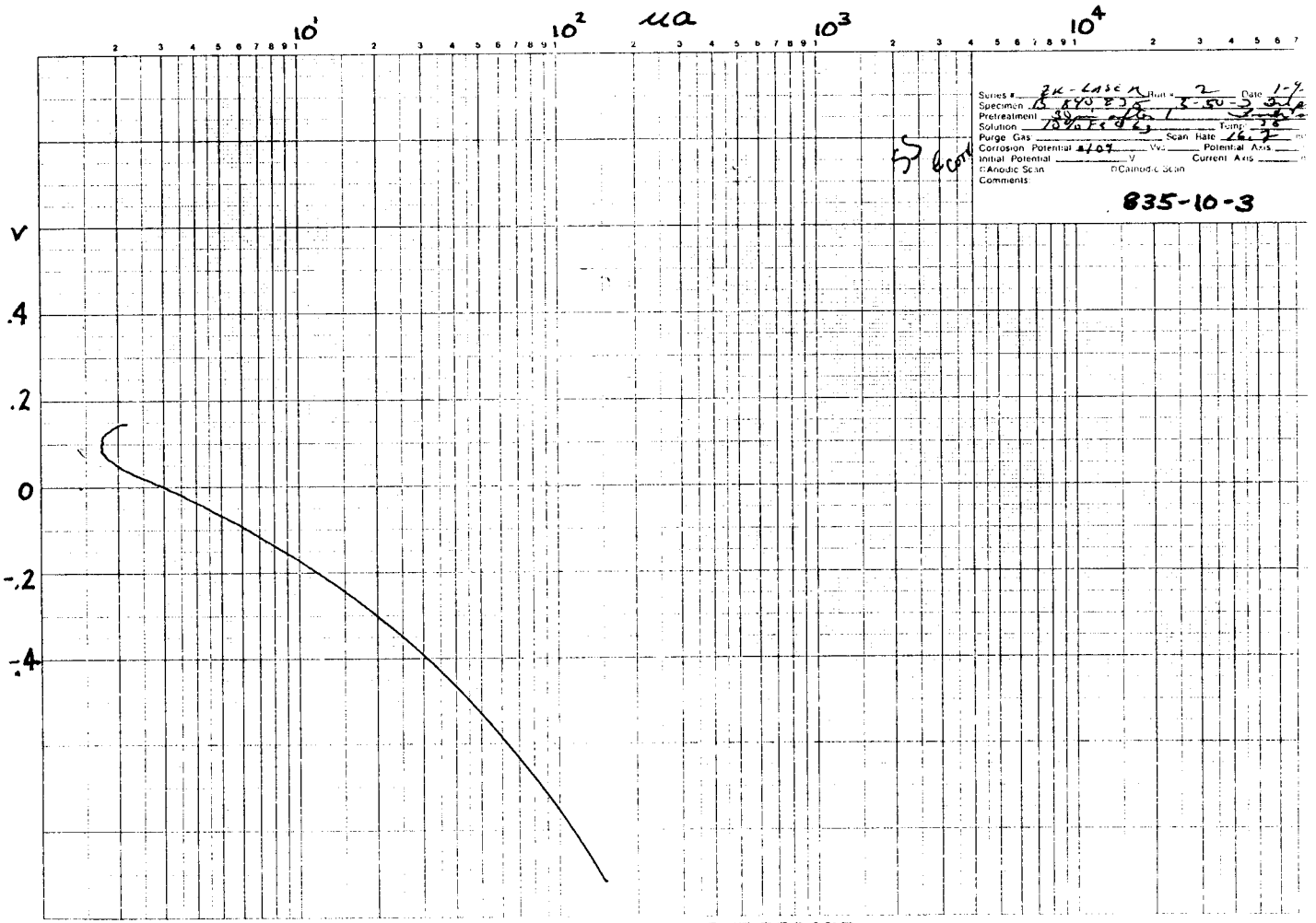

COMMISSION CURVE RECORD

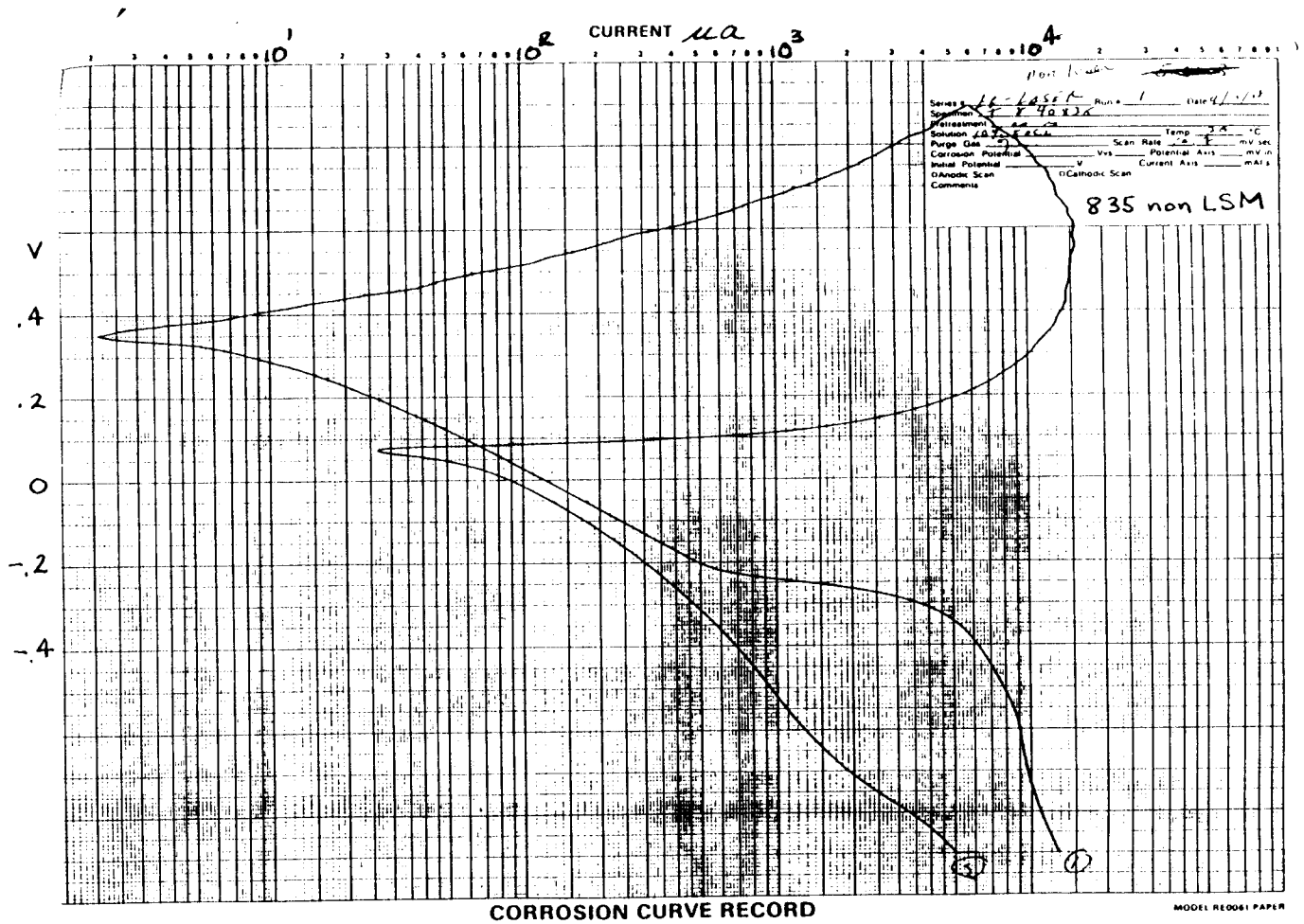

CORROSION CURVE RECORD

MODEL RE0081 PAPER

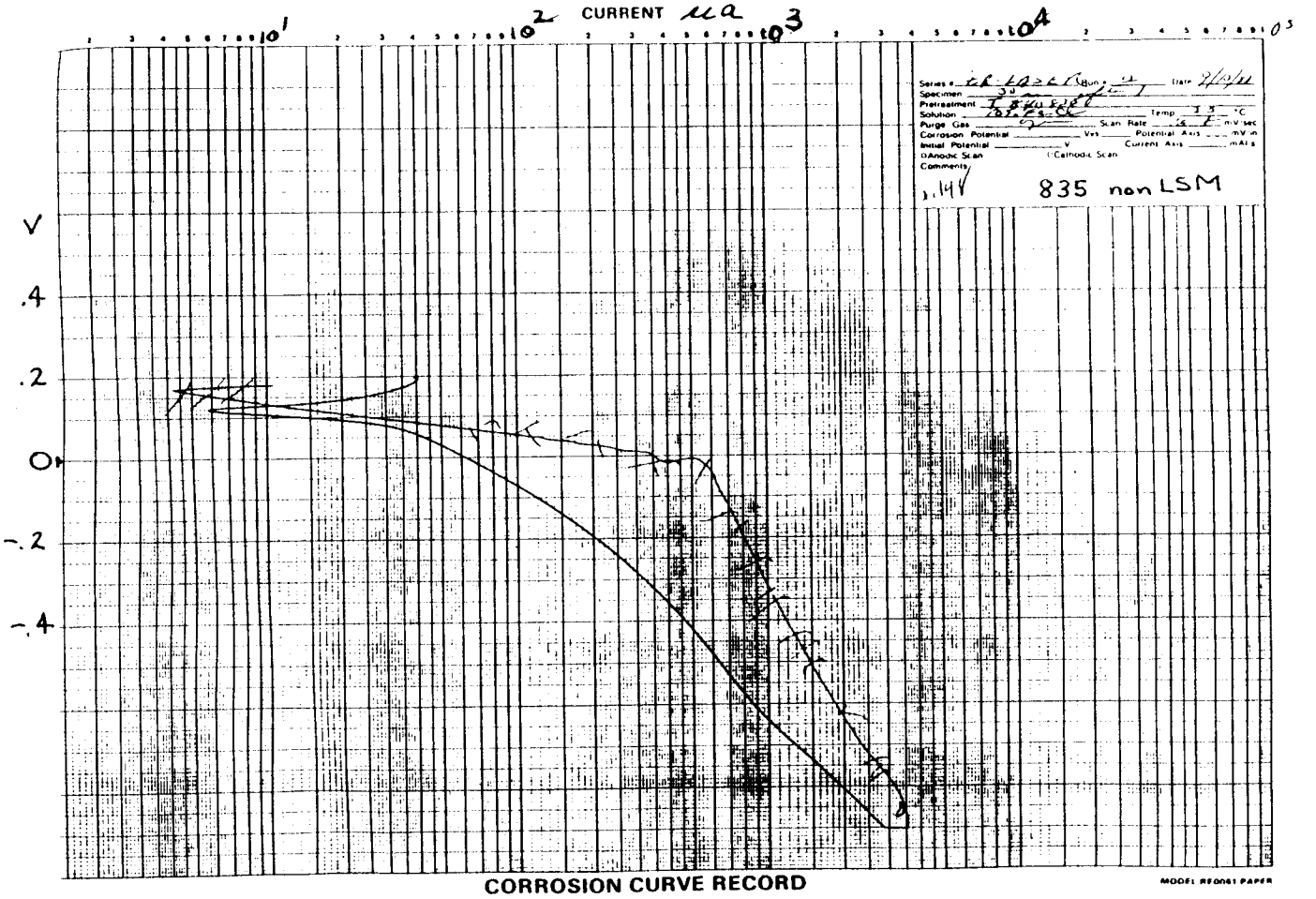
CURRENT μa
V
.4
.2
0
-.2
-.4
835 non LSM
CORROSION CURVE RECORD
MODEL REDMS PAPER

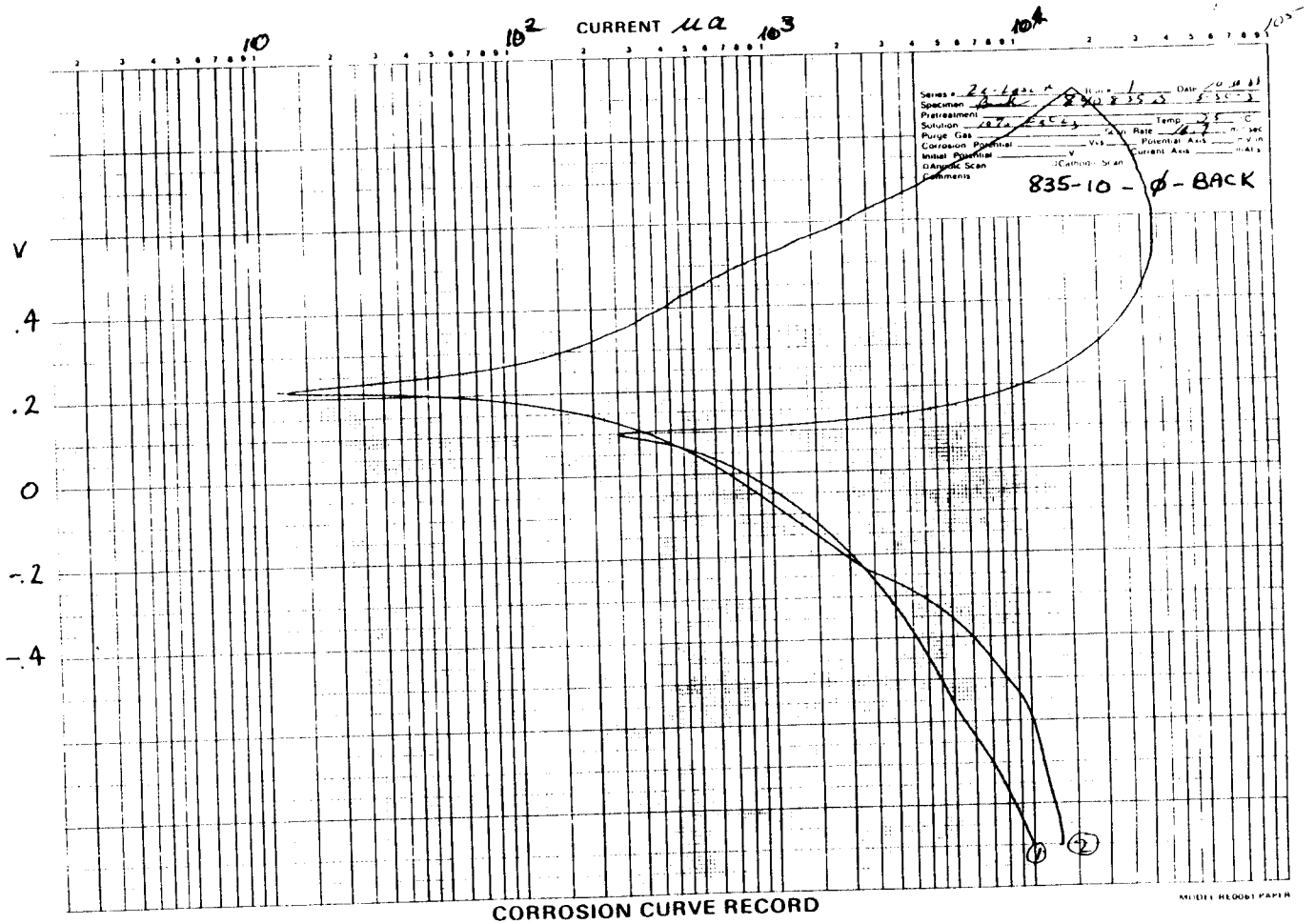
CURRENT μa
10
10²
10³
10⁴
V
.4
.2
0
-.2
-.4
835-10 - Ø - BACK
CORROSION CURVE RECORD

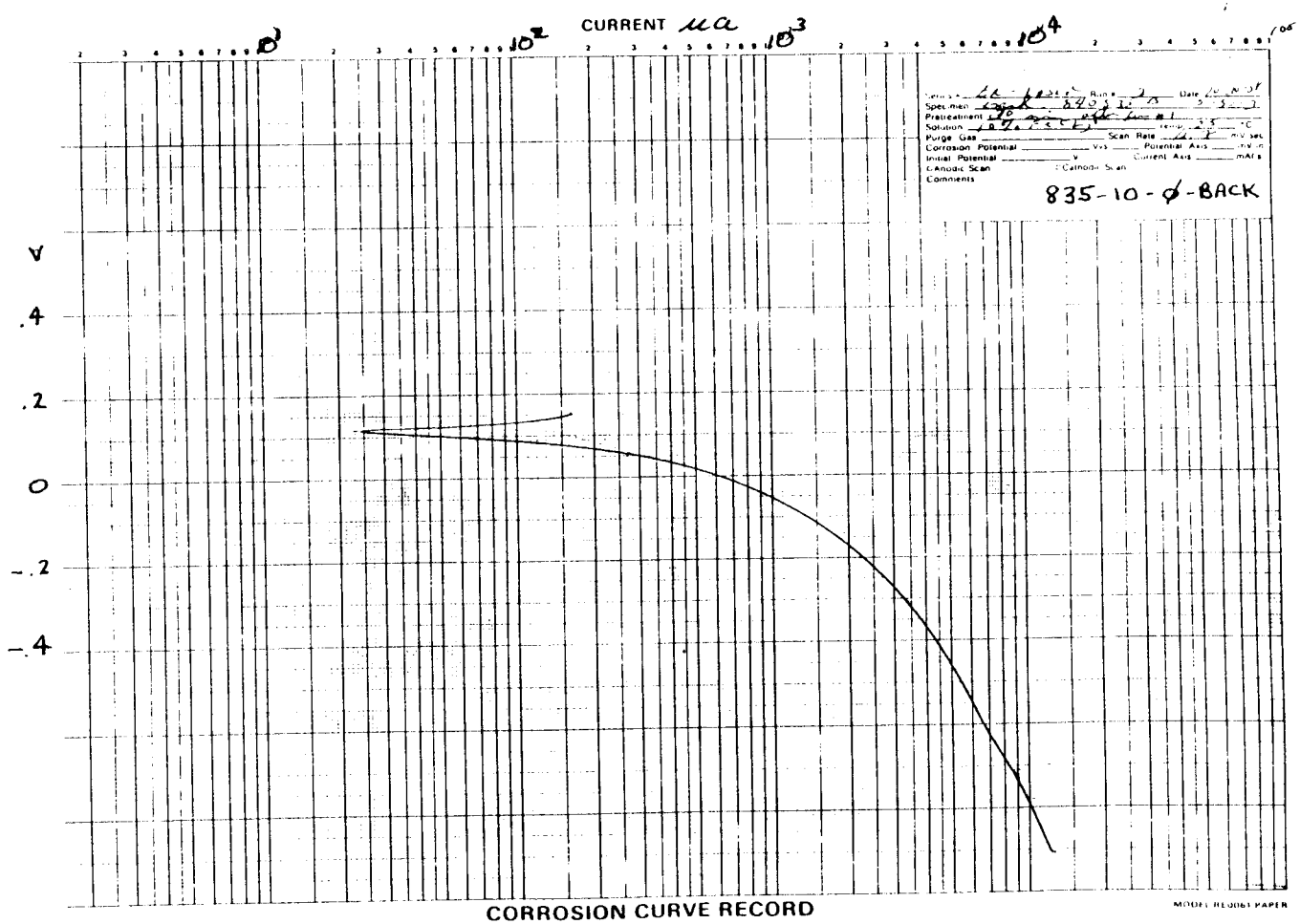
CURRENT μa
10¹
10²
10³
10⁴
10⁵
V
.4
.2
0
-.2
-.4
Run
Date
Specimen
Pretreatment
Solution
Purge Gas
Scan Rate
Corrosion Potential
Potential Axis
Initial Potential
Current Axis
Anodic Scan
Cathodic Scan
Comments
835-10-ϕ-BACK
CORROSION CURVE RECORD
MODEL RE0061 PAPER

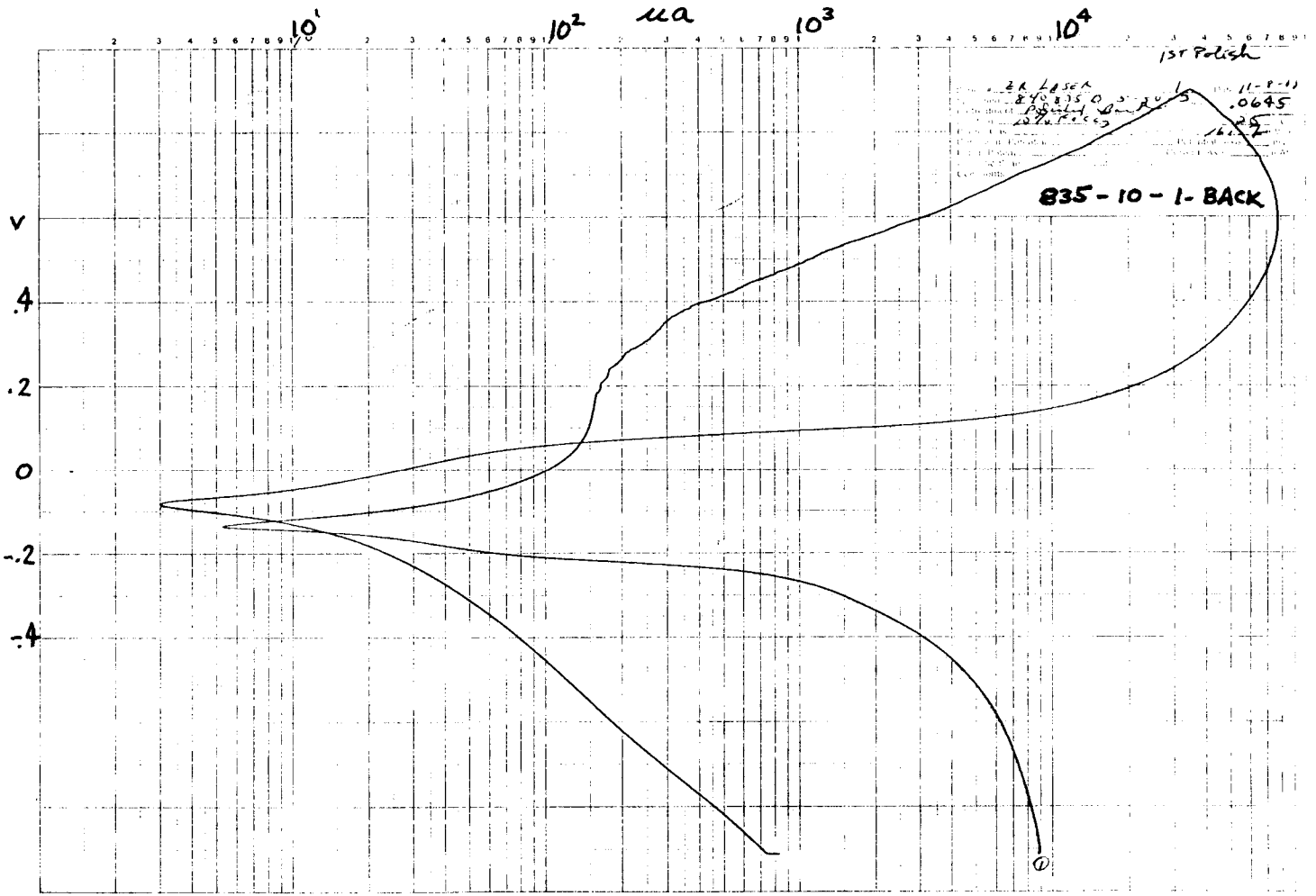

CORROSION CURVE RECORD

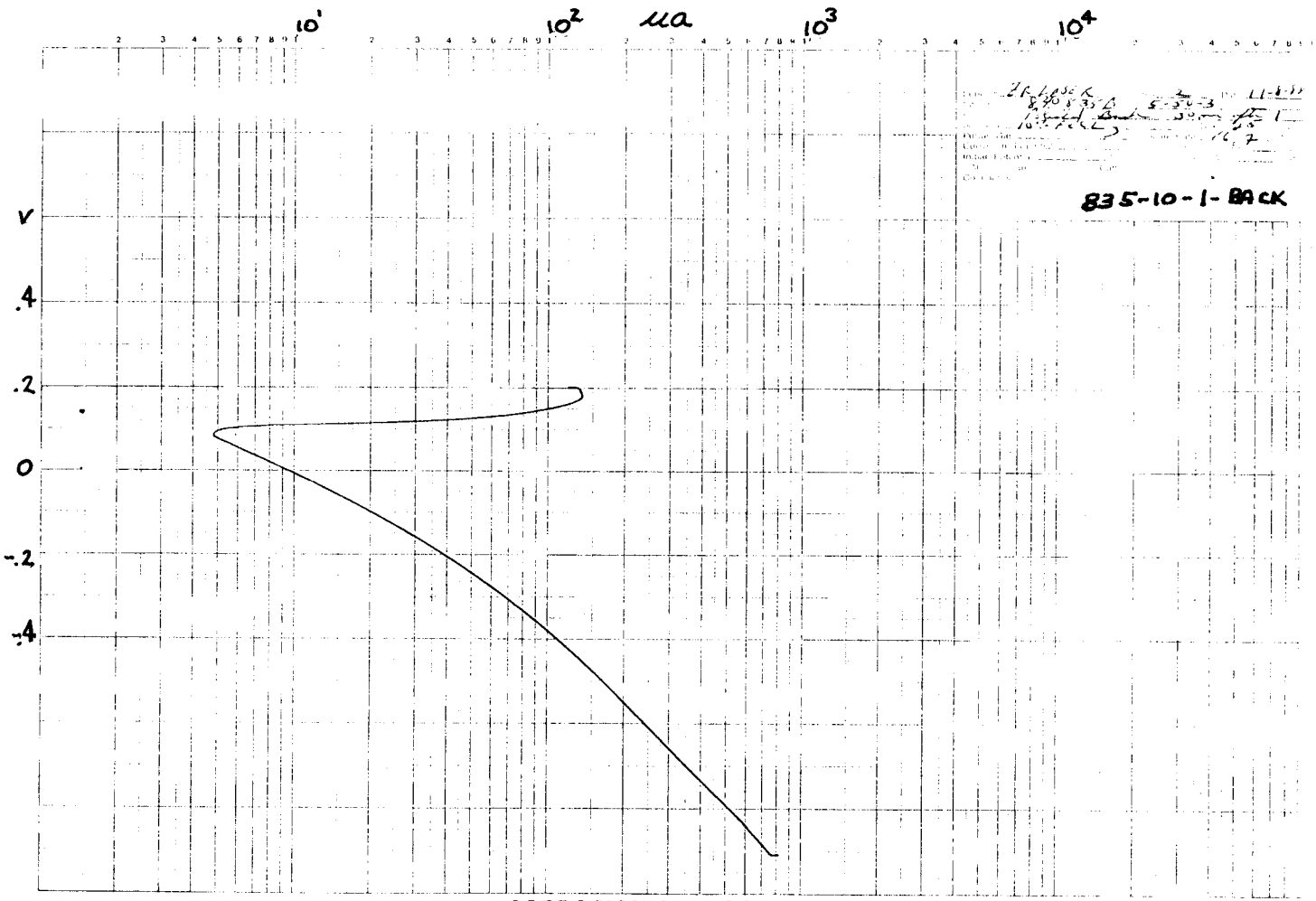

CORROSION CURVE RECORD

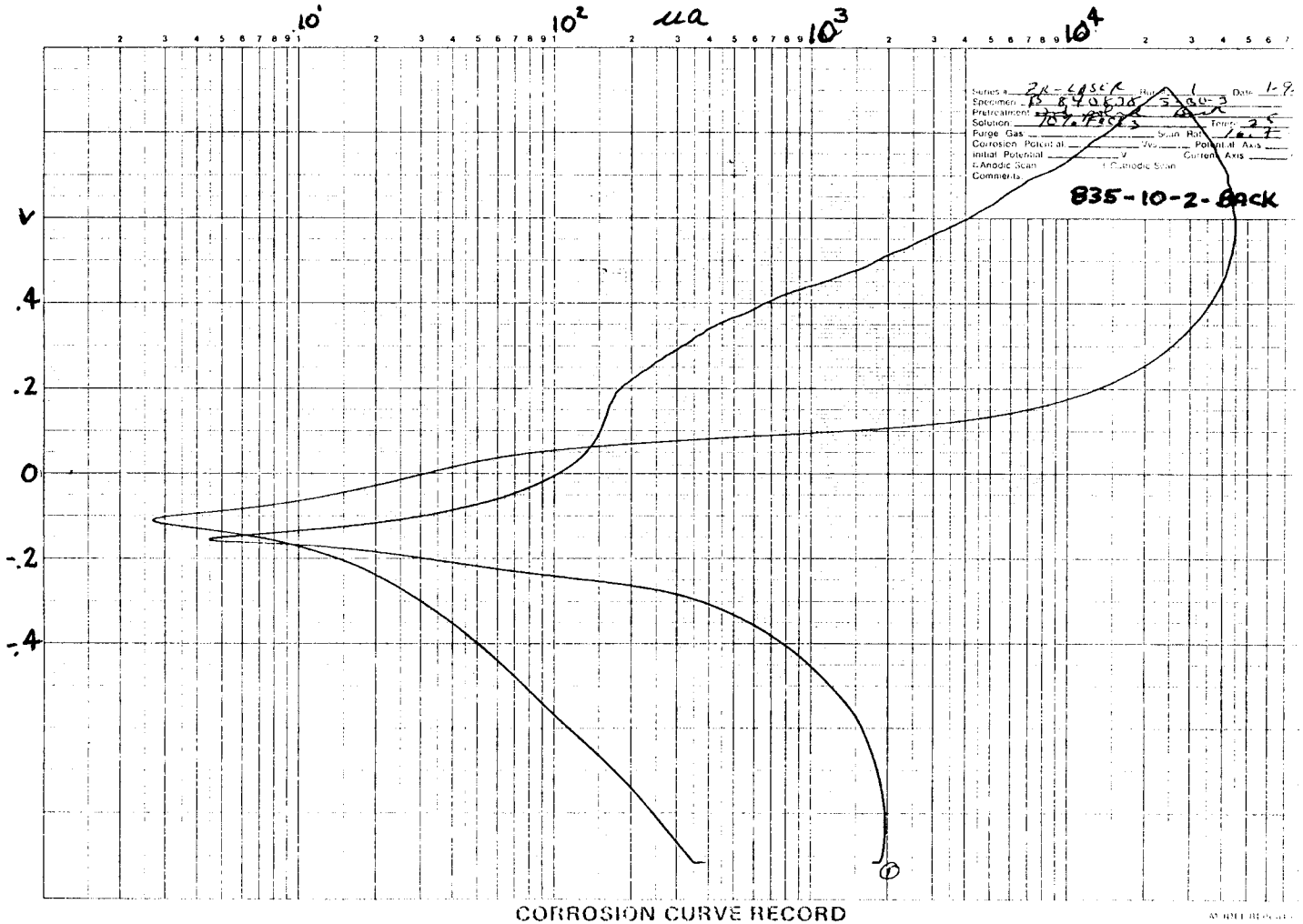

CORROSION CURVE RECORD

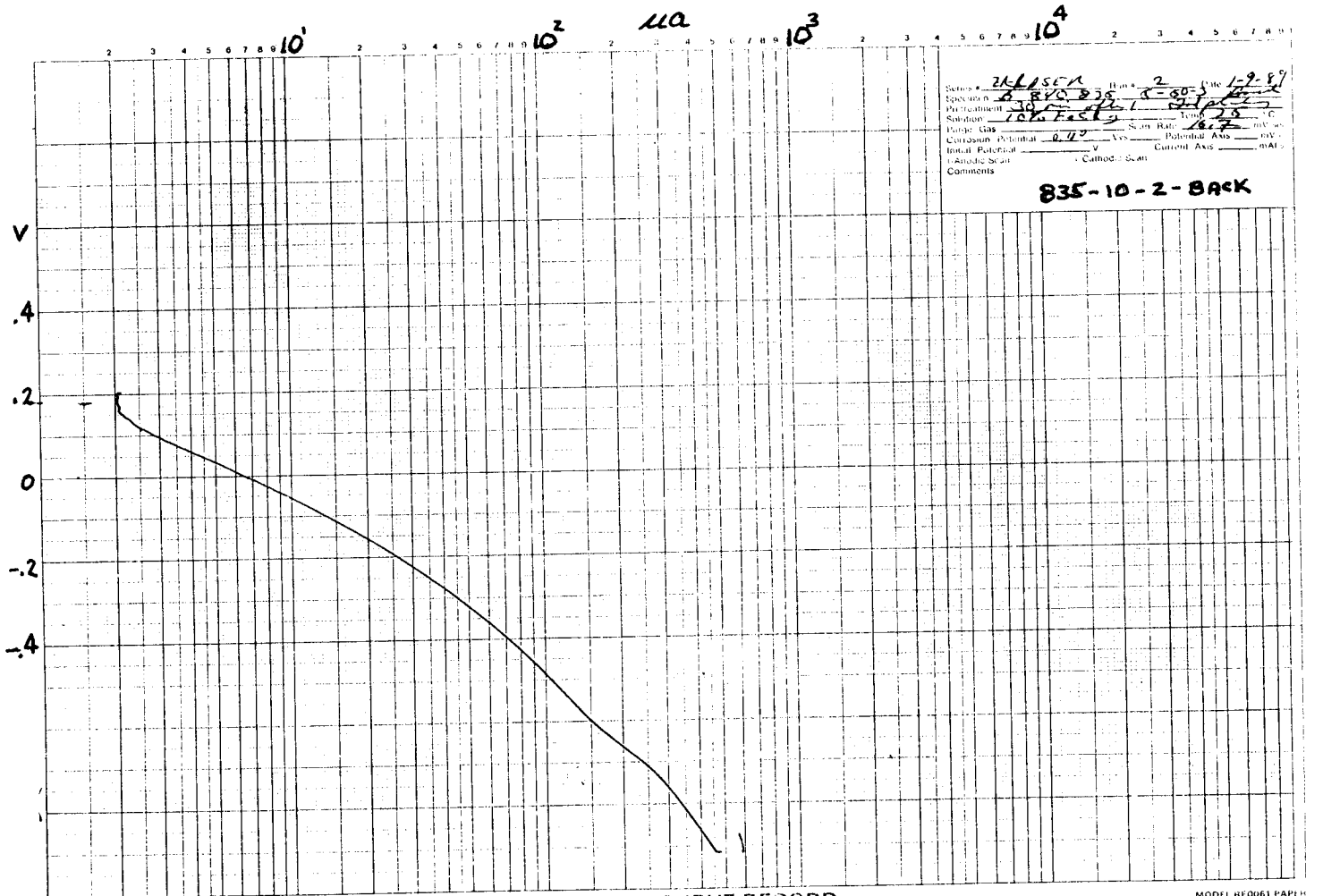

CORROSION CURVE RECORD

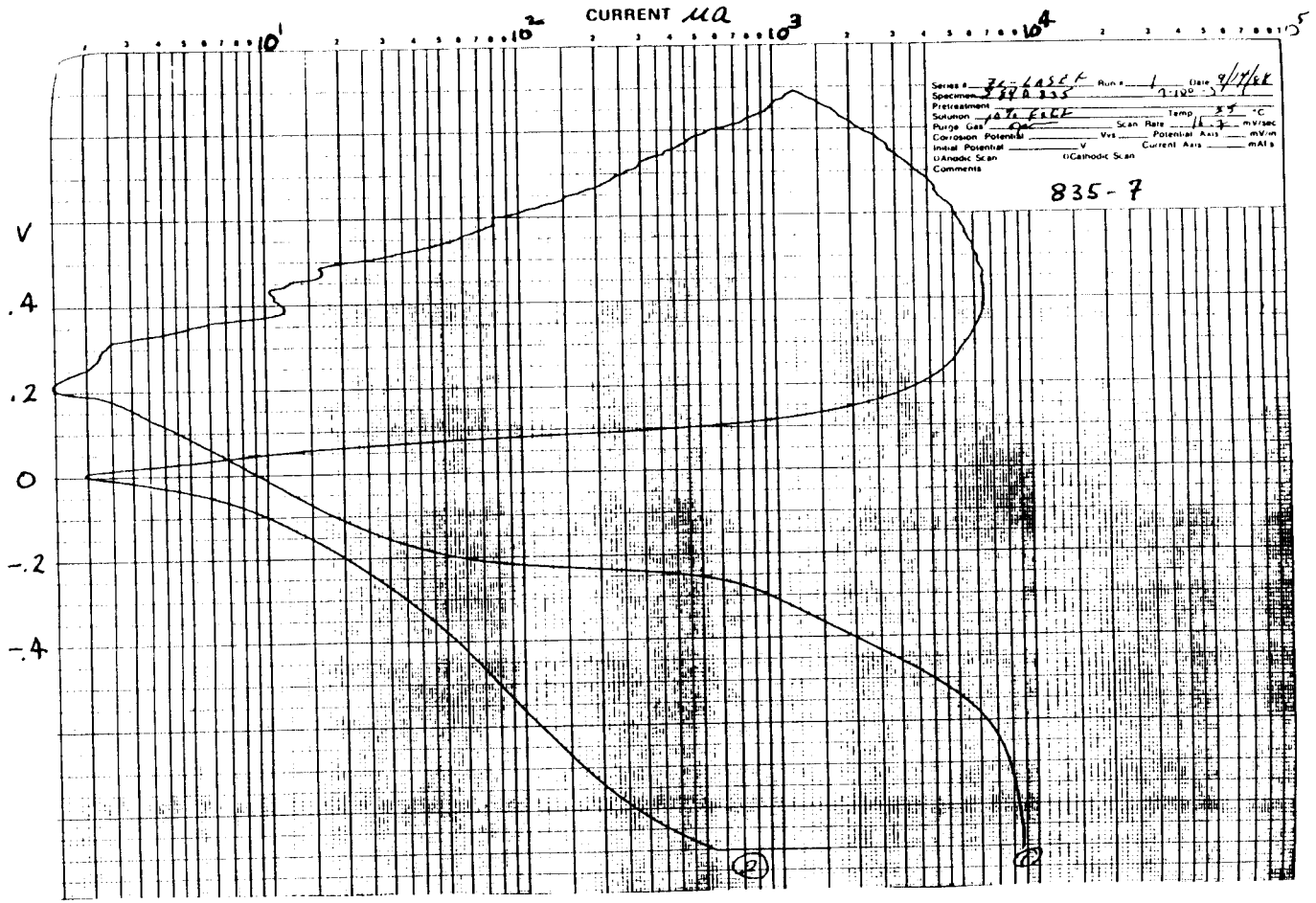
CURRENT μa
10¹
10²
10³
10⁴
10⁵
V
.4
.2
0
-.2
-.4
Series # 76-LASER Run # 1 Date 9/17/82
Specimen 316 835 2-100
Pretreatment
Solution 1N H2SO4 Temp 35 °C
Purge Gas O2 Scan Rate 1.7 mV/sec
Corrosion Potential Vvs Potential Axis mV/in
Initial Potential V Current Axis mA/in
Anodic Scan Cathodic Scan
Comments
835-7

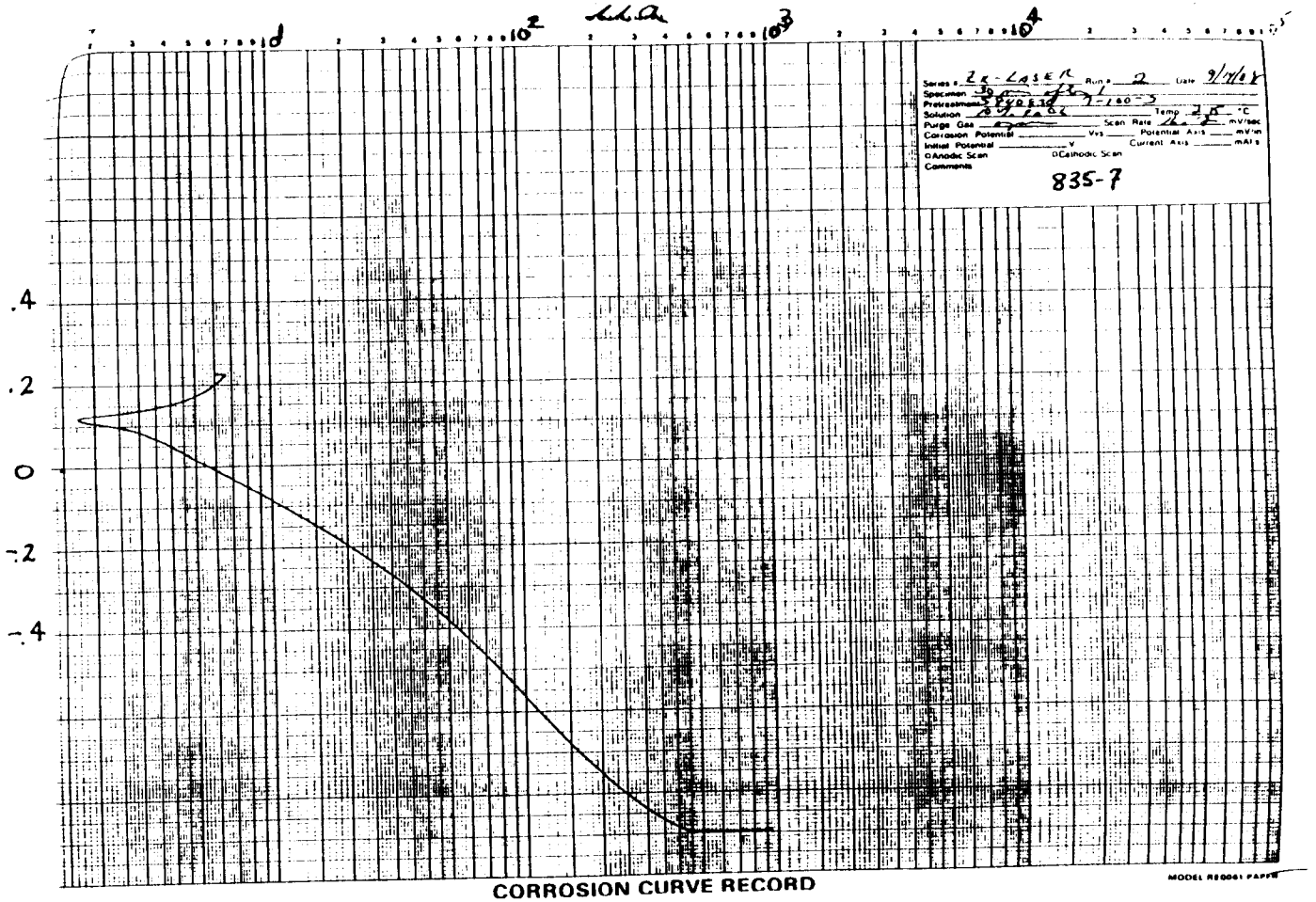

CORROSION CURVE RECORD

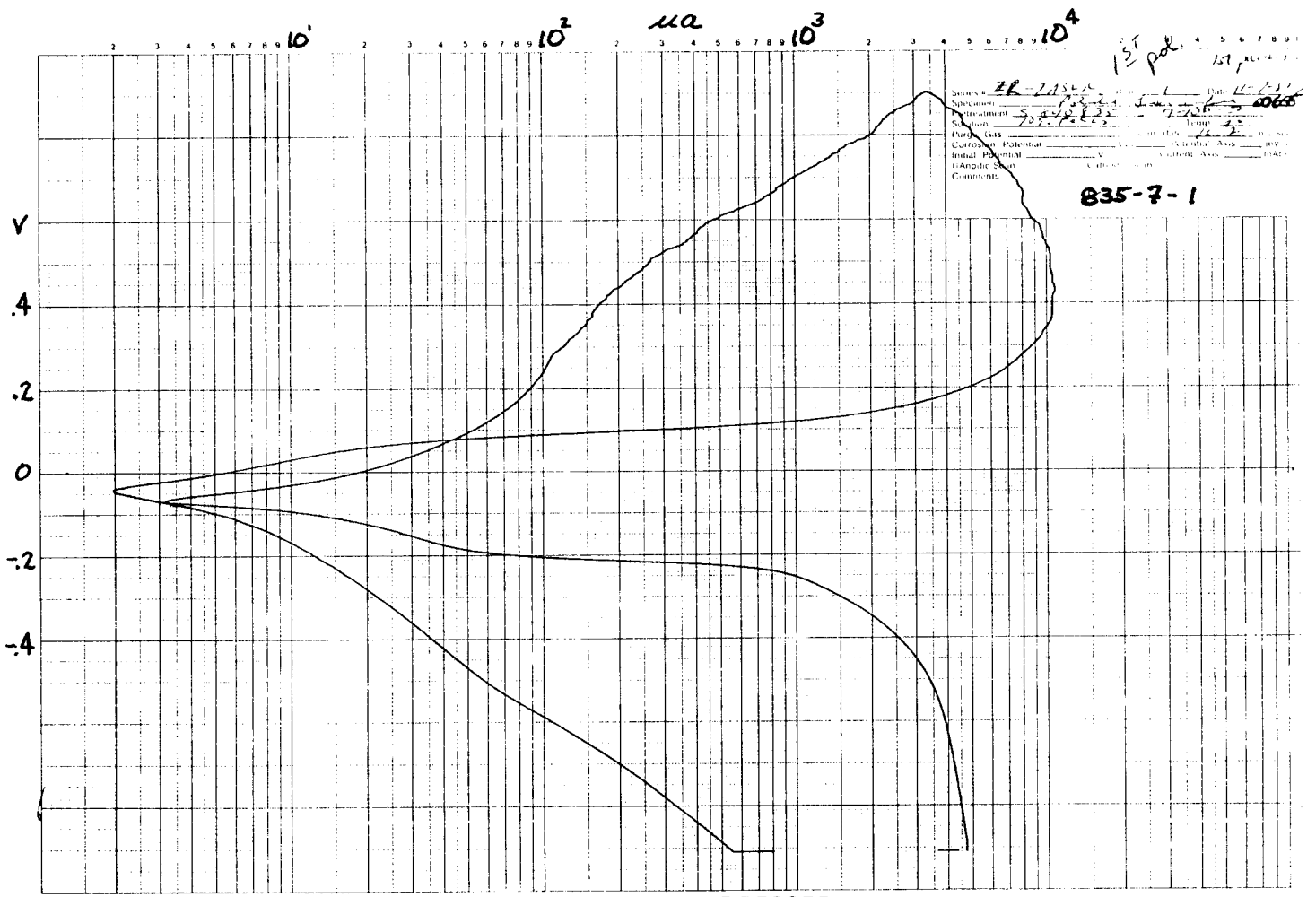

CORROSION CURVE RECORD

MODEL RE0061 PAPER

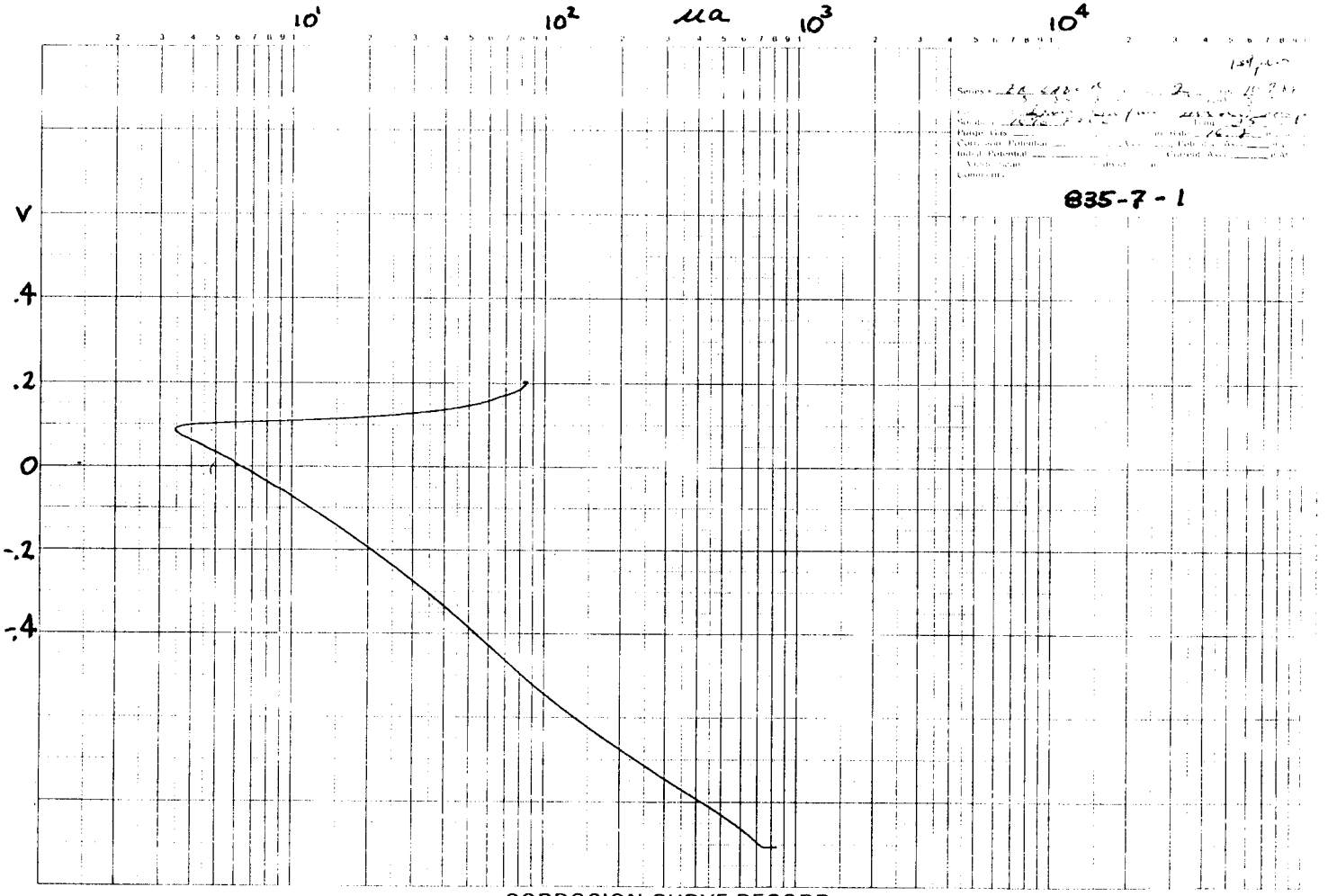

CORROSION CURVE RECORD

MODEL RE-0061 PAPER

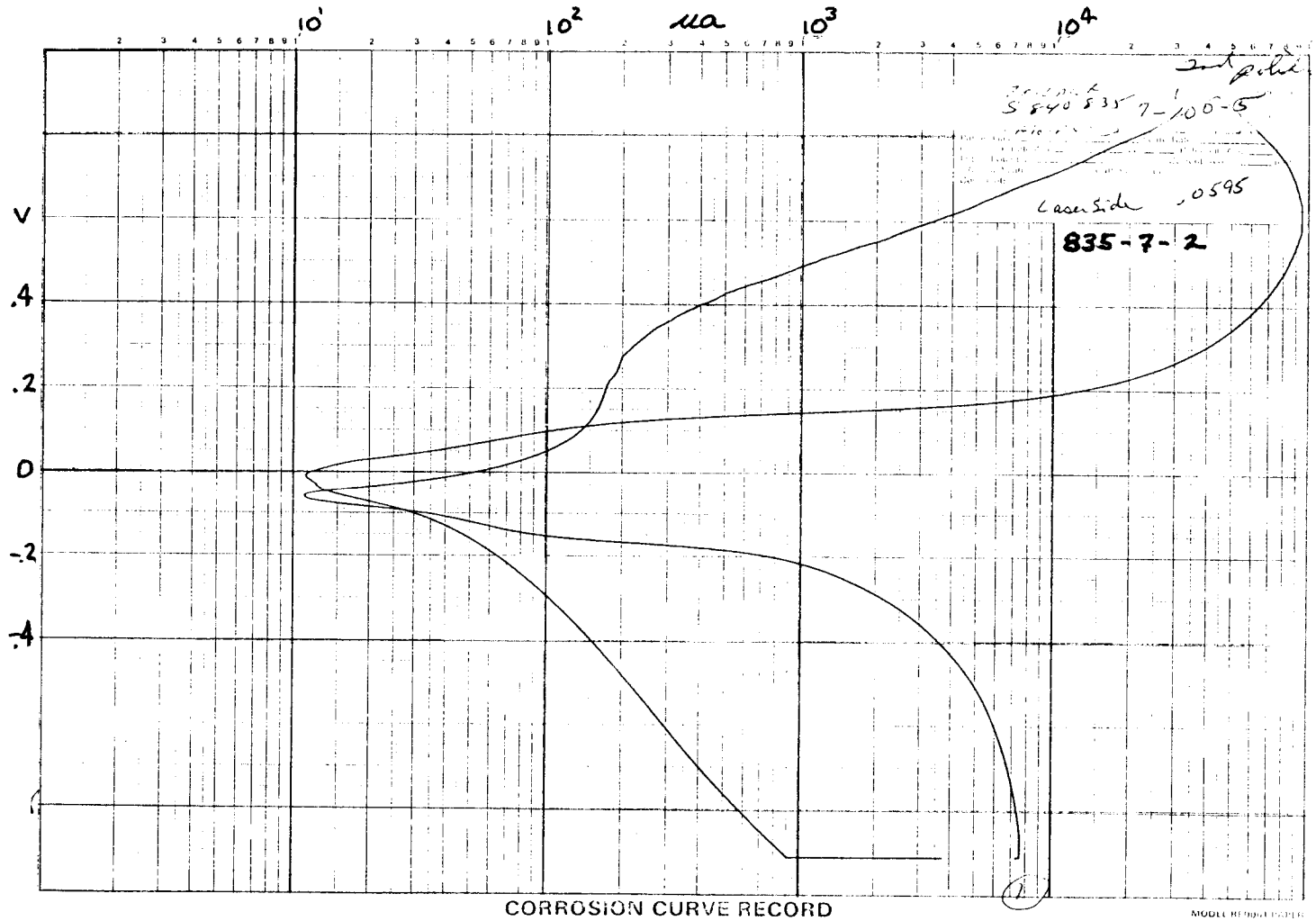
10¹
10²
ua
10³
10⁴
V
.4
.2
0
-.2
-.4
835-7-2
Case Side .0595
CORROSION CURVE RECORD

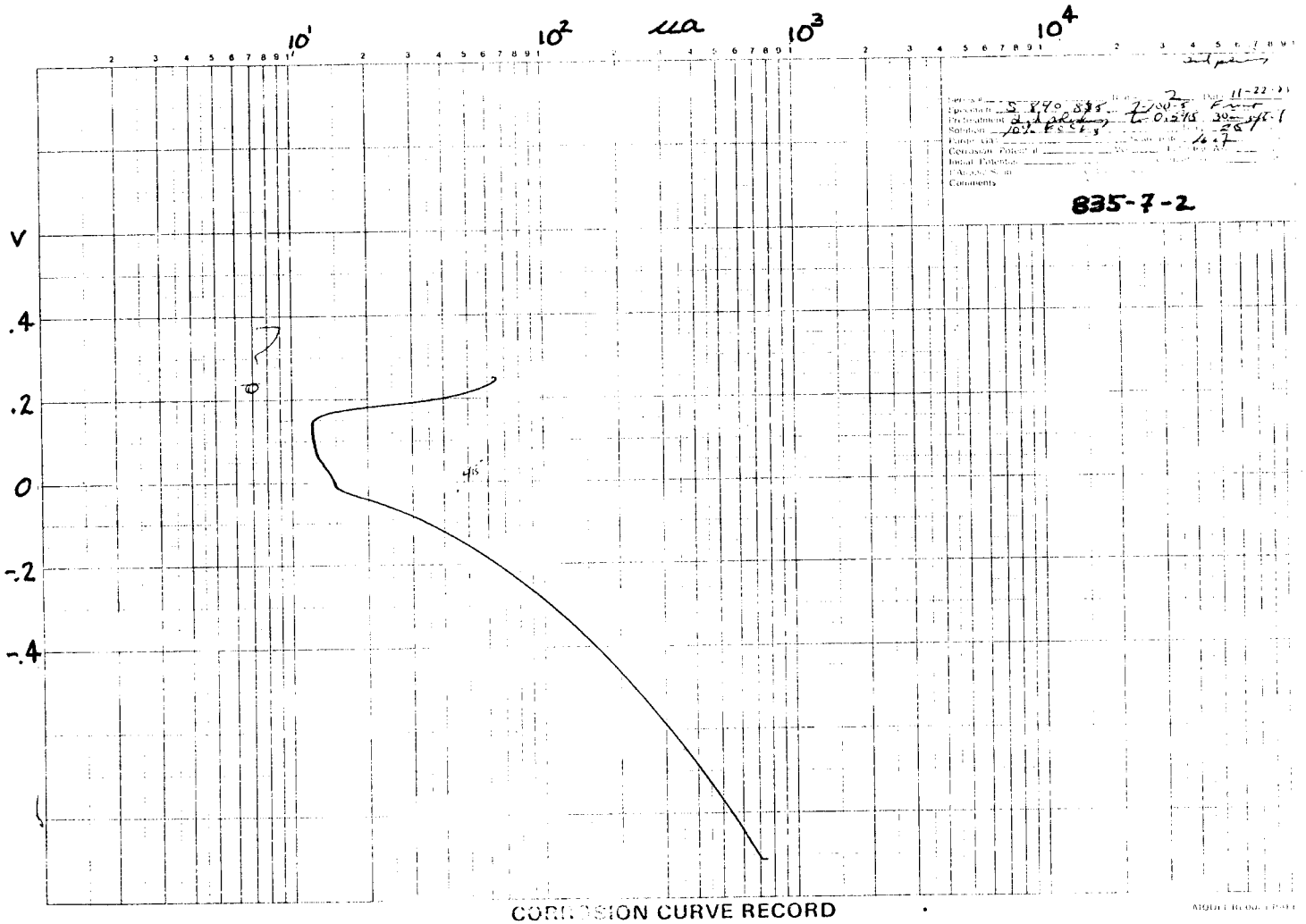

CORROSION CURVE RECORD

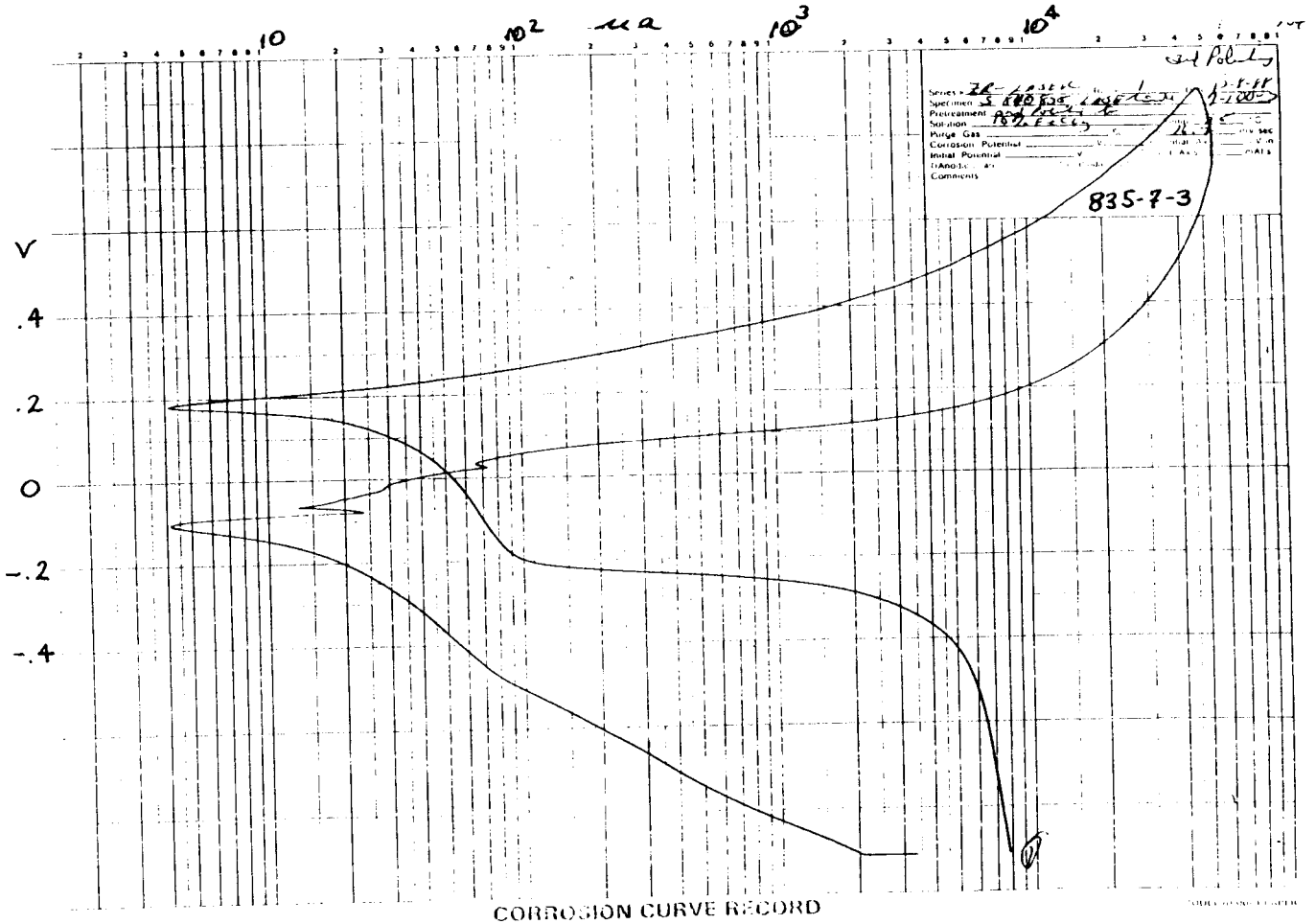

CORROSION CURVE RECORD

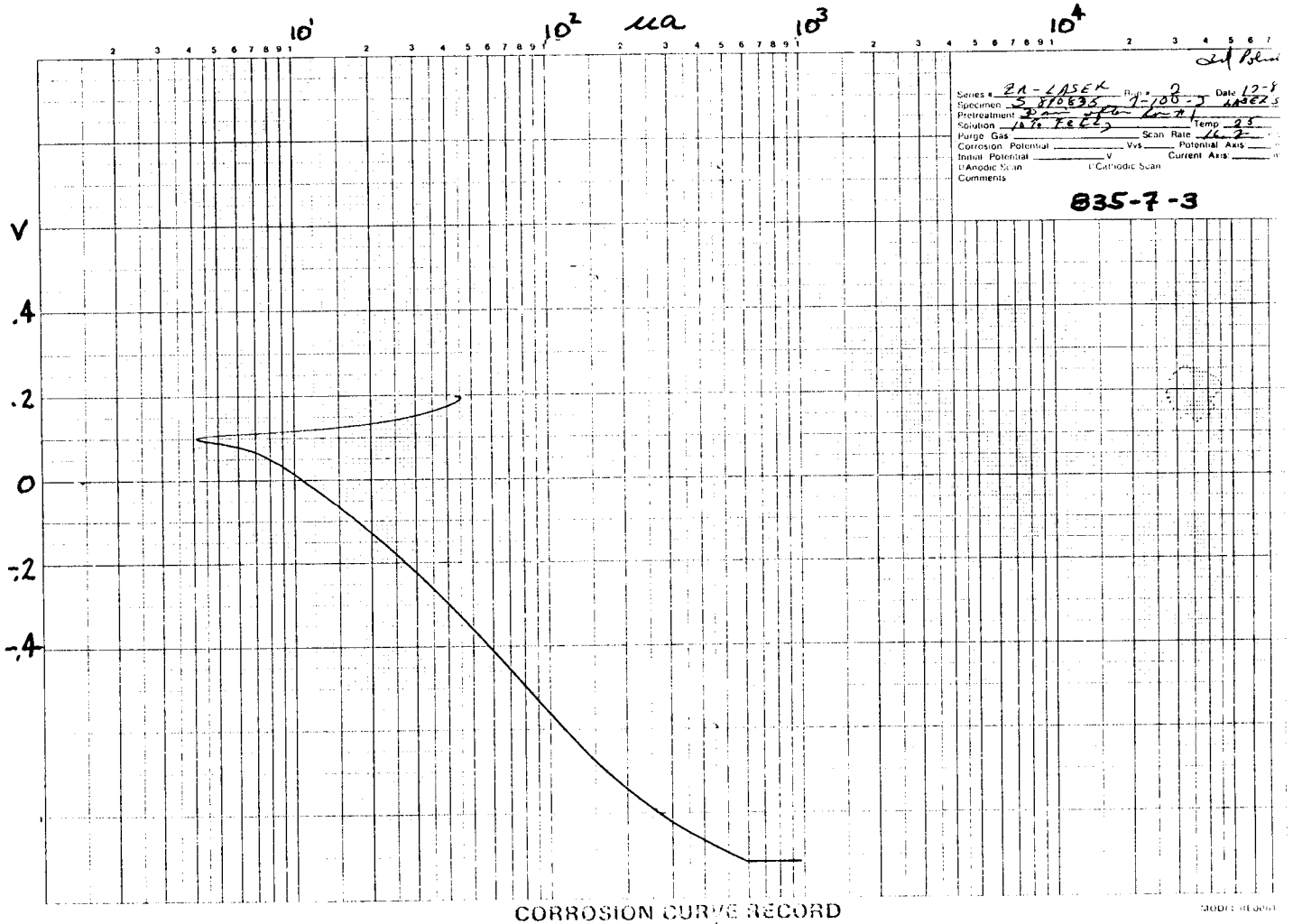

CORROSION CURVE RECORD

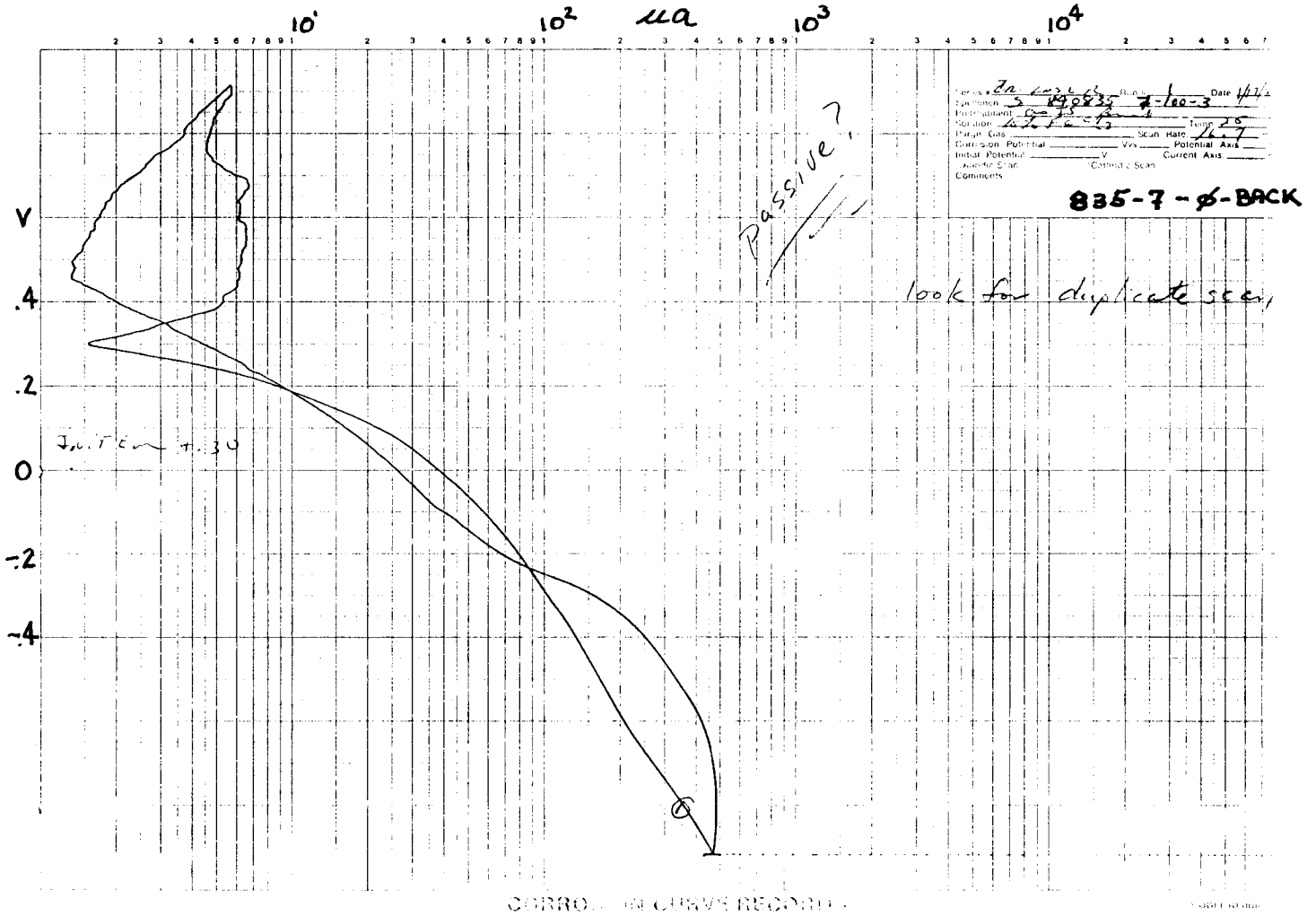
10¹
10²
μa
10³
10⁴
V
.4
.2
0
-.2
-.4
Passive?
look for duplicate scan
835-7-Ø-BACK

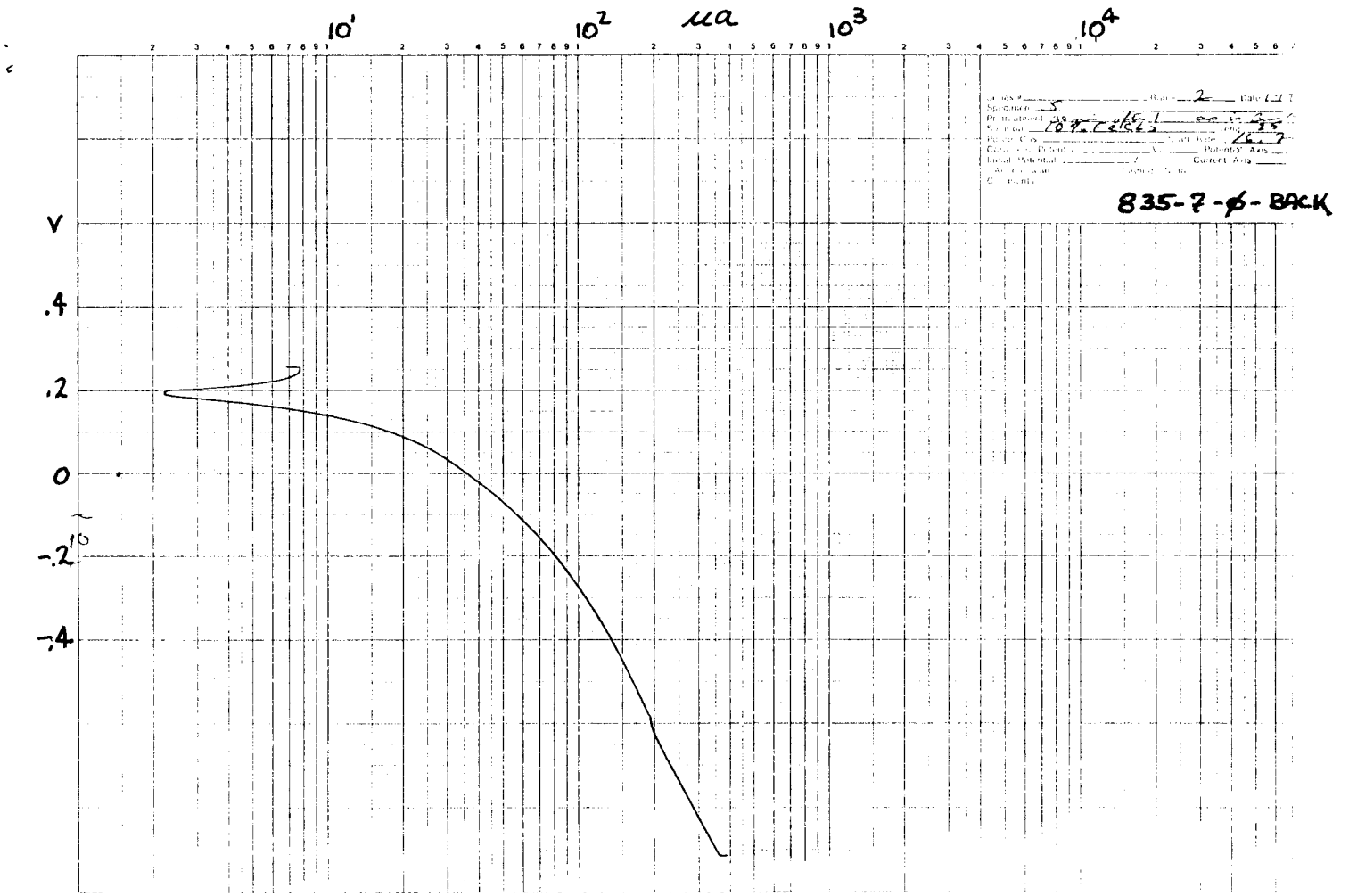

CORROSION CURVE RECORD

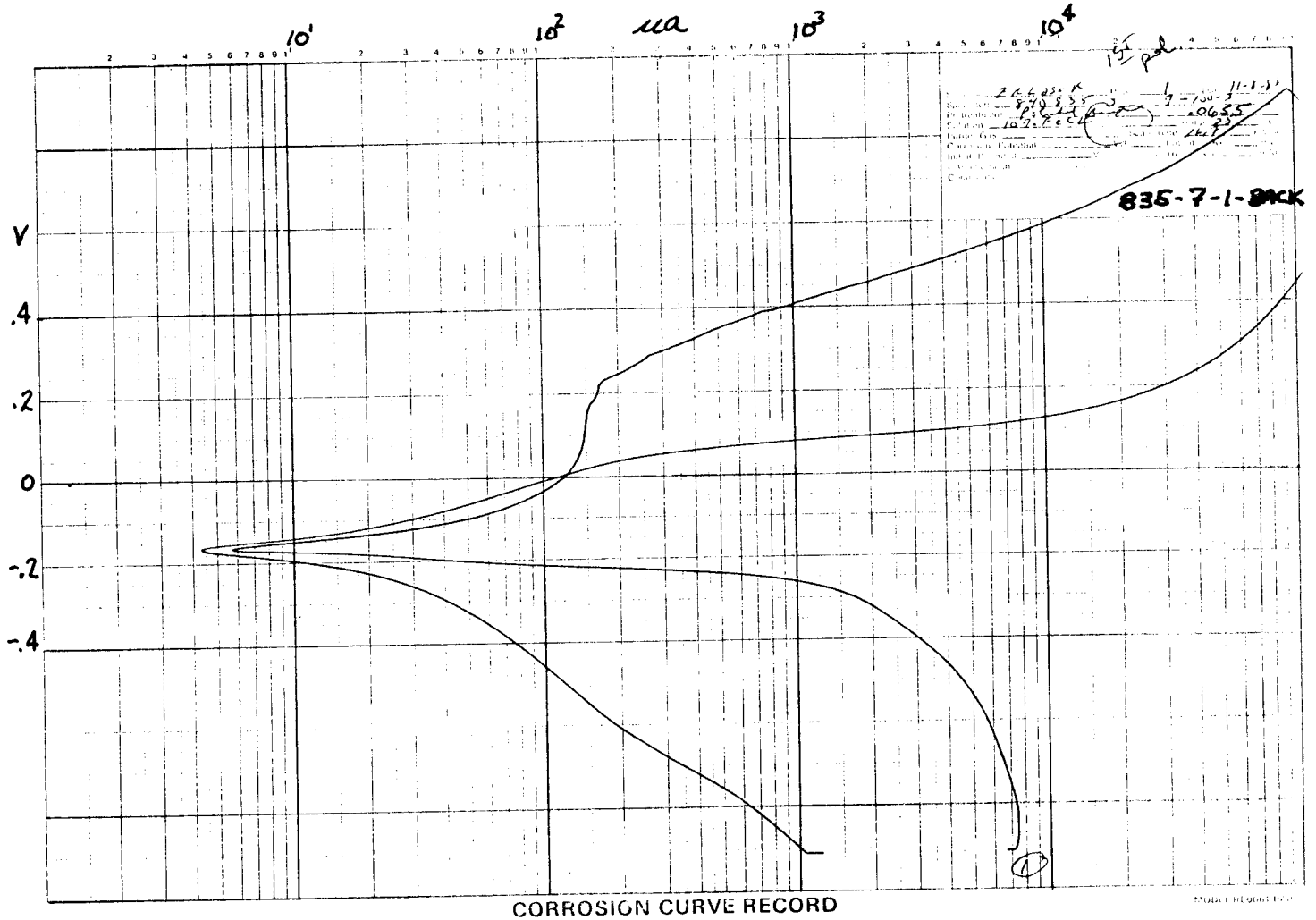

CORROSION CURVE RECORD

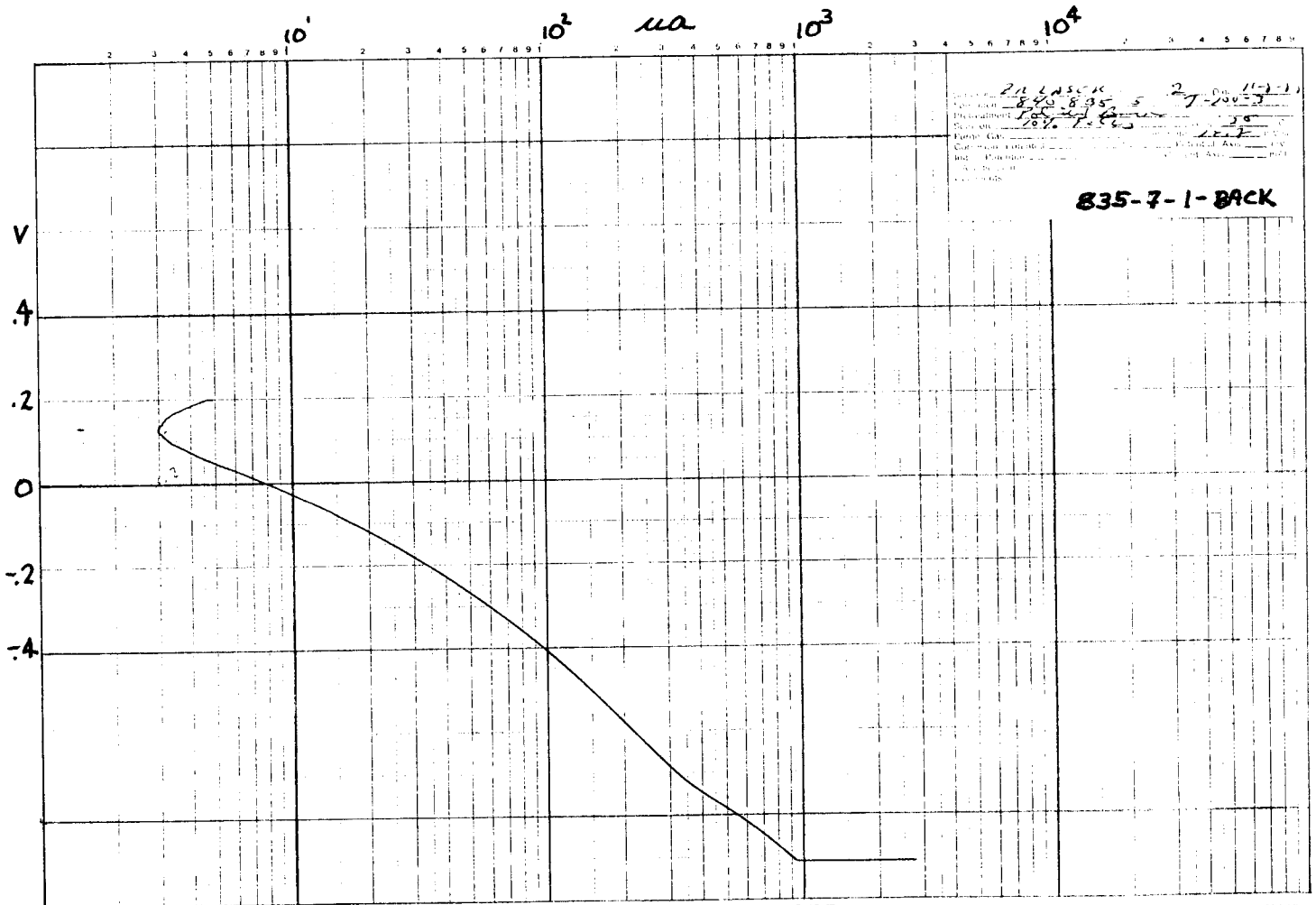

CORROSION CURVE RECORD

MODEL RE0061 PAPER

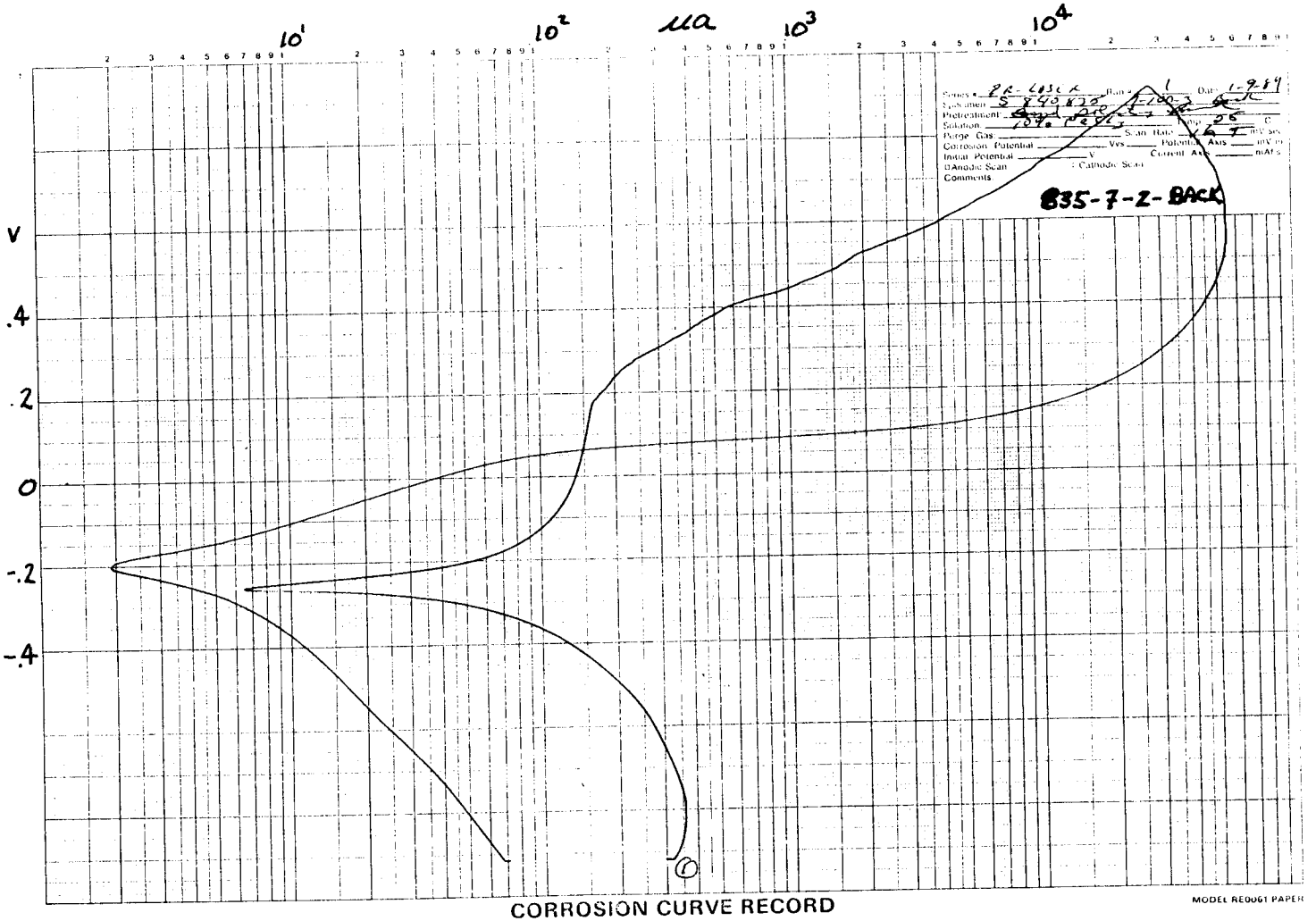

CORROSION CURVE RECORD

MODEL RE0061 PAPER

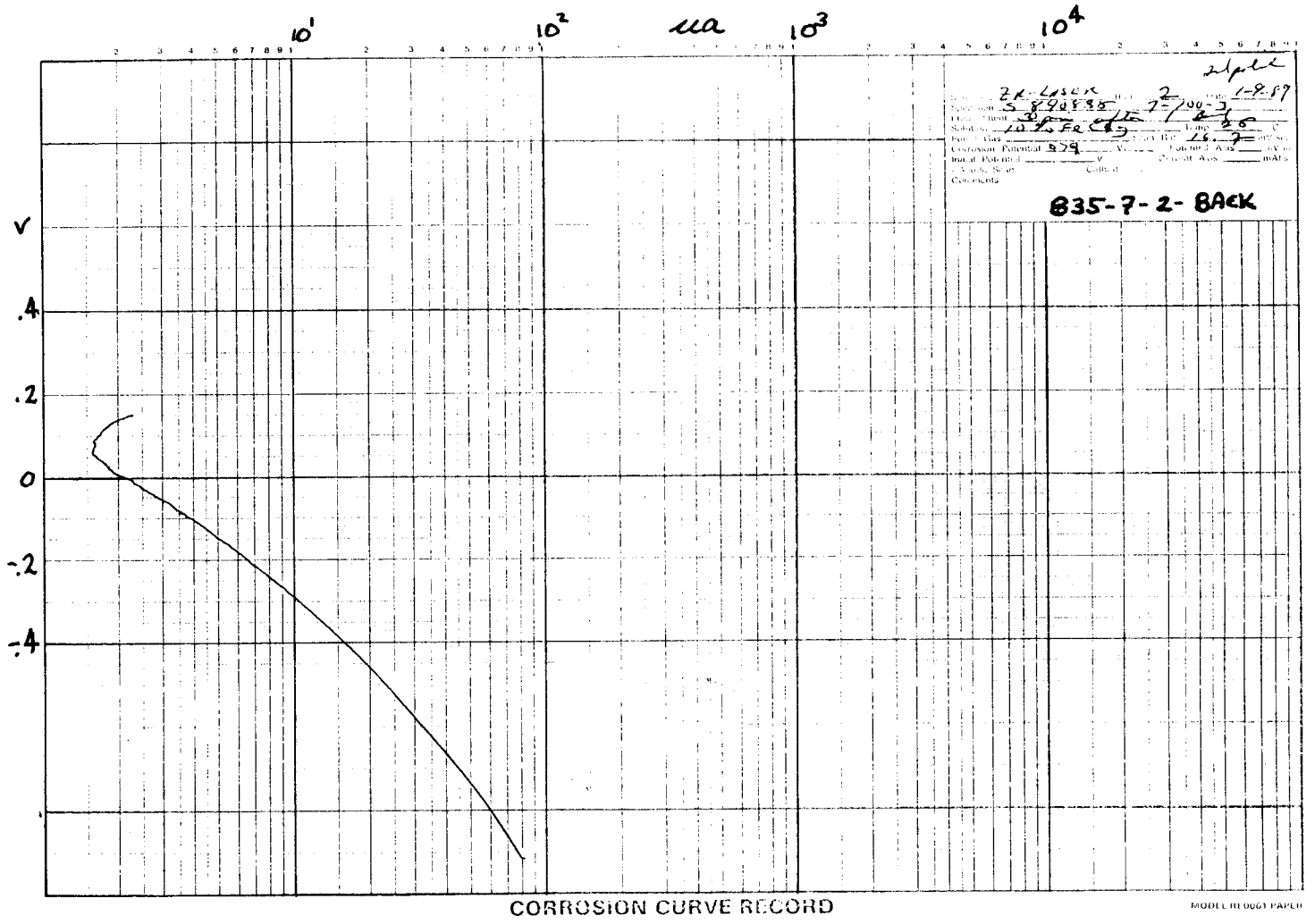
10¹
10²
ua
10³
10⁴
V
.4
.2
0
-.2
-.4
B35-7-2- BACK
CORROSION CURVE RECORD

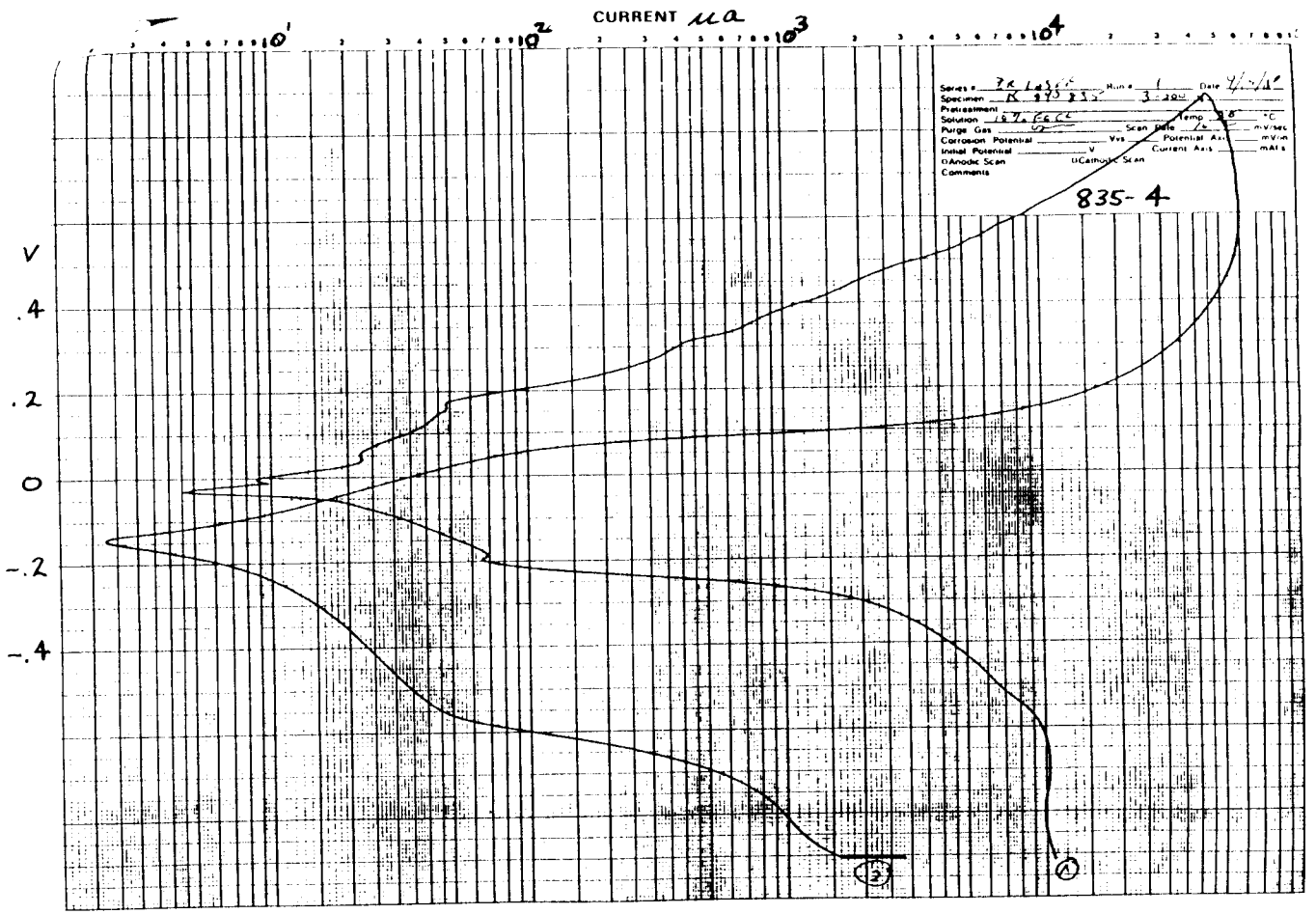
CURRENT μa
10¹
10²
10³
10⁴
V
.4
.2
0
-.2
-.4
Series
Run 1
Date
Specimen
Pretreatment
Solution
Temp
°C
Purge Gas
Scan Rate
mV/sec
Corrosion Potential
Vvs
Potential Axis
mV/in
Initial Potential
V
Current Axis
mA/s
Anodic Scan
Cathodic Scan
Comments
835-4
A
B

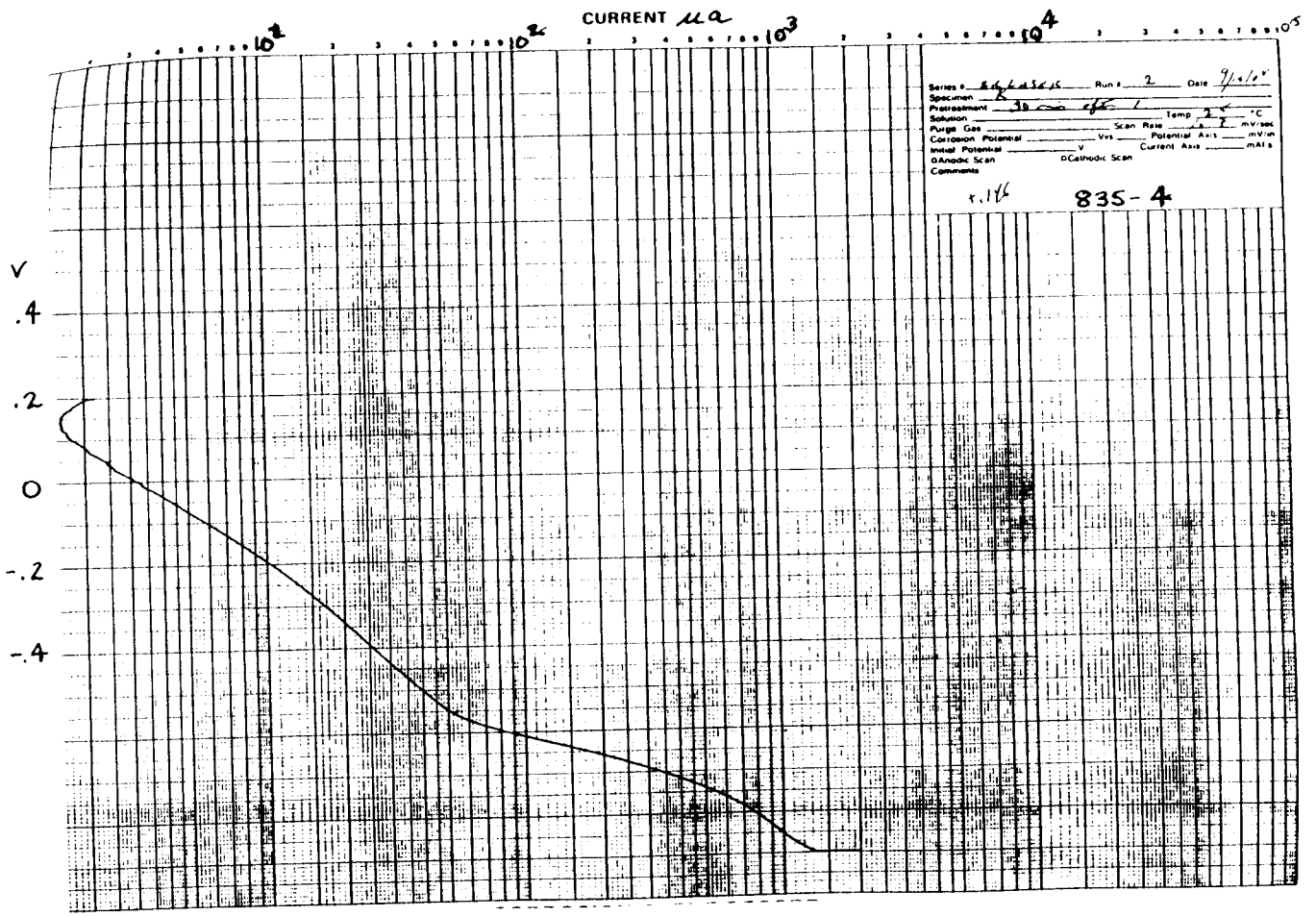
CURRENT μa
10²
10³
10⁴
10⁵
V
.4
.2
0
-.2
-.4
Series # 835-4
Run # 2
Date 9/6/8
Specimen
Pretreatment
Solution
Temp °C
Purge Gas
Scan Rate mV/sec
Corrosion Potential Vvs
Potential Axis mV/in
Initial Potential V
Current Axis mA/in
Anodic Scan
Cathodic Scan
Comments
835-4

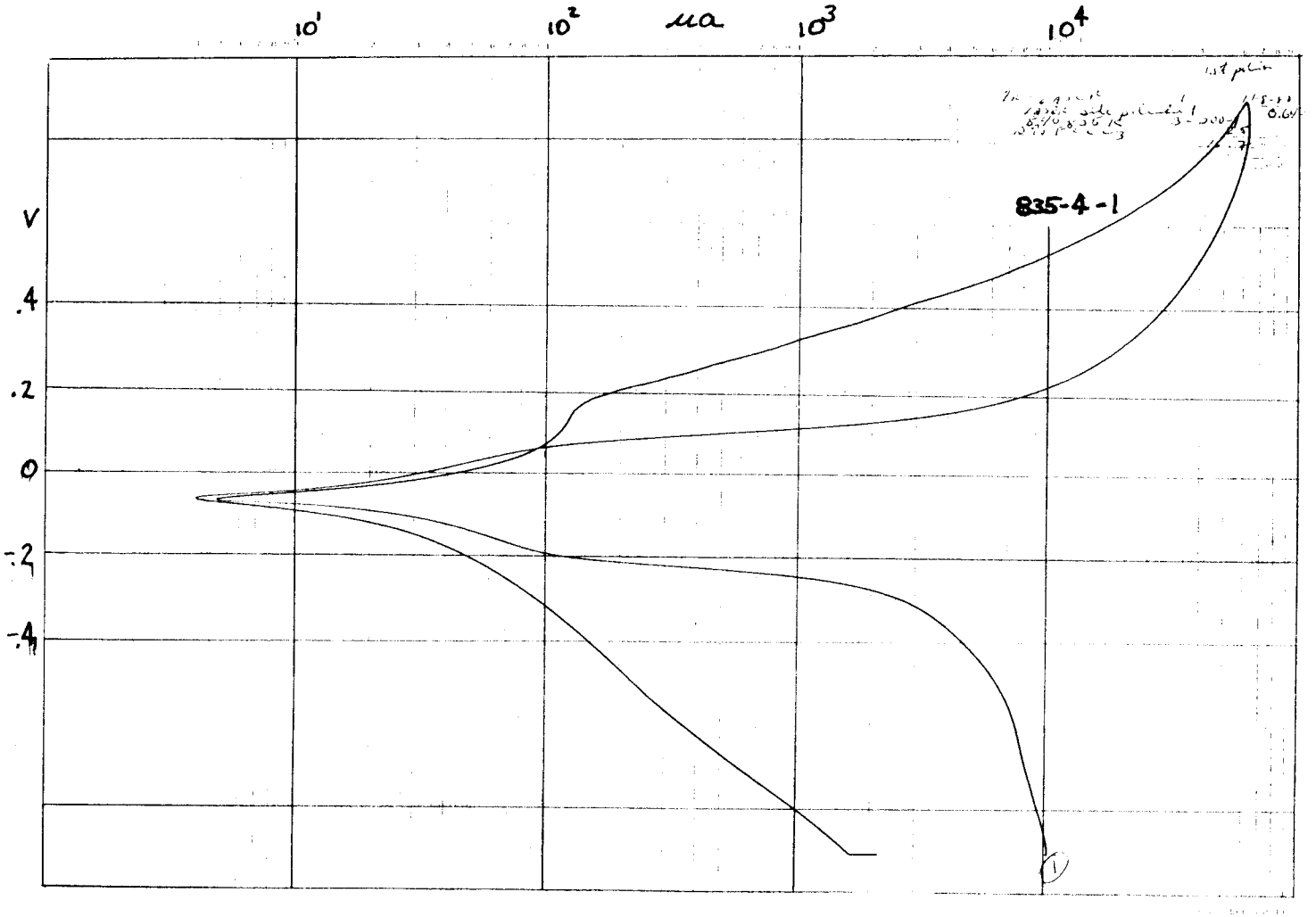
10¹
10²
μa
10³
10⁴
V
.4
.2
0
-.2
-.4
835-4-1

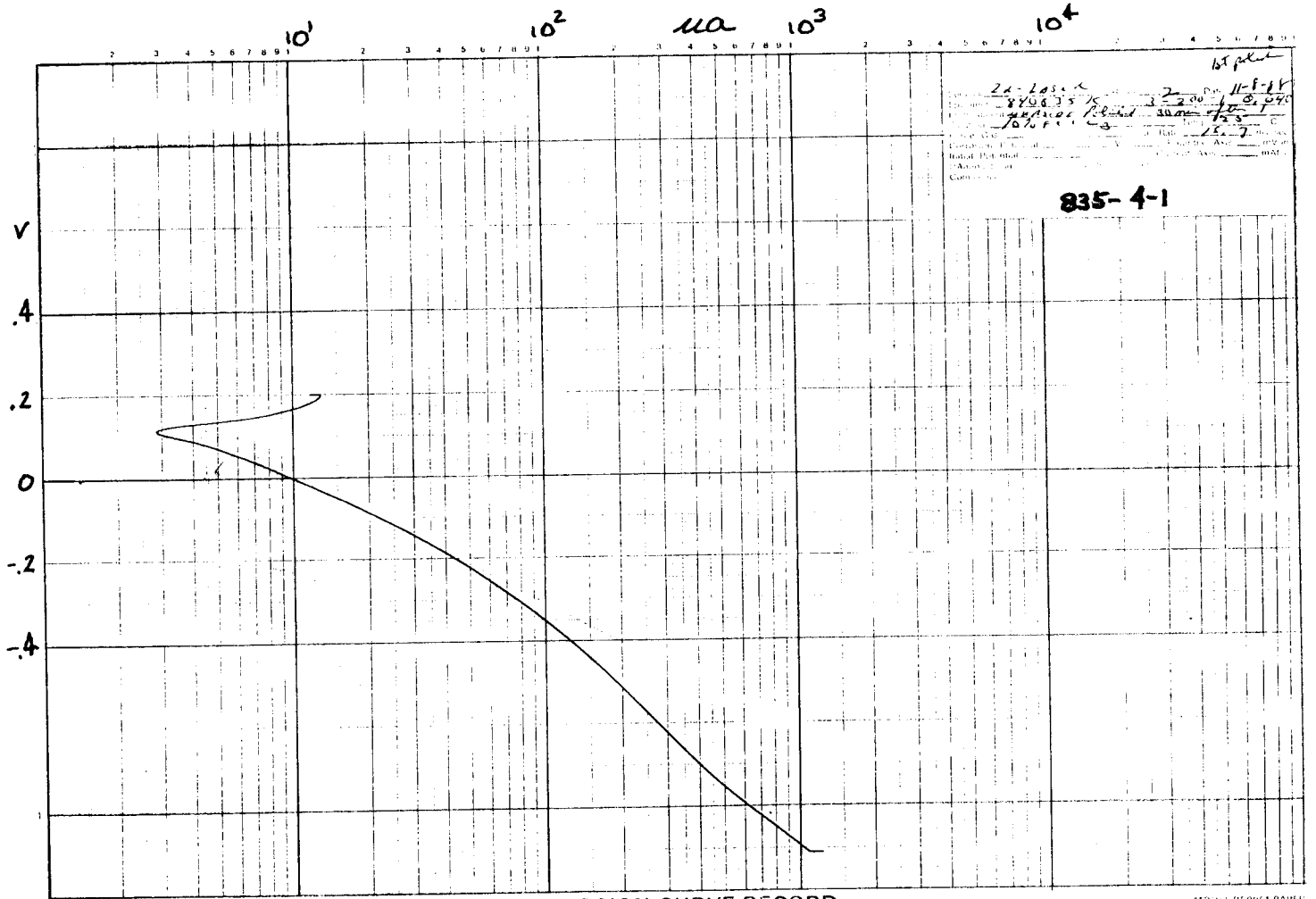

CORROSION CURVE RECORD

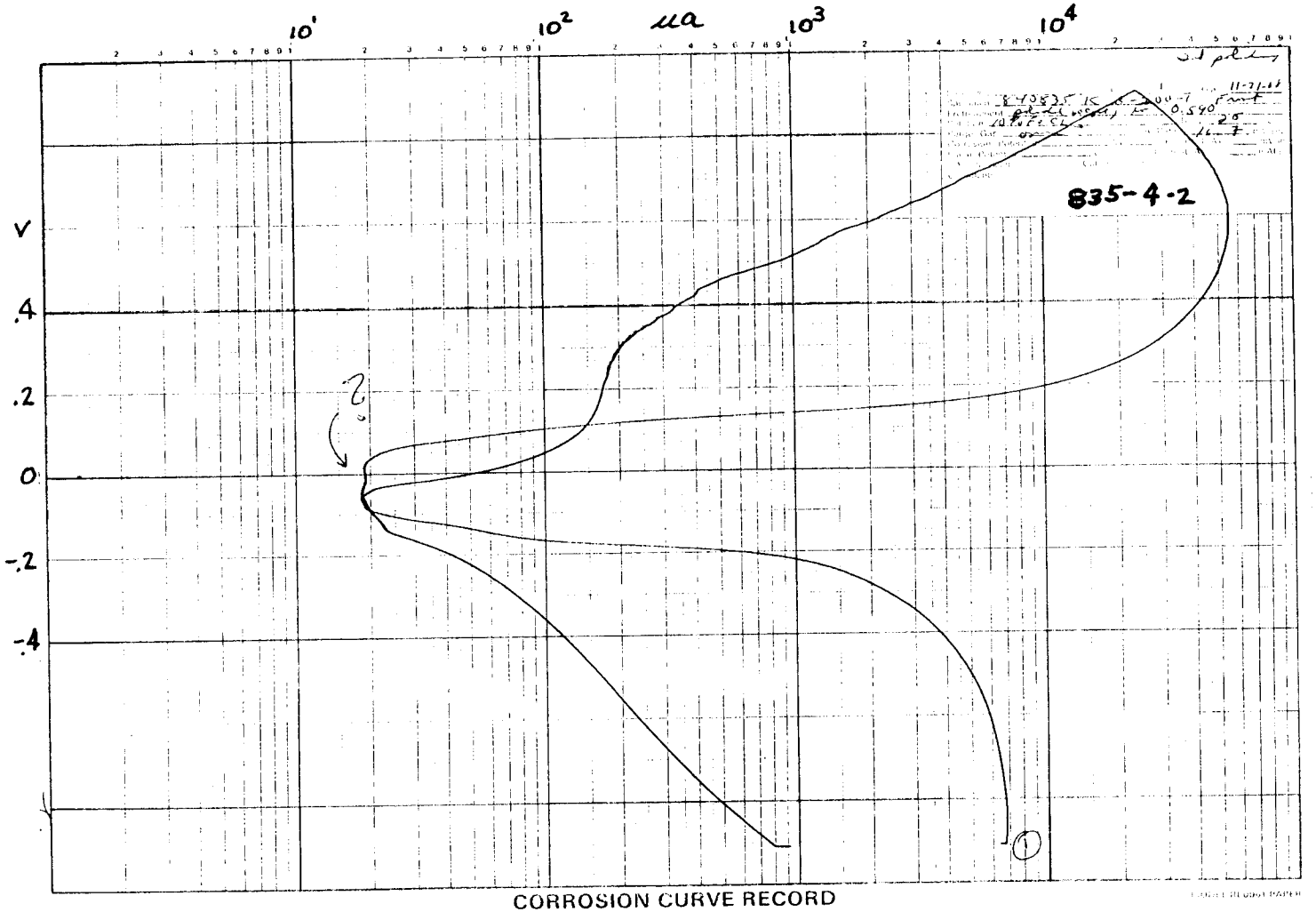

CORROSION CURVE RECORD

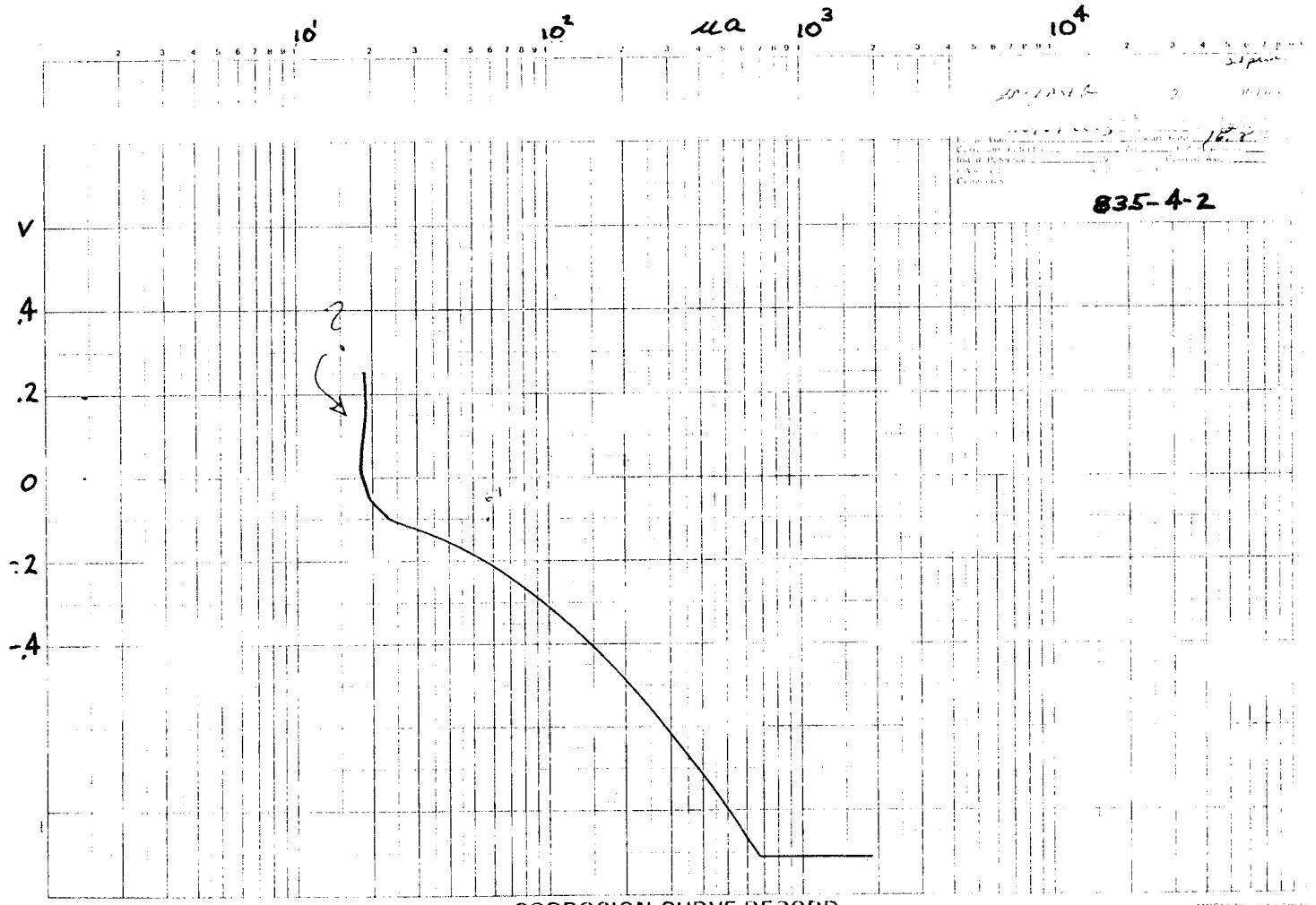

CORROSION CURVE RECORD

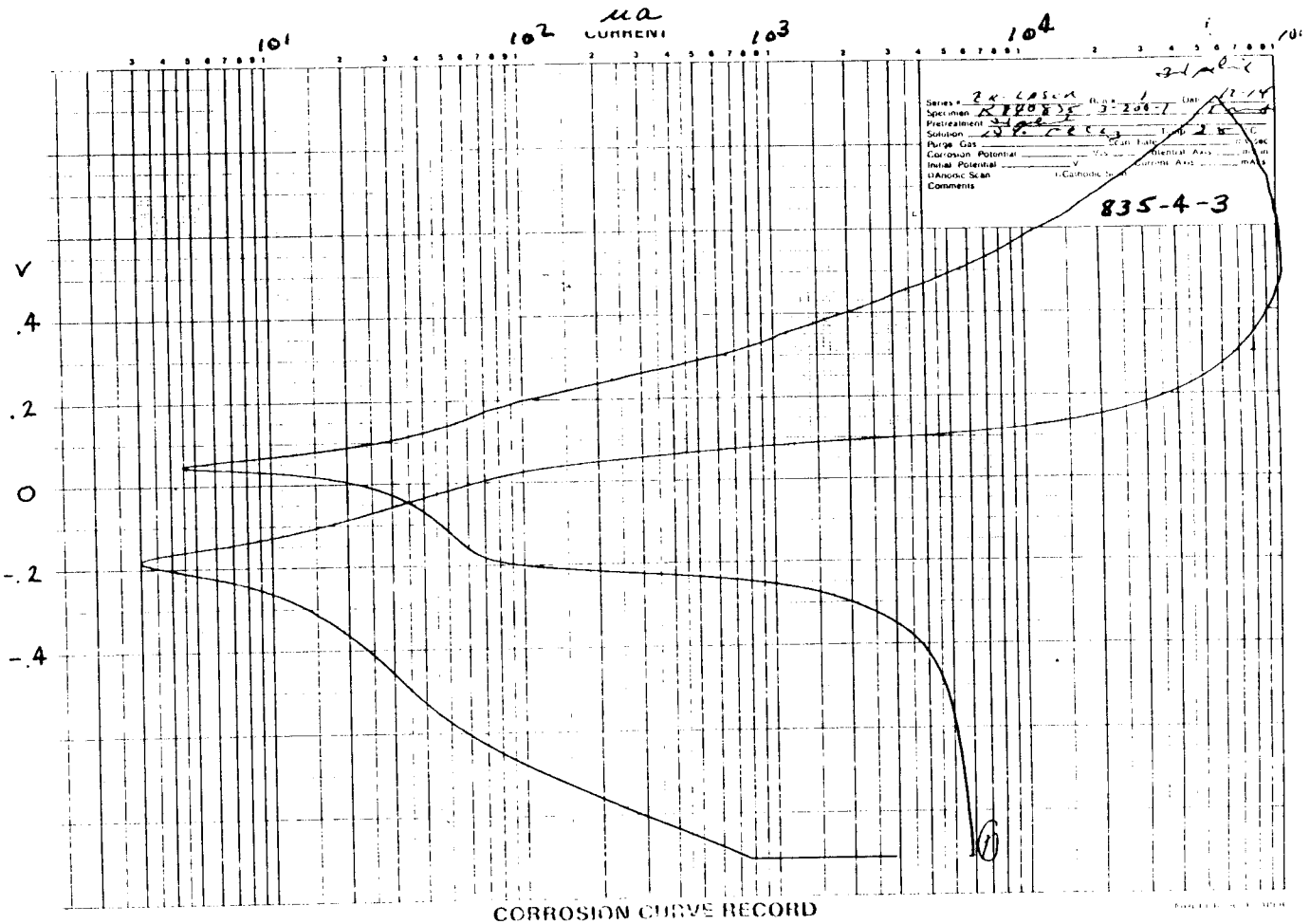

CORROSION CURVE RECORD

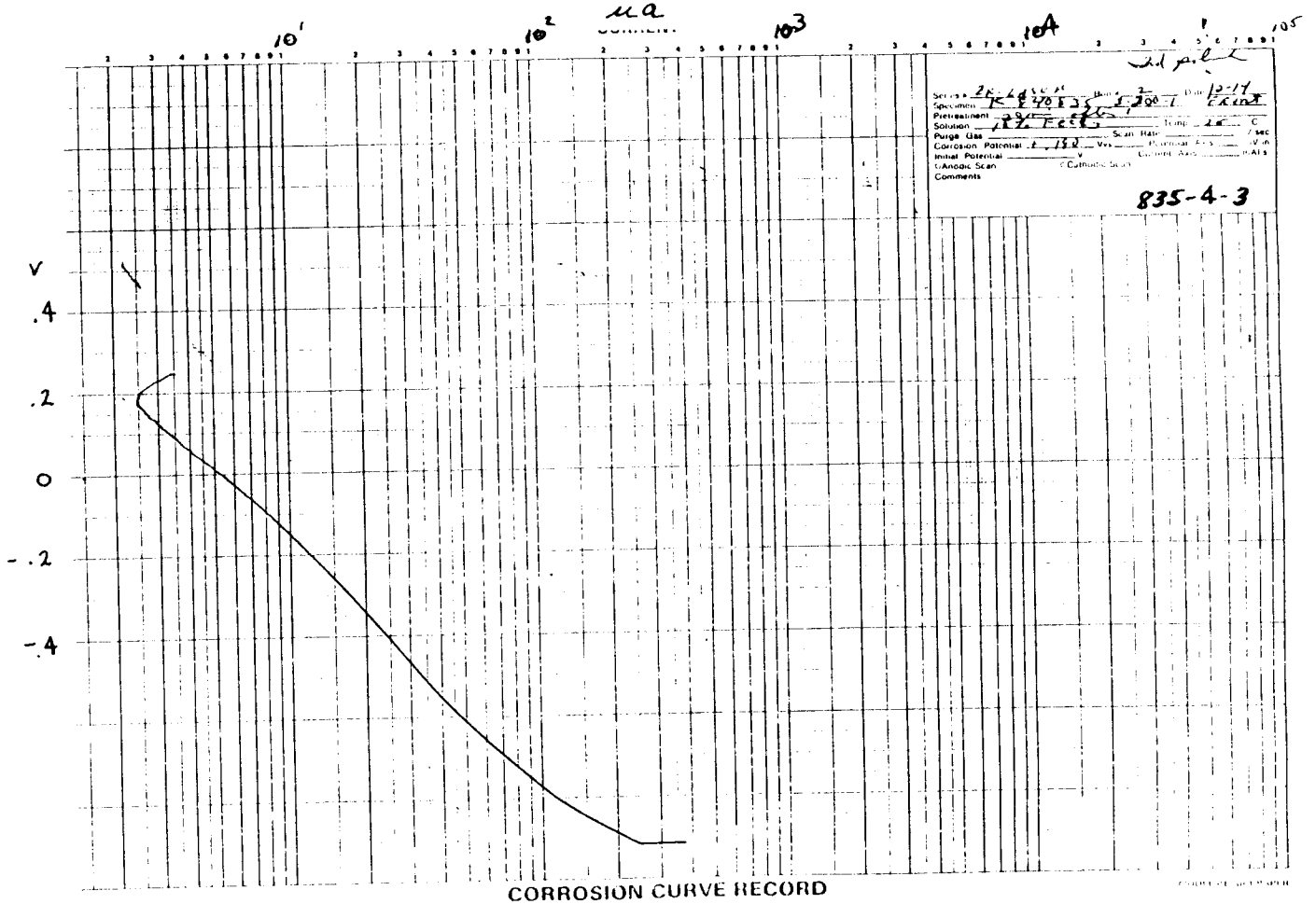

CORROSION CURVE RECORD

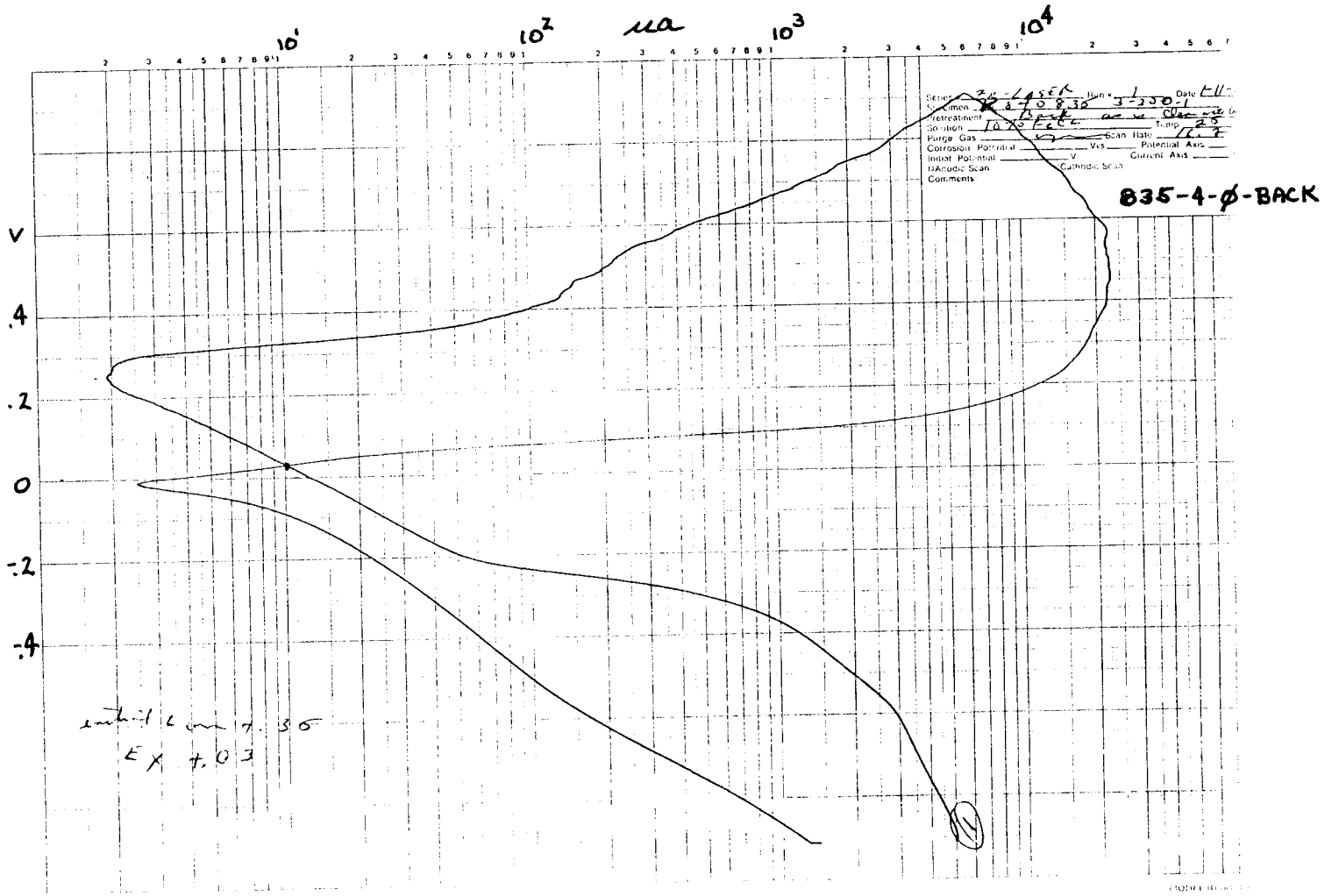
ua
10^1
10^2
10^3
10^4
V
.4
.2
0
-.2
-.4
Series
Specimen
Pretreatment
Solution
Purge Gas
Corrosion Potential
Initial Potential
Anodic Scan
Cathodic Scan
Comments
Run #
Date
Temp
Scan Rate
Potential Axis
Current Axis
835-4-ø-BACK
initial corr 7.35
Ex +.03

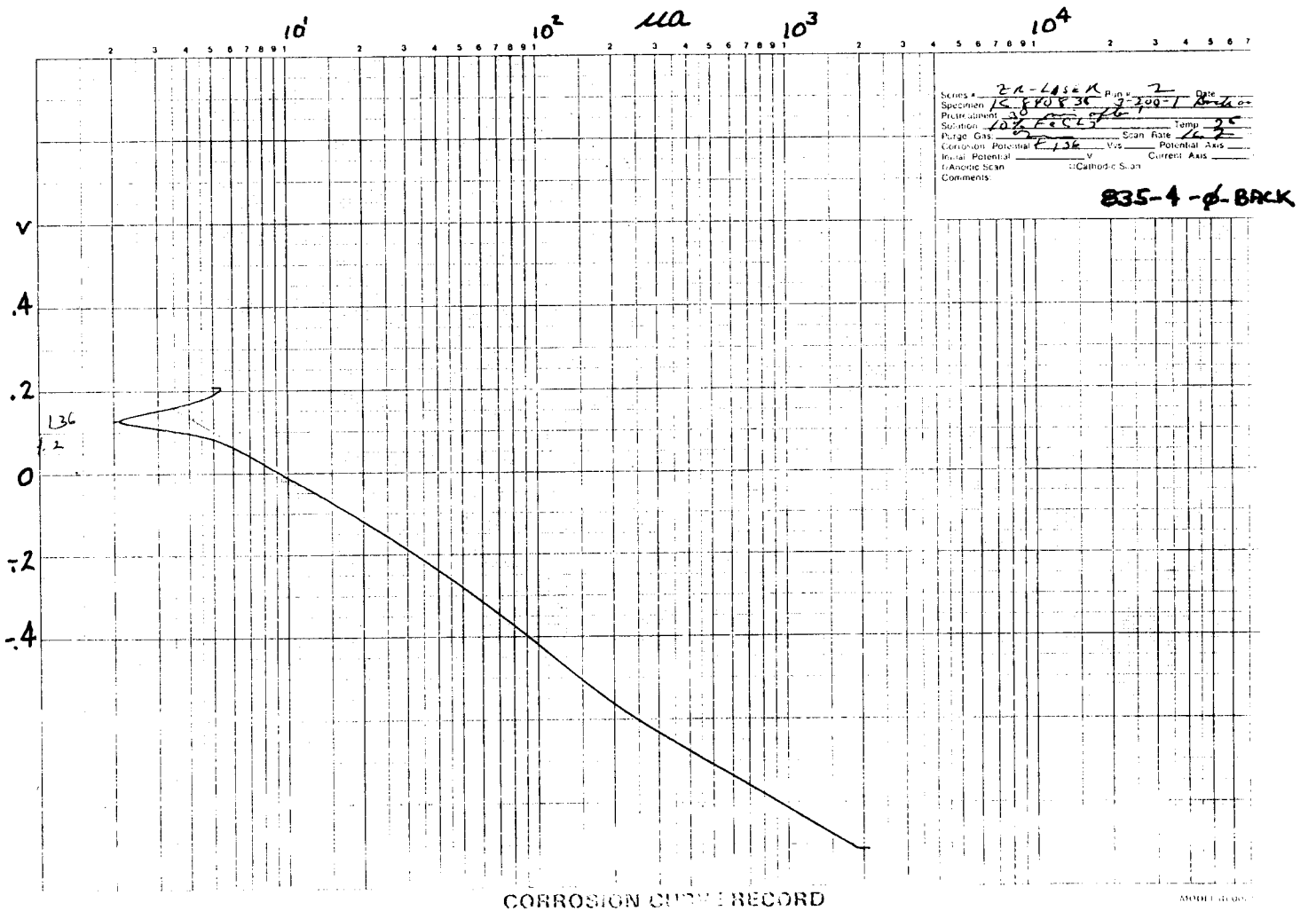
μa
10¹
10²
10³
10⁴
V
.4
.2
0
-.2
-.4
L36
1.2
Series # 2R-LASER Run # 2 Date
Specimen 1C 840835 2-200-1
Pretreatment
Solution 10% FeCl3 Temp 25
Purge Gas Scan Rate
Corrosion Potential -.136 V vs Potential Axis
Initial Potential V Current Axis
Anodic Scan Cathodic Scan
Comments:
835-4-Ø-BACK
CORROSION CURVE RECORD

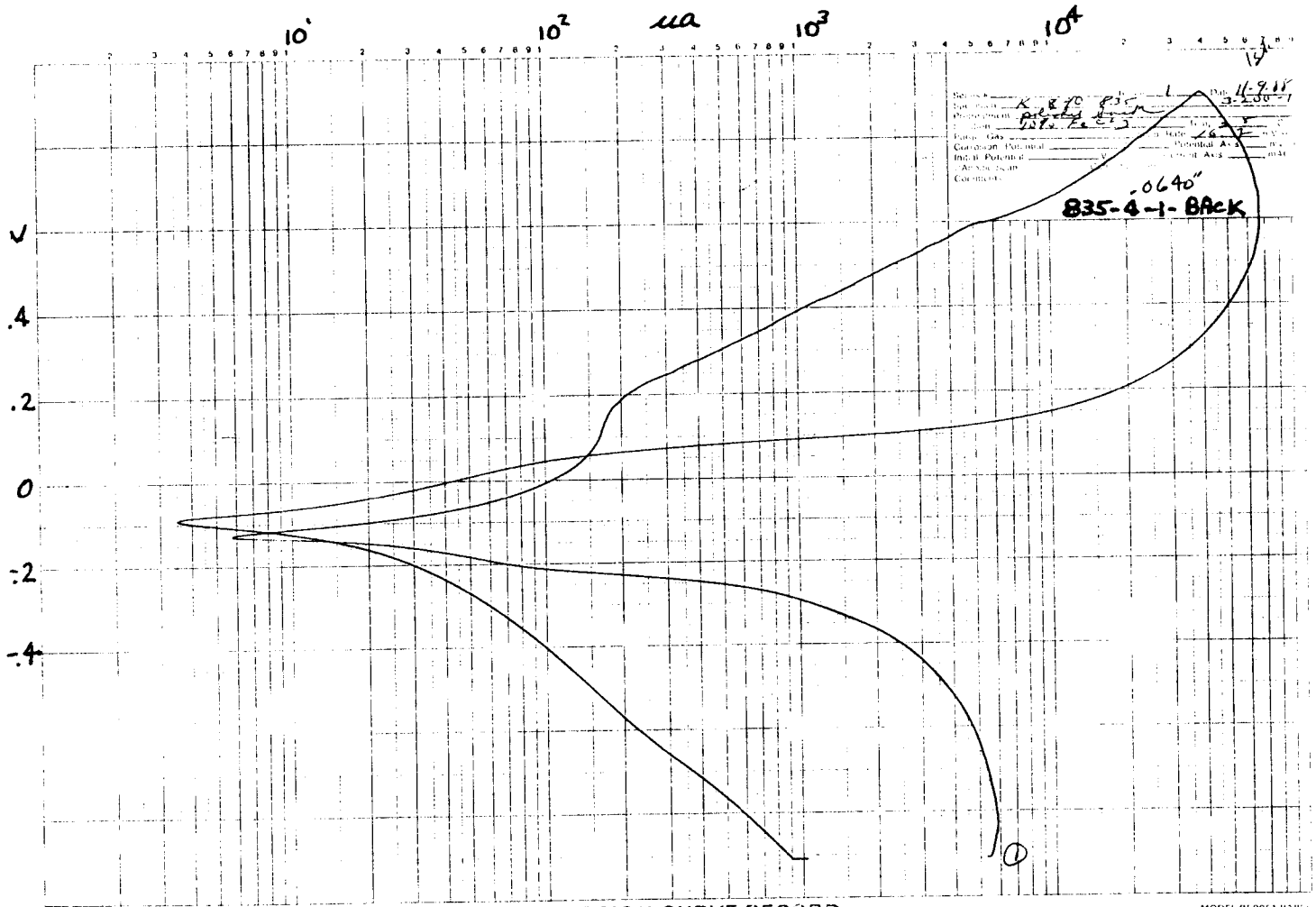
10¹
10²
ua
10³
10⁴
V
.4
.2
0
-.2
-.4
835-4-1-BACK
.0640"
CORROSION CURVE RECORD
MODEL RL0061 PAPER

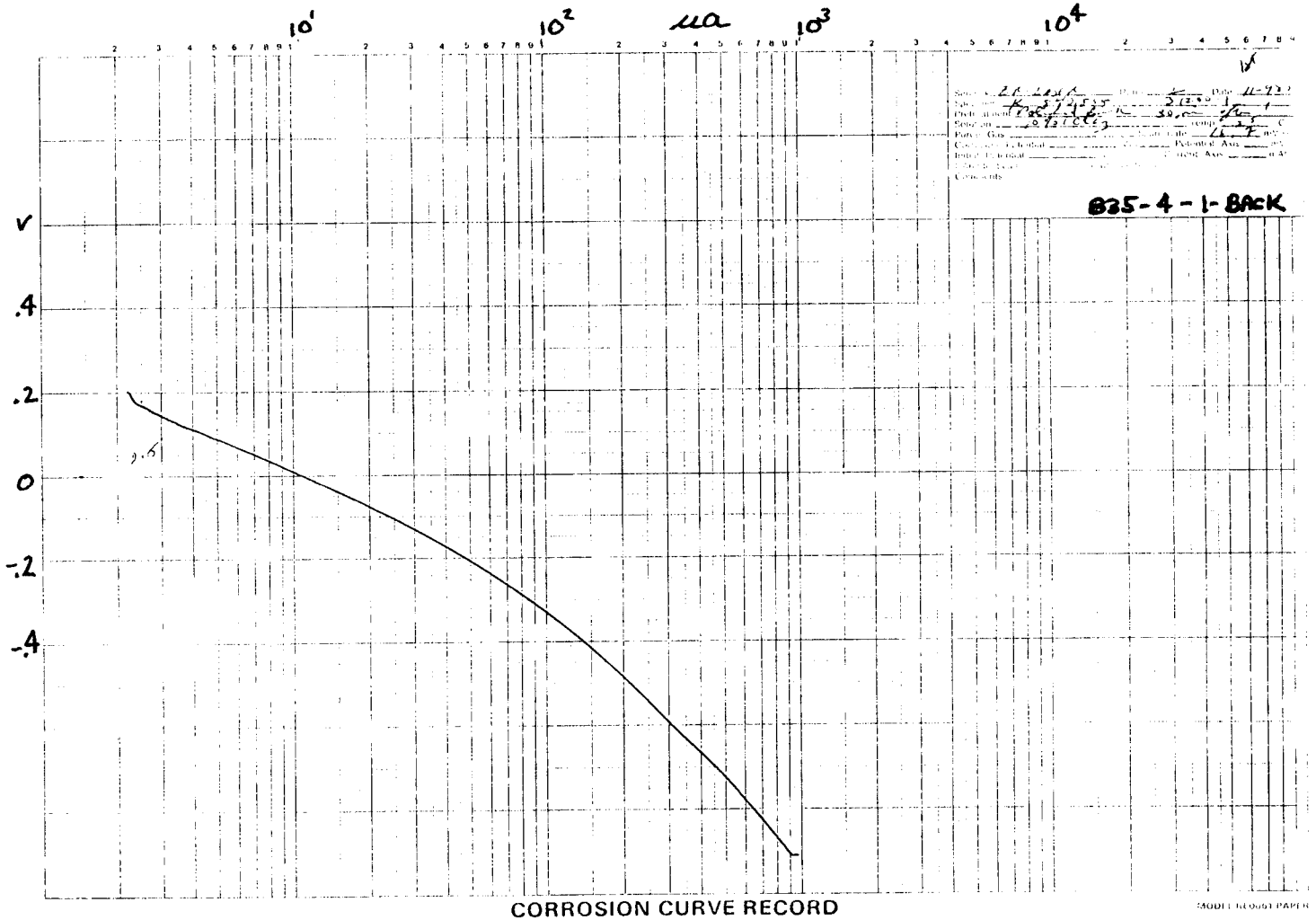

CORROSION CURVE RECORD

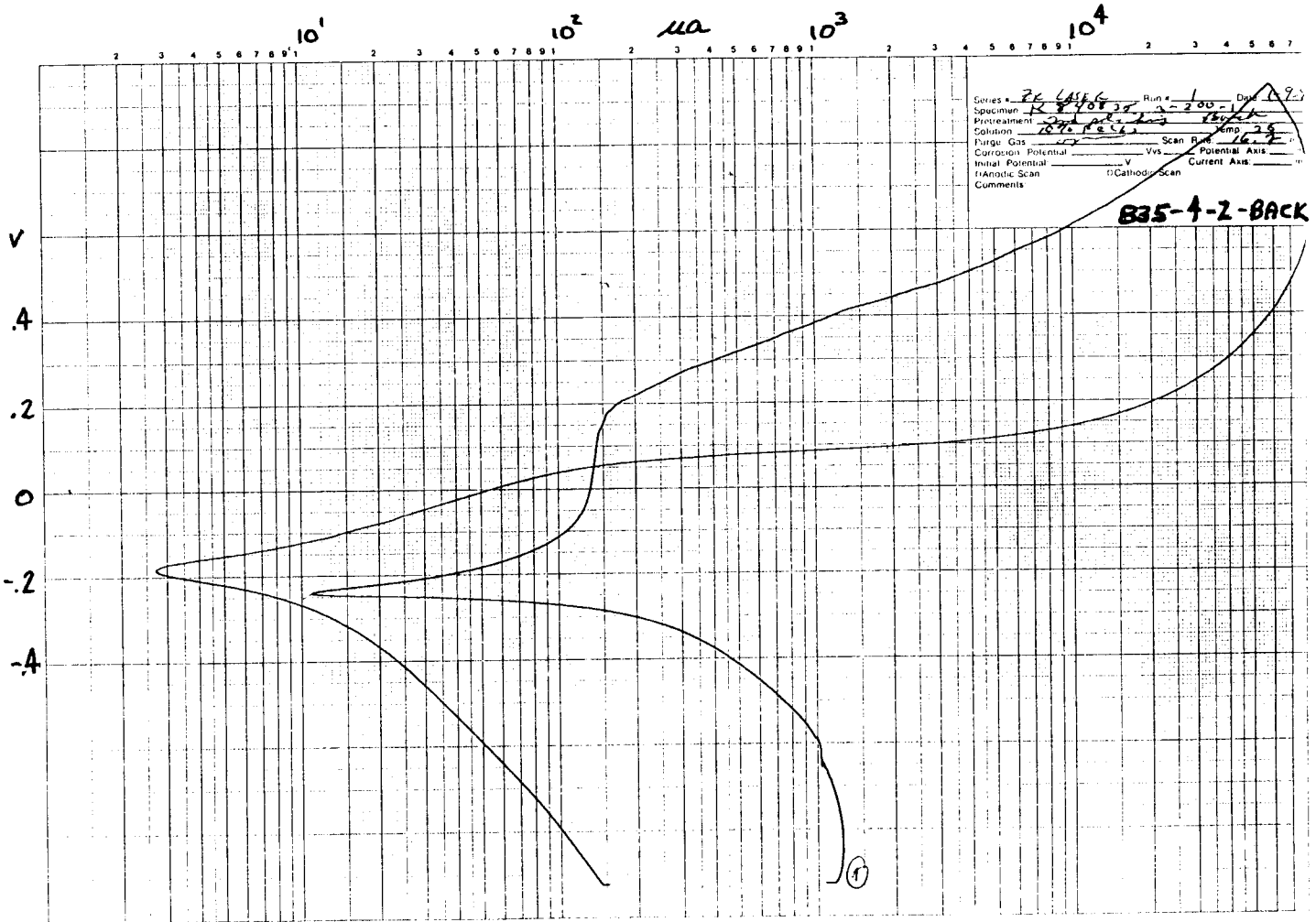

CORROSION CURVE RECORD

MODEL RE0061

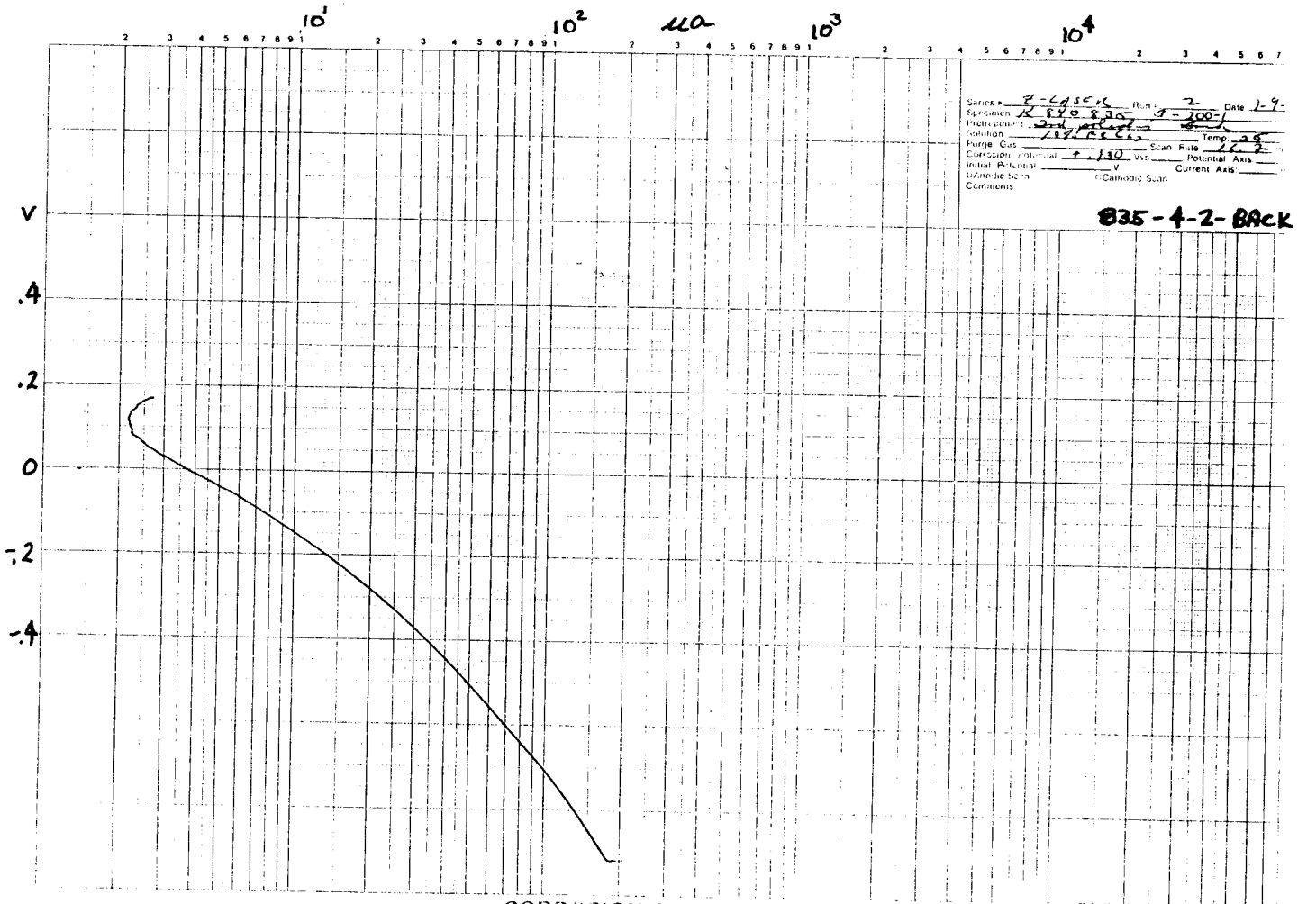

CORROSION CURVE RECORD

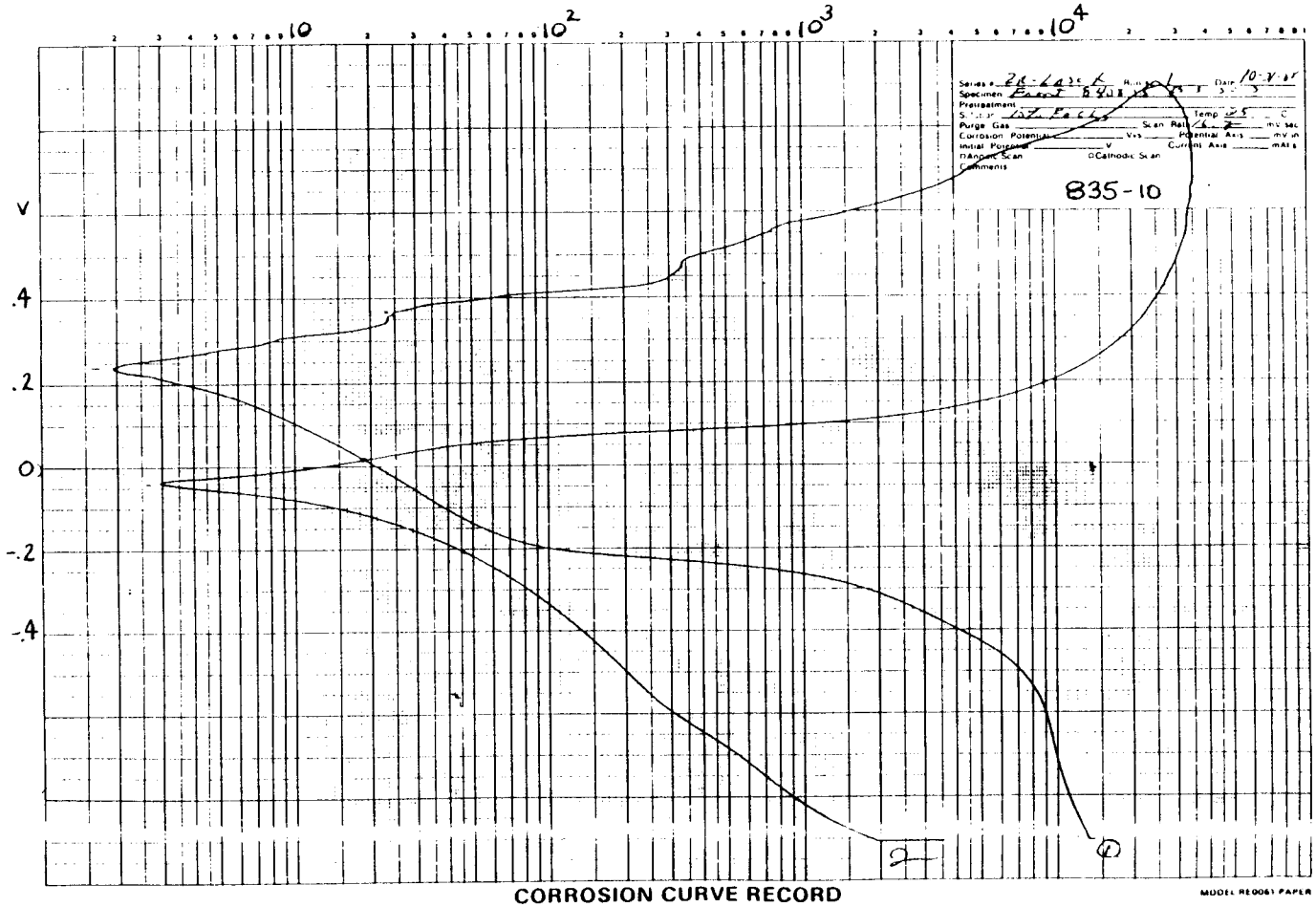

CORROSION CURVE RECORD

MODEL RE0061 PAPER

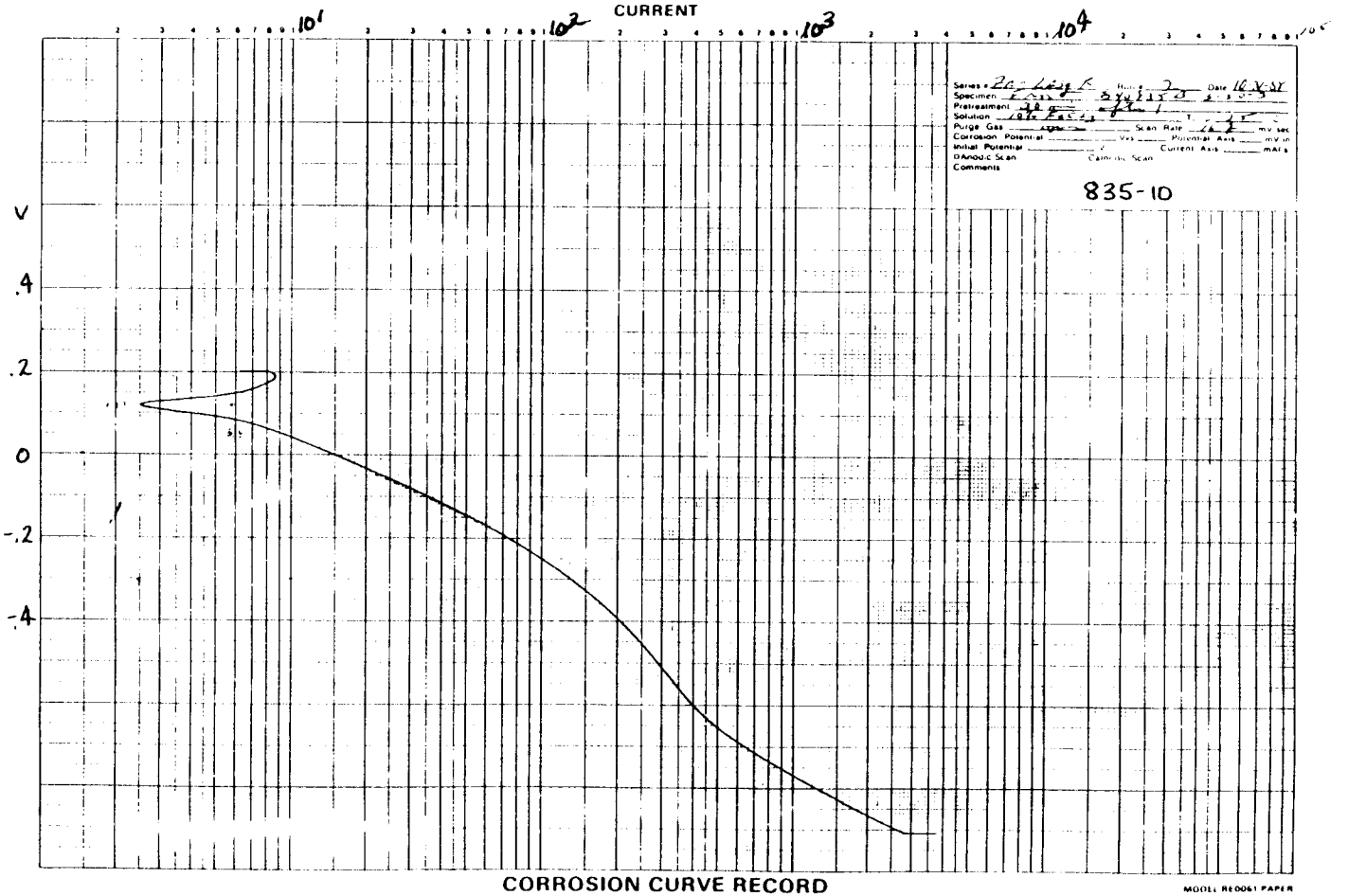

CORROSION CURVE RECORD

MODEL RE0061 PAPER

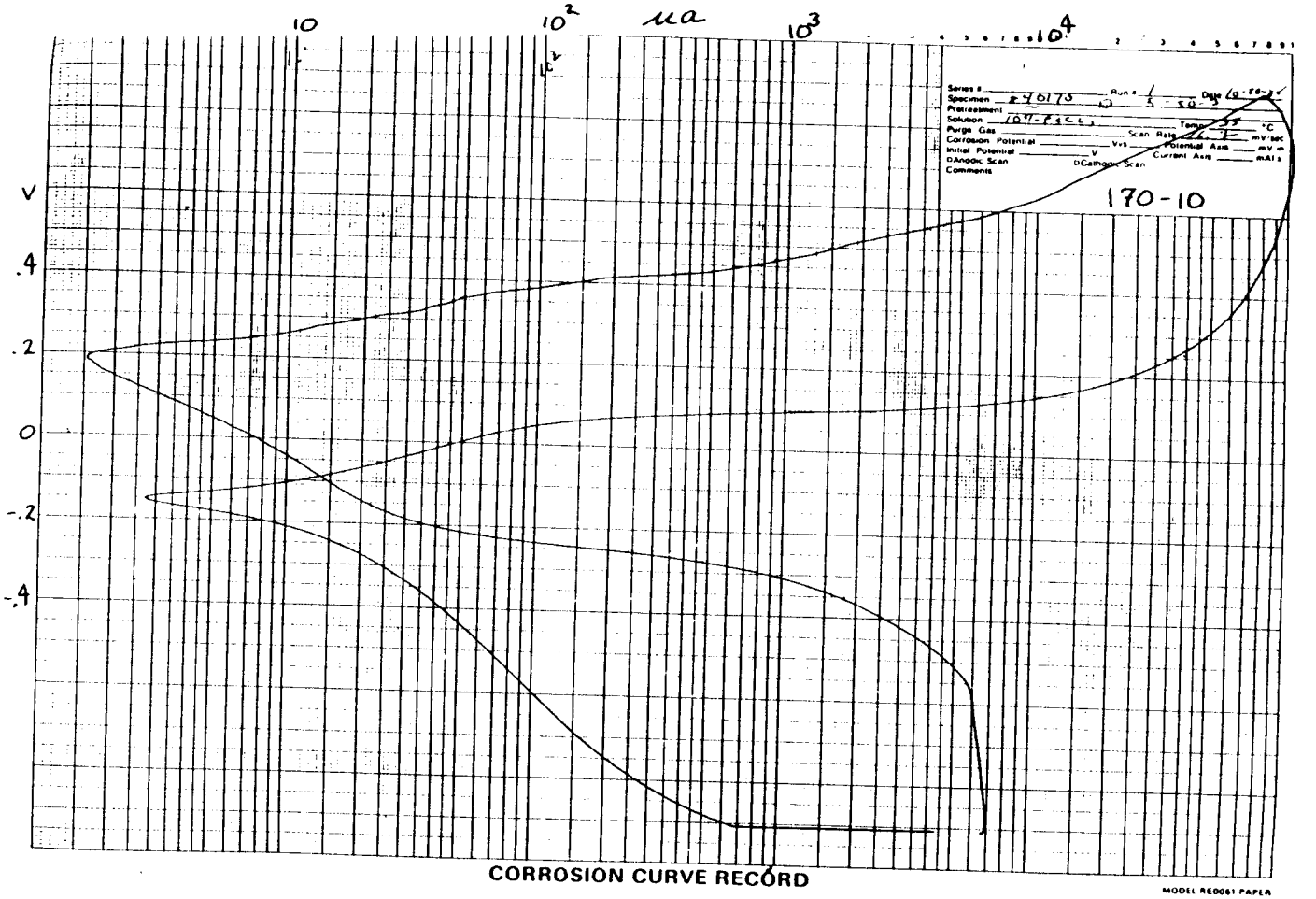

CORROSION CURVE RECORD

MODEL RE0081 PAPER

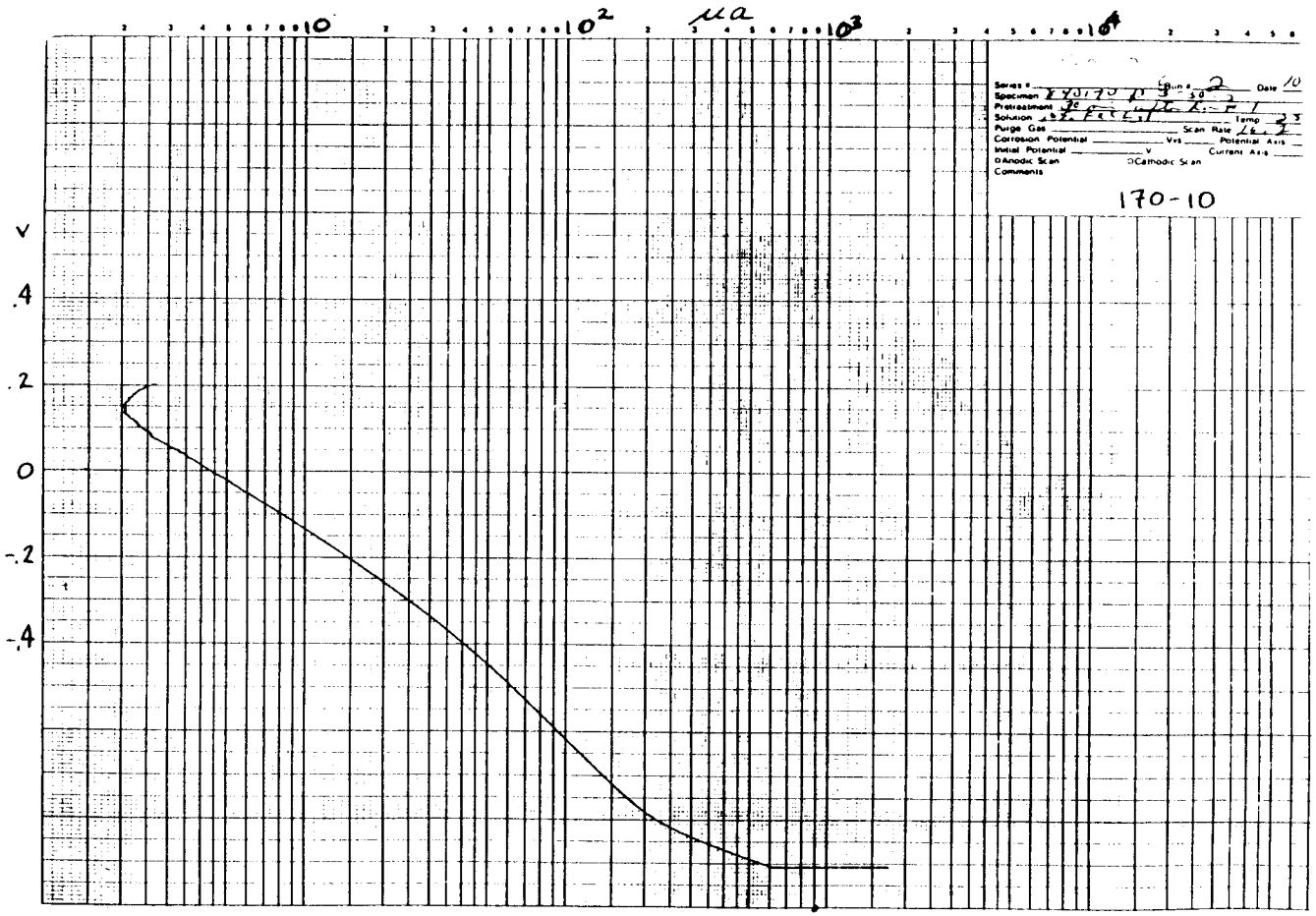
μa
10
10²
10³
10⁴
V
.4
.2
0
-.2
-.4
Series #
Run # 2
Date 10
Specimen
Pretreatment
Solution
Temp
Purge Gas
Scan Rate
Corrosion Potential
Vrs
Potential Axis
Initial Potential
V
Current Axis
Anodic Scan
Cathodic Scan
Comments
170-10

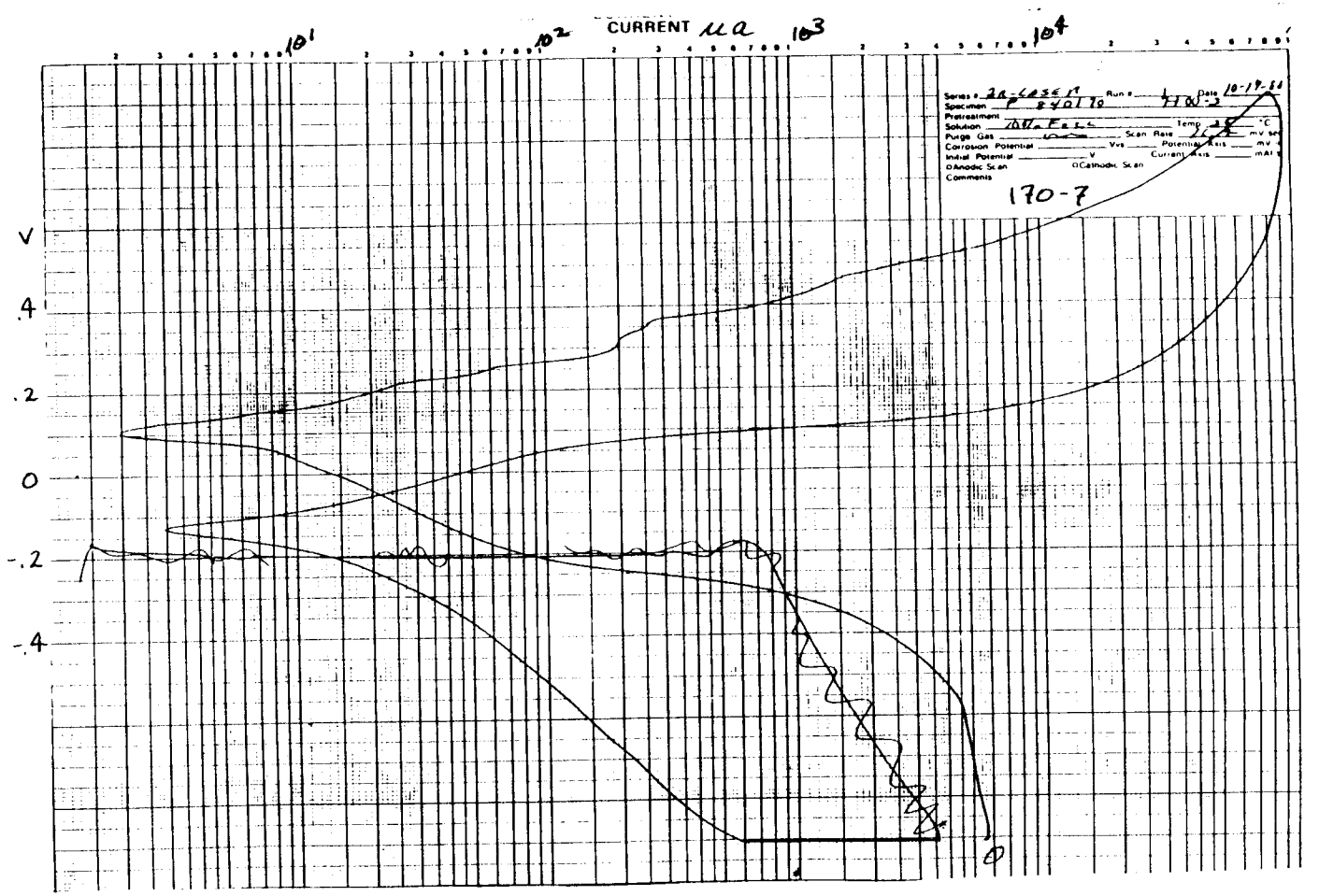
CURRENT μa
10¹
10²
10³
10⁴
V
.4
.2
0
-.2
-.4
Series # 2A-CASE 17
Run # 4
Date 10-19-84
Specimen P 8401 70
Pretreatment
Solution
Temp 25 °C
Purge Gas
Scan Rate
Corrosion Potential
Vvs
Potential Axis
Initial Potential
V
Current Axis
Anodic Scan
Cathodic Scan
Comments
170-7

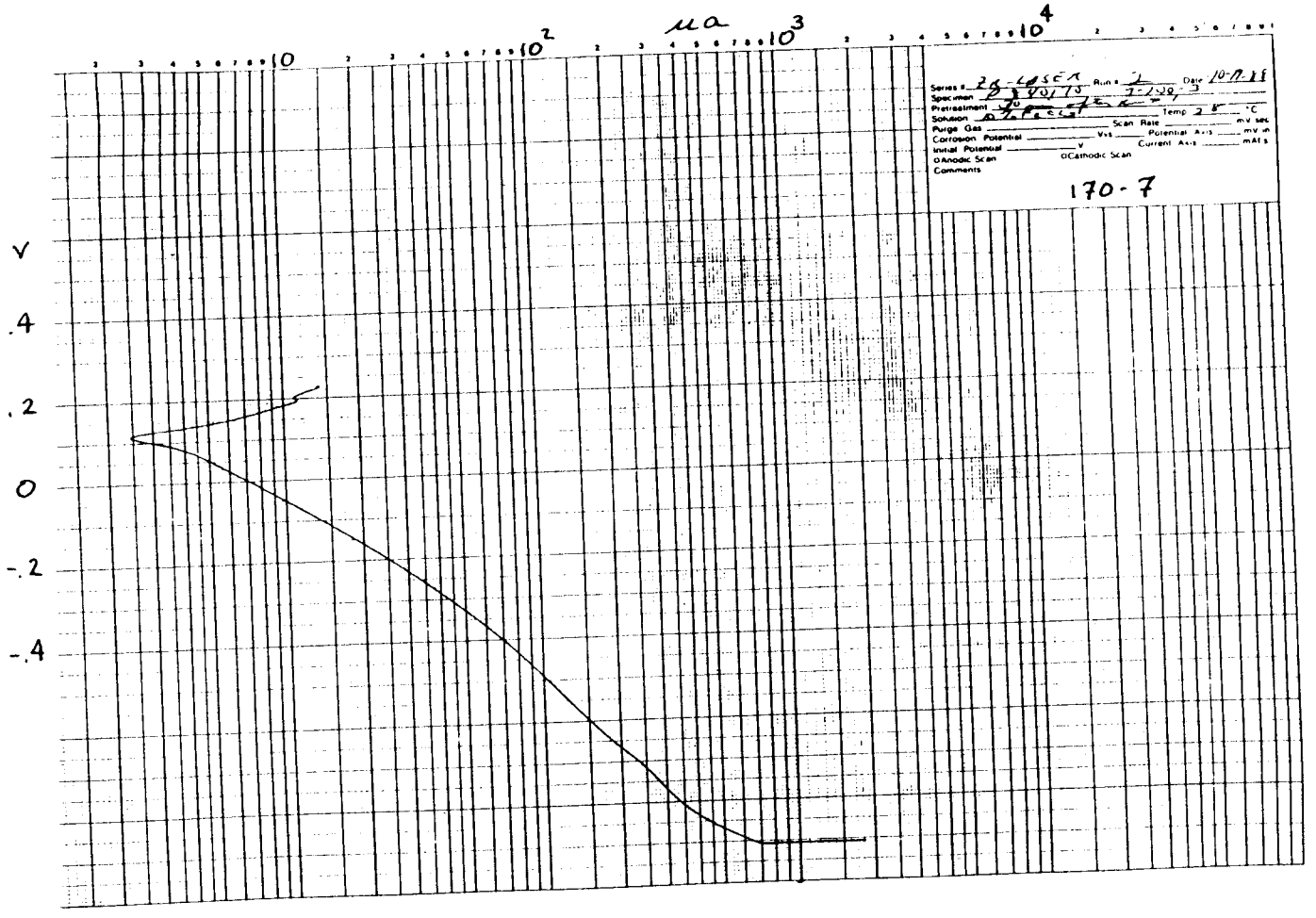
μa
10
10^2
10^3
10^4
V
.4
.2
0
-.2
-.4
Series # 28-LOSCR Run # 1 Date 10-17-88
Specimen B 40/70 2-1/28-3
Pretreatment
Solution
Purge Gas Scan Rate mV sec
Corrosion Potential V vs Potential Axis mV in
Initial Potential V Current Axis mA/s
Anodic Scan Cathodic Scan
Comments
170-7

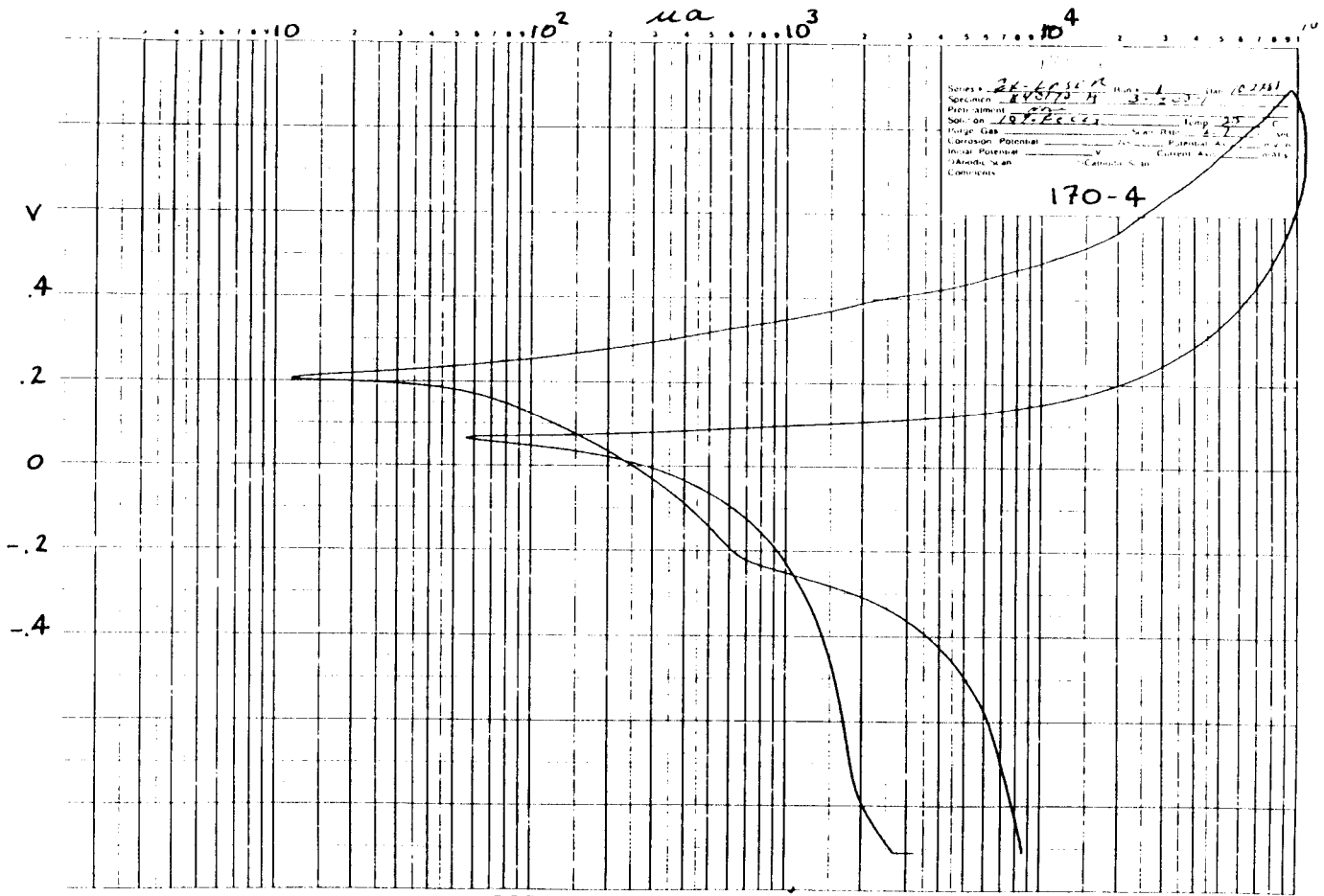

CORROSION CURVE RECORD

MODEL RE0081 EAPLR

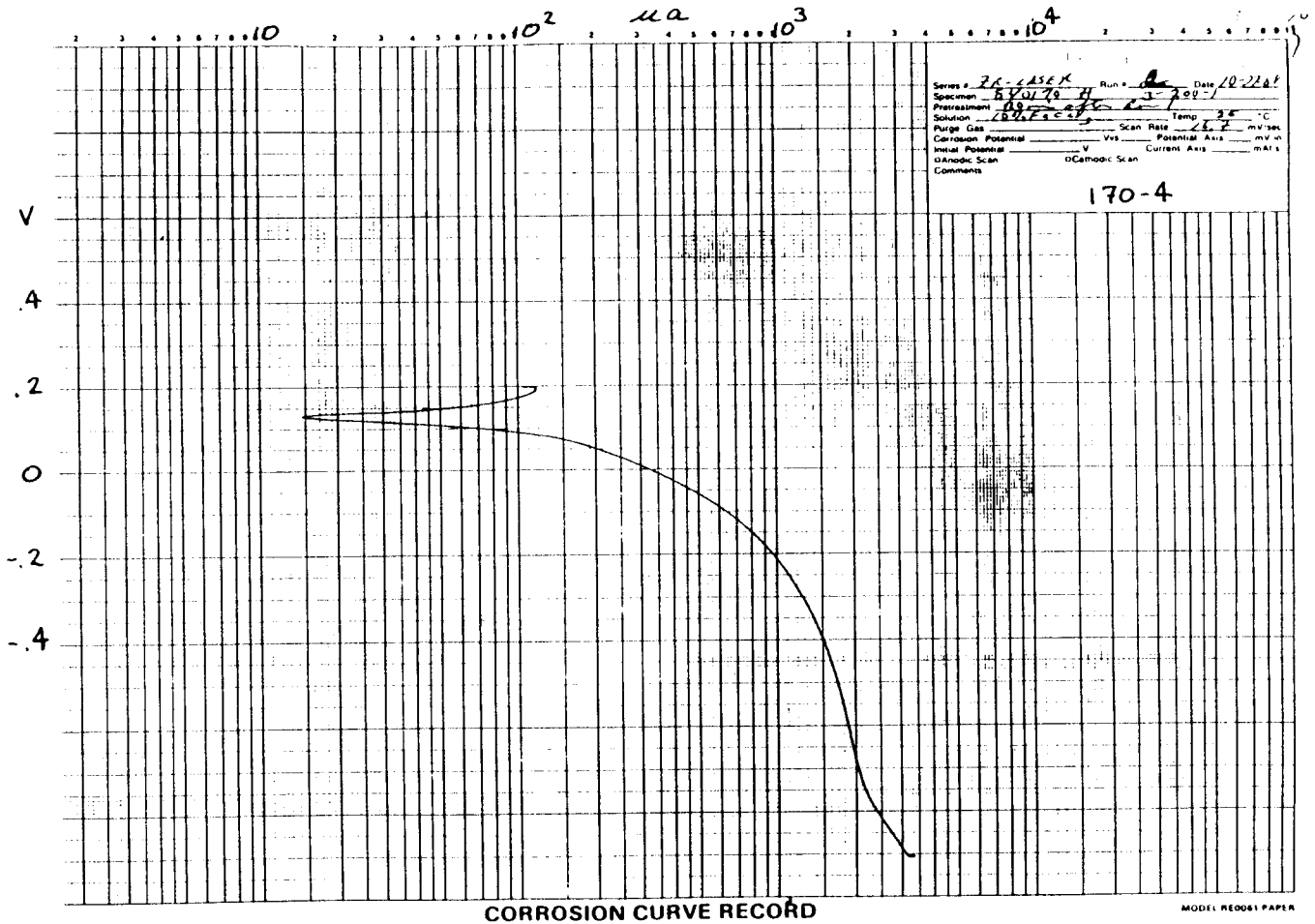
ua
10
10^2
10^3
10^4
V
.4
.2
0
-.2
-.4
Series # ZC-LASER Run # a Date 10-22-81
Specimen BV01 79 H
Pretreatment
Solution
Temp 25 °C
Purge Gas Scan Rate mV/sec
Corrosion Potential Vvs Potential Axis mV/in
Initial Potential V Current Axis mA/in
Anodic Scan Cathodic Scan
Comments
170-4
CORROSION CURVE RECORD
MODEL RE0081 PAPER

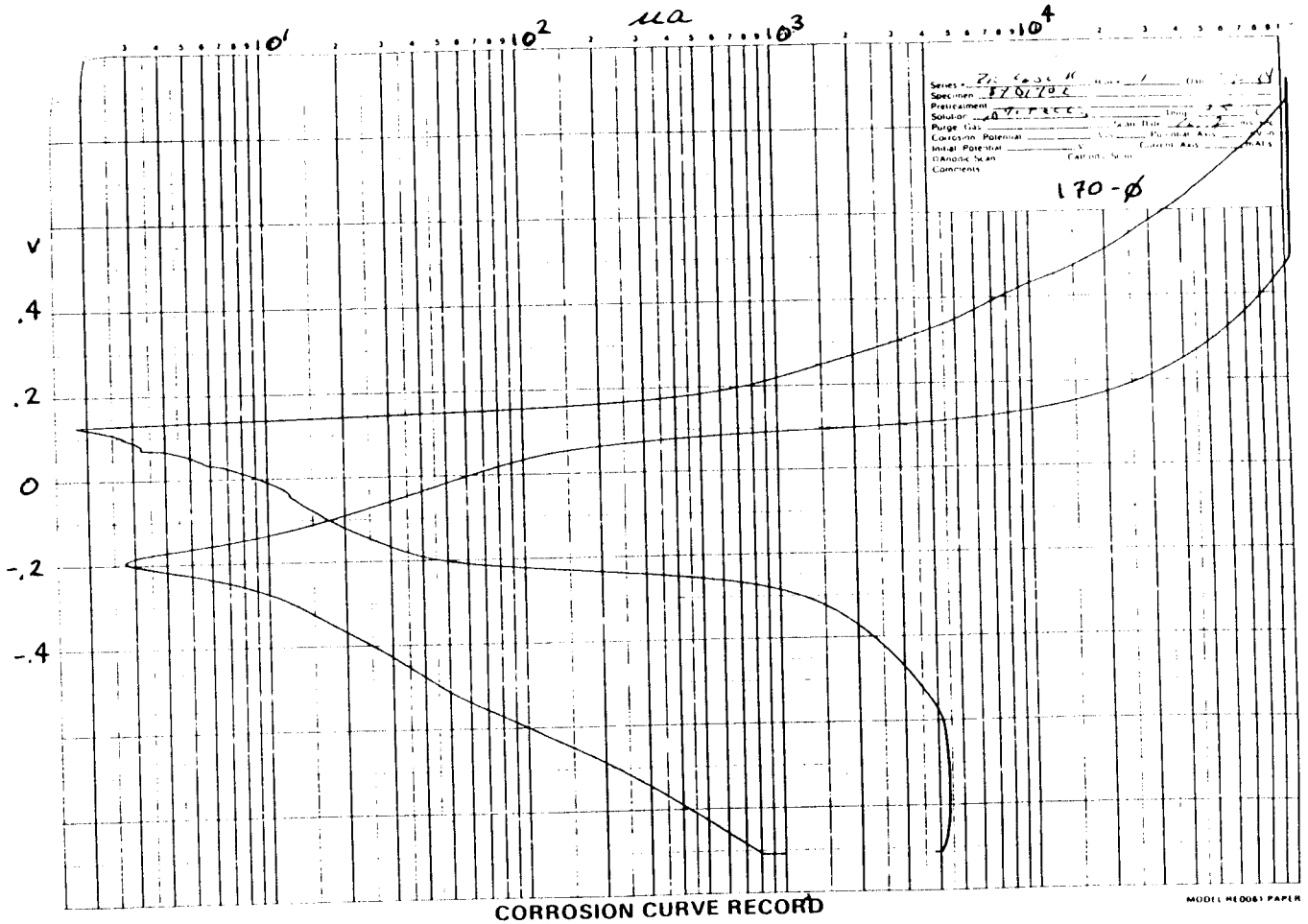

CORROSION CURVE RECORD

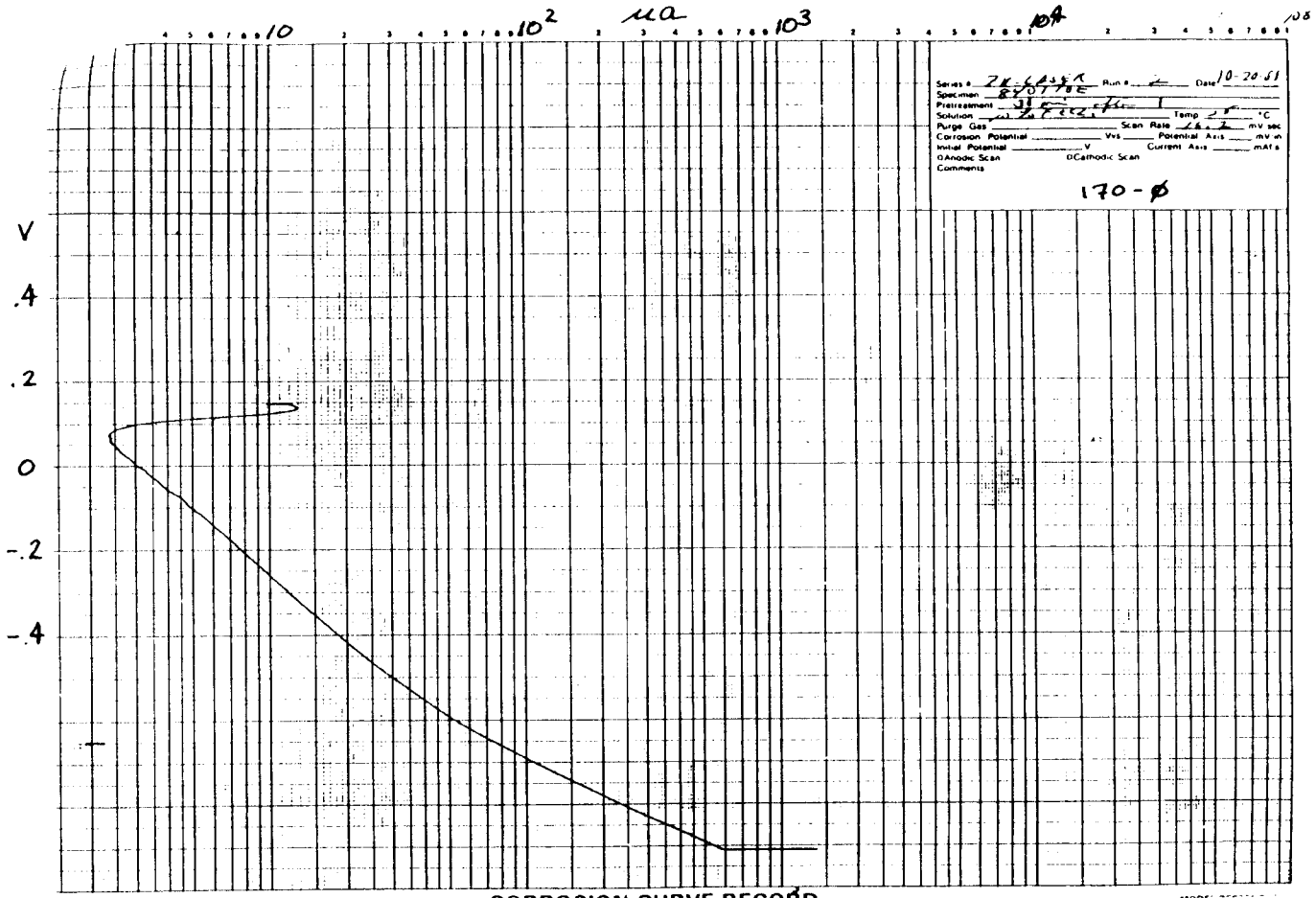

CORROSION CURVE RECORD

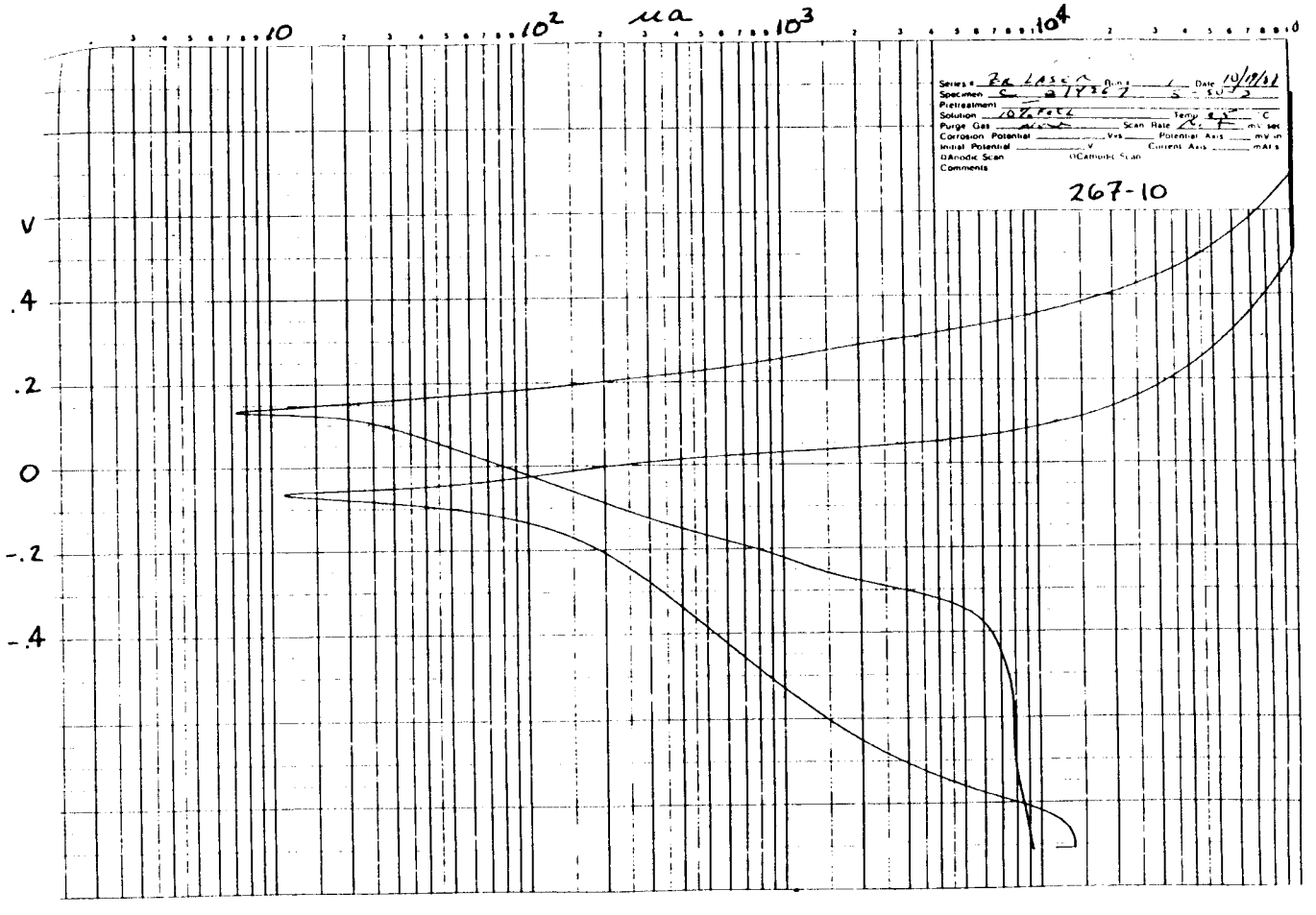
10
10²
μa
10³
10⁴
V
.4
.2
0
-.2
-.4
Series
Specimen
Pretreatment
Solution
Purge Gas
Corrosion Potential
Initial Potential
Anodic Scan
Comments
Date
Temp
Scan Rate
Potential Axis
Current Axis
Cathodic Scan
267-10

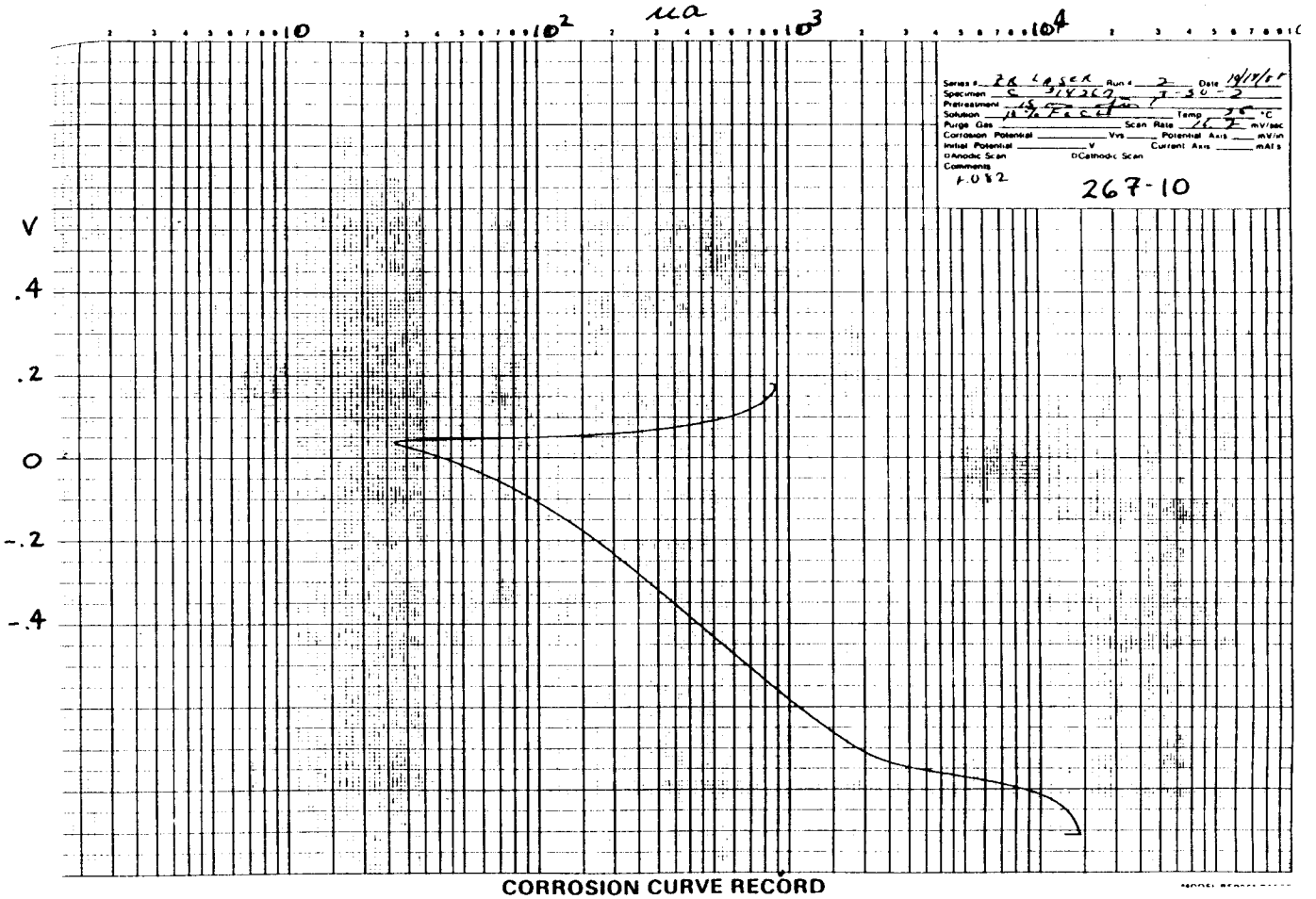

CORROSION CURVE RECORD

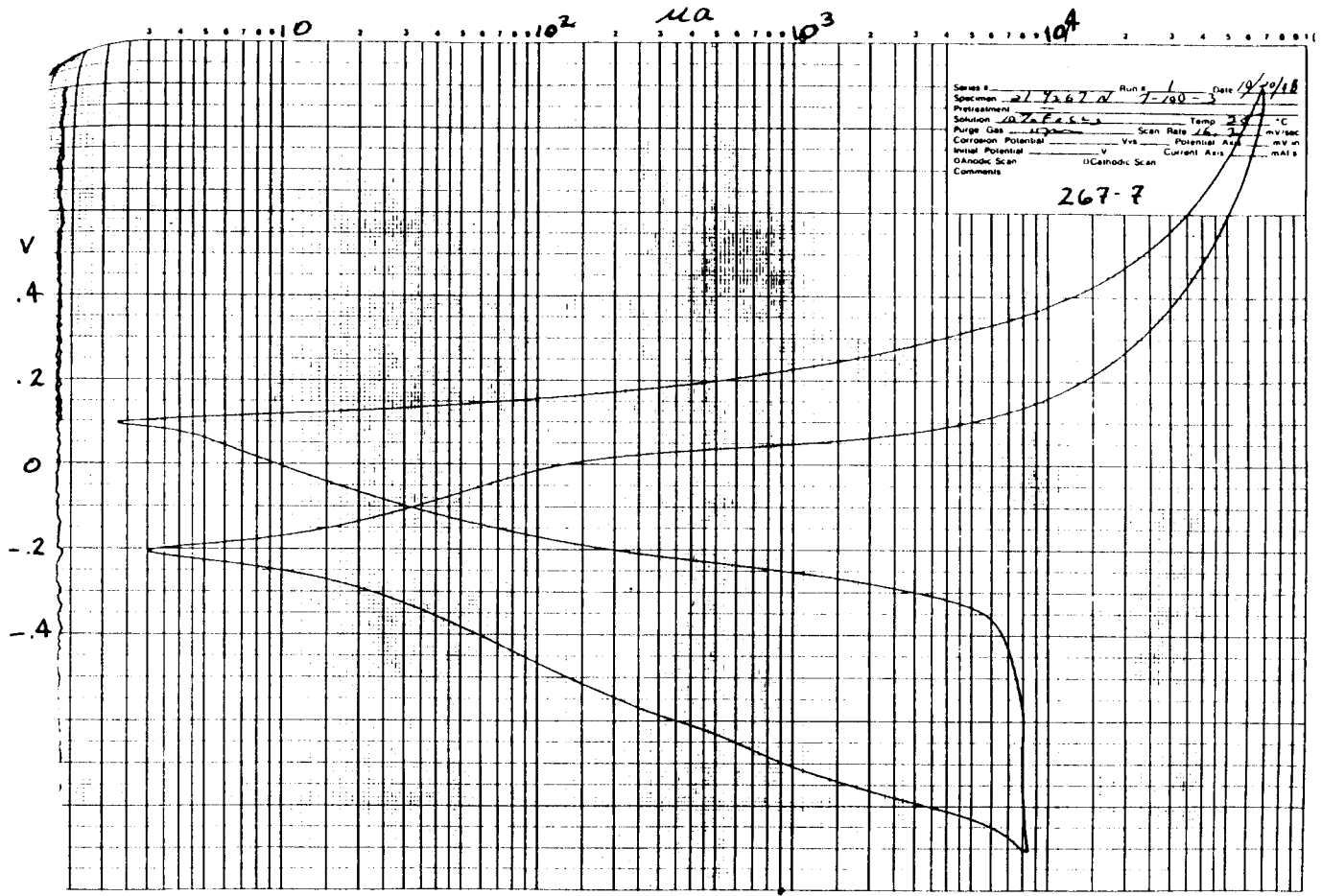

CORROSION CURVE RECORD

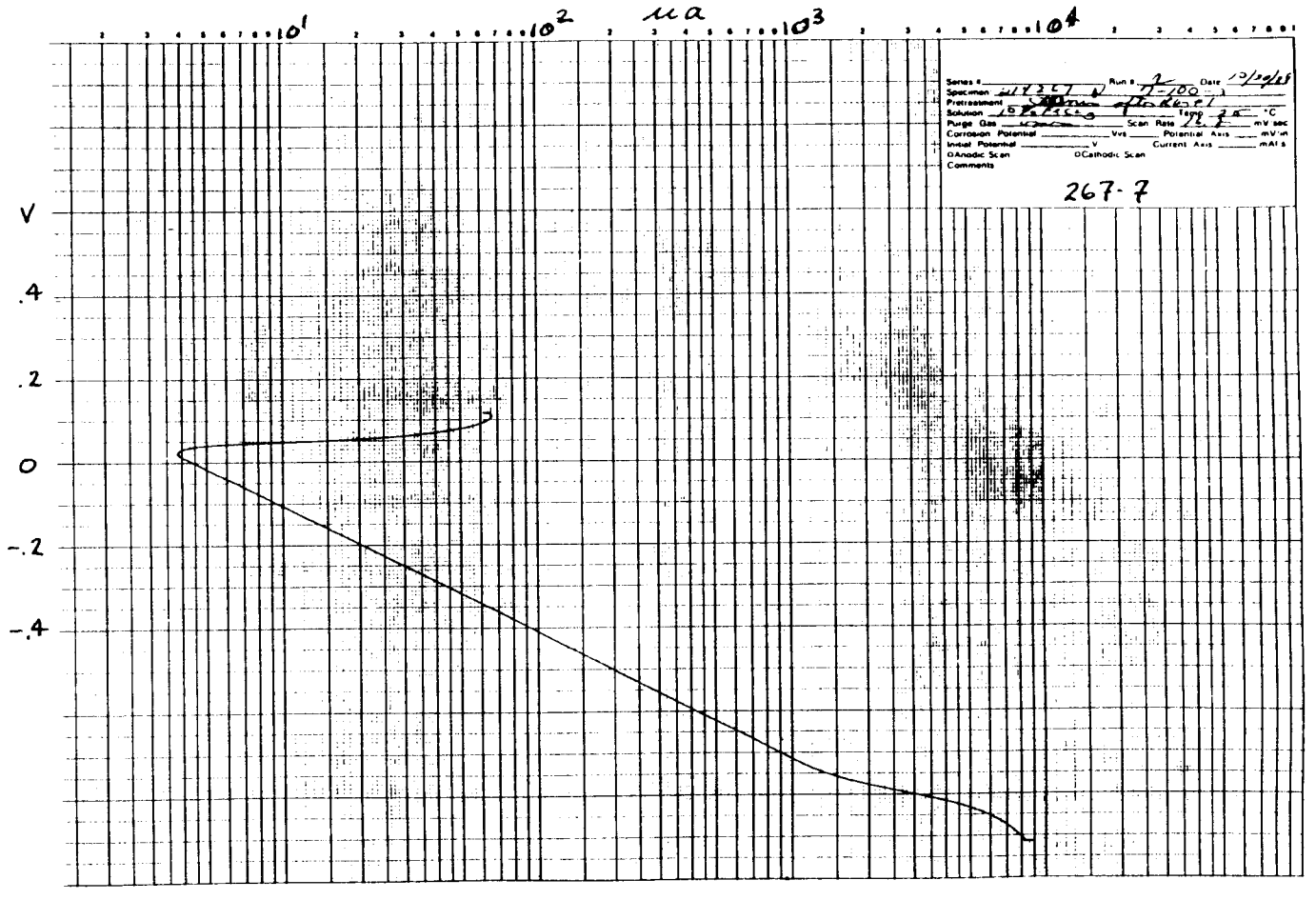
μa
10¹
10²
10³
10⁴
V
.4
.2
0
-.2
-.4
Series #
Run #
Date
Specimen
Pretreatment
Solution
Temp
°C
Purge Gas
Scan Rate
mV/sec
Corrosion Potential
Vvs
Potential Axis
mV/in
Initial Potential
V
Current Axis
mA/in
Anodic Scan
Cathodic Scan
Comments
267-7

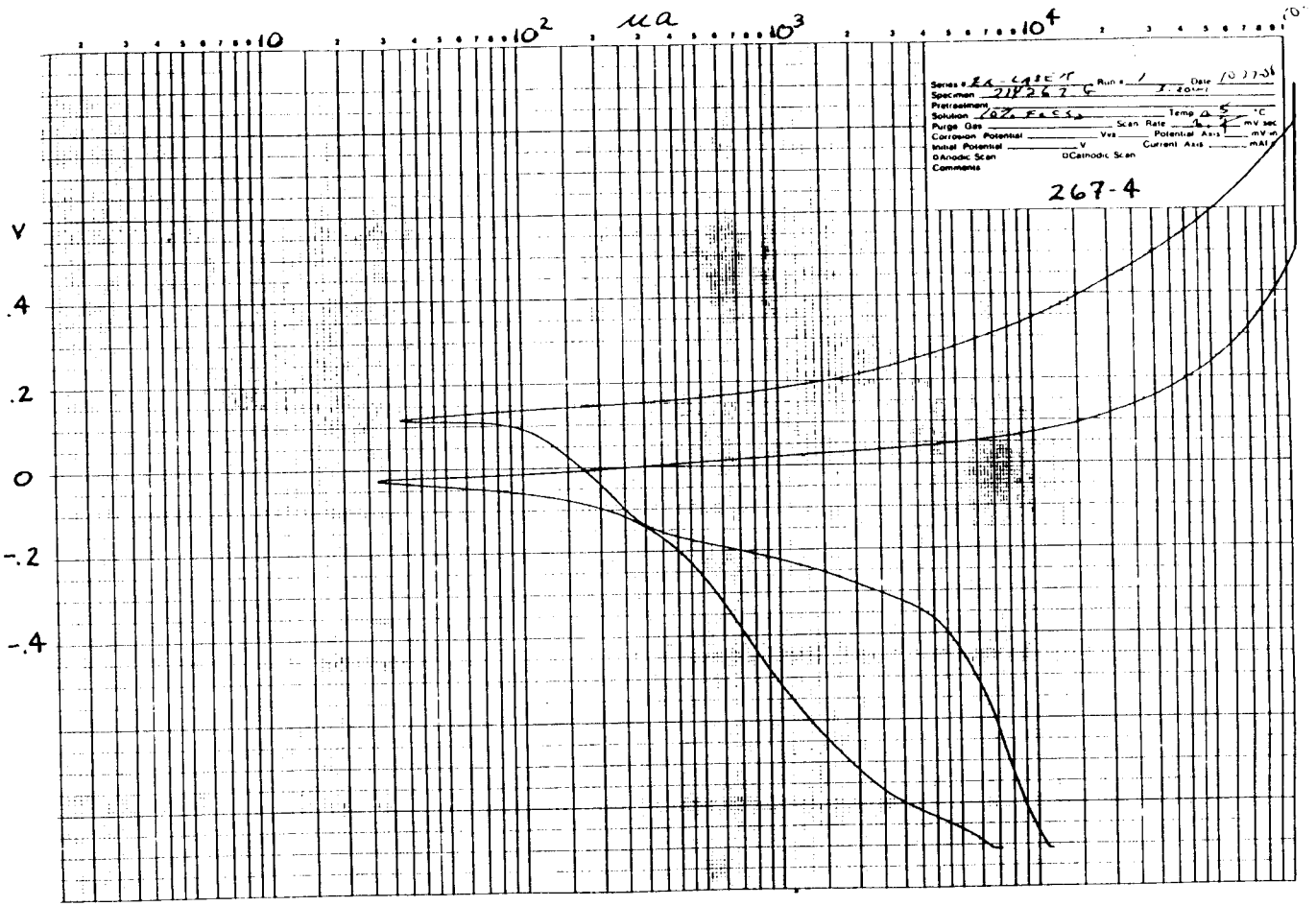
μa
10
10²
10³
10⁴
V
.4
.2
0
-.2
-.4
Series # Run # 1 Date
Specimen
Pretreatment
Solution Temp °C
Purge Gas Scan Rate mV/sec
Corrosion Potential Vvs Potential Axis mV/in
Initial Potential V Current Axis mA/
☐Anodic Scan ☐Cathodic Scan
Comments
267-4

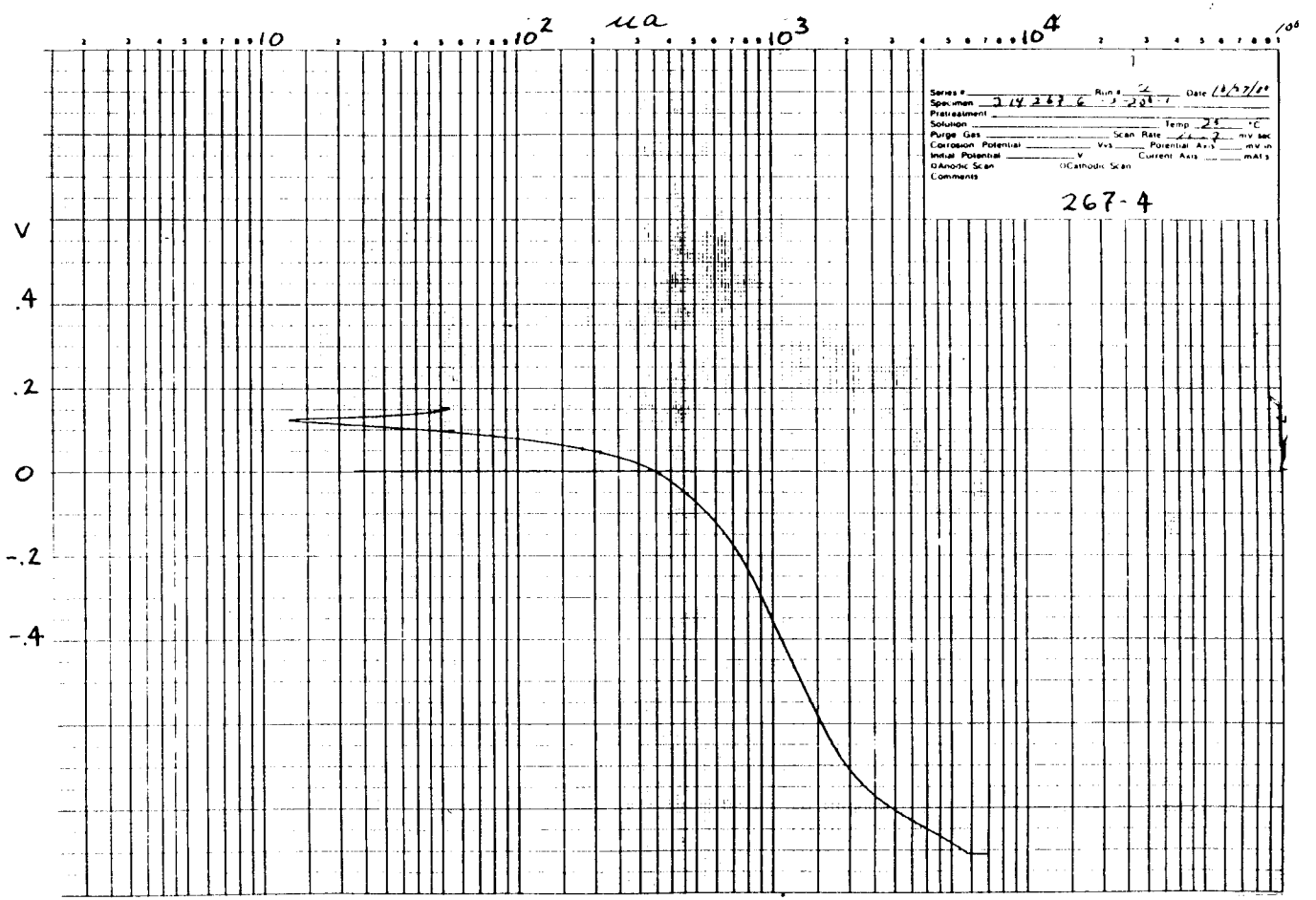
ua
10
10^2
10^3
10^4
10^5
V
.4
.2
0
-.2
-.4
Series #
Run #
Date
Specimen
Pretreatment
Solution
Temp 25 °C
Purge Gas
Scan Rate 2 mV sec
Corrosion Potential
Vvs
Potential Axis
mV in
Initial Potential
V
Current Axis
mA/s
Anodic Scan
Cathodic Scan
Comments
267-4

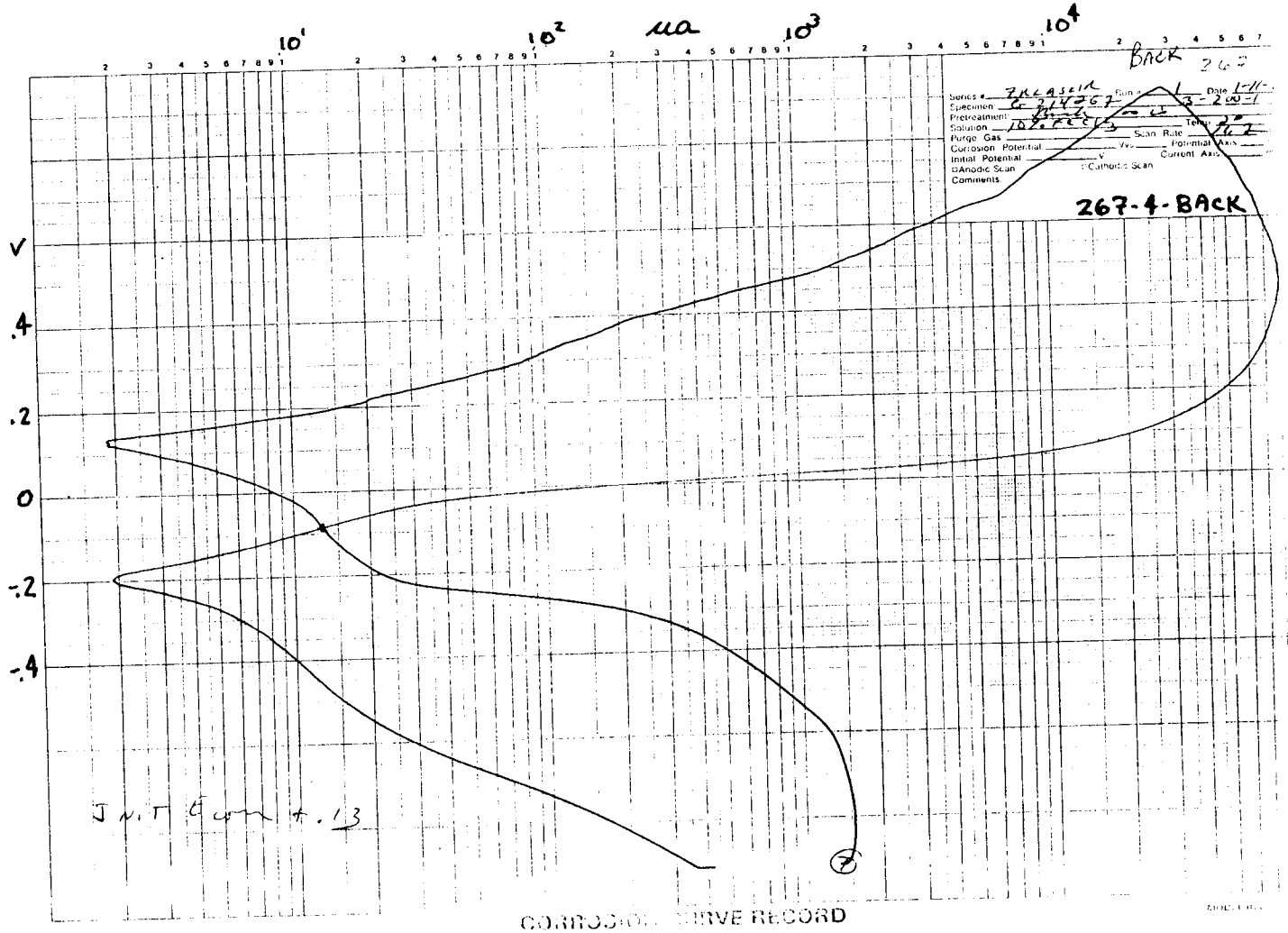
μa
10¹
10²
10³
10⁴
V
.4
.2
0
-.2
-.4
BACK 267
Series # 7KLASER
Date 1-11-
Specimen
Pretreatment
Solution
Purge Gas
Corrosion Potential
Initial Potential
Anode Scan
Cathode Scan
Comments
Scan Rate
Potential Axis
Current Axis
267-4-BACK
Int Com #.13
CORROSION CURVE RECORD

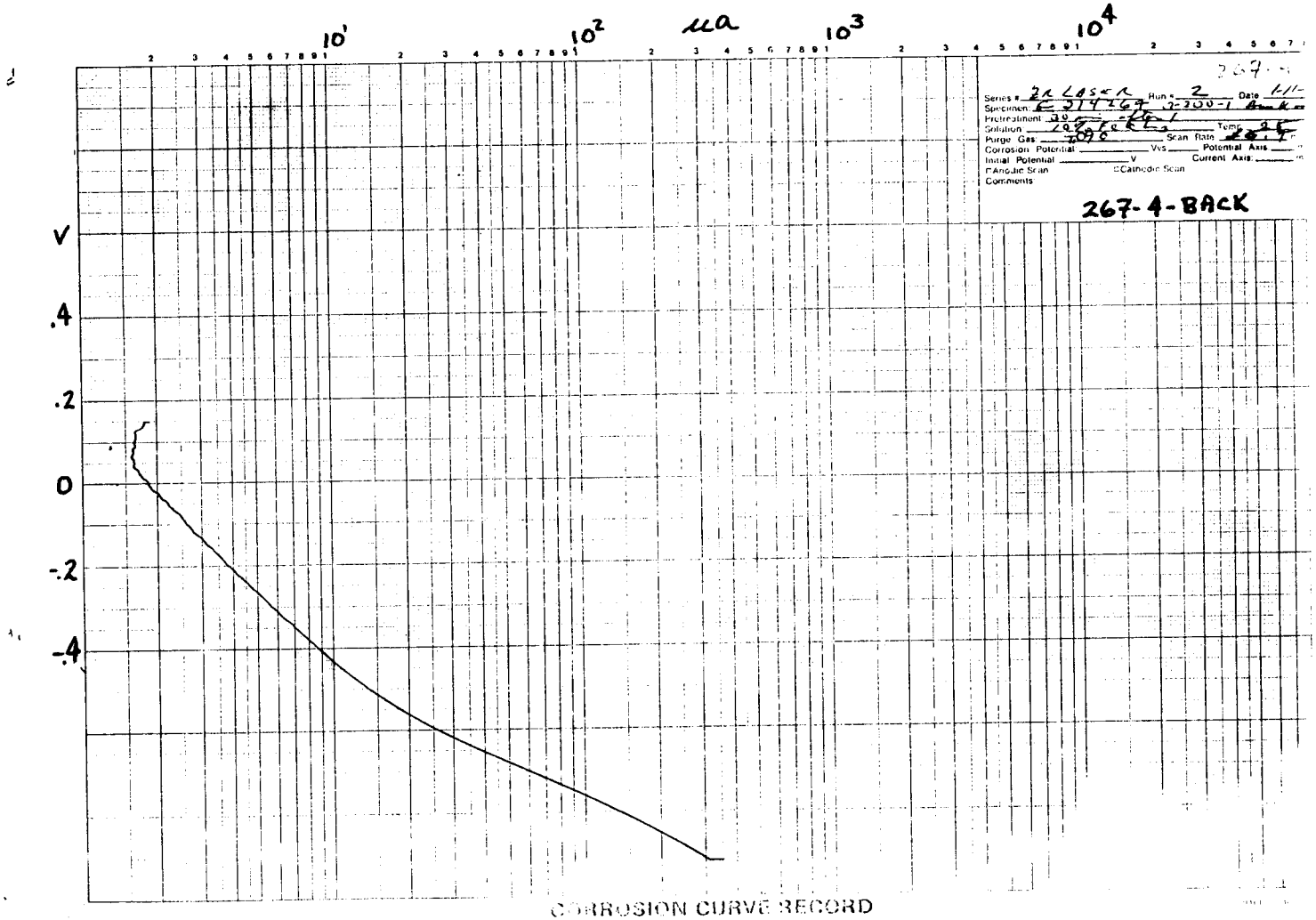

CORROSION CURVE RECORD

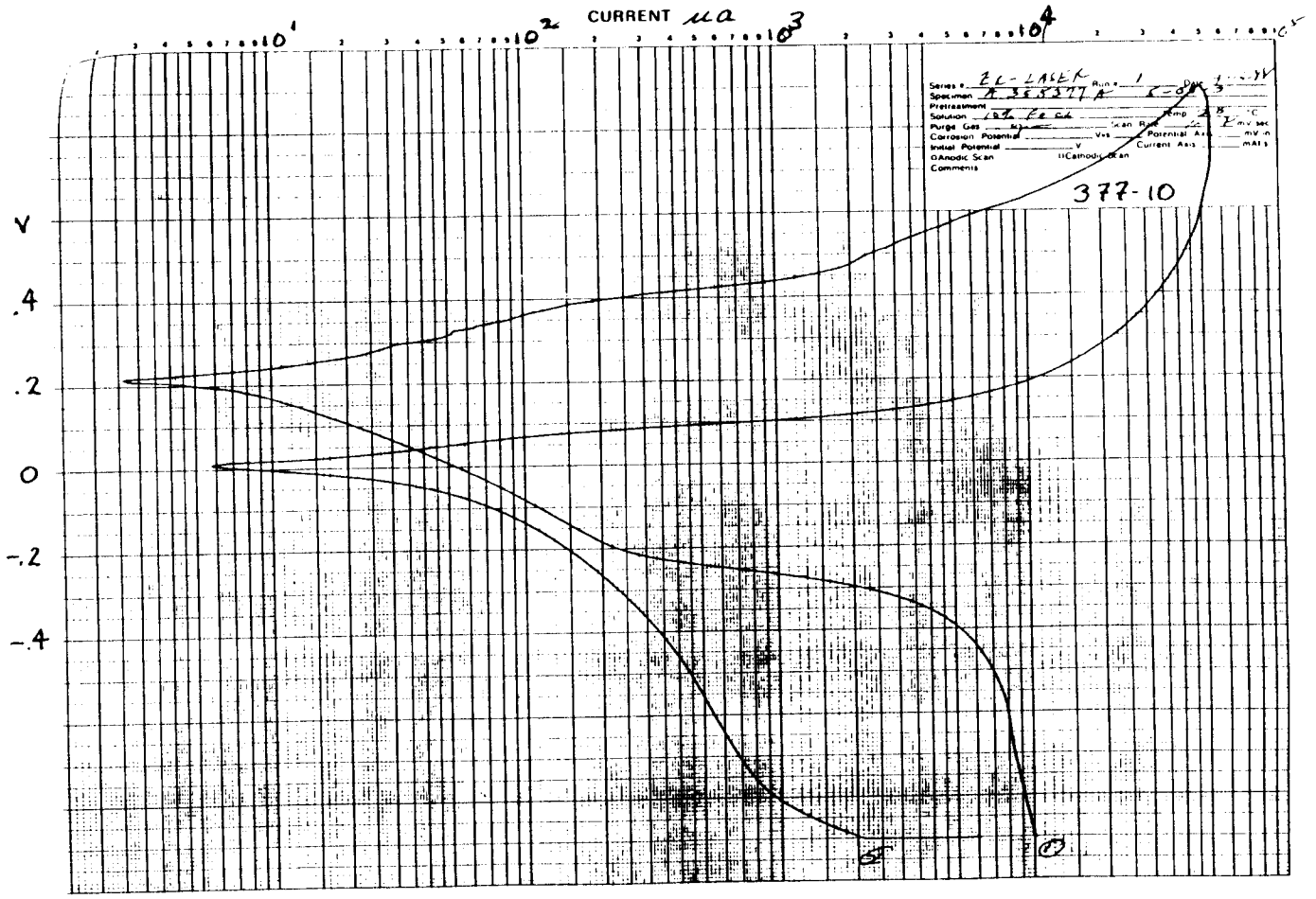
CURRENT μa
V
.4
.2
0
-.2
-.4
377-10

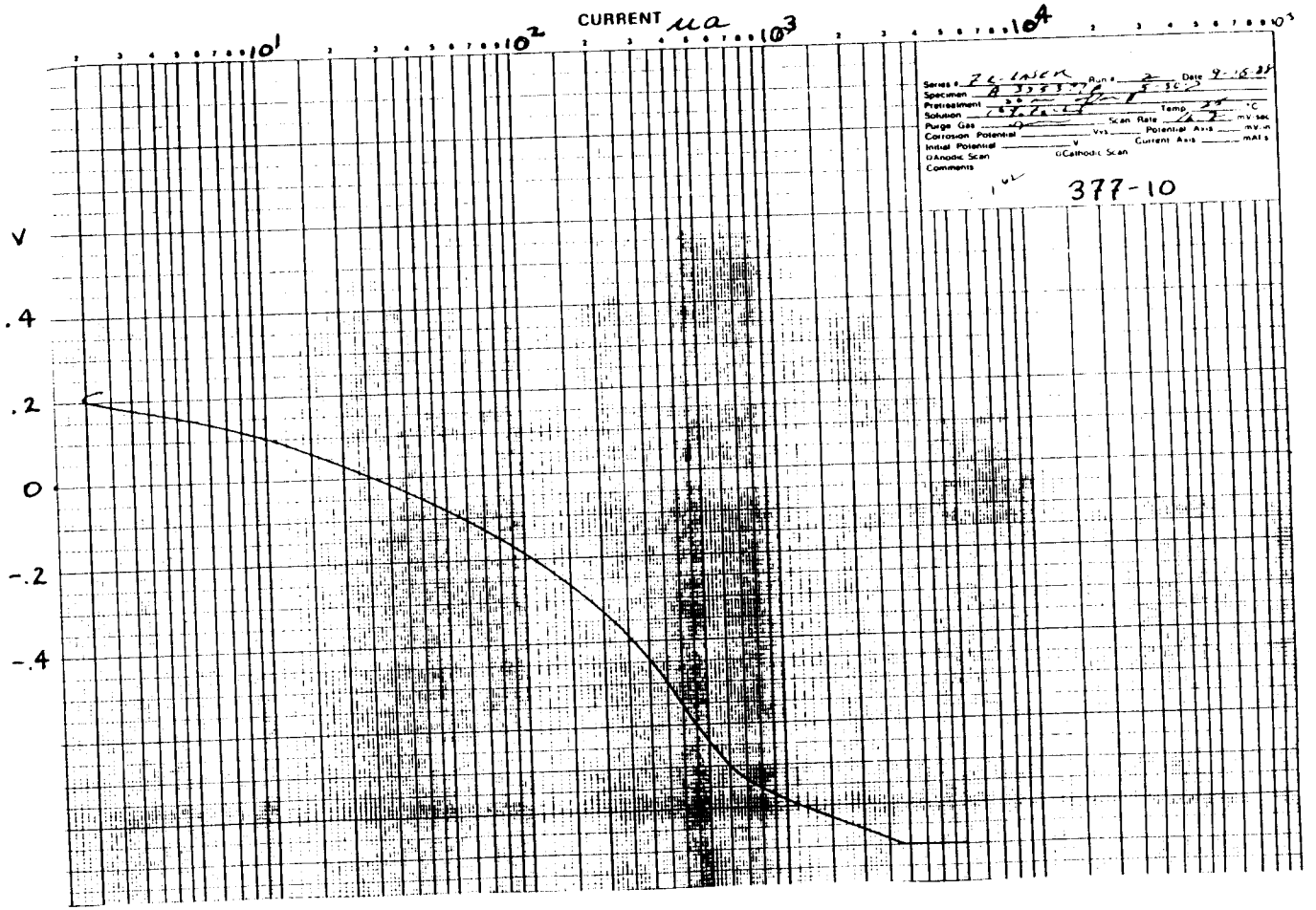
CURRENT μa
10¹
10²
10³
10⁴
V
.4
.2
0
-.2
-.4
Series # 26 LASER
Run # 2
Date 4-16-85
Specimen
Pretreatment
Solution
Temp 25 °C
Purge Gas
Scan Rate 1.2 mV sec
Corrosion Potential Vrs Potential Axis mV in
Initial Potential V
Current Axis mA's
Anodic Scan
Cathodic Scan
Comments
377-10

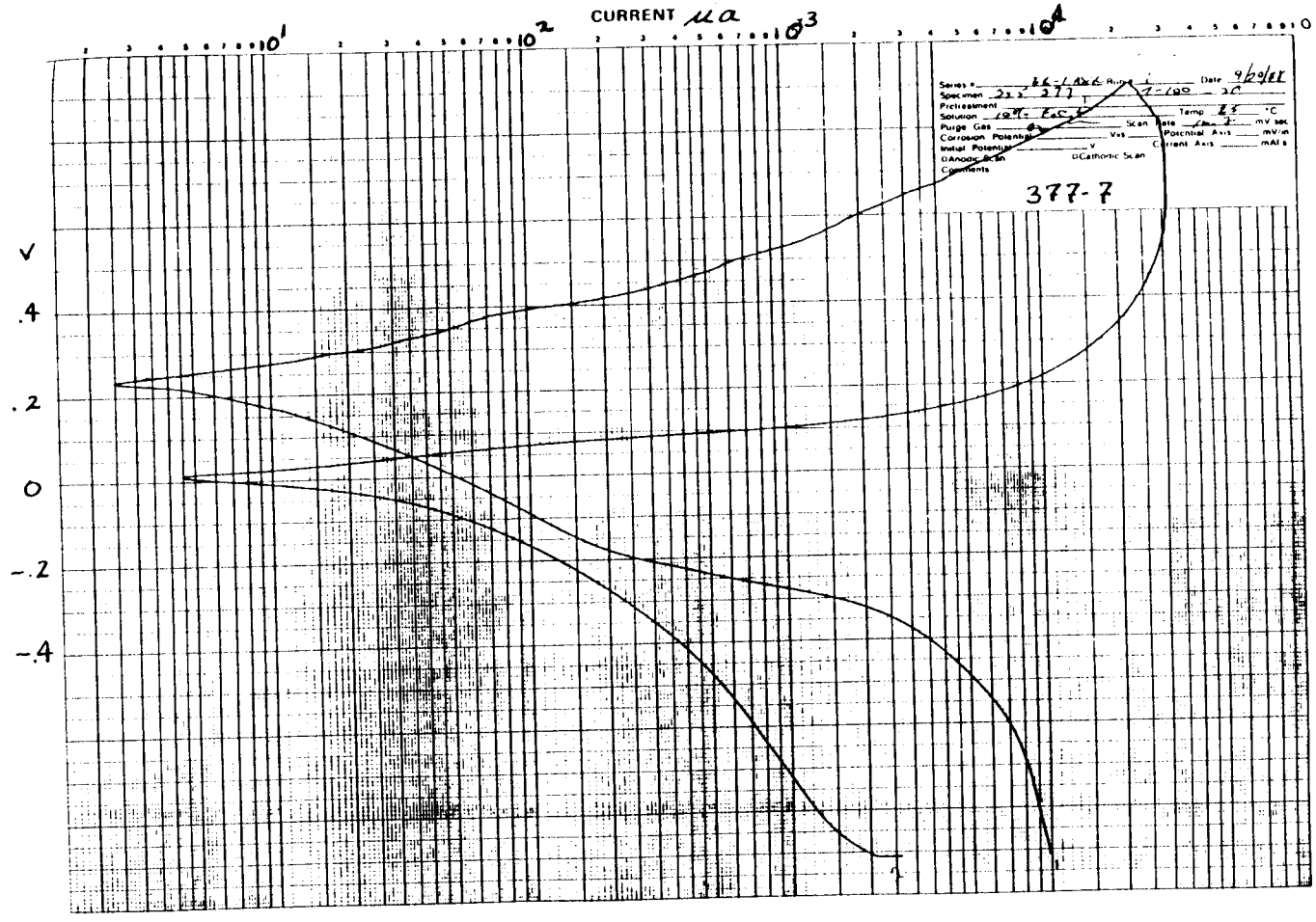
CURRENT μa
10¹
10²
10³
10⁴
V
.4
.2
0
-.2
-.4
Series # 66-1 4x6 Ring 1
Date 9/20/66
Specimen 377
Pretreatment
Solution
Temp 25 °C
Purge Gas
Scan Rate
mV sec
Corrosion Potential
Vs
Potential Axis
mV/in
Initial Potential
V
Current Axis
mA/in
Anodic Scan
Cathodic Scan
Comments
377-7

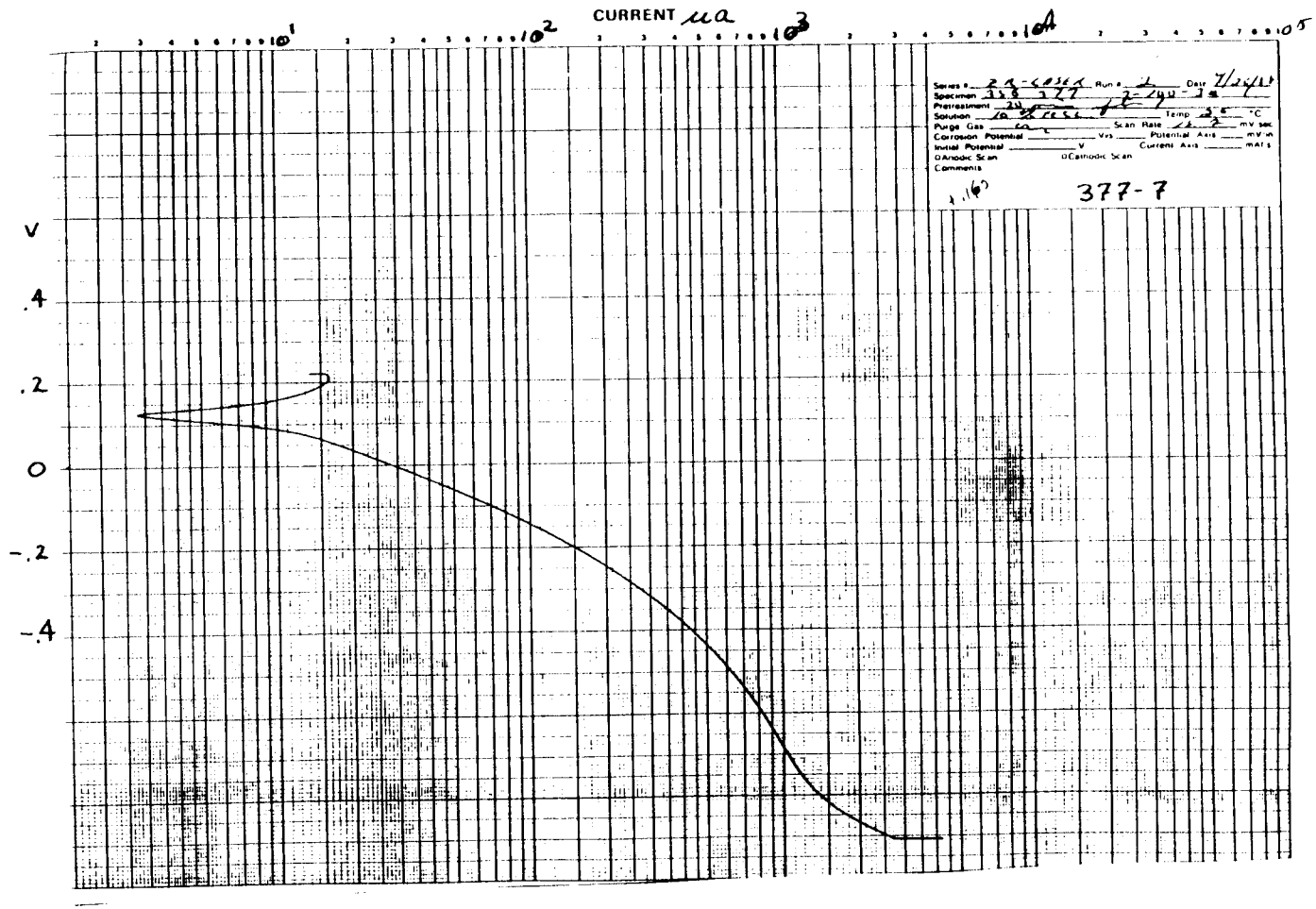
CURRENT μa
V
.4
.2
0
-.2
-.4
377-7

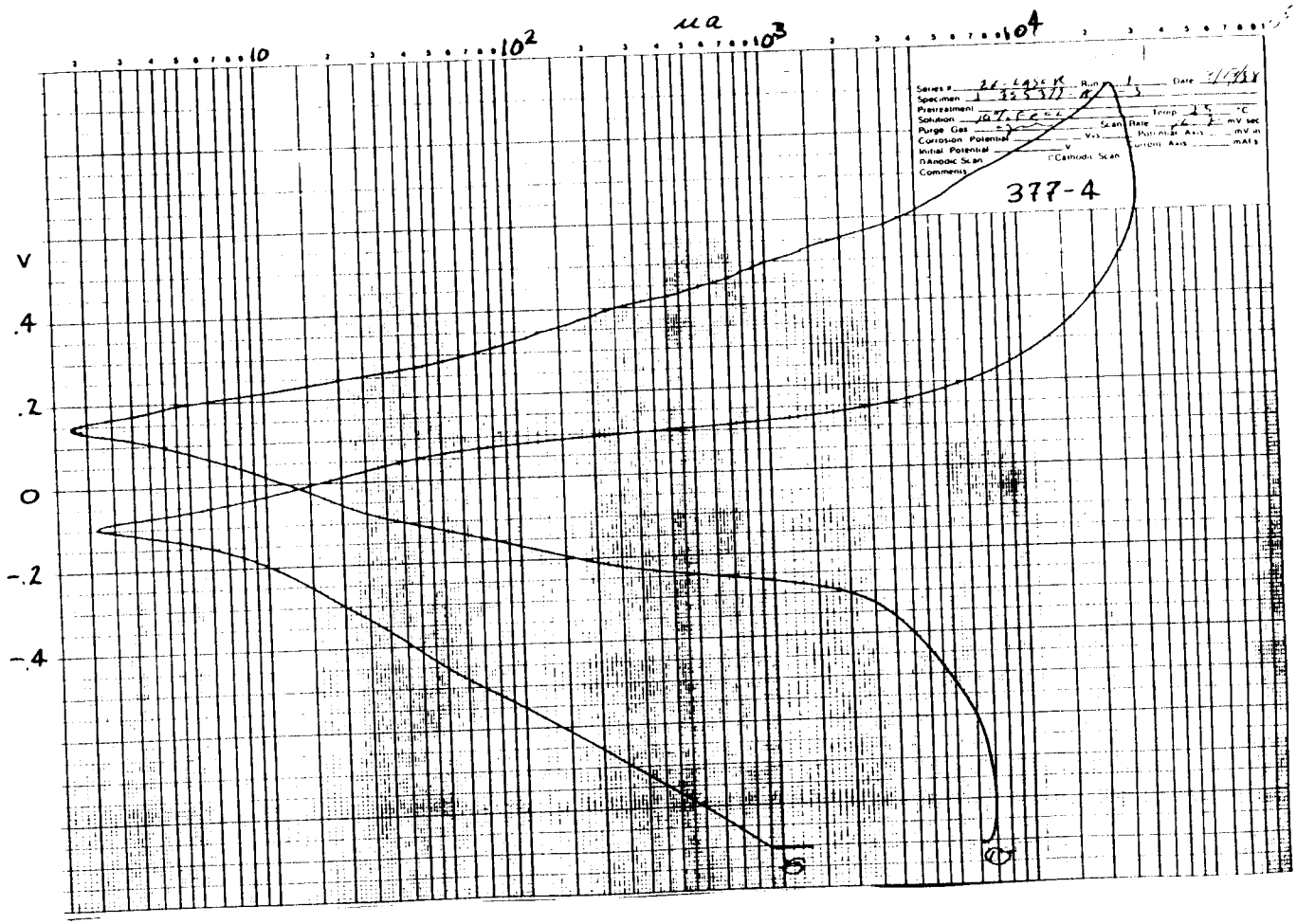
ua
10
10^2
10^3
10^4
V
.4
.2
0
-.2
-.4
377-4

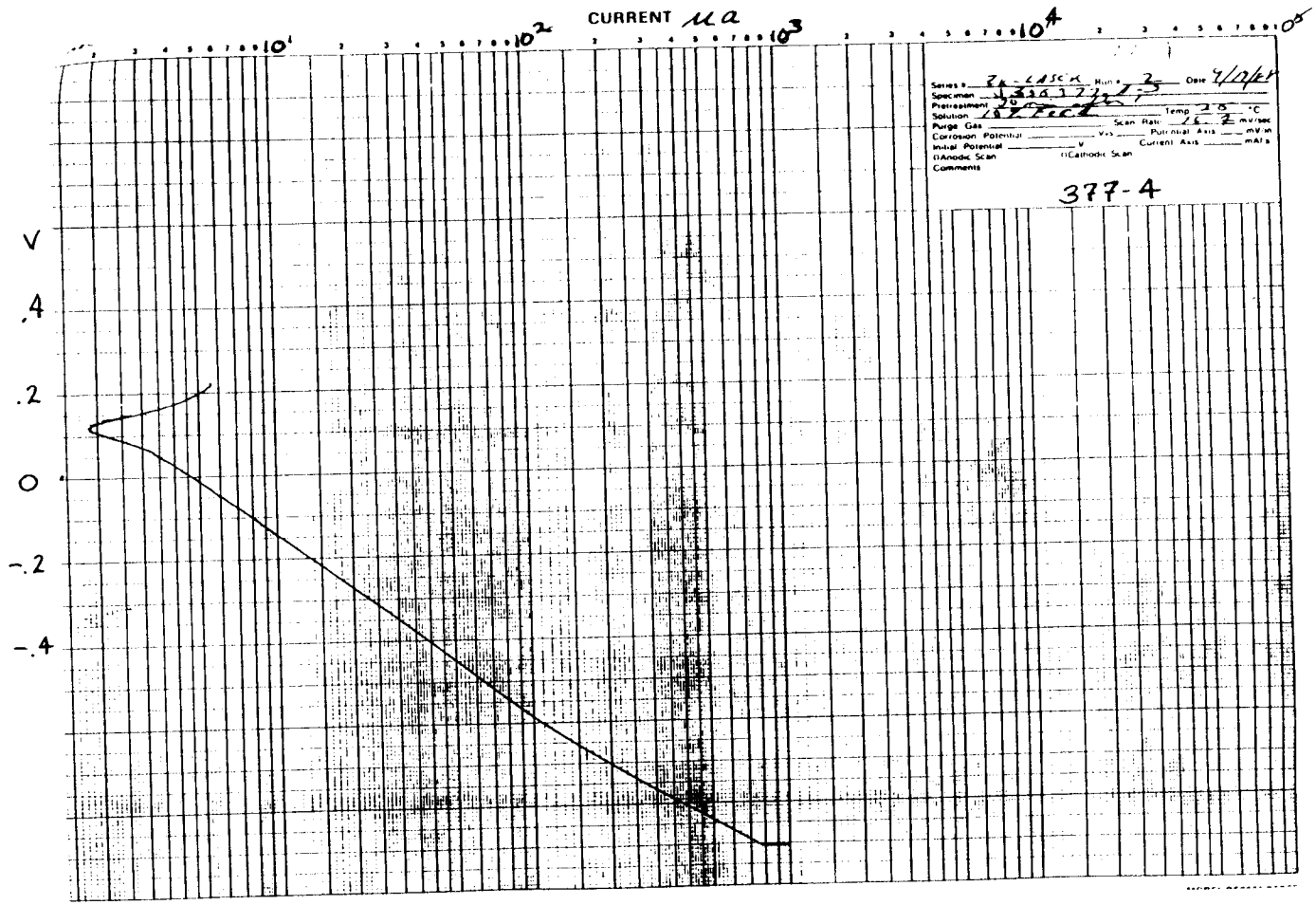
CURRENT μa
V
.4
.2
0
-.2
-.4
Series
Run
Date
Specimen
Pretreatment
Solution
Temp °C
Purge Gas
Scan Rate mv/sec
Corrosion Potential V vs
Potential Axis mV/in
Initial Potential V
Current Axis mA/in
Anodic Scan
Cathodic Scan
Comments
377-4

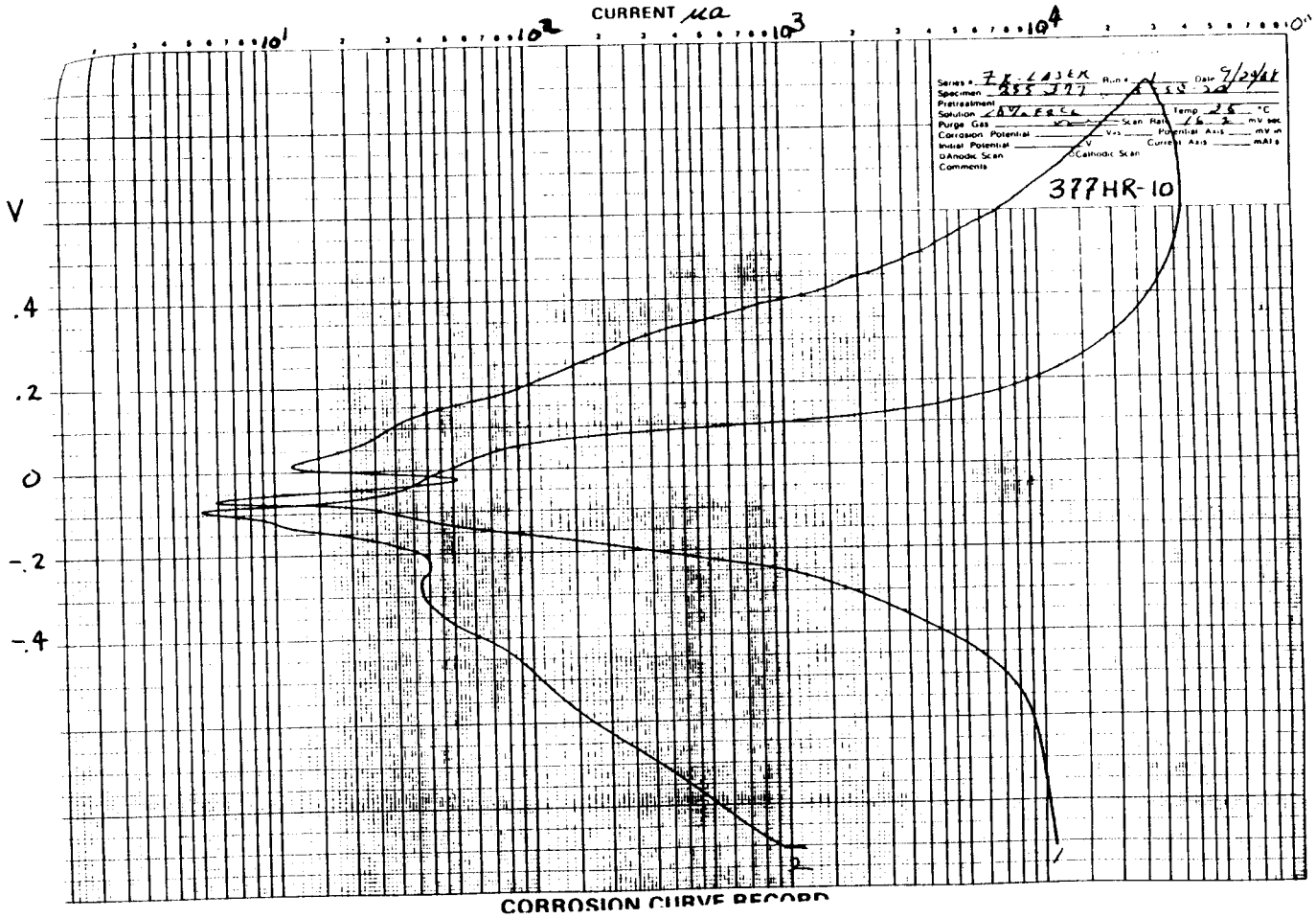
CURRENT μa
V
.4
.2
0
-.2
-.4
Series
Specimen
Pretreatment
Solution
Purge Gas
Corrosion Potential
Initial Potential
Anodic Scan
Cathodic Scan
Comments
Run
Date
Temp
Scan Rate
Potential Axis
Current Axis
377HR-10
CORROSION CURVE RECORD

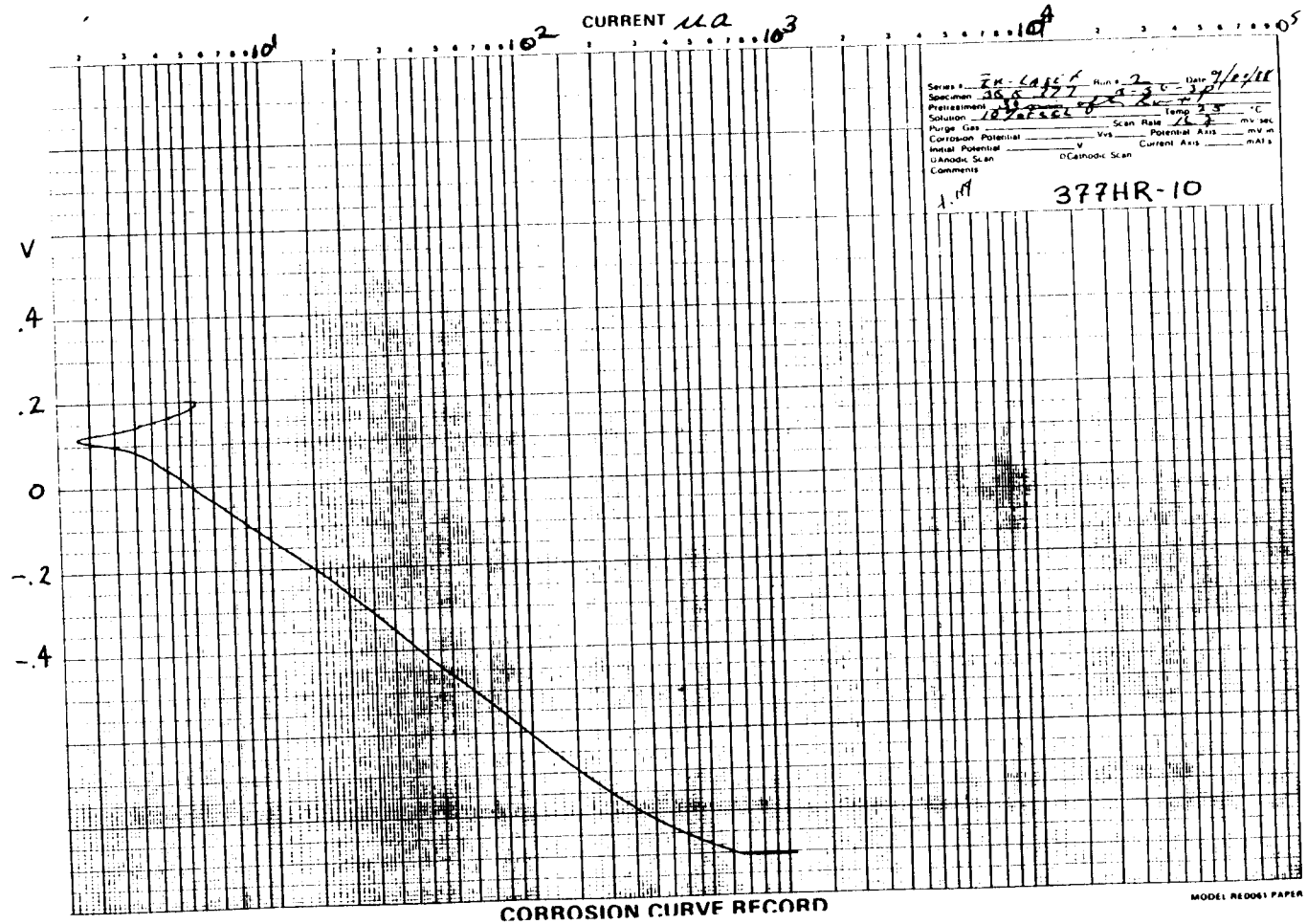
CURRENT μa
10^1
10^2
10^3
10^4
10^5
V
.4
.2
0
-.2
-.4
Series # ZH-LAFC-4 Run # 2 Date 9/20/88
Specimen 304 SS
Pretreatment
Solution 10% NaCl
Temp 23 °C
Purge Gas
Scan Rate 1.2 mV/sec
Corrosion Potential Vvs Potential Axis mV/in
Initial Potential V Current Axis mA/in
Anodic Scan
Cathodic Scan
Comments
377HR-10
CORROSION CURVE RECORD
MODEL RE0061 PAPER

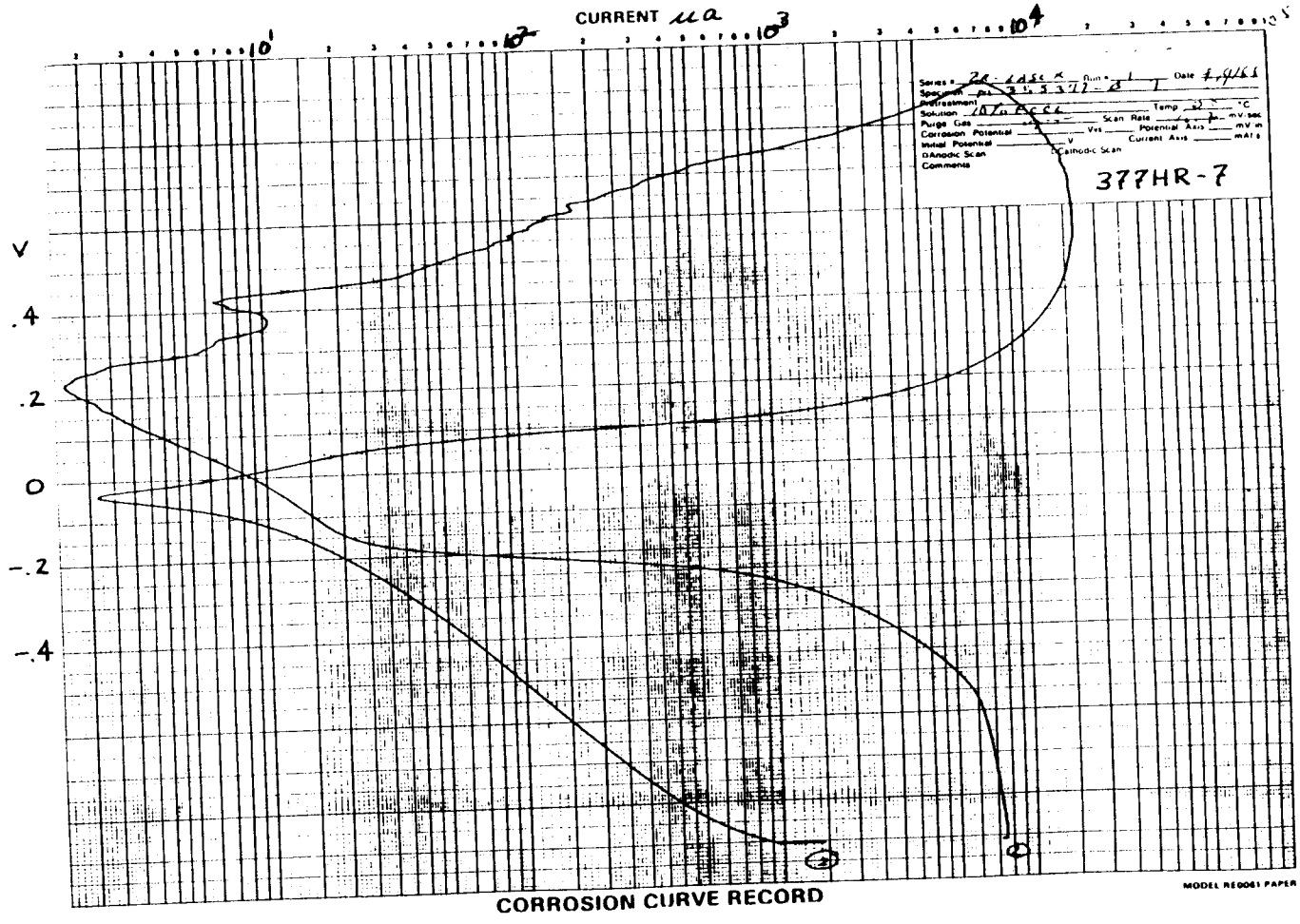

CORROSION CURVE RECORD

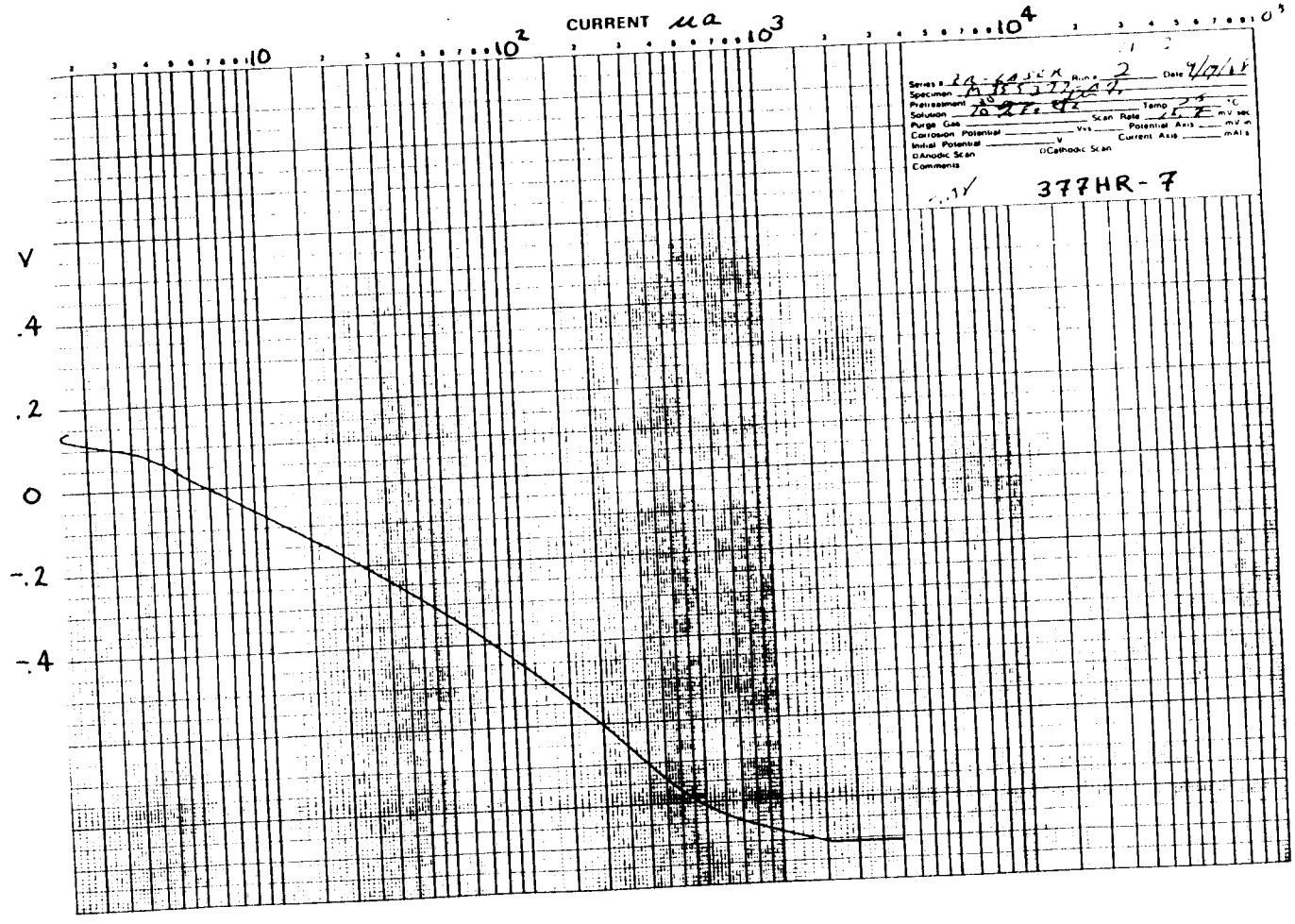
CURRENT μa
10
10^2
10^3
10^4
10^5
V
.4
.2
0
-.2
-.4
Series
Run 2
Date
Specimen
Pretreatment
Temp °C
Solution
Scan Rate mV/sec
Purge Gas
Corrosion Potential Vvs
Potential Axis mV/in
Initial Potential V
Current Axis mA/s
Anodic Scan
Cathodic Scan
Comments
377HR-7

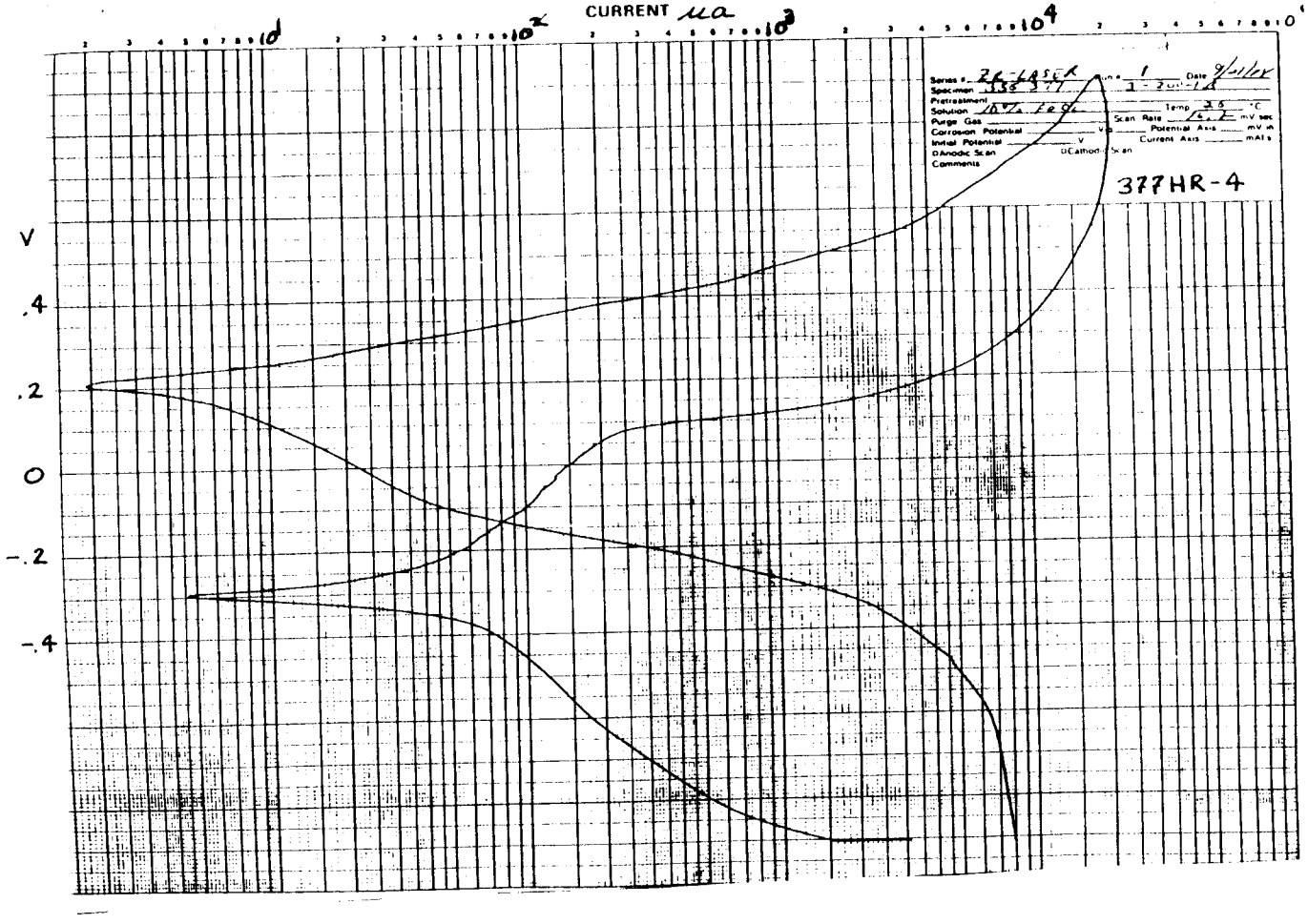
CURRENT μa
V
.4
.2
0
-.2
-.4
377HR-4

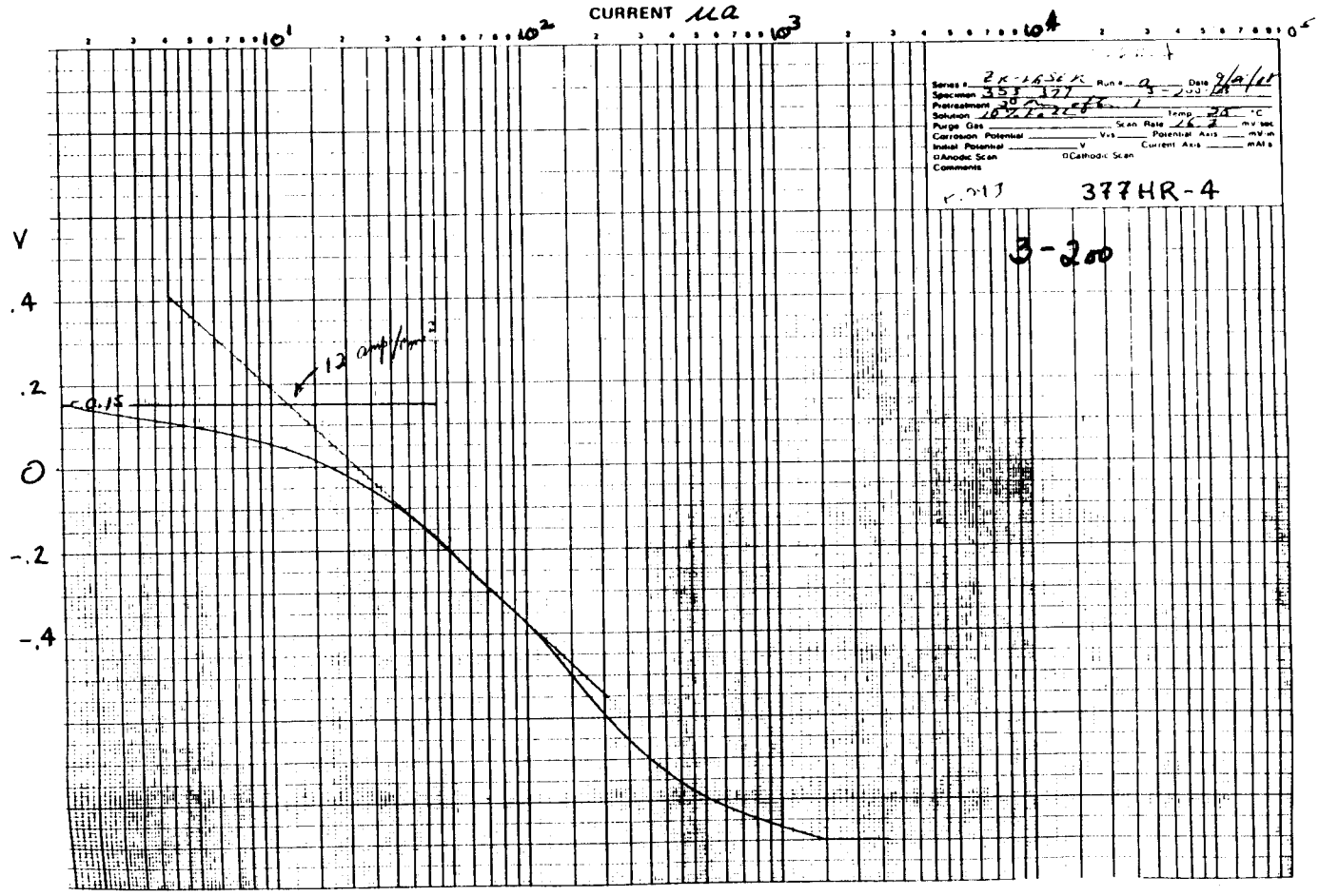
CURRENT μa
V
.4
.2
0
-.2
-.4
-0.15
12 amp/cm²
Series # 2K-16SCR Run # a Date 9/a/ee
Specimen 353 377 3-200 24
Pretreatment 30 min coff 1
Solution 10% H2SO4 Temp 25 °C
Purge Gas Scan Rate 16.2 mv/sec
Corrosion Potential Vs Potential Axis mV/in
Initial Potential V Current Axis mA/in
Anodic Scan Cathodic Scan
Comments
377HR-4
3-200